Distances, Kinematics, and Structure of Nearby Star-forming Regions

by

Marina Alexandrovna Kounkel

A dissertation submitted in partial fulfillment
of the requirements for the degree of
Doctor of Philosophy
(Astronomy and Astrophysics)
in The University of Michigan
2017

Doctoral Committee:

Professor Lee W. Hartmann, Chair
Professor Fred C. Adams
Professor Nuria P. Calvet
Professor Laurent Loinard, National University of Mexico

mkounkel@umich.edu
ORCID ID:0000-0002-5365-1267

TABLE OF CONTENTS

CHAPTER

LIST OF FIGURES

Figure

LIST OF TABLES

Table

LIST OF APPENDICES

Appendix

ABSTRACT

In this thesis I present an analysis of the structure and kinematics of the Orion Molecular Cloud Complex in an effort to better characterize the dynamical state of the closest region of the ongoing massive star formation and to provide a baseline for comparison of the upcoming results from the Gaia space telescope. In order to achieve this goal, I measured stellar parallax and proper motions, using very large baseline radio interferometry of non-thermally-emitting sources.. Based on these observations I measured the average distance in Orion A molecular cloud of 388±5 pc toward the Orion Nebula Cluster (ONC), 428±10 pc toward the southern portion of L1641, as well as the distance in Orion B of 388±10 pc toward NGC 2068, and roughly ∼420 pc toward NGC 2024. These are the first direct distance measurements with $< 5\%$ uncertainty to the regions within the Orion Complex outside of the ONC. Little can be said about the proper motions due to the sparcity of the sample size; however, I identified a number of binary systems and fitted their orbital motion, which allows for the direct measurement of the masses of the individual components. I also identified three stars that have been ejected from the ONC due to the gravitational interactions with its most massive stars.

I complemented the parallax and proper motion measurements with the observations of radial velocities (RV) of the stars toward the Orion Complex, probing the histories of both dynamic evolution and star formation in the region. I found that in the Orion A cloud and in NGC 2024 there exists an asymmetry between the stellar RVs and those of the molecular gas, with a small fraction of the stars stars being preferentially blueshifted relative to the gas. Several possible explanations for this

have been proposed, although presently there is not yet a definitive solution. I also analyzed the multiplicity fraction of the spectroscopic binaries in the ONC, and found that it is largely consistent to what is observed in the nearby field stars.

Finally, I explored the substructure of the ONC by focusing on NGC 1980, a cluster that has previously been identified as foreground to and older than the ONC. I examined these claims to show that there is little evidence that there is a discrepancy in distance between the stellar populations of the ONC and NGC 1980. Additionally, while the stars of NGC 1980 are likely somewhat older than the ONC, their age is consistent with the stellar population of the rest of the Orion A molecular cloud.

CHAPTER I

Introduction

1.1 Properties of star forming clouds

The distribution of gas in the Milky Way is not uniform. Spiral galaxies such as our own contain density waves which result in concentrations of the massive stars and gas along the spiral arms. While individual stars can easily pass through a density wave unobstructed, small clumps of gas collide, grow denser and more massive (Binney & Tremaine, 1987). The dense gas cools down further as the outer layers shield the inner regions from the ionizing photons of the surrounding stars, which, in turn, results in formation of first neutral, and later molecular gas. Stellar feedback (supernovae and solar winds) further assist in this process by piling the gas together.

The giant molecular clouds that form as a result span tens or even hundreds of parsecs in size and have total masses of up to 10^6 $\mathrm{M}_\odot$, have typical temperatures T ∼10—20 K and average densities ρ ∼100—1,000 cm^{-3}. Individual dense patches may become self-gravitating and begin to collapse if a patch is more massive than the Jeans mass M_J (Jeans, 1902) such that

$$M_J = \left(\frac{\pi c_s^2}{G}\right)^{3/2} \rho_\circ^{-1/2} \sim 1\ \mathrm{M}_\odot \left(\frac{T}{10\ \mathrm{K}}\right)^{3/2} \left(\frac{n_{H_2}}{10^4\ \mathrm{cm}^{-3}}\right)^{-1/2}$$

where c_s is the sound speed. While c_s is low ~ 0.2 km s^{-1}, observations of the molecular lines in the molecular clouds show supersonic "turbulent" motions $\sim 2\,\mathrm{km\,s^{-1}}$ (e.g., Bally et al., 1987). Various suggestions have been made to explain this supersonic driving, with one likely possibility being gravitational collapse (Ballesteros-Paredes et al., 2011). These supersonic motions dissipate rapidly (Stone et al., 1998), via shocks that help produce the local increase of densities high enough to produce solar-mass self-gravitating molecular cloud cores. The resulting distribution and properties of cores in a cloud are dependent upon the original cloud geometry and kinematics - topics that I explore observationally in this thesis.

These cores can further collapse to form stars and protoplanetary disks (Section 1.3). The term young stellar object (YSO) has been used to identify newly-formed stars with and without disks and envelopes. A typical giant molecular cloud may form anywhere between few dozens to few thousands of stars. These stars may form a gravitationally bound cluster; 70–90% of all stars originate in clusters (e.g., Carpenter, 2000; Lada & Lada, 2003; Porras et al., 2003). Our Sun may have originally formed in a cluster with at least 1,000 members (Adams, 2010).

Star formation is not a particularly efficient process. Globally, only a few percent of the mass of the available gas will be converted into stars (e.g., Leroy et al., 2008), although in the inner region of a cluster, the star formation efficiency may rise to as much as ∼50% (Hillenbrand & Hartmann, 1998). The remaining gas will be quickly dissipated through stellar feedback, which includes stellar winds and supernovae, after a few Myr.

Disruption of the gas by stellar feedback can then result in many of the stars becoming gravitationally unbound, and they will disperse. The surviving open clusters will also eventually disperse due to gravitational interactions with other molecular clouds (Binney & Tremaine, 1987). Only ∼5% of the clusters currently being formed in the Galaxy may survive to the ages of 100 Myr (Lada & Lada, 2003).

1.2 Overview of the local star-forming regions

The Gould's Belt is a ring encompassing nearby star forming regions that is tilted relative to the plane of the Milky Way by about 15° (Figure 1.1). Whether or not Gould's Belt is a real structure formed 30 Myr ago, possibly formed by a series of supernovae that warped the galactic disk locally, (e.g., Pöppel & Marronetti, 2000), a collision with either high velocity HI clouds (e.g., Comeron & Torra, 1994) or dark matter (e.g., Bekki, 2009), or it is merely a result of the initial local kinematics of the Galaxy (e.g., Olano, 2001) is still debated.

The closest young association of O and B stars is the Scorpius-Centaurus OB2. It can be subdivided into three individual groups, Upper Scorpius (US), Upper Centaurus-Lupus (UCL), an Lower Centaurus-Crux (LCC), with the ages ranging between 11 to 17 Myr (Pecaut et al., 2012), and the distances ranging between 118 to 145 pc (de Zeeuw et al., 1999). It is unclear whether or not these groups were a part of any clusters, but the current consensus is that all of these groups are unbound and merely constitute expanding co-moving groups.

There is no ongoing star formation in the Sco-Cen OB Association; however, a number of significantly younger star-forming clouds are nearby. Particularly, Ophiuchus and Lupus molecular cloud complexes appear to share the 3d spatial bounds with Sco-Cen. Whether the recent star formation has been triggered by an explosive event in the Upper Scorpius that occured a few Myr ago (Preibisch & Zinnecker, 1999; Tachihara et al., 2001), or the earliest epoch of star formation in these clouds predate the possible trigger event and Sco-Cen, Ophiuchus, and Lupus are merely a part of a larger structure (Wilking et al., 2005) is still unclear. Moreover, there are a number of isolated stellar groups, such as the TW Hya and β Pic associations, ϵ and η Chamaeleontis groups, as well as Corona Australis (CrA) and Chameleon molecular clouds that may have originated in vicinity of Sco-Cen OB Association (Mamajek & Feigelson, 2001).

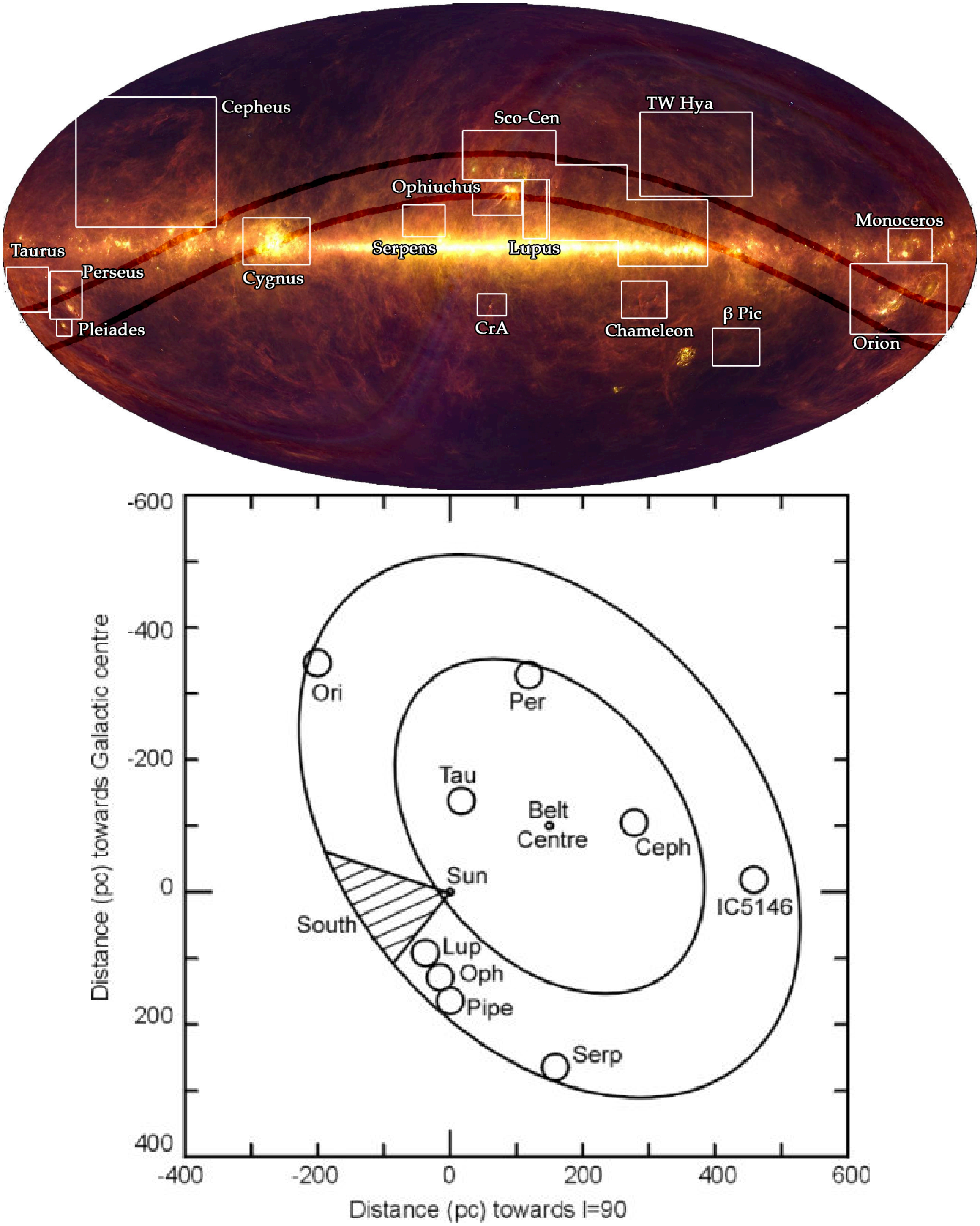

Figure 1.1 Top: Gould's Belt and indentification of the nearby star-forming regions superimposed onto the IRAS map. Bottom: Top-down view of the Gould's Belt from Ward-Thompson et al. (2007) Surrounding the Sun is the Local Bubble, a region that is significantly depleted in gas compared to the typical interstellar medium densities. The local clouds lie on the periphery of the Local Bubble.

The Taurus-Auriga molecular cloud is also found at the distance of ∼150 pc (Loinard et al., 2007). It is most notable as one of the most well-studied populations of young stars with ages of less than a few Myr. A member of the Taurus cloud, T Tau, became a prototype of T-Tauri type objects, that is young stars that have dissipated their surrounding envelope. Due to its proximity allowing resolved studies of the structure surrounding YSOs, studies of Taurus have influenced much of the understanding of star formation (e.g., Joy, 1949; Herbig, 1952; Mendoza V., 1968; Cohen & Kuhi, 1979; Kenyon & Hartmann, 1987, 1995). Although much has been learned about star formation from the many studies of Taurus, its environment and stellar interactions within it may not representative of the massive and dense clusters in which the majority of stars form.

After the Sco-Cen association, the next nearest massive association of young stars is the Orion complex. It is found at a distance of roughly ∼400 pc (Menten et al., 2007, Chapter III), and the entire complex spans several hundred pc in the plane of the sky. Within it a number of clusters and groups of various ages (between a few to ∼ 10 Myr) and masses can be identified (Figures 1.2 and 1.3). At least two and possibly more generations of stars have formed in the region.

The Orion Ia contains the oldest wave of star-formation in the region, with stellar ages of 7—10 Myr (Briceño et al., 2005), and it has already dissipated its molecular gas. This association is dispersed over a distance of order 50-100 pc, very poorly characterized, although it is known to contain such clusters as 25 Ori (Briceño et al., 2007). The stars in the vicinity of the Orion Belt are part of the Ori OB1b, which is somewhat younger, with the typical ages of 4—6 Myr (Briceño et al., 2005). σ Ori cluster is projected on top of it, although the exact relation between them is still unclear (Walter et al., 2008). Surrounding the Ori OB1 association is the Barnard's Loop, an arc of gas highlighting a bubble. The origin of this bubble is unknown, although possibilities include either a supernova (Madsen et al., 2006; Ochsendorf

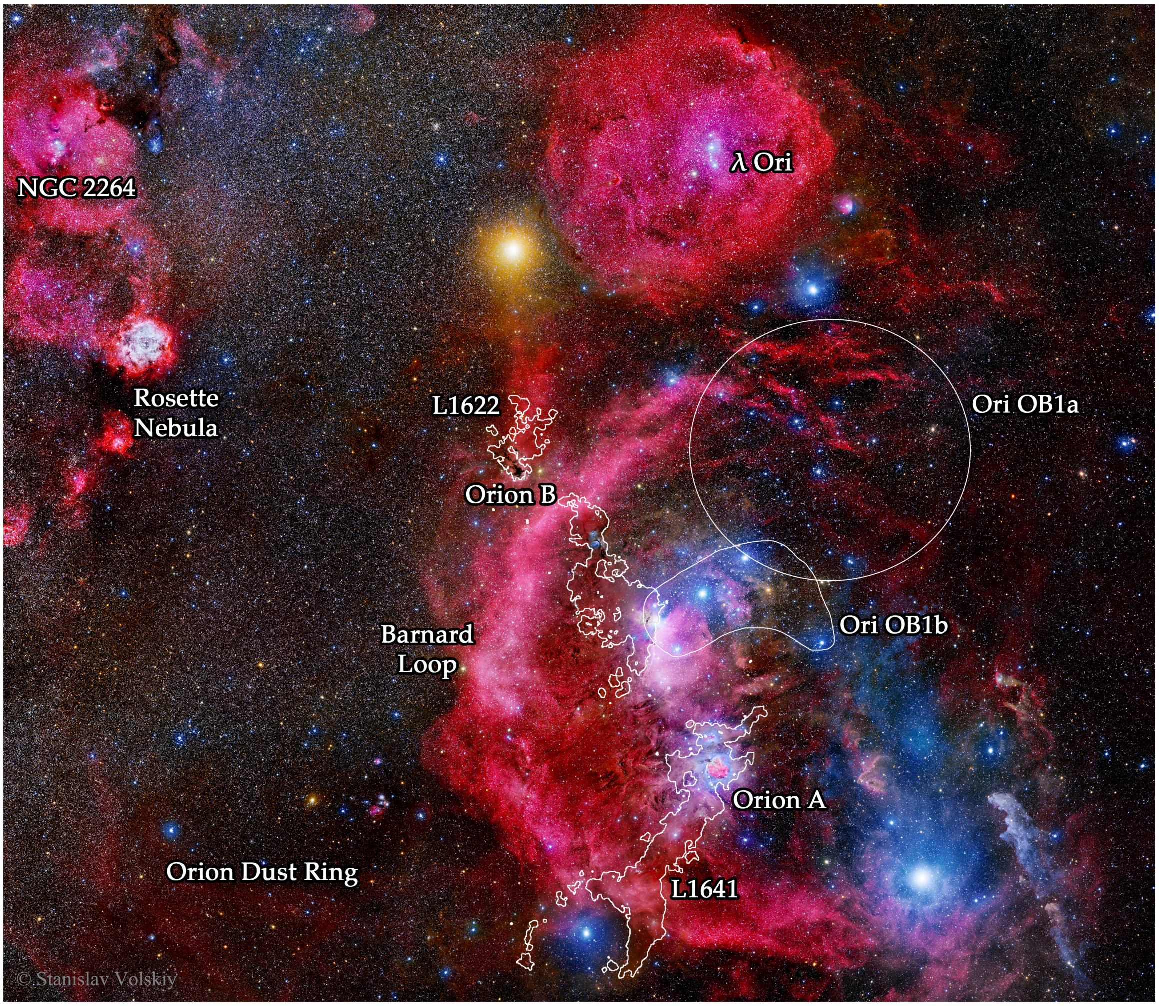

Figure 1.2 Map of the Orion Complex. Image courtesy of Stanislav Volskiy. The image encompasses $\sim 30 \times 20^\circ$ area on the sky.

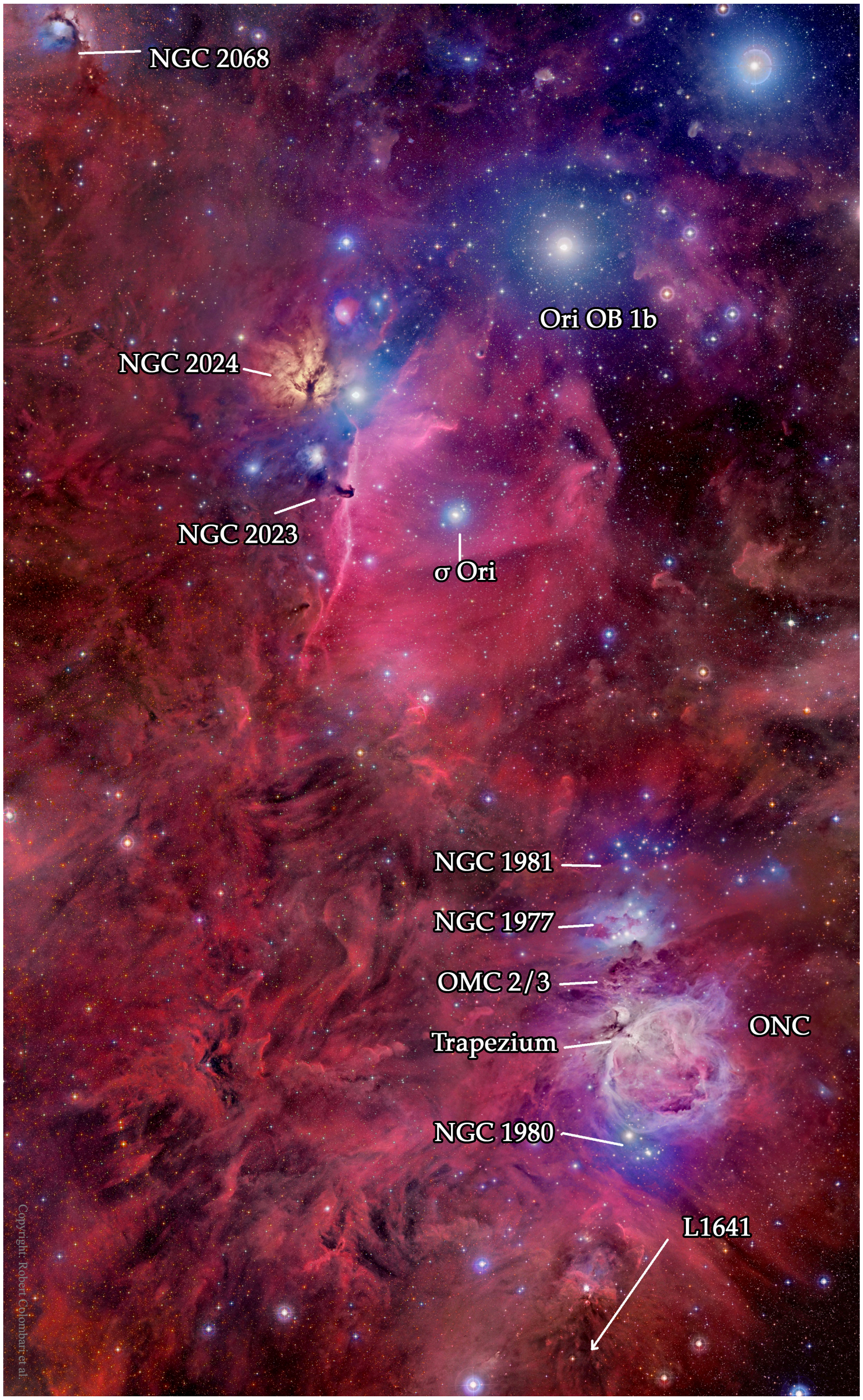

Figure 1.3 Map of the Orion Complex, central part. Image courtesy of Roberto Colombari. The image encompasses ∼ 4.25 × 6.5° area on the sky.

et al., 2015), or photoinozation from the OB stars in Ori OB1b (O'Dell et al., 2011).

At the head of Orion is the λ Ori OB association. A supernova took place there some 1 Myr ago, quenching the epoch of star formation that began 6 Myr ago near the center and ionizing all the gas in the process. However, as the shock wave traveled onward, it triggered new stars to be born in the molecular ring surrounding it (Dolan & Mathieu, 2002).

A similar bubble that has been dubbed the Orion Dust Ring has been recently discovered by Schlafly et al. (2015). Unlike with the Barnard's Loop or λ Ori ring, no possible progenitors are immediately apparent; this ring lacks either massive stars at its center, and currently no cluster to which a deceased massive star have belonged has been identified. At the western edge of the Ring there are two filamentary molecular clouds, Orion A and B. It is possible that the expansion of the bubble from the Orion Dust Ring has assisted in the formation of these clouds.

The Orion Molecular Clouds contain the most recent and ongoing epoch of star formation in the complex. Individual groups and clusters within them are apparent in the distribution of the YSOs towards them (Figure 1.4, Megeath et al., 2012). Kinematic studies can help understand the origin of the groupings (Chapters IV and V) and constraining ages and overall cloud structure require more accurate distance estimates Chapter III).

The most massive cluster in the Orion B molecular cloud is NGC 2024. To the south of it, NGC 2023 (the Horesehead Nebula), which is ionized by σ Ori. Orion B also contains the NGC 2068/2071 cluster that produced two reflection nebulae. Finally, at the northern end of Orion B there is a small cometary cloud, L1622. These regions have ages of < 2 Myr (e.g., Levine et al., 2006; Flaherty & Muzerolle, 2008; Kun et al., 2008).

The northern end of the Orion A contains the most notable cluster in the Complex, the Orion Nebula Cluster (ONC, Hillenbrand, 1997). The ONC contains several

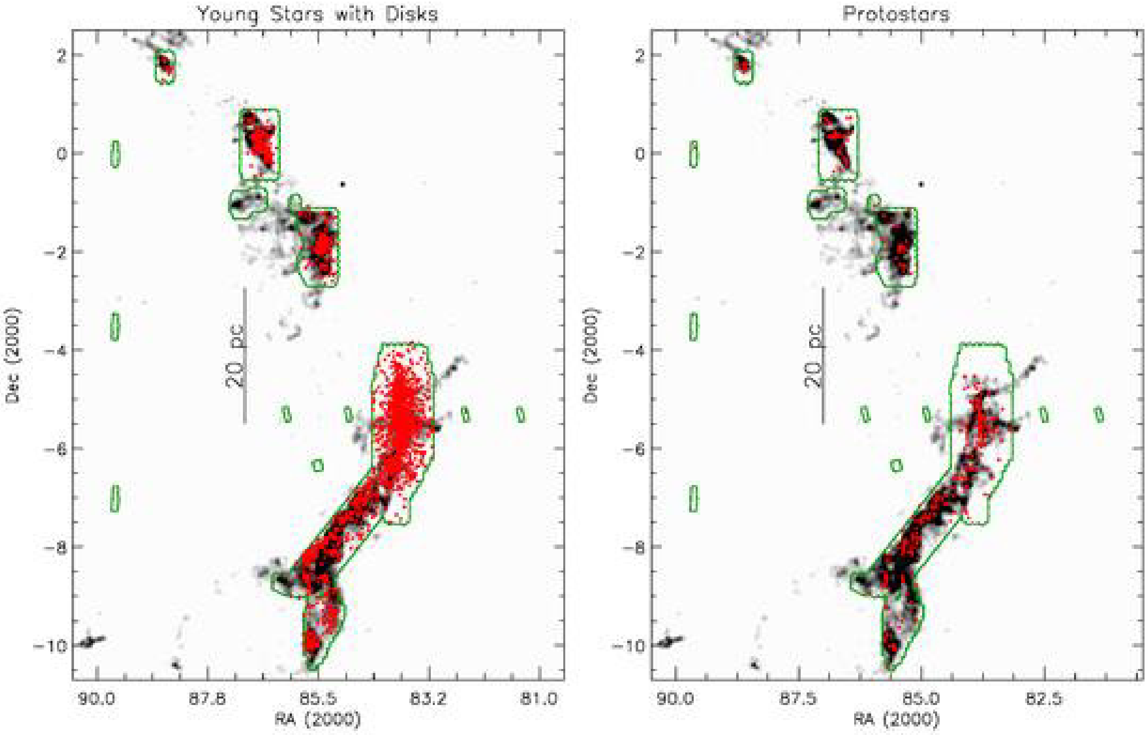

Figure 1.4 The distribution of the YSOs identified from the infrared excess measured from *Spitzer* colors toward the Orion Molecular clouds, overlaid on the greyscale extinction map (Gutermuth et al., 2011). From Megeath et al. (2012).

thousands of YSOs (Megeath et al., 2016), and it is the closest cluster that resembles the potential primordial environment of the Pleiades, and possibly our own Sun. The Trapezium is found at the core of the ONC. It is dominated by four OB stars, θ^1 Ori A, B, C, and D. The winds of the most massive star, θ^1 Ori C, have ionized the surrounding gas, producing the optically visible HII region. North of the Trapezium is a dusty fillament, OMC 2/3, as well as a reflection nebula, NGC 1977. The typical ages of the stars in these regions are $\sim$2 Myr (Da Rio et al., 2010). Further toward the north there is a somewhat older cluster, NGC 1981, with the age of $\sim$5 Myr (Maia et al., 2010). The Orion A molecular cloud extends to the south via the L1641 fillament, with the typical stellar ages of $\sim$3 Myr (Hsu et al., 2012). In between the ONC and L1641 resides NGC 1980, which is centered on the OB star, ι Ori.

Projected near the eastern edge of the Orion Dust Ring is Monoceros OB Association, which hosts such clusters as the Rosette Nebula and NGC 2264. The latter can be thought as similar the ONC in terms of its stellar content, age, and mass, although it is somewhat more distant, at $\sim$900 pc (Sung et al., 1997; Baxter et al., 2009). The ONC and NGC 2264 are the only two massive clusters withing 1 kpc of the Sun. The cluster in Rosette has a similar age, but it is even more massive, containing over 70 OB stars, at the distance of $\sim$1.5 kpc (e.g., Park & Sung, 2002).

1.3 Evolution of YSOs and properties of young stellar populations

As a dense core within a molecular cloud begins to undergo a gravitational collapse, the inner portion of the core will rapidly increase in mass, forming a protostar. The surrounding envelope carries some angular momentum — the initial slow rotation of the core could be achieved through the gravitational interaction with the environment and some turbulence. During the collapse, due to the conservation of angular

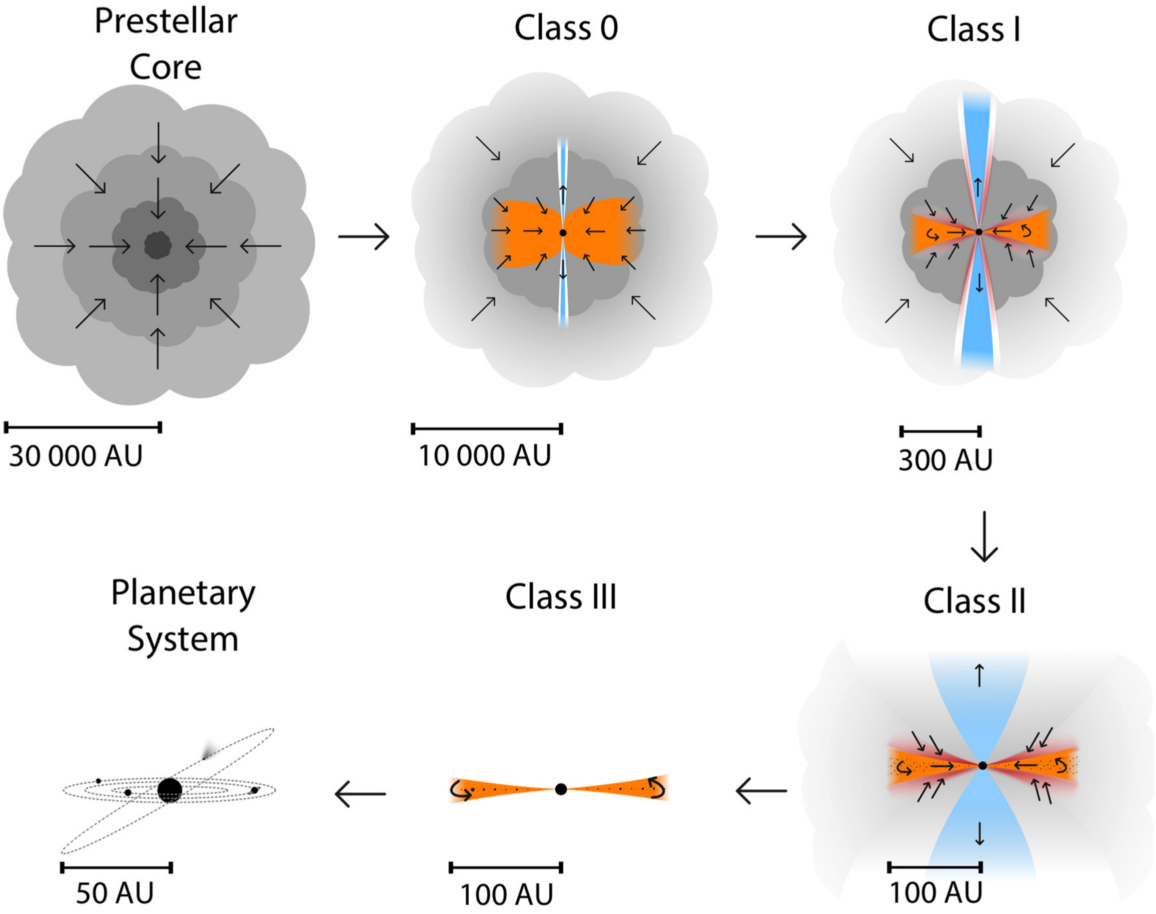

Figure 1.5 Evolution of a YSO, taken from Persson (2014), based on Adams & Shu (1986); Adams et al. (1987). As the dense core within a molecualr cloud undergoes gravitational collapse, a protostar is formed surrounded by an accretion disk, producing outflows and jets (Class 0/I). Eventually, the envelope dissipates (Class II), the disk is consumed through ongoing accretion and planet formation (Class III), and eventually a planetary system such as our own remains.

momentum, the rotation becomes amplified, and the gas of the envelope will at some point become rotationally supported against the collapse, forming a disk surrounding a protostar (Figure 1.5).

As the gas within the disk interacts gravitationally with other regions within the disk, or as it interacts with the magnetic field of the disk, the gas would be able to to lose angular momentum. It is from the accretion through the disk that the protostar is going to continue to gain mass (e.g., Williams & Cieza, 2011). The disk is truncated

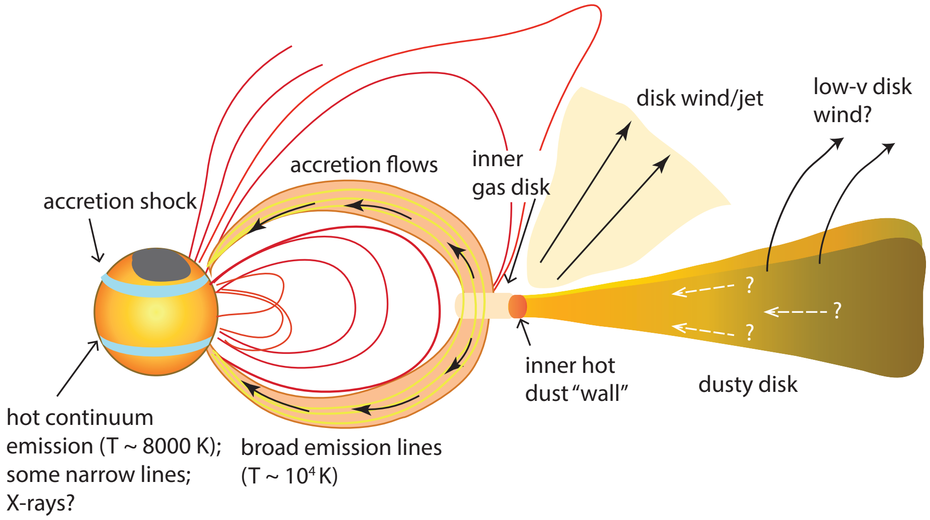

Figure 1.6 Schematic of the accretion processes in YSOs, taken from Hartmann et al. (2016).

near the protostar due to the presence of a strong magnetic field. The infalling gas follows along the magnetic field lines until it lands onto the protostar (e.g., Muzerolle et al., 2001, Figure 1.6). The magnetospheric accretion material produces very broad (and frequently asymmetric) emission lines (most notably Hα and other Balmer lines, as well as He I and O I). The shock that is produced as the result of the infalling gas onto the YSO produces hot (~8000 K) continuum emission which can make it difficult to detect stellar photospheric features, this is referred to as veiling (Calvet & Gullbring, 1998).

Not everything that flows through the disk lands onto the protostar. Approximately 10% of the material gets ejected in the process of accretion (Calvet, 1998). The winds from the disk get interact with the magnetic fields lines, producing outflows and highly collimated jets perpendicular to the plane of the disk (e.g., Najita & Shu, 1994; Anderson et al., 2005). They carry angular momentum away from the protostar.

The disks and envelopes surrounding protostars are very dusty, resulting not only in high degree of extinction at optical and near-infrared regimes, but also excess

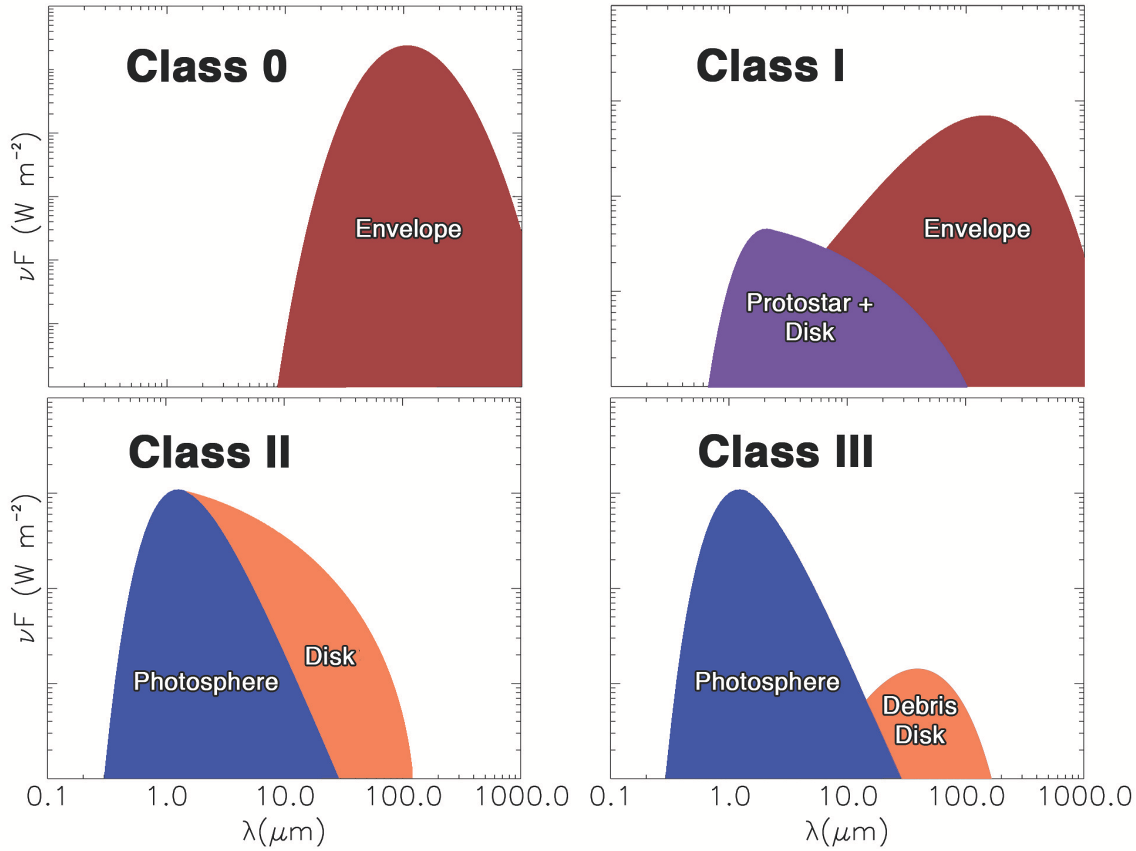

Figure 1.7 A typical spectral energy distribution of YSOs as they evolve.

of longer wavelength emission. A typical spectral energy distribution (SED) of a protostar is shown in Figure 1.7. At the earliest stages, unless viewed along the outflow cavity in the envelope in a polar orientation, the blackbody emission of only the cool dust in the envelope is visible; this stage in protostellar evolution is referred to as Class 0. Later, the shorter wavelength emission of the protostar is starting to become apparent as the dusty envelope becomes less opaque through a continuing collapse – specifically, the polar region clears out due to the mass infall onto the disk. However, the SED is still dominated by the emission from the disk and the envelope. Class I sources are characterized by the positive SED slope at near and mid-IR wavelength.

Eventually, the envelope that provides the gas infalling onto the disk will either be consumed or dissipated through stellar feedback. A disk still surrounds a young star, and some accretion still takes place, but as the major gas reservoir is now absent, the final mass of a young star is now set. Low mass objects are referred as T Tauri type stars, those that have masses $> 2-3\mathrm{M}_\odot$ are referred to as Herbig Ae/Be stars. T Tauri stars with strong accretion are referred to as classical T Tauri stars (CTTSs), they are typically characterized by broad Hα emission lines with widths of over 270 km s^{-1} (White & Basri, 2003); this emission arises in the gas infalling along magnetospheric field lines (Figure 1.6). If the accretion rate is very high, the continuum emission from the accretion shock (Figure 1.6) can be so bright as to "veil" the stellar photospheric contribution, and can make it difficult to assign an accurate spectral type. T Tauri stars in which accretion is not occurring at a significant level and any hot excess and Halpha emission arises from the stellar chromosphere and corona are referred to as weak-lined T Tauri stars (WTTSs).

In terms of their SED, the observed flux of a young star itself will become more pronounced as it is no longer obscured by the dusty envelope, but the dust within the disk will continue to provide excess at near-infrared wavelength. These sources are referred to as Class II objects.

After a few Myr, the ongoing accretion, photoevaporation, and planet formation within the disk will mostly clear the disk of the gas and small dust particles (Figure 1.5). At that stage, little to no infrared excess will be present in the system, and the sources are referred to as Class III objects, for which the observed flux is dominated by the emission from the young star itself. In these sources a debris disk may provide some excess at longer wavelengths, even though near or mid-IR observations with which classification is performed would not show any signature of a disk (Figure 1.7). Typically, Class II objects are CTTSs, and Class III objects are WTTSs, because a continuous presence of the disk results in accretion, and as the disk dissipates, the accretion stops. However, there are some rare exceptions to this as well, such as

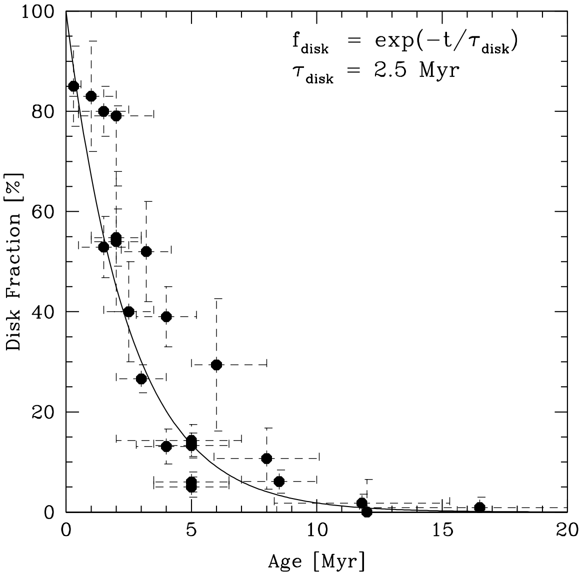

Figure 1.8 Disk fractions of various star forming regions as a function of age. In order: NGC 2024, NGC 1333, Taurus, ONC, NGC 7129, NGC 2068, Cha I, IC 348, σ Ori, NGC 2264, Tr 37, Ori OB1b, Upper Sco, NGC 2362, γ Vel, λ Ori, η Cha, TW Hya, 25 Ori, NGC 7160, β Pic, UCL/LCC. From Mamajek (2009).

sources with the disk holes (which may be caused by planets, e.g., Espaillat et al., 2015). Therefore, while a young star may still posses a substantial outer disk, the material may not necessarily make its way through onto the star in some cases.

In a stellar population a few Myr old it is typical to encounter a mix of sources of various SED classes. The class 0/I protostellar stage typically lasts on the order of the free-fall time of the core from which a star is born, that is on the order of a few tenths of Myr (e.g., Kenyon et al., 1994; Kirk et al., 2005; Evans et al., 2009). The disk lifetimes, on the other hand, last several Myr, although Class II and Class III sources typically exist coevally; some sources process their disks as early as after only a 1 Myr (possibly due to interactions with a close binary companion), while some may retain their disks until almost 10 Myr (Figure 1.8). The overall fraction of disk-bearing sources does appear to correlate with the age of the stellar population, with the half-life of ~1.7 Myr (Mamajek, 2009).

Classification of YSOs is done from the colors to measure infrared excess due to a

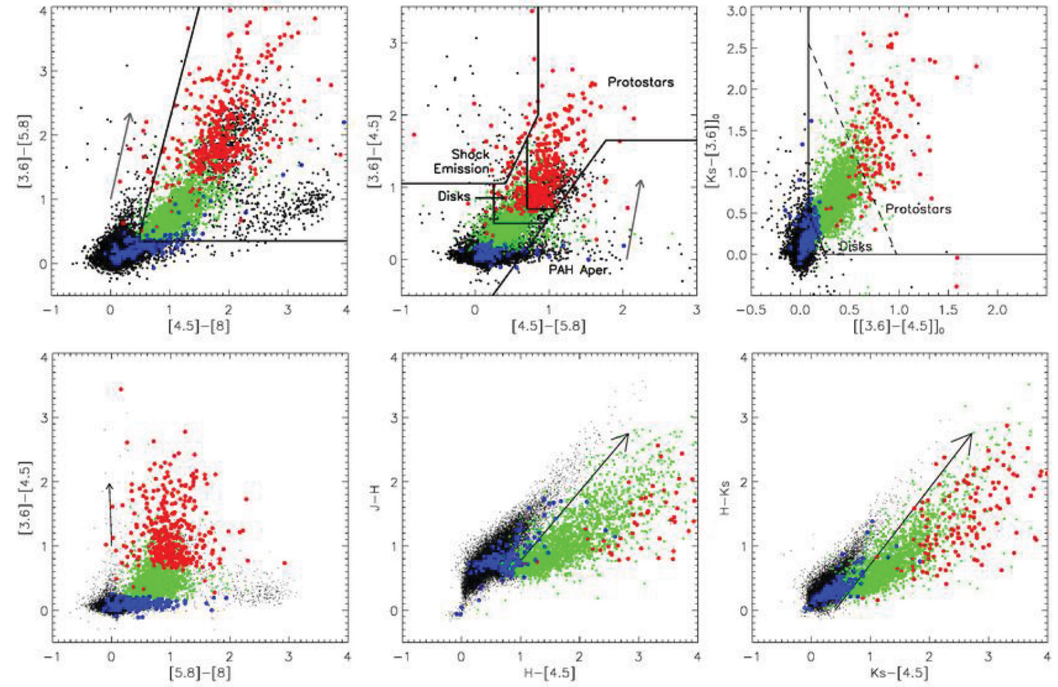

Figure 1.9 Near-infrared colors of YSOs. Red symbols show Class I sources, green are Class II sources, and blue are Class III sources. The black arrow shows the direction of reddening with the magnitudes of (left) 10, (middle) 2, and (right) 5 A_K. From Megeath et al. (2012).

presence of a cool dusty envelope or disk (Figure 1.9). Therefore, infrared photometry, such as that from 2MASS (J, H, K bands), Spitzer (bands centered at 3.6, 4.5, 5.8, 8, 24 μm), and WISE (bands centered at 3.6, 4.6, 12, and 22 μm) are used to determine SED class.

While the basic distinctions between the SED classes are clear in principle, in practice there are complications in interpreting observations. For example, a protostar can appear to be an intermediate case between Class I and Class II if viewed along the polar orientation through the cavity produced by the outflow, such that the extinction is reduced and the central protostar (plus disk) can look essentially like a T Tauri star. Edge-on disk systems can appear to be more like a Class I object due to the disk extinction of the star.

Subject to these caveats, criteria have been developed using IR colors to assign

Classes to YSOs. Class 0/I objects tend to have colors $[4.5] - [5.8] > 0.7$ and $[3.6] - 4.5] > 0.7$. Class II sources have colors $[4.5] - [8.0] > 0.5$, $[3.6] - [5.8] > 0.35$, and $[3.6] - 5.8] \leq \frac{0.14}{0.04} \times ([4.5] - [8.0] - 0.5) + 0.5$ (e.g., Gutermuth et al., 2009). Class III sources have colors that resemble almost pure photospheres without any excess, which can make them difficult to distinguish from more evolved main-sequence stars. Using a combination of different criteria reduces missclassification, and complementary IR spectra can help to improve classification further.

At radio wavelengths, additional gaseous emission components may appear. These contributions may be thermal or non-thermal in origin. Thermal bremsstrahlung from ionized gas can be produced in hot gas, typically from shocks in outflows and by ionized winds (e.g., Bertout, 1983; Reynolds, 1986; Curiel et al., 1987). Optically thick free-free emission tends to have positive spectral index α (defined such that $S_\nu \propto \nu^\alpha$), following the blackbody corresponding to the electron temperature for the optically thin gas, although the slope of the emission flattens out at $\alpha \sim -0.1$ for the optically thin emission (Figure 1.10).

Non-thermal radio emission arises from electrons moving in (and accelerated by) the magnetic fields. Very strong magnetic fields have been measured towards YSOs (e.g., Skinner, 1993; Feigelson & Montmerle, 1999; Johns-Krull et al., 2009). The magnetosphere that is produced by these fields produces very large solar spots (e.g., Donati et al., 2013), coronal X-ray emission several orders of magnitude stronger than that of the main sequence stars (e.g., Getman et al., 2005), flares, and non-thermal radio continuum emission (e.g., Feigelson & Montmerle, 1999). Depending on the strength of the magnetic field, non-thermal emission can be called cyclotron if the electrons are non-relativistic, gyrosynchrotron if electrons are mildly relativistic, and synchrotron if the electrons are ultra-relativistic. Generally, nonthermal emission in YSOs is gyrosynchrotron in nature.

Due to decreasing strength of the magnetic fields further away from the star,

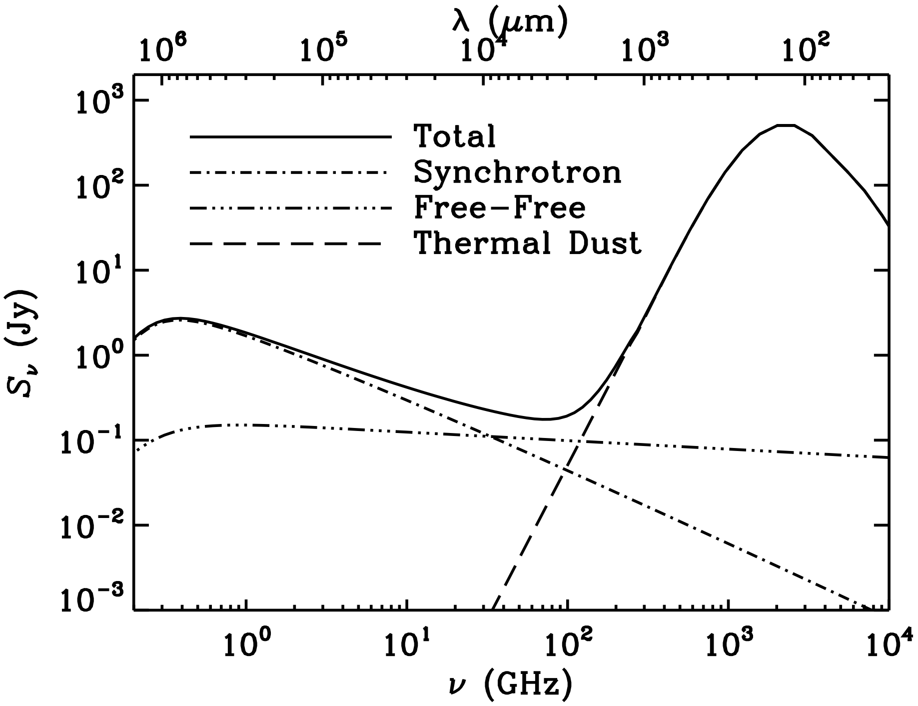

Figure 1.10 An example SED with nonthermal synchrotron (dot-dashed line) and thermal free-free (triple dot-dashed line) radio emission contributions. From Murphy (2011).

the magnetosphere extends to only a few stellar radii; therefore, any nonthermal emission originates relatively close to the star. This emission is highly variable on short timescales and is typically circularly polarized. While it can be difficult to distinguish thermal from nonthermal emission based on the spectral index alone, $\alpha < -0.1$ tends to be a strong indicator of optically thin nonthermal emission.

Gyrosynchrotron emission is observed around a number of Class III sources; not typically observed in Class II and 0/I YSOs. Instead, thermal radio emission is more typically seen (Andre, 1996), probably originating in the wind. Considering that Class II sources have strong magnetic fields, it seems likely that they also produce non-thermal emission, but the free-free absorption in the wind masks this emission.

1.4 Identification of YSO populations

Currently, the largest samples of young star populations have been discovered from Spitzer colors (see Figure 1.4). While these infrared studies have the advantage of being less affected by dust extinction, they only reliably identify objects with infrared excesses and thus are useful to find the Class 0/I/II YSOs. However, populations of stars > 1 Myr old contain large number of Class III stars whose infrared colors are indistinguishable from those of older main sequence stars. Other methods must be employed to find these Class III objects.

One indicator is that of chromospheric emission lines such as Hα. Because solar-type magnetic chromospheric and coronal activity decays with age, pre-main sequence stars tend to have stronger Hα and X-ray emission, and these properties can be used to identify Class III members, as well as their younger counterparts (e.g., Getman et al., 2005). Hα emission is useful to identify young stars roughly from mid-K to M spectral types (both CTTSs and WTTSs); unfortunately Hα becomes weak in hotter stars due to contrast with the brighter, hotter stellar photospheres.

Another useful indicator is that of Li I 6707Å absorption; this is the most reliable indicator of youth in late type stars. After most of the mass of the star has been accreted, young stars contract toward the main sequence, radiating energy produced by the release of gravitational potential energy. Low mass stars evolve along the Hayashi track, and they change little in terms of their surface temperature (Figure 1.11), however, the temperature in the interior of a young star rises. When the core temperature of a star reaches $\sim 14\times10^6$ K, a process which depending on the mass of the star will take few to several 10^7 yr, it will reach zero age main sequence and become a true star that is capable of ${}^1_1$H fusion (Clayton, 1983). Before that, however, at the core temperatures of only a few 10^6 K, some light elements could begin to be processed. This includes ${}^7_3$Li in particular, which will be rapidly depleted through a fusion with protons producing ${}^4_2$He. Higher mass stars, which have managed to create a radiative zone in their interior by the time Li begins processing, will still retain some of it in their outer layers which would not mix the material into the core. But in fully convective low mass stars where the gas is fully mixed, Li will be fully depleted in the entire star. Therefore, the presence of the Li I absorption feature in the spectra of low mass stars later than K4 is among the best indicators of youth, which otherwise may be difficult to distinguish from more evolved stars (Figure 1.12). This technique is reliable for identifying stars with stellar ages up to a few tens Myr, although late K and early M stars will process Li sooner than late M stars, after only ∼10 Myr. By the age of 100 Myr, only substellar objects will still have a substantial amount of Li remaining in their interiors (Baraffe et al., 2015).

Finally, if optical or near-IR spectra are available, extinction corrections can be made to enable the placement of stars in a color-magnitude or equivalent HR diagram (assuming the distance is known), thus providing direct estimates of the ages. However, for increasingly distant star-forming regions, contamination by foreground older dwarfs is not negligible, requiring other indicators (Hα, IR excess, X-ray/radio emission) to refine membership.

1.5 Problems in star formation

There are a number of important questions that relate to the star formation and cluster evolution that are still left unanswered. What is the nature of the turbulence which is involved in compressing gas to form stars? Is the star formation within the giant molecular clouds a fast process, in which the gas immediately starts collapsing under its own weight on the free fall time scale (e.g., Hartmann & Burkert, 2007; Elmegreen, 2007; Kuznetsova et al., 2015) and the turbulence itself is also due to gravitational acceleration, or is the gas originally supported by an unknown mechanism which counteracts the collapse (e.g., Tan et al., 2006; Hennebelle, 2012), slowing star formation? One potential way of distinguishing these two models is through ob-

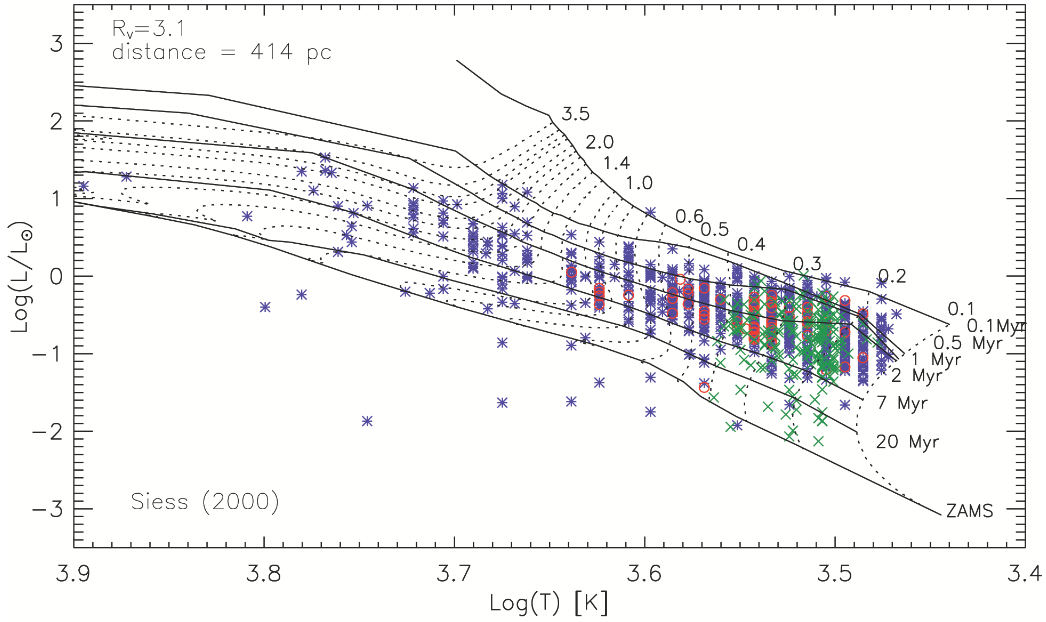

Figure 1.11 HR diagram of the sources in the ONC, from Da Rio et al. (2010) overaid on the pre-main sequence evolutionary tracks from Siess et al. (2000) for stellar masses from 0.1 to 3.5 $M_\odot$, with isochrones from 0.1 to 20 Myr.

serving the substructure of individual clusters forming throughout the cloud. In the case of the cold collapse, the substructure would rapidly begin to dissipate as the clusters will be dynamically mixed in only a few Myr. On the other hand, hot collapse would preserve the substructure for a much longer period of time (e.g., Scally & Clarke, 2002). Therefore, in order to begin to validate one of these models with observational evidence, it is imperative to determine both the three-dimensional structure, the three-dimensional kinematics, as well as the age of stars within young clusters.

What is the 3-D structure of star-forming clouds? For example, in projection, Orion A and B appear to be part of a bubble (Schlafly et al., 2015), but is this projection representative of the true morphology of this region? Are these clouds, or the clusters within these clouds, found at the same distance? This would affect age determinations of stars within these clouds. What are the intercluster kinematics? How are the individual clusters connect and interact with each other? This contributes to an understanding of the initial conditions, as well as evolution of various star

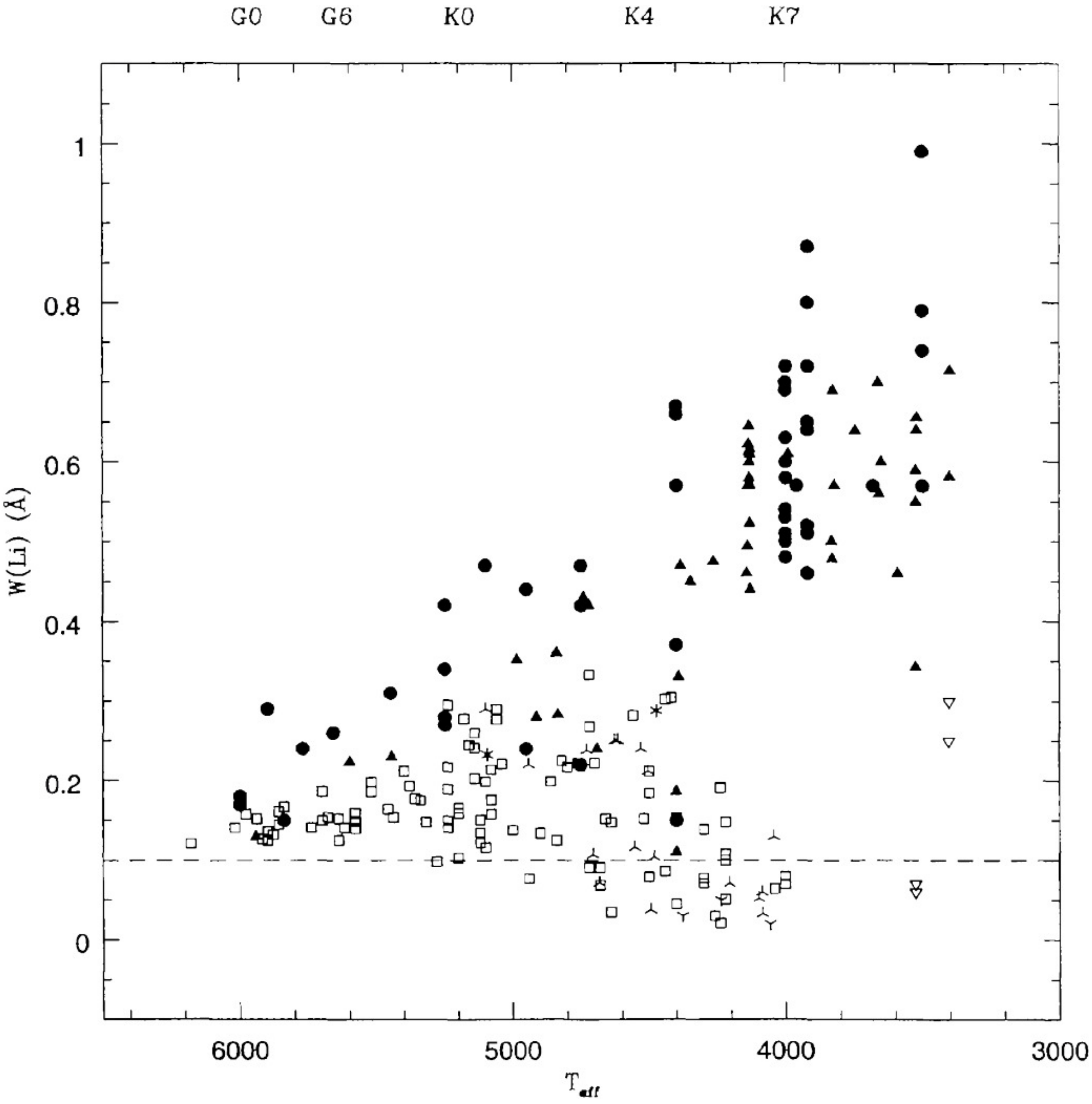

Figure 1.12 Distribution of equivalent widths for Li I in T Tauri stars (filled symbols) and sources in Pleiades (open symbols) as a function of effective tempearture. From Briceno et al. (1997). As discussed in Section 1.4, Li depletion occurs rapidly in low mass stars, and it is fully processed by the ages of 100 Myr in all but substellar objects. In sources with higher mass and higher effective temperature, Li will not be depleted due to stellar evolution, the lower equivalent width are a result of ionization of Li in stellar atmospheres.

forming regions. What is the cluster substructure and what are the intracluster kinematics of the stars and gas? This probes the dominant modes that are directly involved in star formation. Which stars are the actual members of the star-forming clouds, and which are foreground (or background) contaminants?

Six-dimensional understanding of stellar positions and kinematics are crucial for addressing these questions. Accurately measured distances to the stars are important in order to understand cloud geometry, which, in turn, can be used to test the star formation models. Distances are also imperative for refining stellar ages, which require accurate luminosities, which, in turn, get compared to the theoretical evolutionary tracks along the HR diagram (e.g. Figure 1.11). Kinematics of stars are useful for testing membership, discovering multiple systems, and identifying kinematic substucture, particularly in the cases where comparison with the kinematics of the molecular gas from which young stars form is possible. The velocity dispersion of star-forming regions, while supersonic with respect to the cold gas, is relatively small ($\sim$2 kms, e.g. Bally et al., 1987), and thus they require high resolution observations.

Five out of six dimensions of the stellar phase space (position on the sky, parallax, and proper motions) can be obtained through high resolution astrometry obtained over a course of a prolonged period of time, long enough to observe movement of a source in the plane of the sky. The remaining component of motion, radial velocity (RV), requires measuring the Doppler shift in the spectral observations of a source.

The latter is can be obtained with spectrographs that provide sufficiently high spectral resolution to measure individual stellar RVs relative to the dispersion velocity of the cluster. However, multi-object spectrographs such as Hectochelle, M2FS, or APOGEE are highly beneficial in order to minimize the observing time, since individual clusters may contain hundreds of stars. These spectrographs allow observations of several hundreds of sources spread over $0.5^\circ - 1^\circ$ field of view simultaneously. Different filters in these spectrographs offer different advantages. In optical spectrographs, such as the Hectochelle and the M2FS, Mg I filter with central wavelength of ∼5170Å is particularly useful for measuring RVs, as that portion of the spectrum contains a very large number of absorption lines in late type stars that can be used for cross-correlation. Observations of $H\alpha$ and Li I filters, on the other hand, are useful for eliminating non-members; this is particularly important for constraining the older population of YSOs. Near infrared spectrographs, such as APOGEE, on the other hand, are capable of detecting sources that are affected by the extinction and cannot be seen in optical wavelengths.

Astrometric observations are often limited not necessarily by the angular resolution but by the pointing accuracy of the telescope, which can frequently be as large as a few arcseconds. To improve the coordinates after the fact, it is possible to reference the coordinate grid between the individual exposures to each other with a sufficiently large field of view, but, as a result of this the parallax and proper motions may be underestimated. If the positions are referenced to the cluster sources, all of which are found at a similar distance and have similar kinematics, parallax measurements would be impossible, and proper motion sensitivity would be significantly degraded, and often would require a baseline in time of several decades in order to be measured. If the reference sources are chosen among the background stars, since they do not remain completely stationary between the observations (and parallactic movement would be in the same direction), some biases would still be present; however it is possible to improve the pointing to 1 mas (e.g., Donaldson et al., 2016). But, as the parallax and proper motions grow increasingly small the further the object is from the Sun, this technique cannot probe distances and kinematics with sufficient accuracy for a detailed analysis of all but the closest star forming regions.

Currently, few instruments are capable of astrometric precision better than 1 mas. Among them is the *Gaia* space telescope (Lindegren et al., 2012), which is a successor to the *Hipparcos* mission (Perryman & ESA, 1997). Through simultaneously processing data from two fields of view separated by a wide 106.5° angle, as well as repeatedly scanning of the entire sky, *Gaia* is capable of narrowing down the uncertainty in astrometry down to within 100 μas (Gaia Collaboration et al., 2016). *Gaia* will provide parallaxes and proper motions for over a billion stars down to $G < 20.7$ mag, and it will be able to expand the horizon of stars with precisely measured distances from ∼100 pc to over 1 kpc away from the Sun. It is worth noting that even though there are a number of star-forming regions in that distance, since *Gaia* is an optical telescope, its performance may be degraded due to high degree of extinction and nebulosity that are typically associated with young stellar objects (YSOs).

Another instrument which is capable of similar astrometric precision as *Gaia* is the Very Large Baseline Array (VLBA), a radio interferometer. All of its pointings are referenced to distant quasars, providing an unmoving reference frame. Because the VLBA operates in the cm regime, in order to maintain resolution comparable to that of optical telescopes such as *Gaia*, larger baselines are required. The VLBA consists of 10 antennas working in unison, each one 25 m in diameter, with the largest baseline between them of over 8,600 km (Figure 1.13).

The signal of all the individual antennas is recorded separately, and it is later correlated and phase-referenced. The signal cannot remain coherent outside ∼1" of the phase center, although, the VLBA correlator does allow defining multiple phase centers in a given field. Blindly defining phase centers across the entire field of view is highly impractical, as this will generate very large volumes of high resolution data not containing any signal; these data would need to be processed and stored. Therefore, it is necessary to explicitly know the location of the sources with precision to better than 1" beforehand. Additionally, sources with low surface brightness cannot be correlated through large baselines. The brightness temperature T_B of a source in the Rayleigh-Jeans regime is given by

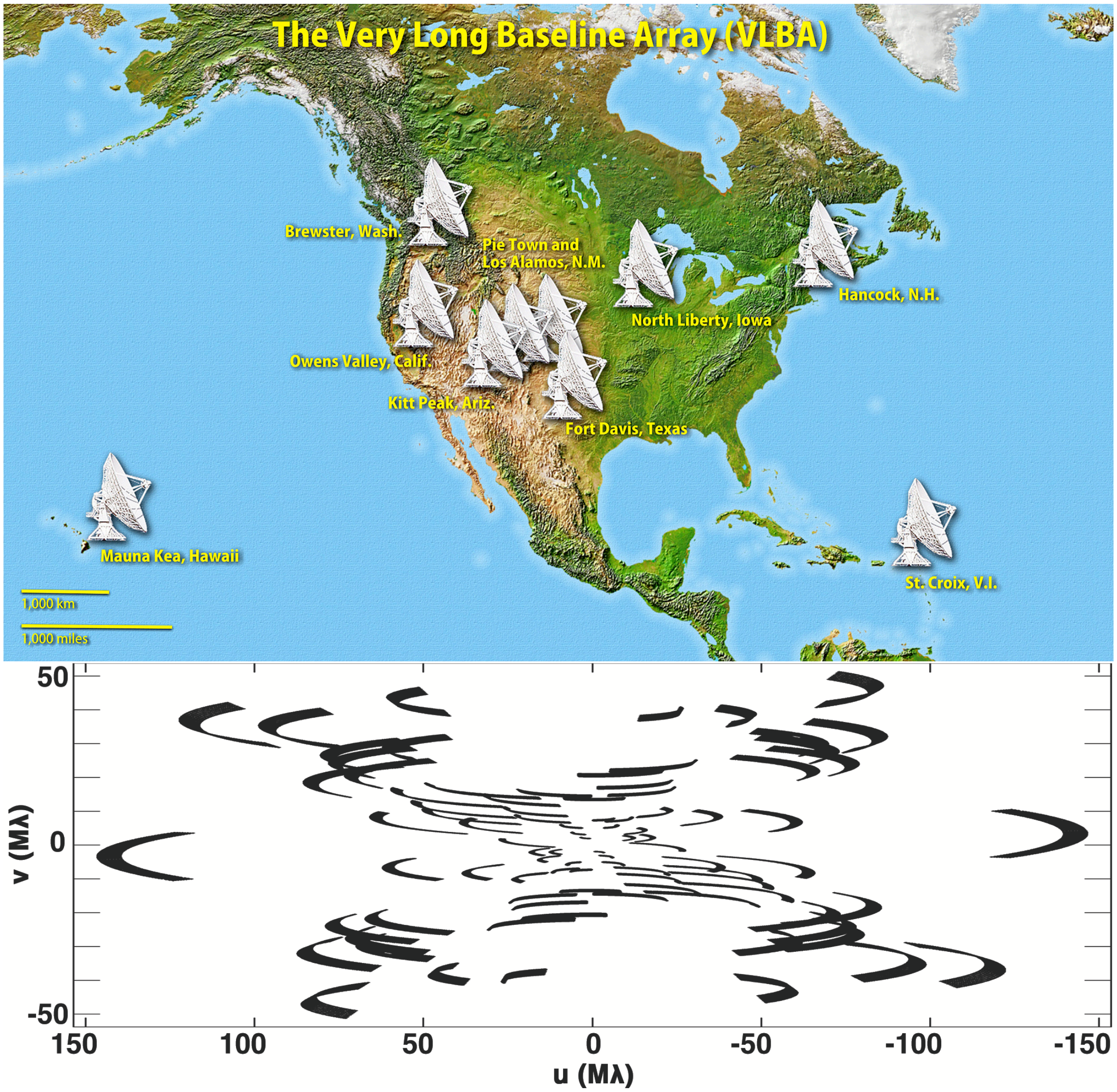

Figure 1.13 Top: Location of the VLBA anntenas. Bottom: An example of a ypical uv coverage of the VLBA.

$$T_B = \frac{1.36\lambda^2 S}{a \times b}$$

where λ is the wavelength in cm, S is the flux density in mJy, and a and b are the beam major and minor axes, in arcsec. The size of the beam produced as a result of the largest VLBA baseline at 5 cm is 1.2 mas; therefore to detect a source with a flux of 1 mJy, it would need to have $T_B \sim 8.5 \times 10^6$ K. Therefore, VLBA is unable to image thermal radio emission, and only non-thermally emitting sources (which are comparatively rare) are detected. For these reasons, on its own VLBA is not ideal as a survey instrument. However, it can be complemented by the Very Large Array (VLA) for this purpose.

The VLA is a network of 27 dishes, each one 25 m in diameter, that can be positioned in four configurations with maximum baselines ranging between 1—36 km. All of the VLA antennas are separate from the VLBA (although the VLA, or any other radio telescope that is a part of the High Sensitivity Array network, can be phased in the VLBA observations if necessary). Compared to the VLBA, the VLA has a significantly lower resolution, but it does have a better sensitivity due to the larger total collecting area of all the antennas combined, and it also has a better uv coverage due to the larger number of antennas in a more compact configuration. Therefore, the VLA is much better suited for large-scale mapping experiments. The VLA can be used to identify suitable radio-emitting sources that could be later be studied with the VLBA.

Given that *Gaia* and VLBA observations will have differing biases but they are both capable of directly measuring parallax and proper motions without additional assumptions, VLBA observations provide the best benchmark for comparison of the astrometric solutions produced by *Gaia* for the sources that are observed in common, and it can detect sources that are inaccessible to Gaia due to a combination of extinction and nebulosity.

As discussed in Section 1.2, there are a number of star-forming regions that offer unique environments in terms of their star formation history, ages, mass, as well as distance, influencing the ability of conducting resolved studies. As the Orion Complex is the closest clustered region that is still forming stars and it is the most representative of the typical mode of star formation, it is a rich and uniquely positioned laboratory of star formation, and I will focus on it in this thesis to address the above questions to provide additional insight into the processes of star formation and to further understanding of early evolution of giant molecular clouds and star clusters, utilizing the aforementioned techniques and methods.

Previously, there have been few attempts focused in obtaining the true three-dimensional structure of the Orion Complex. Most studies that probed the distance to the Complex focused exclusively on the ONC. The most precise distance estimates were obtained from trigonometric parallax toward non-thermally emitting YSOs (389^{+24}_{-21} pc, Sandstrom et al., 2007; 414±7 pc, Menten et al., 2007), and H_2O and SiO masers (437±19 pc, Hirota et al., 2007; 418±6 pc, Kim et al., 2008) all of which were found in the Trapezium cluster. The studies that estimated the distances to the other clusters of the Complex (e.g., Brown et al., 1994; Dolan & Mathieu, 2001; Jeffries et al., 2006; van Leeuwen, 2007; Lombardi et al., 2011; Schlafly et al., 2014) had either very uncertain measurements or averaged distances over very large areas, although they are typically not dissimilar to the distance that is found to the ONC. As a result, frequently little distinction is made in the distance toward the different parts of the Orion Complex.

Within the ONC, some attempts have been made to identify substructure. In particular, it has been proposed that there is an older (∼5 Myr) population that is in the foreground to the ONC by as much as 10—40 pc, and that it includes NGC 1980 (Alves & Bouy, 2012; Pillitteri et al., 2013; Bouy et al., 2014). However, recently, some doubt has been expressed whether this population is indeed as unrelated to the rest of the Orion A as has been originally believed (Da Rio et al., 2016; Fang et al., 2017).

A number of studies analyzed the kinematics of the Orion Complex. A particular focus has been given to the RV studies. Many notable works include the surveys of not the stellar RVs, but rather those of the molecular gas in the Orion A and B (e.g., Bally et al., 1987; Kramer et al., 1996; Kun et al., 2008; Nishimura et al., 2015). Given that young stars are formed from the molecular gas, it is generally expected that its kinematics provides a good approximation for the kinematics of the young members. With the advancements of multi-object spectrographs, detailed studies of stellar RVs became more practical. Analyses of the RV in the ONC using optical spectra have been conducted by Sicilia-Aguilar et al. (2005), Fűrész et al. (2008), and Tobin et al. (2009), each one increasing in scope of the number of sources and number of epochs obtained for each source in order to rule out the effects of multiplicity. These studies have revealed a notable discrepancy in the velocity dispersion between the stellar RVs and those of the molecular gas. Da Rio et al. (2016) have conducted a survey of the Orion A with the goal of obtaining RVs from the near-infrared spectra to test the effect of extinction, although the discrepancy remained largely unaffected. A number of interpretations of this are possible, including cluster substructure, although only one kinematic and two spacial dimensions make it difficult to distinguish between them.

Few stellar RV studies were conducted in the Orion B, primarily due to the high extinction in the cloud. Flaherty & Muzerolle (2008) obtained optical spectra of only 32 YSOs in NGC 2068; in large these sources showed no considerable deviation in RV from that of the molecular cloud. Some surveys targeting stellar have been conducted outside of the molecular clouds (e.g., Jeffries et al., 2006; Briceño et al., 2007; Sacco et al., 2008), although, they were primarily concentrated near previously identified comoving groups, since the membership of the dispersed population (such as the Ori

OB1a, for example) remains to be rather uncertain.

On the other hand, the analysis of proper motions toward the Orion is made somewhat difficult because the complex is located near the galactic anticenter. Combined with its distance, any motions in the plane of the sky are small and difficult to measure. Among the best studies of proper motions in the Orion Complex is the work by Jones & Walker (1988) based on the photographic plates obtained throughout 20 year baseline, although the analysis is limited only to 15' field-of-view centered on the Trapezium. Since then proper motions have also been analyzed using imaging in radio with the VLA, although the analysis has also been limited only to the Trapezium cluster (Dzib et al., 2017). On the basis of these data, currently there is no evidence of rotation, expansion, or contraction. This is, however, only one cluster in the Complex, and no dedicated proper motion study has been conducted in the other clusters. Some sources throughout the Complex were monitored by *Hipparcos* (Perryman & ESA, 1997), and some were also calculated though the U.S. Naval Observatory CCD Astrograph Catalog survey (UCAC, the most recent data release by Zacharias et al., 2017), although large errors and a relatively small sample size for sources with confident detections still preclude any detailed analysis of the proper motions.

1.6 Thesis outline

My thesis has been published in five peer reviewed papers. In Chapter II I present the VLA survey of the Orion Complex with the goal of identifying all the radio emitting sources in the region, including those that could be used for the astrometric observations (Kounkel et al., 2014). Chapter III is focused on the VLBA observations of the VLA identified sources, and it presents the parallax and proper measurements to 27 stars in the Complex (Kounkel et al., 2017c). This work is the first to include direct parallax observations of stars in the Orion Complex outside of the ONC with better than 5% uncertainty. This work was conducted as part of the Gould's Belt Distances Survey (GOBELINS) in an effort to probe the 5-dimensional structure of the Gould's Belt via the observations of most of the nearby star-forming regions.

Chapters IV and V complement the distance and proper motion measurements from GOBELINS with RV measurements obtained from spectral observations of the stars in the Orion Complex. Chapter IV focuses on the long-term monitoring of the ONC as well as NGC 2264 (NGC 2264 is a somewhat more distant analogue to the ONC, not part of the Orion Complex, Kounkel et al., 2016a). The purpose of these observations is two-fold. First, I identify spectroscopic binaries, and I use them to compare the multiplicity function of these massive clusters in comparison to the field. I also compare the stellar RV distribution to that of the molecular gas, improving the agreement between them compared to the previous studies, as well as look for signatures of possible substructure. Chapter V expands this analysis to the stars in the Orion B molecular cloud (Kounkel et al., 2017b). In Chapter VI I look at the previously identified subcluster in the ONC, namely NGC 1980, in order to verify the claims that it is an older cluster that is found in the foreground of the ONC (Kounkel et al., 2017a). Finally, in Chapter VII I present the conclusions and outline future the future work that will need to be conducted as a result of it.

CHAPTER II

The Gould's Belt Very Large Array Survey. III. The Orion region

We present results from a high-sensitivity (60 μJy), large-scale (2.26 deg^2) survey obtained with the Karl G. Jansky Very Large Array as part of the Gould's Belt Survey program. We detected 374 and 354 sources at 4.5 and 7.5 GHz, respectively. Of these, 148 are associated with previously known young stellar objects (YSOs). Another 86 sources previously unclassified at either optical or infrared wavelengths exhibit radio properties that are consistent with those of young stars. The overall properties of our sources at radio wavelengths such as their variability and radio to X-ray luminosity relation are consistent with previous results from the Gould's Belt Survey. Our detections provide target lists for follow-up Very Long Baseline Array radio observations to determine their distances as YSOs are located in regions of high nebulosity and extinction, making it difficult to measure optical parallaxes. Published in 2014, ApJ, 790, 49.

2.1 Introduction

The Orion Molecular Clouds are one of the nearest active star-forming regions, containing several thousand pre-main sequence stars as well as a substantial number of massive stars including the O7 binary θ^1 C Ori in the center of the Orion Nebula Cluster (ONC). The stellar populations in the two main Orion A and B clouds can be divided into distinct clusters such as the ONC, OMC 2/3, NGC 2023, 2024, 2068 and 2071, and Lynds 1622, along with the more distributed population in the L1641 region (Bally, 2008; Muench et al., 2008; Meyer et al., 2008; Gibb, 2008; Reipurth et al., 2008; Allen & Davis, 2008; Hsu et al., 2012). The λ and σ Ori clusters, while not part of the Orion A and B clouds, are also considered to be part of the Orion OB1 association (Mathieu, 2008; Walter et al., 2008).

In order to fully understand the history of star formation in Orion, it is important to determine accurate distances as well as kinematics. The spatial positions, three-dimensional velocities, and ages of the stars are essential to testing theories of star cluster formation. However, accurate distance measurements to these stars are needed, as uncertainties of 20% or more in the distance can translate into errors of 40% in total brightness or luminosity, resulting in a 70% error in ages for low-mass stars (Hartmann, 2001).

The distance to the Orion Complex has been a subject of much debate over the years, with accepted distances ranging from 380 to 520 pc (Reipurth, 2008). It is only recently that a firmer estimate of 414±7 pc, obtained by using high-resolution radio interferometry of four stars in the central regions of the ONC (the Trapezium), has come to be accepted (Menten et al., 2007). However, these four stars may not be representative of the main cluster, much less of the entire Orion A/B complex that spans a range projected on the sky of 100 pc. Furthermore, it is known that stars from a somewhat older group, the Orion Ia association, lie in front of the main Orion A molecular cloud by as much as 50–100 pc (Bally, 2008; Alves & Bouy, 2012), confusing attempts to identify the true young stellar population.

The most direct method to determine the distance of a star is through observing its parallax. However, it becomes increasingly difficult to determine at large distances and toward regions with high nebulosity. For an object located 500 pc away the parallax is only 2 mas; to determine the distance to an accuracy of 2% a measurement error of only 40 μas is required. Such accuracy cannot be obtained with current ground-based optical techniques, or from the *Hubble Space Telescope*, but can be achieved using very long baseline interferometry at radio wavelengths. The Very Long Baseline Array (VLBA) is one of the largest interferometers with 10 different sub-arrays located across the United States and a maximum effective baseline of 8611 km. It can produce such accuracy and can complement *Gaia* in regions of star formation, where extinction and nebulosity pose problems for optical surveys.

Since VLBA has a very high spatial resolution, sources need to have high surface brightness in order to be detected. Therefore, good candidates are those that are suspected to emit non-thermally at radio frequencies. Not all young stars are non-thermal emitters, so it is necessary to perform a survey at lower resolution to identify candidates and rule out background quasars. In particular, objects classified as Class III stars based on their infrared spectral energy distribution (SED) tend to exhibit gyrosynchrotron non-thermal emission that is related to magnetic activity of the star. This emission is frequently associated with a high degree of circular polarization and variability (Dulk, 1985).

The Gould's Belt Very Large Array Survey is an ongoing large-scale effort to map all the neighboring star-forming regions in radio frequencies and to identify likely non-thermal radio emitters. These stars will be later used to determine accurate distances and three-dimensional structure and kinematics across all regions using VLBA (Dzib et al., 2013; Ortiz-León et al., 2015; Dzib et al., 2015; Pech et al., 2016). In this chapter, we focus on Very Large Array observations of the Orion Molecular Cloud Complex. In Section 2.2 we describe the observation details and in Section 2.3 we present an overview of the detected objects. We analyze the source properties in Sections 2.4 and 2.5 and summarize our conclusions in Section 2.6.

Table 2.1. Dates of the observations of each map at each epoch as well as the observed regions. The total number of fields covering that region is given in parentheses.

Map #	Field	Epoch 1	Epoch 2	Epoch 3
Map 1	λ Ori (12), L1622 (3), NGC 2068 (15)	07/04	07/30	08/25
Map 2	NGC 2068 (12),NGC 2023 (14), σ Ori (4)	07/04	07/30	08/28
Map 3	σ Ori (7), ONC (23)	07/04	07/30	08/28
Map 4	ONC (30)	06/25	07/24	08/29
Map 5	ONC (30)	07/02	07/24	08/29
Map 6	ONC (26), L1641-N (4)	06/27	07/23	08/26
Map 7	L1641-N (12), L1642-C (8), L1641-S (10)	07/03	07/23	08/27

2.2 Observations

Fields in the Orion A and B molecular clouds were observed with the Karl G. Jansky Very Large Array (VLA) in its A configuration. The 210 individual fields have been split into 7 maps, with 30 fields being observed per map, as follows: 12 in λ Ori, 3 in L1622, 27 are shared between NGC 2068 and NGC 2071, 14 are shared between NGC 2023 and NGC 2024, 11 in σ Ori, 109 in the Orion Nebula Cluster (ONC), 16 in L1641-N, 8 in L1641-C, and 10 in L1641-S (see Figures 2.1-2.7). All the maps were imaged closely in time, and a total of three epochs separated by approximately a full month were acquired in summer 2011 (Table 2.1). Two 1 GHz frequency bands were observed simultaneously, at 4.5 and 7.5 GHz. Fields were positioned in such a way as to provide a uniform coverage over the extended area surrounding the known positions around young stars. Assuming a FWHM diameter of the primary beam of 10' and 6' at 4.5 and 7.5 GHz respectively, the total area covered by our observations is 2.26 and 1.35 deg^2, respectively.

3C 138 was used as the flux calibrator for all the fields. Three phase calibrators were observed: J0532+0732 for λ Ori; J0552+0313 for L1622, NGC 2068; J0541-0541 for NGC 2023, 2024, σ Ori, ONC, and all of the L1641 fields. The observational setup was the same as described in Dzib et al. (2013). Data were reduced and

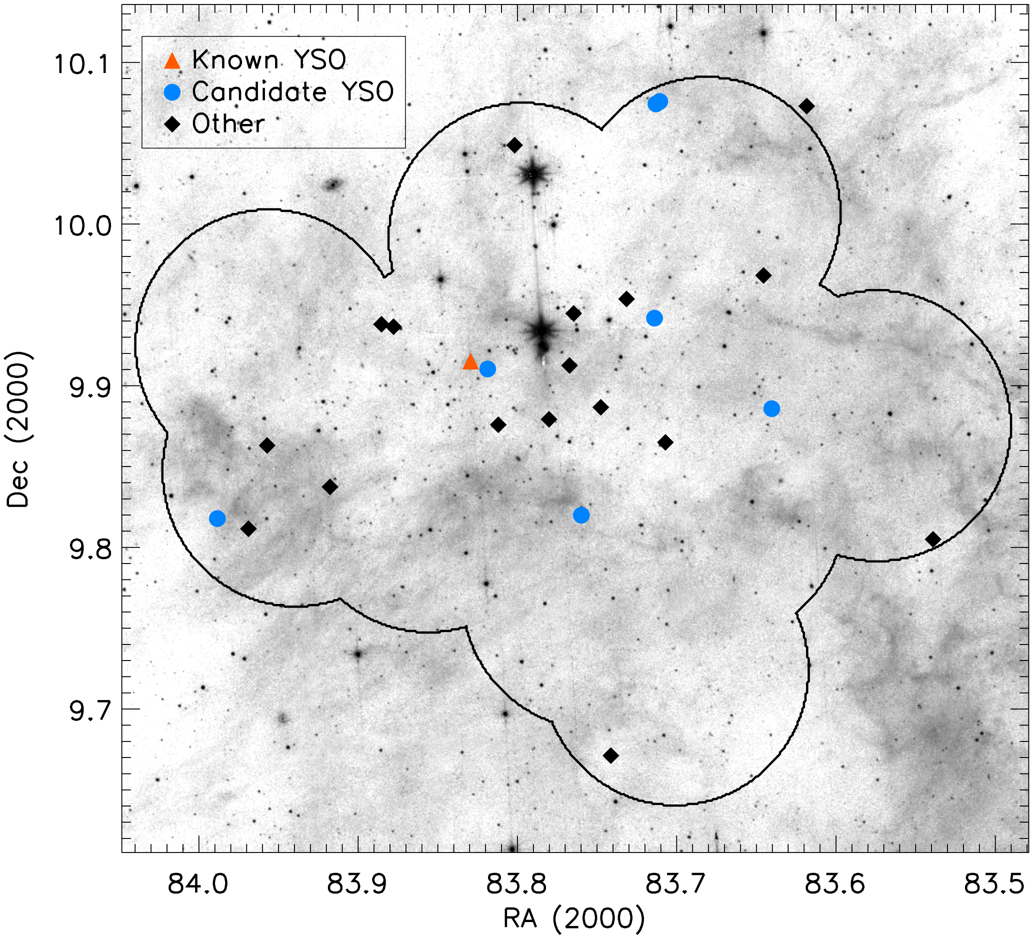

Figure 2.1 The λ Ori field. The 8.0 μm Spitzer map is taken from Barrado y Navascués et al. (2007). The outline shows the radio coverage of the field with VLA at 4.5 GHz with FWHM diameter of the primary beam of 10'; symbols show the positions of the detected objects. Red triangles represent objects that have been identified as YSOs in previous surveys; blue circles are candidate YSOs based on their radio properties; black diamonds are all the remaining objects. See Section 2.3 for a description of each category.

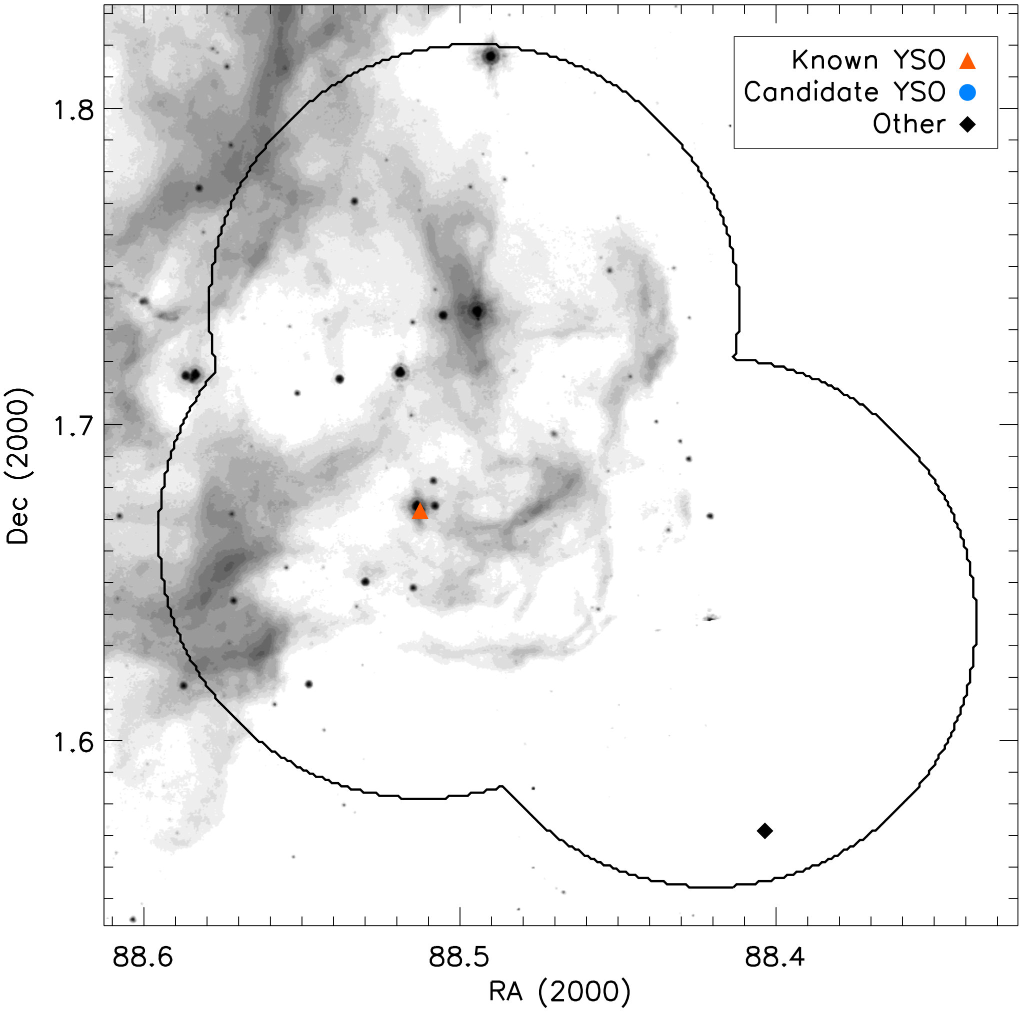

Figure 2.2 Same as Figure 2.1, but showing the Lynds 1622 region. The 8.0 μm Spitzer map is taken from Megeath et al. (2012).

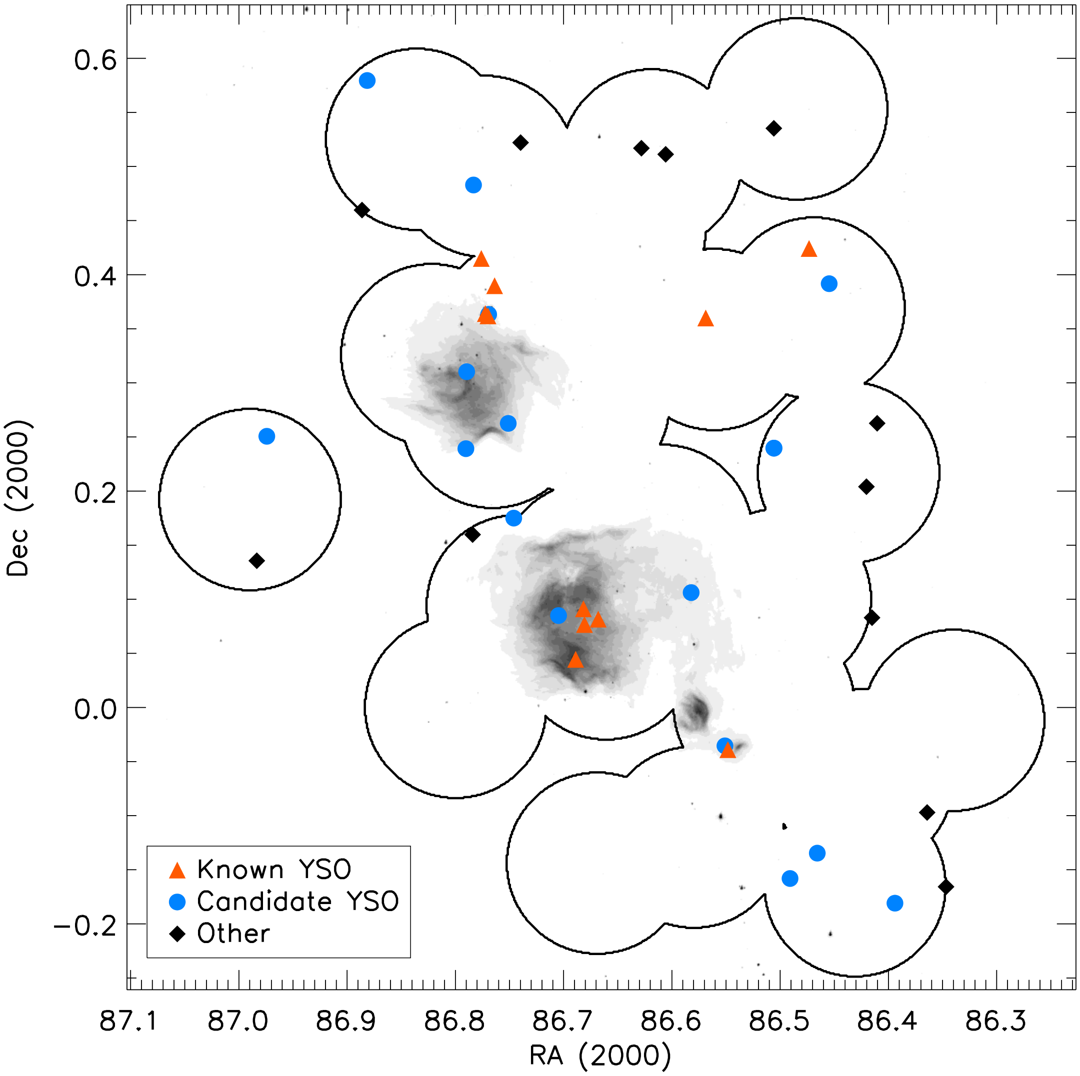

Figure 2.3 Same as Figure 2.2, but showing the NGC 2068 and NGC 2071 regions.

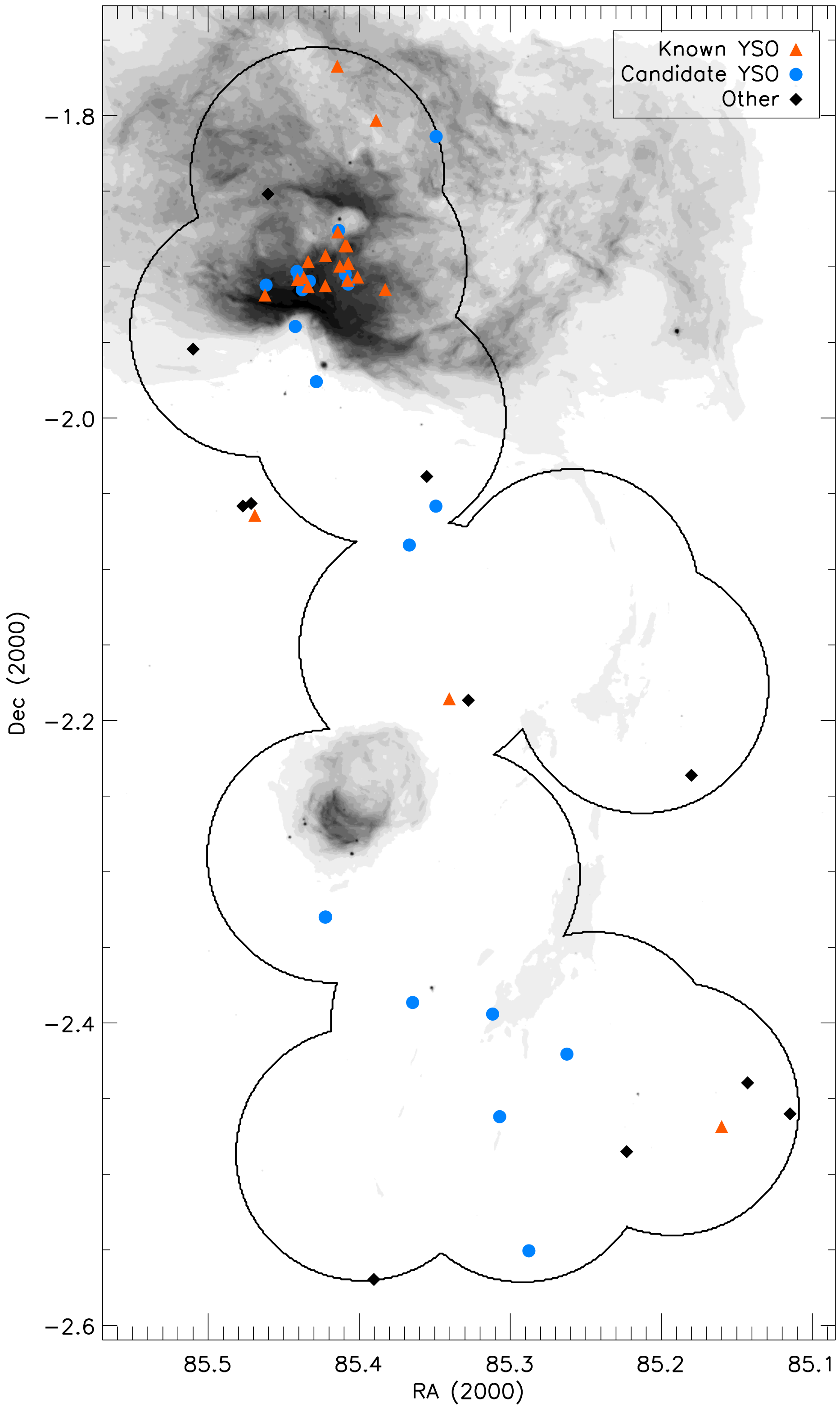

Figure 2.4 Same as Figure 2.2, but showing the NGC 2023 and NGC 2024 regions.

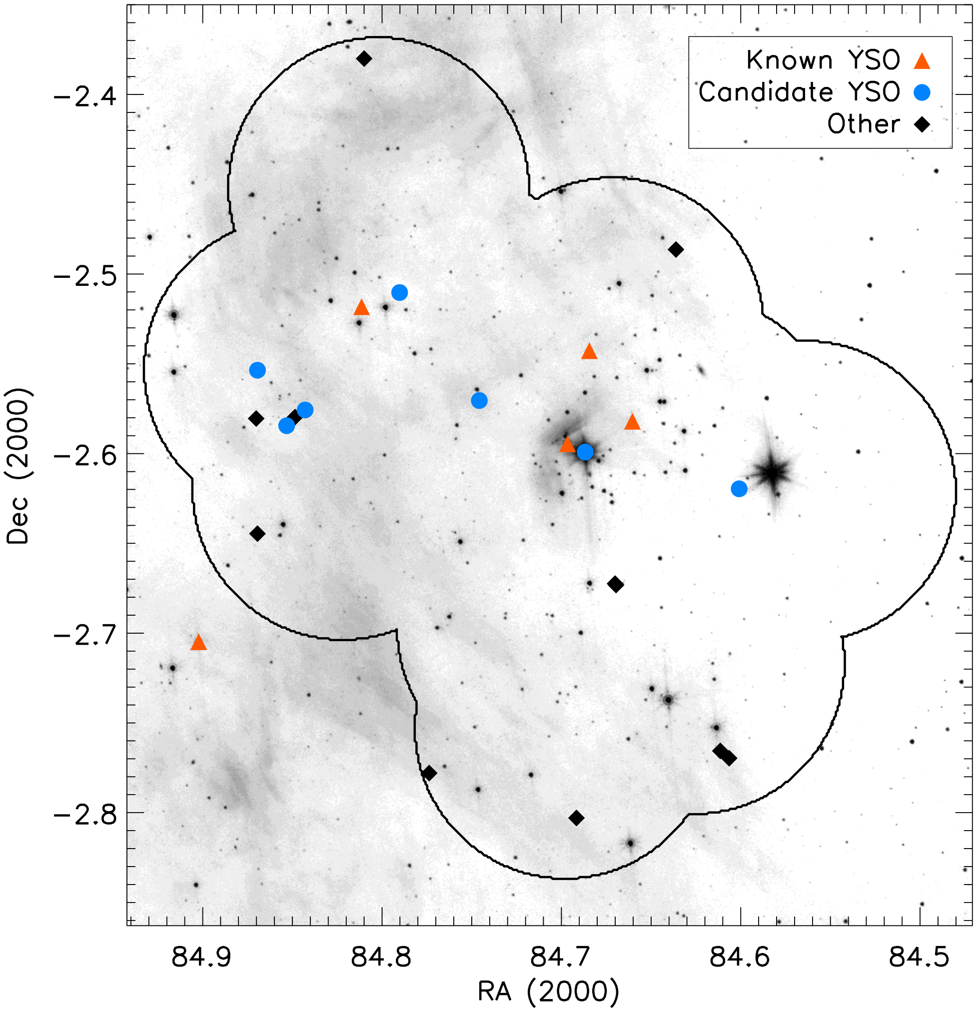

Figure 2.5 Same as Figure 2.1, but showing the σ Ori field. 8.0 μm Spitzer map is taken from Hernández et al. (2007).

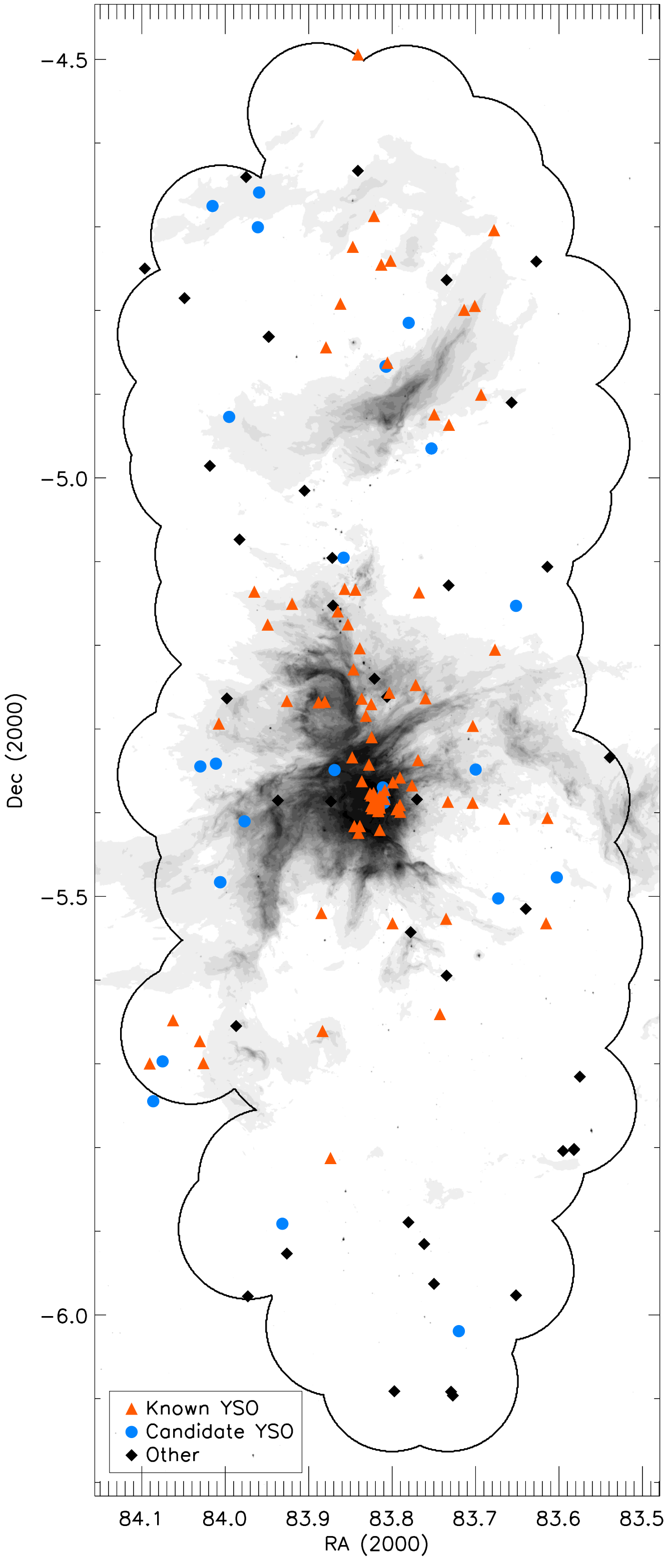

Figure 2.6 Same as Figure 2.2, but showing the Orion Nebula Cluster region.

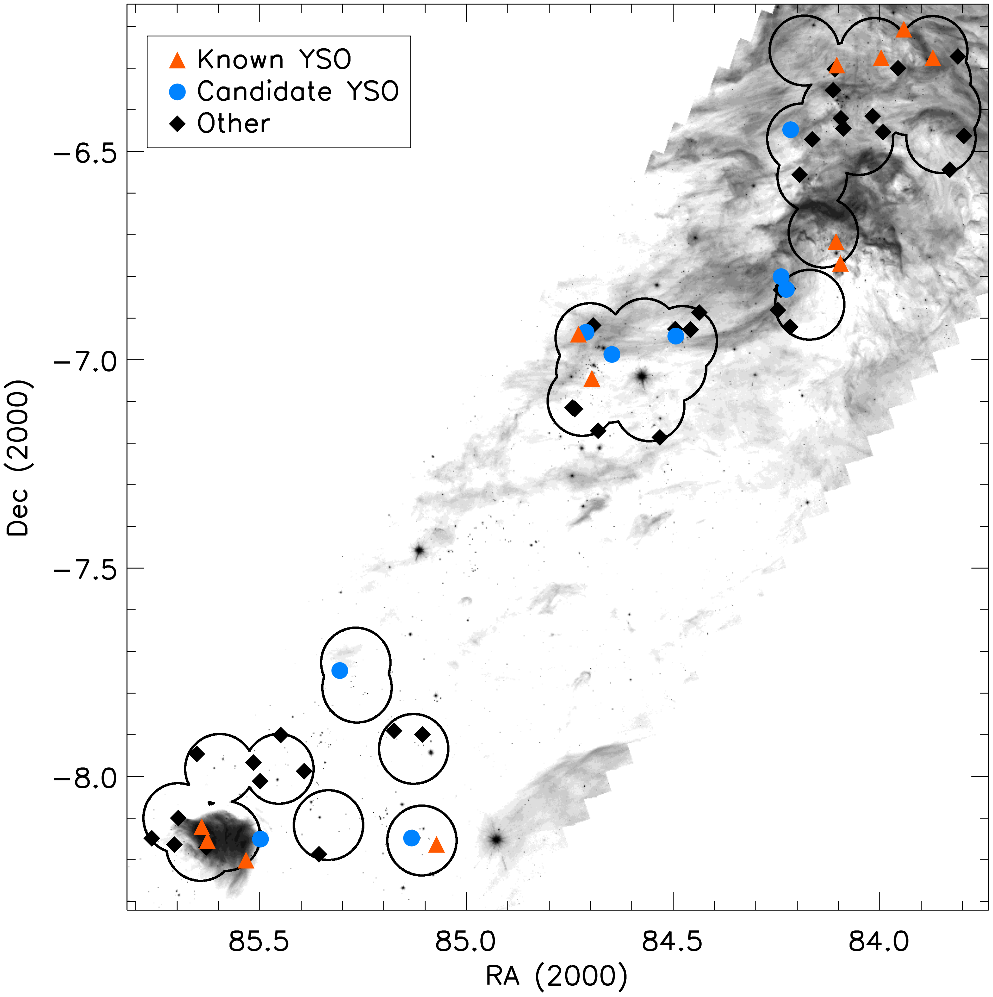

Figure 2.7 Same as Figure 2.2, but showing the Lynds 1641 region.

analyzed using Astronomical Image Processing System (AIPS). Images of individual fields were constructed and corrected for the primary beam response in a standard fashion separately for all three epochs at both 4.5 and 7.5 GHz.

We achieved a nearly uniform rms noise of 60 μJy beam^{-1} at both frequencies in all the regions. The only exception to this is in the Trapezium region due to nebular emission; there the noise was 200 μJy beam^{-1} after excluding baselines smaller than 150 kλ during imaging to remove extended emission.

2.3 Results

Sources were identified through a visual inspection of the individual fields at 4.5 GHz during the cleaning and imaging process since an automated source identification was deemed to be not sufficiently advanced and produced results that were too unreliable. An example of produced images is shown in Figure 2.8. In particularly clustered regions such as Trapezium and NGC 2024, in addition to standard imaging, data from all three epochs were combined into a single image for source identification purposes only to improve statistical significance of each detection. Rms noise in the vicinity of an object was extracted using IMSTAT over a region of size 10,000–100,000 pixels.

We have detected a combined total of 374 sources among three epochs for all the regions (Table 2.2). Since they were taken as part of Gould's Belt Very Large Array Survey, we assign them a name of GBS-VLA J*hhmmss.ss-ddmmss.s*, where J*hhmmss.ss-ddmmss.s* is the J2000.0 coordinate of each source.

Fluxes at 4.5 and 7.5 GHz were measured by performing a two-dimensional Gaussian fitting for each object in all three epochs using JMFIT. We consider two sources of uncertainty in flux — statistical noise in the images and a systematic uncertainty of 5% from possible errors in the absolute flux calibration. We also present the calculated spectral index α defined such that flux dependency on frequency is $S_\nu \propto \nu^\alpha$.

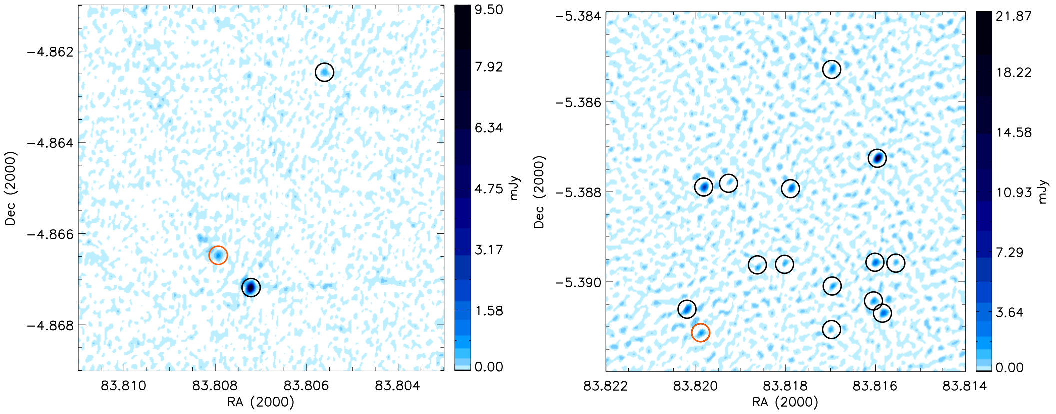

Figure 2.8 Example of a single epoch cleaned 4.5 GHz VLA map of a region with typical noise level (left) and a high noise region such as the Trapezium (right). Identified sources are circled. Black circles show objects that have been previously identified in the various multi-wavelength surveys, orange are the new detections.

Table 2.2. Radio sources detected in Orion

GBS-VLA Name	$f_{4.5}$[1](mJy)	Var.[2](%)	$f_{7.5}$[1](mJy)	Var.[2](%)	Spectral Index[3]	Variable?[4]
J053450.56+100433.0	117.42±0.31±5.87	23.2±14.9	39.20±0.11±1.96	46.9±35.5	-2.27±0.15	n
J053451.13+100427.4	101.15±0.27±5.06	19.1±15.0	39.39±0.11±1.97	41.9±35.4	-1.95±0.15	n
J053428.42+100422.6	9.23±0.17±0.46	7.3±18.0	2.89±0.09±0.14	16.4±43.4	-2.41±0.16	n
J053512.43+100255.5	2.34±0.15±0.12	14.3±16.5	1.35±0.10±0.07	33.7±30.2	-1.14±0.25	n
J053434.92+095805.6	0.66±0.12±0.03	24.2±33.1	0.43±0.08±0.02	30.8±44.7	-0.90±0.56	n

Only a portion of the table is show here. The full table is available on-line at
`http://iopscience.iop.org/0004-637X/790/1/49/suppdata/apj497441t2_mrt.txt`

[1] Highest detected flux between three epochs. The first quoted errors correspond to the statistical error calculated by `JMFIT`, and the second error is the 5% absolute flux uncertainty.

[2] The errors include the statistical and absolute uncertainty. > indicates lack of detection at one of the epochs, and variability is calculated with flux of the remaining two epochs. — with quoted flux indicates only a single epoch detection.

[3] The errors include the statistical and absolute uncertainty.

[4] Variability of at least 50% or lack of detection at one or more epoch with the source located in the inner half of the beam.

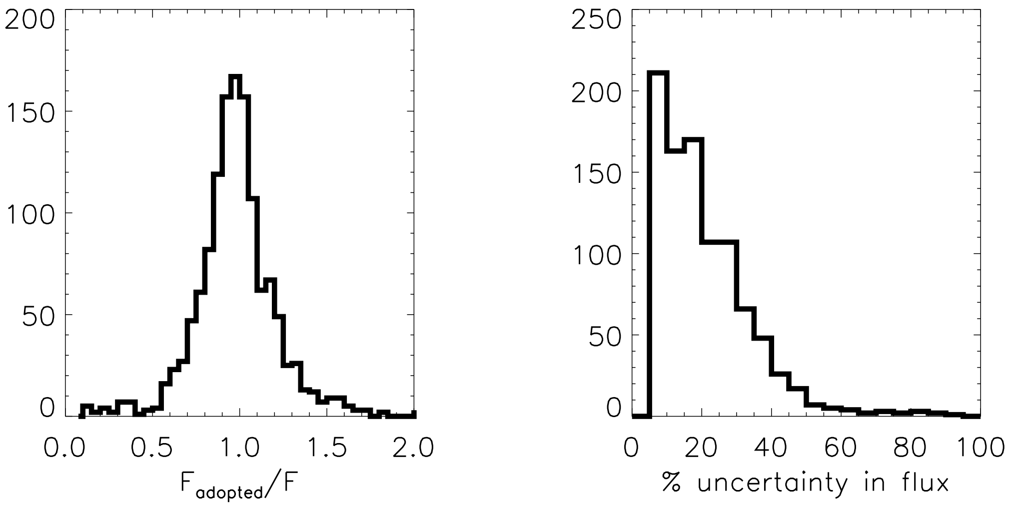

Figure 2.9 Left: Histogram of fraction of adopted flux (detection closest to the beam center) to flux of all the other detections of the same source at 4.5 GHz. Right: The percentage of measured and systematic 5% uncertainties added in quadrature relative to the measured flux. Both plots include data from all three epochs. Sources with a high degree of uncertainty in the flux have been identified at positions corresponding to a more confident detection in at least one of the epochs.

All sources but one had fluxes greater than five times the rms noise in at least one epoch. The remaining source, GBS-VLA J053518.67−052033.1, was detected at two epochs with maximum detection probability of 4.9σ in a single epoch data. It is found in the Trapezium region, and has known counterparts in other wavelength regimes.

Since our fields have been positioned in a way to provide uniform sensitivity, there was significant overlap between them. Therefore, for many of our sources we have several detections at different positions on the beam within the same epoch. Whenever this was the case, we selected a detection in which a source would be closest to the beam center to provide the adopted flux for the epoch. For each source, we present only the epoch with the largest flux at each frequency. Based on the overlap, we determine that our coordinates are generally accurate to <0.2”. Similarly, total flux uncertainty is on the order of 20%, which is recovered by the combined measured and systematic uncertainties in the data (Figure 2.9).

Table 2.3. Maximum observed plolarization for the sources at any epoch.

GBS-VLA Name	4.5 GHz polz (%)	7.5 GHz polz (%)
J053450.56+100433.0	6.8 (L)	19.0 (L)
J053451.13+100427.4	6.9 (L)	20.8 (L)
J054601.35+001422.9	7.0 (L)	15.9 (L)
J054601.41+001422.8	7.6 (L)	—
J054121.69−021108.3	2.7 (R)	6.0 (R)
J053513.73−045201.9	2.6 (L)	3.6 (L)
J053558.88−045537.7	2.8 (L)	5.1 (L)
J053518.37−052237.4	2.5 (R)	6.1 (R)
J053515.83−052314.1	3.4 (R)	6.4 (R)
J053424.63−052838.5	1.4 (L)	1.6 (L)
J053554.46−052437.1	10.5 (L)	22.6 (L)
J053657.32−064802.1	12.5 (L)	—
J053835.54−065913.7	5.3 (L)	—

We calculated the variability as the difference between highest and lowest measured flux, normalized by the maximum flux. Uncertainties in the variability were calculated by adding statistical and systematic errors in quadrature for both epochs and combined using error propagation. These percentages are quoted for 4.5 and 7.5 GHz in columns 3 and 5 of Table 2.2. For uncertainties in variability, we also consider uncertainty from the pointing error of VLA primary beam as described by Dzib et al. (2014). While the coordinate grid itself is largely unaffected, the location of the phase center of the primary beam itself is usually uncertain to 10 – 20" (Rupen, 1997), which results in an inconsistent response that becomes particularly important in the outer edges of the field. For an object located $3'$ from the center, this could lead to 8% uncertainty in variability at 4.5 GHz and 23% at 7.5 GHz.

We identified true variable sources as those exhibiting a change in flux greater than 50% at either frequency. Additionally, we also considered sources to be variable if they were not detected at one or more epochs and were located in the inner half of the beam. Sources for which circular polarization was confidently detected are listed in Table 2.3.

We cross-referenced our catalog of sources with previous major radio, infrared, optical and X-ray surveys of the regions published in the literature (Table 2.4). We

Table 2.4. Radio sources with known counterparts

GBS-VLA Name	Object Type[1]	X-ray[2]	Optical[3]	IR[4]	Radio[5]
J053428.42+100422.6	—	—	—	—	NVSS
J053530.67+095611.3	—	LOX 130	—	—	—
J053519.05+095454.9	YSO	LOX 98	BSM 9	HMC 4155	—
J053516.49+095437.3	Galaxy	—	—	2M	—
J053459.44+095312.0	—	LOX 51	—	—	—

Only a portion of the table is show here. The full table is available on-line at `http://iopscience.iop.org/0004-637X/790/1/49/suppdata/apj497441t4_mrt.txt`

[1] In parentheses listed YSO class, if known.

[2] LOX=Franciosini & Sacco (2011); 3XMM=Xmm-Newton Survey Science Centre (2013); SSM=Skinner et al. (2009); SGB=Skinner et al. (2003); CCS=Caballero et al. (2010); RRS=Ramírez et al. (2004); TKT=Tsujimoto et al. (2002); COUP=Getman et al. (2005); SOXS=Pillitteri et al. (2013)

[3] BSM=Bayo et al. (2011); TYC=Perryman & ESA (1997); UCAC4=Zacharias et al. (2012); H97=Hillenbrand (1997); DRS=Da Rio et al. (2009); HHA=Hsu et al. (2012)

[4] HMC=Hernández et al. (2010); 2M=Cutri et al. (2003); MGM=Megeath et al. (2012); PBZ=Peña Ramírez et al. (2012); HHM=Hernández et al. (2007); MAD=Bouy et al. (2009); ISOY=Morales-Calderón et al. (2011); TKK=Tsujimoto et al. (2003)

[5] NVSS=Condon et al. (1998); G99=Gibb (1999); RRA = Reipurth et al. (2004); RR=Rodriguez & Reipurth (1994); RRC=Reipurth et al. (1999); GMR=Garay et al. (1987); AVE=Anglada et al. (1998); ARC=Avila et al. (2001)

have generally considered sources in these surveys to be counterparts if they had positional coincidences less than 1”, but have allowed for larger offsets if the combined uncertainty between the databases was large.

Of 374 detected sources, 261 have been previously found at another wavelength region, while 113 are new detections. 146 sources have been detected in X-rays, 94 at optical wavelengths, 218 at infrared, and 63 in previous radio surveys. For sources with infrared counterparts we display infrared colorcolor diagrams in Figure 2.10. Of the previously identified sources, 1 is extragalactic, while the other 148 as young stellar objects (YSOs). Of the YSOs, 106 have been placed on the standard class system based on the IRAC colorcolor classification of Allen et al. (2004). There are 11 Class 0/I, 26 Class II, and 70 Class III type stars (Table 2.4).

A total of 225 sources are either new detections or, to our knowledge, have not been previously classified in the literature. Of these remaining objects, we have

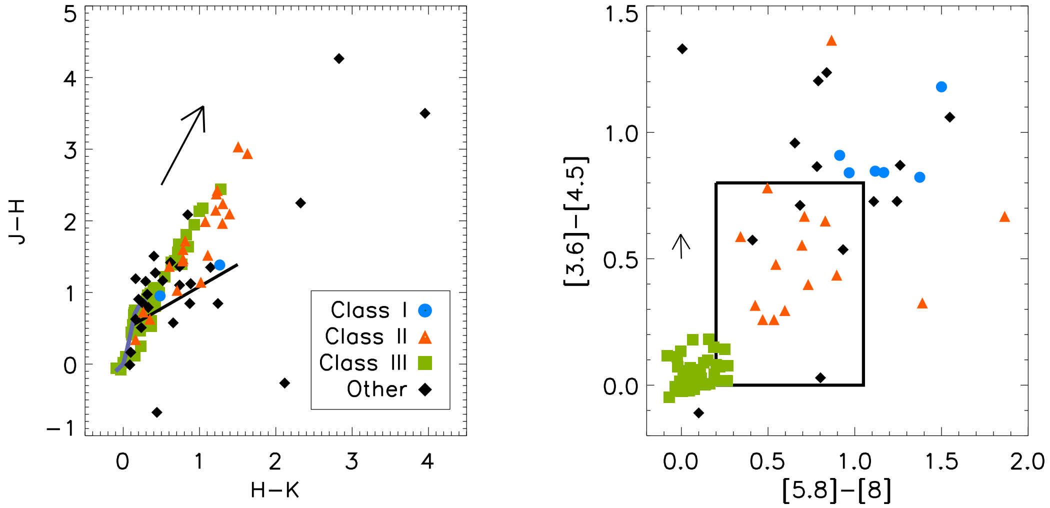

Figure 2.10 Color-color diagrams for sources with infrared counterparts from Table 2.4, identified according to their evolutionary classification, when known. Arrows show the reddening vector of 1 A_K, from Megeath et al. (2012). On the left plot, a black line shows the location of the CTTS locus as identified by Meyer et al. (1997), which corresponds to the intrinsic de-reddened colors of the young stars with disks. A purple line shows typical colors for pure photospheres (Bessell & Brett, 1988). On the right plot, the rectangle shows the approximate colors of Class II stars as identified by Allen et al. (2004)

.

Table 2.5. Young stellar object candidates based just in their radio properties

GBS-VLA Name	Var$_{4.5}$ (%)	Var$_{7.5}$ (%)	Spectral Index
J053450.56+100433.0	23.2±14.9	46.9±35.5	-2.27±0.15
J053451.13+100427.4	19.1±15.0	41.9±35.4	-1.95±0.15
J053451.35+095630.4	>12.3±57.5	—	-0.40±0.92
J053516.49+095437.3	43.3±65.2	—	-0.69±1.39
J053433.68+095308.8	>22.6±69.5	>26.3±78.9	-0.58±1.39

Only a portion of the table is show here. The full table is available on-line at
`http://iopscience.iop.org/0004-637X/790/1/49/suppdata/apj497441t5_mrt.txt`

identified 86 as exhibiting variability or high levels of circular polarization (Table 2.5). While we cannot exclude the possibility that any of them are extragalactic in nature, quasars are not expected to vary as strongly on timescales of few weeks to few months (Hovatta et al., 2008), and exhibit very weak circular polarization (Saikia & Salter, 1988), so these sources are likely YSO candidates. Using the same criteria of variability and circular polarization would identify only 107 of the 148 previously-known YSOs; thus we cannot tell which of the remaining 139 unidentified sources are YSOs or extragalactic objects. Further identification of YSOs will depend upon forthcoming VLBA parallax measurements.

2.4 Discussion

2.4.1 Radio properties of the YSO population

We analyzed the radio properties of objects that have been previously identified as YSOs with a known SED class. We compared the spectral indices in Figure 2.11. UnlikeDzib et al. (2013) who found the spectral index to be more negative for more evolved sources, we found no statistically significant difference in the spectral index between stars of different classes, and the median value for all three evolutionary classifications is consistent with zero.

Figure 2.12 shows variability of the classified YSOs. This is not representative of

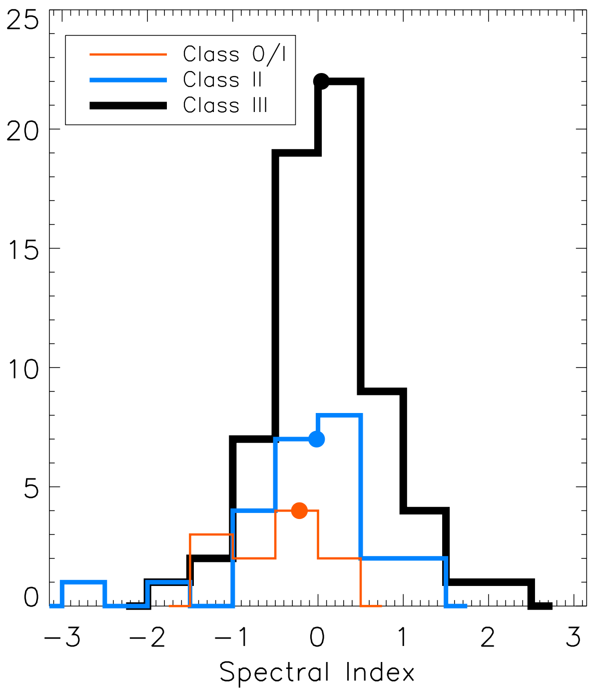

Figure 2.11 Spectral index distribution of the known and classified YSOs in our sample. Typical uncertainties of the spectral index 4.5 – 7.5 GHz are 0.6. Circles show the median value for each SED class.

the total variability, as we do not include upper limits on the sources that were not detected in one or more epochs, which would skew distribution to be more variable for all of the classifications. Rather, we look at the relative distribution between different SED classes. As in Dzib et al. (2013), we found that more evolved YSOs tend to be on average more variable as compared to their younger counterparts. This is likely due to non-thermal gyrosynchrotron emission becoming more prevalent over thermal bremsstrahlung radiation for older YSOs (Feigelson & Montmerle, 1999).

2.4.2 The radio - X-ray luminosity relation

Güdel & Benz (1993) found an empirical relation between X-ray and radio luminosity for magnetically active stars, suggesting that mechanisms that drive emission in both of these wavelengths are related. We compare our results to the Güdel-Benz relation.

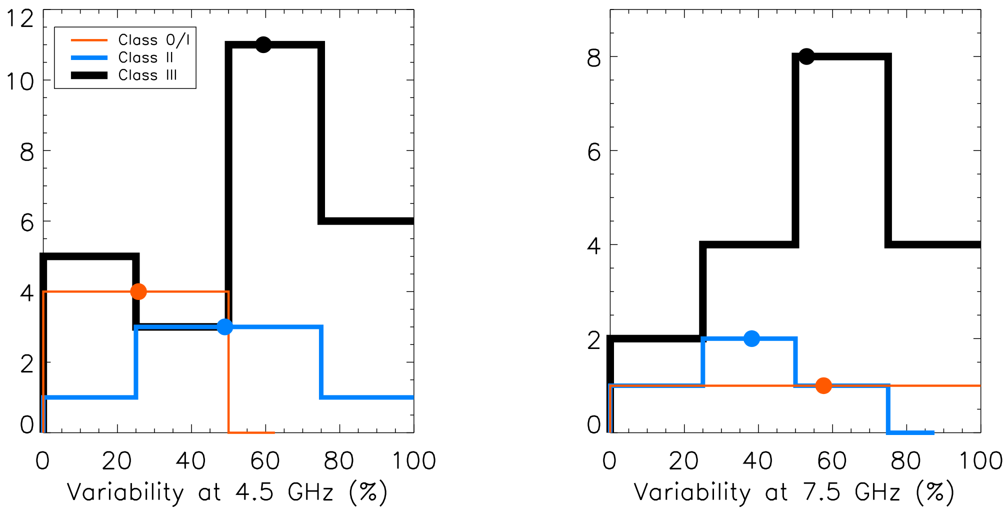

Figure 2.12 4.5 and 7.5 GHz variability of the known and classified YSOs in our sample. Only the sources which were detected at all three epoch are includeds. Typical uncertainties in variability are 25%. Circles show the median value for each SED class.

$$\frac{L_X}{L_R} \approx 10^{15.5\pm1.5}$$

in Figure 2.13. Of 148 known YSOs in our sample, 114 have cited X-ray luminosities in either 3XMM-DR4 Source Catalogue (Xmm-Newton Survey Science Centre, 2013) or in COUP Survey (Getman et al., 2005). We did not include other X-ray surveys for a more consistent sample. We corrected all luminosities to the adopted distance of 414 pc (Menten et al., 2007). As Dzib et al. (2013) found in their analysis of the Ophiuchus region and Forbrich & Wolk (2013) found in their studies of the ONC, we find that the X-ray emission of YSOs in our sample is underluminous compared to the Güdel-Benz relation.

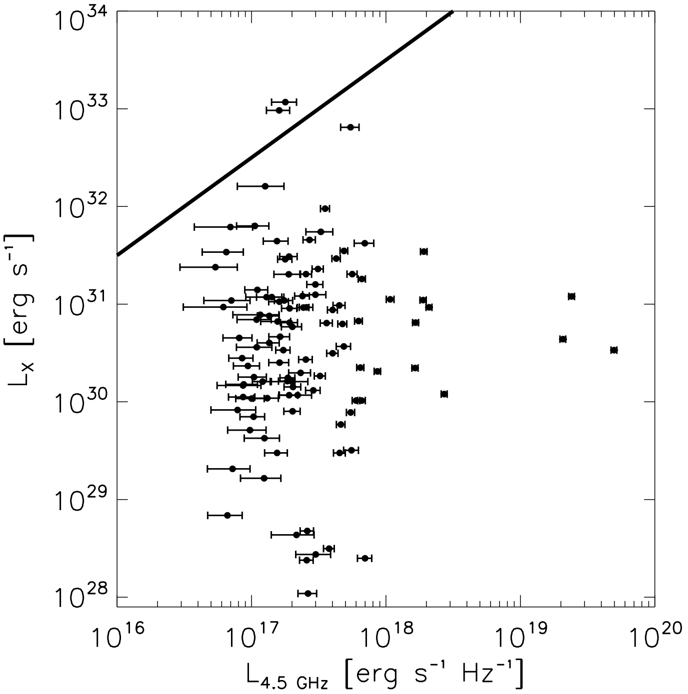

Figure 2.13 X-ray luminosity as a function of radio luminosity for stars in our sample. The black line is the approximate Güdel-Benz relation.

2.5 Comments on some individual sources

2.5.1 GMR F

GMR F = GBS-VLA J053518.37−052237.4 is located in the central ONC region, not far from the Trapezium cluster. It has been identified in several multi-wavelength surveys and is a known variable star, with infrared photometry consistent with being a Class III YSO (Megeath et al., 2012). It emits non-thermally at radio wavelengths, and it was one of the four stars used by Menten et al. (2007) to measure distance to the Trapezium with VLBA.

GMR F is one of the few sources which we detected in more than three epochs, as fields which contained it were split between two different maps. We observed it undergoing a strong flare (Figure 2.14), in which the flux has increased by the factor of 90% at both 4.5 and 7.5 GHz. It displayed noticeable circular polarization that was particularly pronounced in the last epoch, after the flux of the source started to

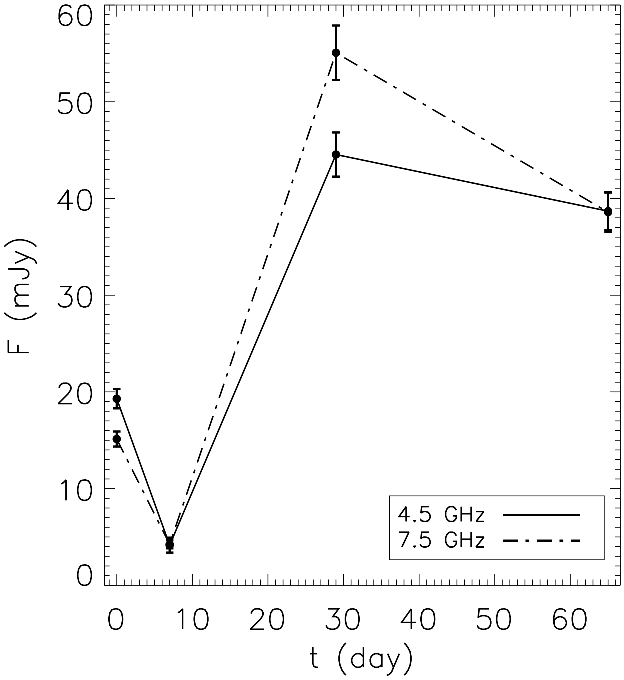

Figure 2.14 Light curve of GMR F at 4.5 and 7.5 GHz from Julian Date 2455737 to 2455802.

decline.

2.5.2 GBS-VLA J054121.69−021108.3

GBS-VLA J054121.69−021108.3 is a star located near NGC 2023. It has been previously observed by Reipurth et al. (2004) at radio wavelengths using the VLA at 8.3 GHz. They measured its flux to be on the order of 50 mJy; since it was far from the beam center they could not give more exact values. It was later identified by Mookerjea et al. (2009) and Megeath et al. (2012) as a Class II YSO using data from *Spitzer Space Telescope*. It reportedly has no optical or submillimeter counterparts.

We observe the maximum flux of this source to be 243 and 245 mJy at 4.5 and 7.5 GHz, respectively (Figure 2.15). The maxima at each wavelengths did not occur at the same epoch; the maximum flux at 4.5 GHz was observed at the same time as the smallest flux at 7.5 GHz at just 137±7 mJy. This object does not show sufficient levels of variability (>50%) over the short observation period for us to identify it as

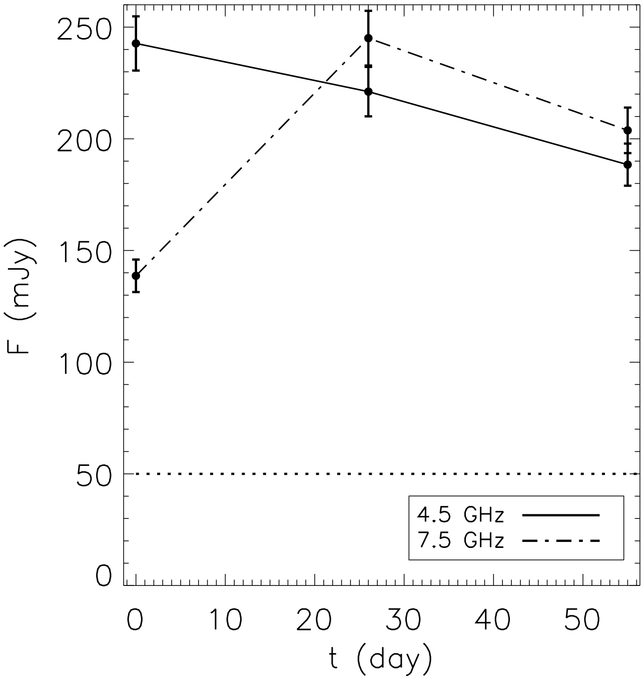

Figure 2.15 Light curve of GBS-VLA J054121.69−021108.3 at 4.5 GHz from Julian Date 2455746 to 2455801. Dotted line at 50 mJy shows the 8.3 GHz flux measured by Reipurth et al. (2004) 3400 days prior to our observations.

a variable star; however, combined with the detection by Reipurth et al. (2004), it undeniably shows longer term variability. This star may be a flaring source which we caught near its high state. Additionally, the centimeter flux density of this source is the highest ever reported in association with a young star.

This source was detected in the NRAO VLA Sky Survey (NVSS) at 1.4 GHz (Condon et al., 1998) with a flux density of 98.4±3.9 mJy in observations made on 1995 March 5. We have analyzed the VLA archive observations of project AV187, finding a 1.4 GHz flux density of 72.6±2.3 mJy for observations taken on 1991 April 14 and 15. This result confirms the long-term variability of GBS-VLA J054121.69-021108.3.

2.6 Conclusions

We report on radio observations in several regions in the Orion Molecular Cloud complex, namely λ Ori, Lynds 1622, NGC 2068, NGC 2071, NGC 2023, NGC 2024, σ Ori, ONC, and Lynds 1641. Our observations provide high sensitivity and angular resolution over 2.26 deg^2. We detected a total of 374 sources, of which 148 had been previously identified as YSOs. 86 unclassified sources exhibit radio properties that are consistent with those of young stars. These sources will be used as targets for future VLBA observations to determine the distance to and kinematics of these regions. These results will complement upcoming measurements from *Gaia* and provide more concrete distances toward regions of high nebulosity or sources without optical counterparts.

CHAPTER III

The Gould's Belt Distances Survey (GOBELINS) II. Distances and structure toward the Orion Molecular Clouds

We present the results of the Gould's Belt Distances Survey of young star-forming regions toward the Orion Molecular Cloud Complex. We detected 36 young stellar objects (YSOs) with the Very Large Baseline Array, 27 of which have been observed in at least three epochs over the course of two years. At least half of these YSOs belong to multiple systems. We obtained parallax and proper motions toward these stars to study the structure and kinematics of the Complex. We measured a distance of 388±5 pc toward the Orion Nebula Cluster, 428±10 pc toward the southern portion L1641, 388±10 pc toward NGC 2068, and roughly ∼420 pc toward NGC 2024. Finally, we observed a strong degree of plasma radio scattering toward λ Ori. Published in 2017, ApJ, 834, 142.

3.1 Introduction

Young star-forming regions toward Orion have been the subject of much interest, as they are the closest regions of a massive young stellar population. The star formation in the Orion Complex is concentrated in two molecular clouds, Orion A and

B, with clusters such as the Orion Nebula Cluster (ONC) and L1641 in Orion A, and NGC 2023/2024, NGC 2068/2072, and L1622 in Orion B. These clusters represent the most recent episodes of star formation in the region, which belong to the Orion OB1c and 1d subassociation, containing stars spanning ages from ∼1 Myr up to 6 Myr (Bally, 2008). In addition to the clusters in the main cloud, other stellar groups in Orion host very young stars, like σ Ori in the OB1b subassociation, and the groups of the λ Ori association at the northernmost end of the complex. Finally, a somewhat older (8-12 Myr) population is contained within the OB1a subassociation, where most of the parental gas has already been removed.

Over the course of the last century, many attempts have been made to measure distances to the Complex, particularly toward the ONC. Some of the earliest measurements were as high as 2000 pc (Pickering, 1917) and as low as 185 pc (Kapteyn, 1918). Eventually most measurements settled in the 350-500 pc range and obtained through various means, most typically through zero-age main sequence fitting. Much of the scatter originated from inconsistent assumptions, models, and sample selection (see review by Muench et al., 2008).

For some time, the most widely used distance was 480±80 pc, obtained from proper motions of H_2O masers toward the Orion BN/KL region (Genzel et al., 1981). In the last decade, however, direct stellar parallax measurements of nonthermal emitting masers and stars were made possible through radio very long baseline interferometry (VLBI). Menten et al. (2007, hereafter MR) obtained a distance of 414±7 pc from observations of four stars - GMR A, F, G, and 12 - in the central (Trapezium) region of the ONC. Sandstrom et al. (2007, hereafter S07) also observed GMR A and obtained a somewhat closer distance of 389^{+24}_{-21} pc. Hirota et al. (2007) and Kim et al. (2008) observed H_2O and SiO masers to obtain a distance of 437±19 pc and 418±6 pc respectively in the Orion BN/KL region.

Other major efforts to measure a distance toward the ONC include Jeffries's

(2007). He used stellar rotation to estimate distances of 440±34 pc for his entire sample and 392±2 pc including only stars without active accretion. Stassun et al. (2004) obtained a distance of 419±21 pc through monitoring the kinematics of a double-line eclipsing binary system, assuming a value for the solar bolometric luminosity of $M_{\text{bol},\odot} = 4.59$, although their distance estimate decreased to 390±21 pc with $M_{\text{bol},\odot} = 4.75$. Kraus et al. (2009) obtained a dynamical distance of 410±20 pc based on modeling the orbit of the close binary θ^1 Ori C. Some attempts have also been made to obtain distances from dust extinction maps not just toward the ONC, but also toward several distinct regions in the Orion Complex. Lombardi et al. (2011) estimated a distance of 371±10 pc toward Orion A and 398±12 pc toward Orion B using extinction maps measured from the Two-Micron All Sky Survey. Schlafly et al. (2014) provided distance estimates of 20 distinct regions through extinction from PanSTARRS photometry, although many of them are highly uncertain.

While the distance measured by MR is currently considered as canonical, it is based on a small sample of four stars. In addition, the MR stars all lie within the central regions of the ONC; however, the Complex spans 100 pc projected on the sky, so it would not be surprising if the different regions of the cloud have substantially different distances, and it would not be surprising if the regions have differing radial distances of the same order. Therefore even if the distance toward the ONC is known with high accuracy, by applying this distance to other regions, an inherent uncertainty of 20%, for example, could be introduced, as the Complex is located at the distance of 400 pc. This propagates to an error of 40% in luminosity, to 70% in the ages of young stars (Hartmann, 2001).

Currently an ongoing mission of the *Gaia* space telescope is obtaining astrometry toward optically visible sources across the entire sky to measure parallaxes accurate to 100 μas for G<17 mag stars (de Bruijne et al., 2014), which should provide accuracy in distance measurements to within 5%-10% up to 1 kpc. VLBI observations can provide an important independent check on optical parallax measurements, as shown by the comparison of VLBI with *Hipparcos* distances for the Pleiades (Melis et al., 2014). In addition, radio VLBI can be useful for measuring sources in regions of high extinction and/or significant nebulosity, as is the case in many regions of Orion.

In this chapter we present radio VLBI observations of stellar parallaxes of young stellar objects (YSOs) identified toward the Orion Complex, hereby significantly expanding the number of stars in Orion with known distances and kinematics. This work is done as part of Gould's Belt Distances Survey (GOBELINS, Loinard et al., 2011), which is dedicated to measuring stellar parallaxes toward the Ophiuchus (Ortiz-León et al., 2017a), Serpens (Ortiz-León et al., 2017b), Taurus, Perseus, and Orion star-forming regions.

3.2 Observations

The observations presented in this chapter were made with the National Radio Astronomy Observatory's Very Long Baseline Array (VLBA) at 5 GHz with a 256 MHz bandwidth (spanning the range of 4.852-5.076 GHz). They span a period of two years from 2014 to 2016 March, with observations preferentially scheduled near the equinoxes, to target the maxima of the parallactic eclipse along right ascension. All the fields were observed in groups of three per observing session, for a total of 56 observing sessions under the code of BL175 (Table 3.1). Each session was planned as follows: a primary calibrator was alternated between observing each field, and after five iterations encompassing all the fields, three secondary calibrators were observed. The duration of each pointing was 2 minutes for targeted fields and ∼1 minute for each of the calibrators. The geodetic block was observed at the beginning and the end of each session (the frequency of the observations of this block spanned the 4.596-5.076 GHz range). The total observing time was ∼1 hr per field. In addition, we spent 1.5 hr per session on the primary calibrator and 0.1 hr on each of the secondary calibrators.

During correlation, each field was reduced to a series of small patches only a few arcseconds in diameter, and each patch was centered at a phase center corresponding to the targets within a field (a description of the process is presented in Ortiz-León et al., 2017a). Targets were identified from the Very Large Array (VLA) survey of the Orion Complex by Kounkel et al. (2014). In that survey 374 sources were detected, out of which 148 were associated with known YSOs and 86 were identified as YSO candidates on the basis of their radio properties out of the remaining sources that could not be classified by other means. The criteria for candidacy included (1) detectable circular polarization, or (2) short-term radio variability >50% at either 4.5 or 7.5 GHz. For the first two epochs of the VLBA Orion observations, 40 fields were observed (Table 3.1). The total number of fields was chosen on the basis of the number of hours awarded for GOBELINS. We accommodated observations of all five star-forming clouds targeted by the program, and the field centers were distributed in such a way as to maximize the number of known YSOs observed. After two epochs, we were already able to begin to distinguish between galactic and extragalactic sources on the basis of motion of the sources between epochs. Twelve fields where no galactic sources have been detected were removed from the survey and six new fields were added to include more isolated YSOs from the VLA survey. The number of fields has been further cut to only 26 for epoch 4, and to 17 for epoch 5.

The data were reduced in the AIPS (Greisen, 2003) following the standard prescription for the VLBA data. The multiband delays were removed using the DELZN task based on the geodetic sources (Reid & Brunthaler, 2004). The phase gradient across the sky was then calibrated using secondary calibrators with the ATMCA task. When multiple sources were observed in the same field, the same calibration was applied to all sources. Positions of all the sources were referenced to the primary calibrator. Finally, all sources were imaged and the positions of all point sources were

Table 3.1. Dates of the VLBA observations.

#	R.A. (J2000)	Dec. (J2000)	Epoch 1 Date / Field name	Epoch 2 Date / Field name	Epoch 3 Date / Field name	Epoch 4 Date / Field name	Epoch 5 Date / Field name
1	05:35:13.5550	-05:21:37.8875	03/24/14 GD1	09/21/14 EG1	02/26/15 FB1	09/01/15 FP1	02/25/16 FA1
2	05:35:28.5199	-05:10:11.9953	03/24/14 GD2	09/21/14 EG2	02/26/15 FB2	09/01/15 FP2	02/25/16 FA2
3	05:35:57.8954	-05:23:01.0259	03/24/14 GD3	09/21/14 EG3	—	—	—
4	05:35:32.0330	-05:39:38.5578	—	—	02/26/15 FB3	09/01/15 FP3	—
5	05:34:51.3847	-04:55:18.2572	03/10/14 GE1	09/22/14 EH1	02/27/15 FC2	08/31/15 FQ2	03/01/16 HV2
6	05:34:51.3847	-05:09:09.6415	03/10/14 GE2	09/22/14 EH2	02/27/15 FC3	08/31/15 FQ3	03/01/16 HV3
7	05:34:31.9858	-05:28:33.5795	03/10/14 GE3	09/22/14 EH3	02/27/15 FC1[a]	08/31/15 FQ1	03/01/16 HV1
8	05:35:49.5816	-05:16:05.3335	03/08/14 GF1	09/30/14 EI1	02/28/15 FD2	09/05/15 FR2	03/05/16 HW2
9	05:35:59.2812	-04:56:41.3956	03/08/14 GF2	09/30/14 EI2	—	—	—
10	05:36:08.9806	-05:41:01.8254	03/08/14 GF3	09/30/14 EI3	02/28/15 FD3	09/05/15 FR3	03/05/16 HW3
11	05:35:02.4698	-05:16:05.3335	—	—	02/28/15 FD1	—	—
12	05:35:16.3262	-04:41:26.8728	03/01/14 GG1	10/02/14 EJ1	03/01/15 FE1	09/13/15 FS1	03/08/16 HX1
13	05:35:19.0975	-04:49:45.7032	03/01/14 GG2	10/02/14 EJ2	03/01/15 FE2	09/13/15 FS2	03/08/16 HX2
14	05:35:46.8103	-05:29:56.7182	03/01/14 GG3	10/02/14 EJ3	03/01/15 FE3	—	—
15	05:35:02.4698	-05:34:47.7026	03/09/14 GH1	10/03/14 EK1	03/03/15 FF1	09/05/15 FR1	03/05/16 HW1

Only a portion of the table is show here. The full table is available on-line at `http://iopscience.iop.org/0004-637X/834/2/142/suppdata/apjaa4f02t1_ascii.txt`

[a] Field was repositioned to RA=05:34:34.7570 DEC=-05:25:47.3027

Table 3.2. Assumed positions of the calibrators

Calibrator[a]	α (J2000)	δ (J2000)
J0539-0514	05:39:59.937192	-05:14:41.30174
J0529-0519	05:29:53.533450	-05:19:41.61678
J0541-0541	05:41:38.083371	-05:41:49.42843
J0532-0307	05:32:07.519261	-03:07:07.03799
J0517-0520	05:17:28.110157	-05:20:40.84222
J0542-0913	05:42:55.877408	-09:13:31.00660
J0553-0840	05:53:41.891558	-08:40:01.90151
J0527-1002	05:27:24.060380	-10:02:57.26651
J0558-0055	05:58:44.391460	-00:55:06.92375
J0600-0005	06:00:03.503368	-00:05:59.03477
J0552+0313	05:52:50.101499	+03:13:27.24311
J0536+0944	05:36:31.978172	+09:44:20.63128
J0532+0732	05:32:38.998486	+07:32:43.34572
J0519+0848	05:19:10.811128	+08:48:56.73450
J0544+1118	05:44:52.199795	+11:18:49.92568
J0530+1331	05:30:56.416747	+13:31:55.14954
J0547+1223	05:47:06.276323	+12:23:46.24477

[a] When imaged, secondary calibrators are offset from these positions as their coordinates are referenced to the primary calibrator.

extracted using the JMFIT task. More details on data reduction are presented in Ortiz-León et al. (2017a).

Positions of all sources were referenced relative to the primary calibrators (Table 3.2). The arrangement of the primary and secondary calibrators for each field is described in Table 3.3. This configuration was preserved through all the epochs. The exception to this were the λ Ori fields, as their primary and secondary calibrators were extended, which resulted in uncertain astrometry. We propose that plasma scattering from the supernova bubble 2.5–3° in radius around λ Ori is responsible for the image blurring (see Appendix A). An attempt was made to switch to a different nearby calibrator that would improve the astrometry. However, as the assumed absolute positions of the calibrators are not referenced relative to each other, a positional offset was introduced to the sources in the field.

A few other calibrators do have some structure, most likely due to jet activity; however, an evolving jet structure should not significantly influence measured par-

Table 3.3. Calibrators setup for the observed fields

Field #	Primary	Secondary 1	Secondary 2	Secondary 3
1, 2, 3, 4, 8, 9, 10, 11, 12, 13, 14, 15, 16, 17	J0539-0514	J0529-0519	J0541-0541	J0532-0307
5, 6, 7, 35, 36	J0529-0519	J0539-0514	J0532-0307	J0517-0520
18, 19, 20, 37	J0539-0514	J0541-0541	J0529-0519	J0542-0913
21, 22, 23	J0542-0913	J0541-0541	J0553-0840	J0527-1002
24, 25, 26	J0532-0307	J0539-0514	J0541-0541	J0558-0055
27, 28, 29, 45, 46	J0558-0055	J0600-0005	J0552+0313	J0532-0307
30, 31, 32, 33, 34	J0532-0307	J0539-0514	J0529-0519	J0558-0055
38, 39	J0536+0944	J0532+0732	J0544+1118	J0530+1331
40	J0552+0313	J0600-0005	J0558-0055	J0606-0024
41	J0552+0313	J0532-0307	J0558-0055	J0606-0024
42, 43, 44	J0541-0541	J0539-0514	J0529-0519	J0542-0913

allaxes (MR), particularly if the main source is point-like and the jet emission is sufficiently displaced. The two most notable calibrators with structure are J0539-0514 and J0532-0307. The former produced many errors in the calibration solutions as it was not bright enough during the first two epochs, with a typical flux of ∼30 mJy; the substructure was not immediately apparent, but during the third epoch its flux had increased to ∼50 mJy, resulting in a significant improvement in the calibration, and there was a clear emission from a second component at a position angle of ∼240°, ∼1 mas away; this emission persisted during all the remaining epochs. The latter calibrator, J0532-0307, always had a spatially resolved second component at p.a. ∼150°, ∼10 mas away.

Our VLBA survey fields covered a total of 300 sources from the VLA survey. As VLBA detections generally require nonthermal emission due to their high brightness temperatures, only 116 objects have been detected (although some of them can be resolved into multiple objects or a jetted structure). We report only on objects that either (1) were detected in at least two epochs, or (2) had a single detection $> 5\sigma$ (Figure 3.1). The remaining undetected objects most likely emit only thermally. Thirty-six of the detected systems can be definitely identified as YSOs on the basis of astrometric motion, and 57 are most likely associated with active galactic nucleus

Table 3.4. Positions of sources identified in at least two epochs or with a single $> 5\sigma$ detection. The uncertainties for both α and δ are given in the units of mas.

VLBA	YSO?	R.A. (J2000, mas)	Dec. (J2000, mas)	Date (JD)	Flux (mJy)	Field rms (mJy)
1	n	5:35:29.221269± 0.361	-5:05:44.137403± 0.491	2456741	0.593± 0.171	0.074
1	n	5:35:29.221299± 0.157	-5:05:44.136384± 0.402	2456922	0.570± 0.174	0.072
1	n	5:35:29.221302± 0.172	-5:05:44.136521± 0.361	2457080	0.673± 0.192	0.072
1	n	5:35:29.221309± 0.945	-5:05:44.136624± 0.418	2457266	1.695± 0.488	0.079
1	n	5:35:29.221302± 0.254	-5:05:44.136877± 0.485	2457444	0.702± 0.192	0.052

Only a portion of the table is show here. The full table is available on-line at
`http://iopscience.iop.org/0004-637X/834/2/142/suppdata/apjaa4f02t4_mrt.txt`

(AGN) activity. The remaining 23 objects have detection in only one epoch or have astrometry too poor to make a definitive determination (Table 3.4).

Out of 148 objects in the VLA survey that were known YSOs in the literature, 36 have been detected with VLBA. Three of these sources have been falsely identified, as we cannot confirm their membership in the Orion Complex on the basis of their astrometry. GBS-VLA J054121.69-021108.3 (=VLBA 55), GBS-VLA J053542.27-051559.3 (=VLBA 110), and GBS-VLA J053532.03-053938.6 (=VLBA 139) all previously identified as YSOs on the basis of optical and IR emission, but they do not show a significant astrometric offset between epochs.

Kounkel et al. (2014) identified 86 VLA sources as candidate YSOs, based on their radio properties, and we detected 26 of them with the VLBA. Only three of these can be confirmed as YSOs in the Orion region. The criteria for selection used by Kounkel et al. (2014) appear to be not entirely reliable: while a strong variability at 4.5 GHz can indeed be used to distinguish galactic from extragalactic sources, the same cannot be said for 7.5 GHz (Figure 3.2). Similarly, the degree by which circular polarization can be affected by beam squint has been significantly underestimated. Out of nine sources with observed VLA circular polarization detected in this program, we can confirm only two as YSOs.

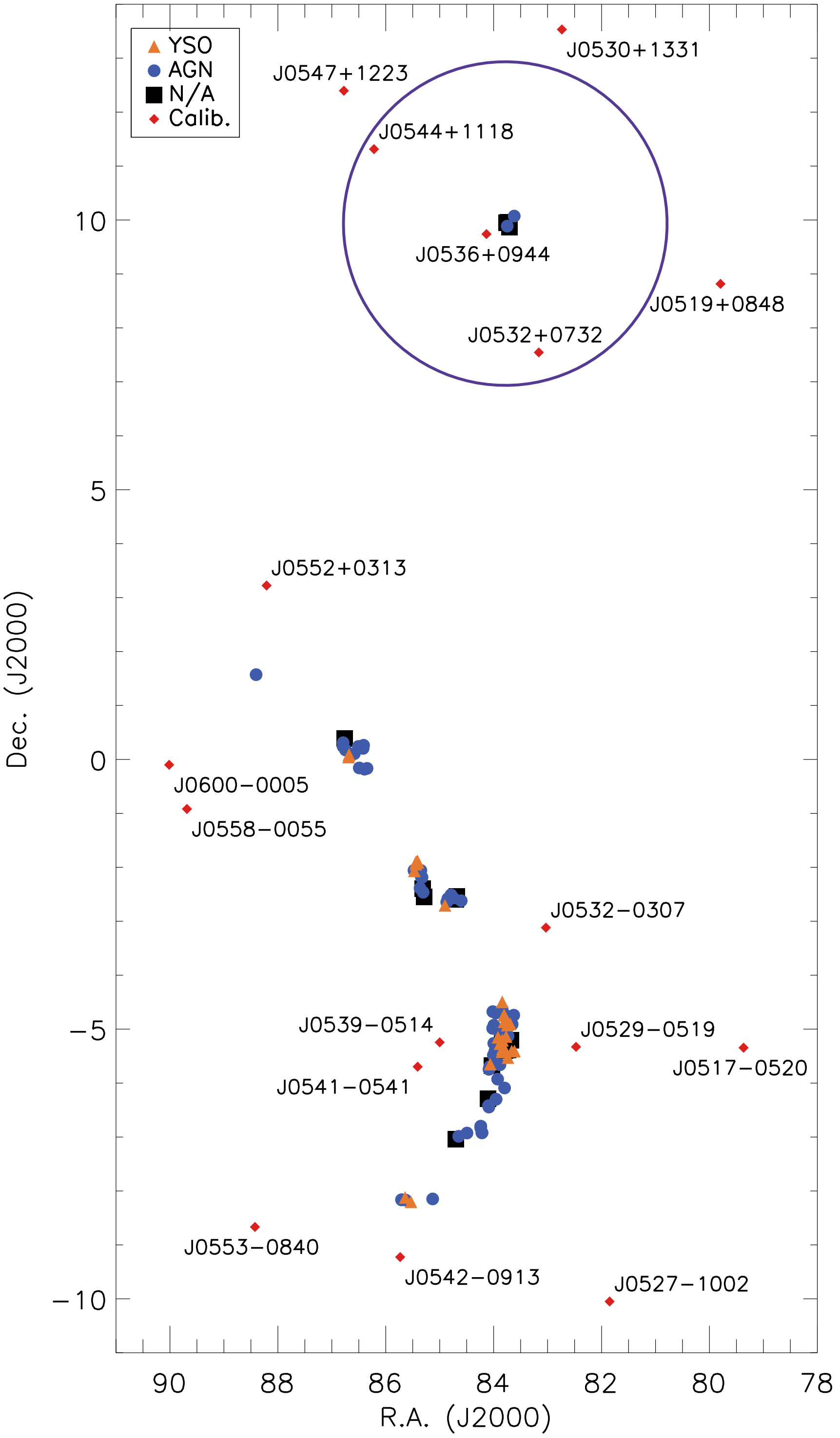

Figure 3.1 Locations of the sources observed by this program. They are separated into the confirmed YSOs, sources that are most likely associated with the AGN activity, and the ones that could not be identified as either due to either insufficient number of epochs observed, or due to poor astrometry. Locations of all the calibrators are also included with their names. The circle at the top of the figure is 3° in radius, and it shows the approximate position of the λ Ori ring.

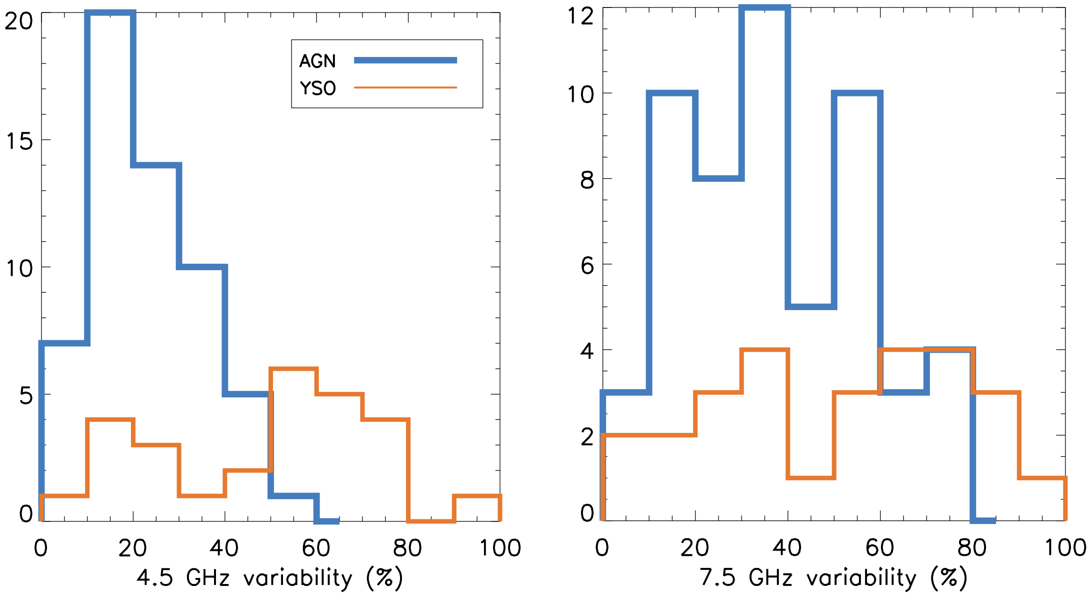

Figure 3.2 Variability reported by Kounkel et al. (2014) for all sources that can be distinguished as galactic and extragalactic on the basis of VLBA astrometry.

3.3 Fitting

To fit the parallax and the proper motions, the IDL routine MPFIT (Markwardt, 2009) was used. This routine fits a given model to data by minimizing least-squares fit. At the end of each iteration, it outputs only a single array with the weighted differences between the data and the model, and any number of equations can be solved simultaneously.

For a single object, the motion of a star in the plane of the sky is prescribed by

$$\alpha(t) = \alpha_0 + \mu_\alpha \cos\delta t + \pi f_\alpha(\alpha, \delta, t)$$

$$\delta(t) = \delta_0 + \mu_\delta t + \pi f_\delta(\alpha, \delta, t)$$

where α_0 and δ_0 are positions of the star at a given reference time, and μ_α and μ_δ are the components of the proper motion. f_α and f_δ are the projections over α and δ of the parallactic eclipse, and they are given by (e.g. Seidelmann, 1992)

$$f_\alpha = (X \sin\alpha - Y \cos\alpha)/\cos\delta$$

$$f_\delta = X \cos\alpha \sin\delta + Y \sin\alpha \sin\delta - Z \cos\delta$$

where X, Y and Z are the barycentric coordinates of the Earth in units of AU, tabulated using the Python package Skyfield[1].

The uncertainties in the fitted parameters are twofold. First, they depend on the positional uncertainties of all the individual detections of the stars as measured by JMFIT, driven by the resolution of VLBA and the flux of the object. This does not take into account possible various systematic offsets in positions between different epochs, which could be significantly larger than nominally quoted positional uncertainties. Typically, the estimation of errors due to systematic offsets is usually done by examining the goodness of the parallactic fit and scaling positional uncertainties until the reduced χ^2 of the fit becomes equal to 1 (e.g., MR; S07).

Approximately half of GK main-sequence stars and 30% of M stars belong to multiple systems (Duquennoy & Mayor, 1991; Fischer & Marcy, 1992; Raghavan et al., 2010; Duchêne & Kraus, 2013), and the motion of the binary projected onto the plane of the sky can degrade the goodness of the fit. These multiple systems can be roughly divided into three categories, based on the effect they have on parallax and proper motion fit.

1. Binaries with orbital periods much longer than the total monitoring time covered by this program (e.g., >>10 years). As the star would only barely move in its orbit, this motion would be approximately linear. It is possible to introduce and fit for an acceleration term to correct for the minor shifts due to nonlinearity. Determination of the parallax should not be affected by these binaries.

---

[1] `http://rhodesmill.org/skyfield/`

Proper motion would not represent the true proper motion of the system, as it is strongly affected by the orbital motion of the star.

2. Binaries with intermediate orbital periods. The effects of the binary motion cannot be ignored during the parallactic fit due to the noticeably changing acceleration of the star; therefore, it is necessary to fit the Keplerian parameters for the binary and the parallax simultaneously. The main orbital parameters are the semimajor axis a_1 of the primary, the orbital period P, the eccentricity e, the argument of the pericenter ω, the time of passage of the pericenter T_P, the inclination i, the argument of the ascending node Ω, and in case of the astrometric binary with both components detected, the mass ratio q. The mean anomalies for the dates of observations are calculated with a given P and T_P. Then a true anomaly θ and a radius from the center of mass r are determined along a Keplerian orbit with a given e for the positions corresponding to these mean anomalies. This orbit is scaled and projected onto the plane of the sky through

$$\alpha(t) = a_1 r(\cos(\theta + \omega)\sin\Omega - \sin(\theta + \omega)\cos\Omega\cos i)/\cos\delta$$

$$\delta(t) = a_1 r(\sin(\theta + \omega)\sin\Omega\cos i + \cos(\theta + \omega)\cos\Omega)$$

For secondary stars, θ is rotated by 180°, and a_2 is used instead, which is scaled from a_1 by q. The fitting code is not optimized for determining several of the Keplerian parameters in a robust manner, as MPFIT is not a global optimizer and can get stuck in the local minima if the initial guesses for the parameters are not optimal. For this reason, we explore a parameter grid of the initial guesses of P in steps of 0.2 years, e in steps of 0.1, T_P in steps of $P/12$, and in steps of 30°. The final values of these parameters can be fine-tuned by the code, and the remaining orbital and parallactic parameters are fitted directly. The uncertainties are determined from the combination of the uncertainties produced by the fits as well as the scatter in the fits from the various initial guesses for the parameters in the grid. Due to a limited number of available epochs, there is a minor dependency in some of the fitted parameters (e.g., parallax and proper motions) between the different realizations of the fits, although the exact trend between the fitted distance and proper motions may be more or less systematic depending on any number of factors, e.g., number of epochs monitored, inclination, or any other physical properties of the system (Figure 3.3), although the uncertainties in the parameters do take the range of scatter into account. The results of these fits are typically comparable within 1σ to the fits produced by the Binary Star Combined Solution Package from Gudehus (2001). The comparison of these two implementations of the binary fitting algorithm is discussed in Ortiz-León et al. (2017a).

3. Binaries with an orbital period smaller than the time between the consecutive epochs of observation (e.g., <6 months). As the stars in these compact binaries should not move far from their center of mass, the overall fit should approximate that of a single star but with somewhat larger uncertainties in the parallax due to the random sampling of the positions of the star in its orbit, and the effect becomes minimal with a sufficiently large number of epochs. If the star in question belongs to a known spectroscopic binary with a constrained orbit, then by superimposing the orbit onto the parallactic motion it is possible to minimize this offset and determine a more reliable distance through fitting of the inclination i and the longitude of the ascending node Ω for the system. In this case e, P, $a_1 \sin i$, T_P, ω, and q are held fixed to the known values from the spectroscopic orbital solutions.

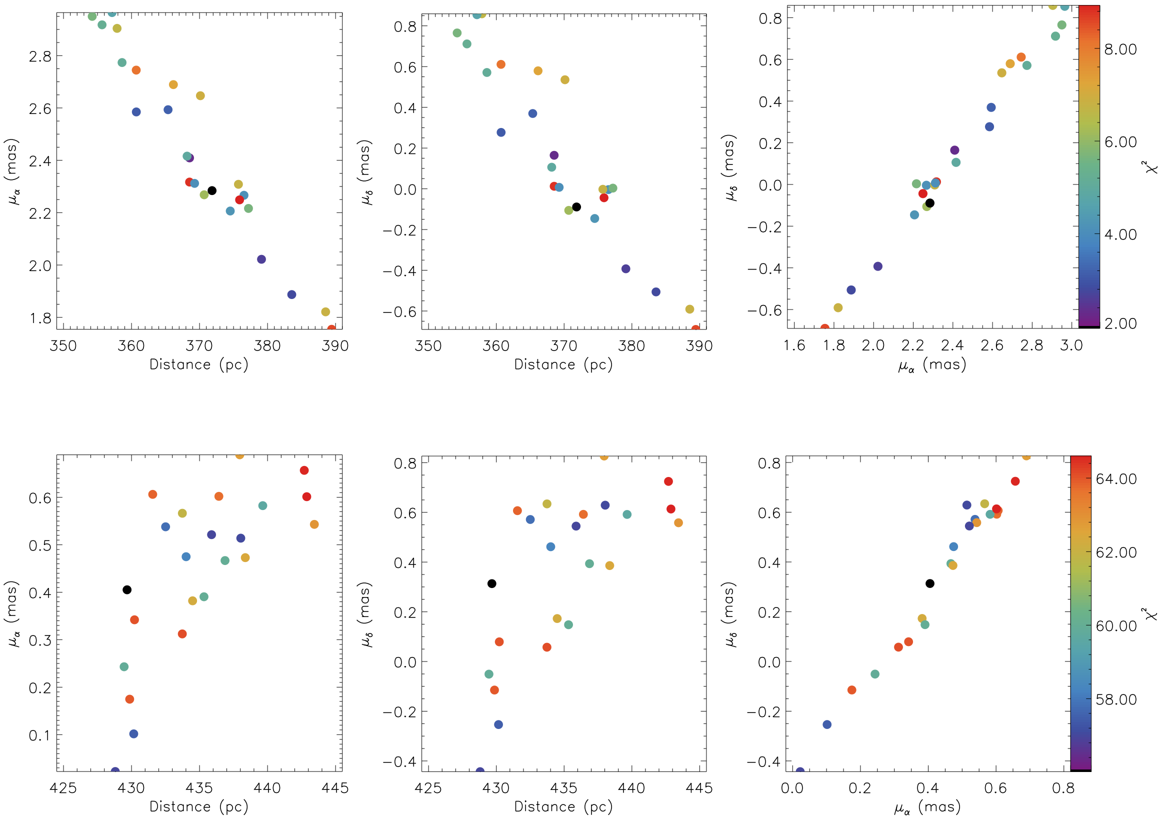

Figure 3.3 Dependence and scatter in the fitted distance and proper motions of the astrometric binaries VLBA 4/107 (top) and VLBA 61/62 (bottom) in the different realization of the fit up to the reduced χ^2 of 10 and 65 respectively.

3.4 Discussion

Twenty stars have been detected toward the ONC, and we present distance solutions to 15 of them. Six of these stars belong to the Trapezium cluster. Two stars have been detected toward L1641, three toward NGC 2068, and one toward σ Ori. Seven stars have been detected toward NGC 2024, and we present preliminary distance solutions to five of them. These solutions are presented in Table 3.5 and discussed in Appendices B for the ONC and C for the remaining regions. The individual fits are presented in Figure 3.4.

Three stars are found to be astrometric binaries with both components detected: VLBA 4/107, 27/28, and 61/62. We presently can fit for the orbital motion of VLBA 4/107 and 61/62, the parameters of which are presented in Table 3.6. Another two, VLBA 58 and 68, are also identified as belonging to multiple systems with an intermediate period on the basis of their astrometry, although only a single star has been detected. In addition, VLBA 125, 126, and 145 have been detected in only three epochs, but they also show possible signatures of multiplicity. Six stars - VLBA 6, 9, 11, 19, 27, and 34 are known spectroscopic binaries with short periods. The distance solution of VLBA 11, 19, and 34 incorporates the orbital motion. The parameters of the orbit are presented in Table 3.7. Another four stars - VLBA 4/107, 8, 11, and 27/28 - have also either known or identified long-period companions in addition to the aforementioned nearby companions (with the exception of VLBA 8, they belong to high-order multiple systems).

3.4.1 Revised distance to the Trapezium

Out of six stars observed in the Trapezium, four have been previously observed by MR, although those authors have incorporated only three of them into the distance solution for the cluster. A simultaneous parallactic fit of all the stars found toward the Trapezium in this program results in a distance of 383±3 pc. This fit is produced

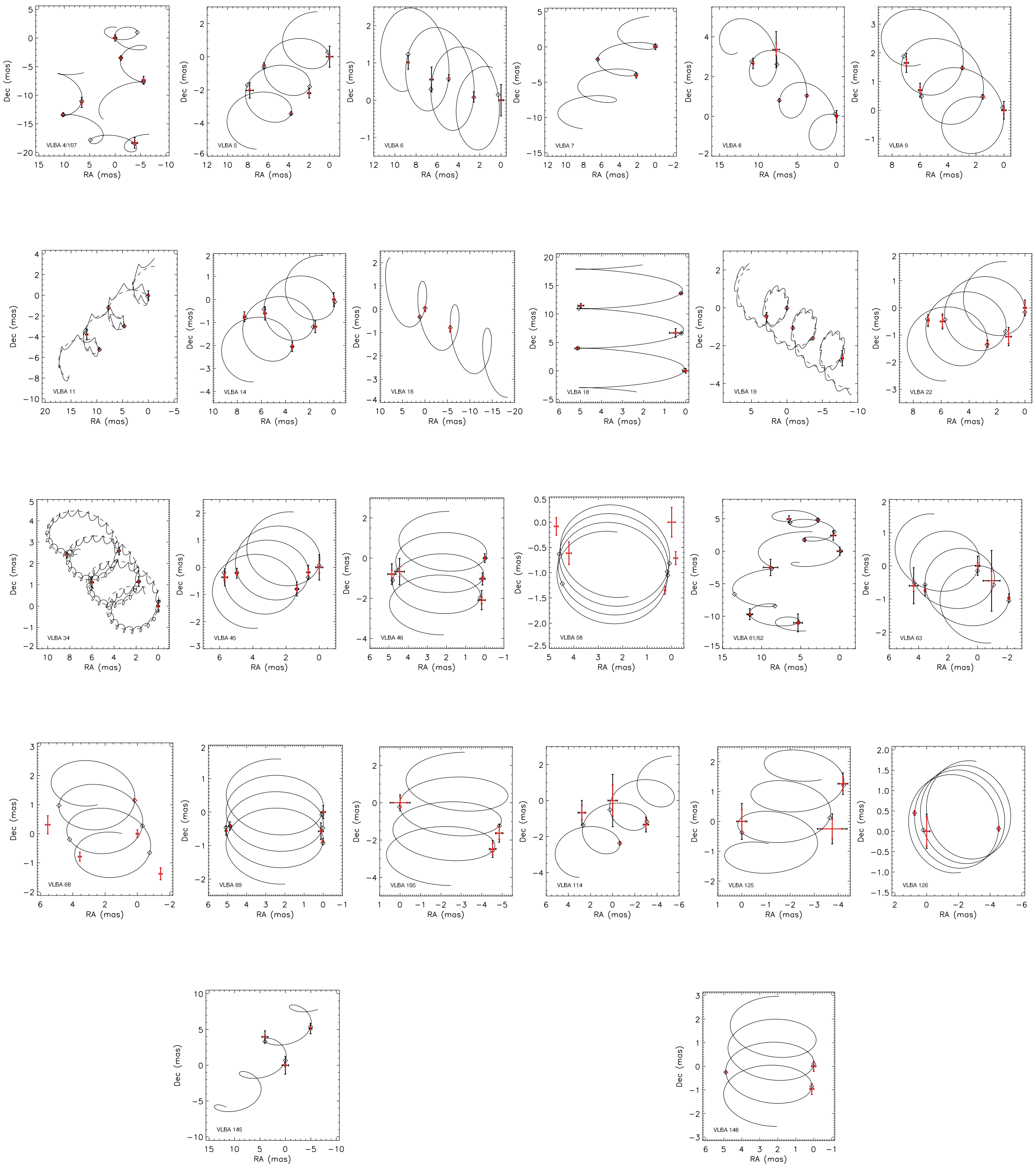

Figure 3.4 Best fits for the data. Red error bars show astrometric uncertainties produced by JMFIT, black error bars show uncertainties scaled by the value needed to achieve $\chi^2 = 1$. Diamonds show expected position of a star at the time of the observations based on this fit. Dashed lines indicates the fit assuming a single star for spectroscopic binaries.

Table 3.5. Distance and proper motion solutions

VLBA	Common Names	Spectral Type	Region	Parallax mas	Distance pc	μ_α mas year^{-1}	μ_δ mas year^{-1}
5	GMR A		Trapezium	2.673±0.112	374±15	1.81± 0.11	-1.62± 0.13
6[b]	GMR F	K1IV (H97)	Trapezium	2.567±0.051	389± 7	2.38± 0.08	0.55± 0.14
7[a]	GMR H		Trapezium	2.684±0.109	372±15	2.22± 0.18	-3.80± 0.55
8	GMR G	K4III (H97)	Trapezium	2.646±0.041	377± 5	3.82± 0.10	1.60± 0.17
9[b]	θ^1 Ori E	G2IV (M12)	Trapezium	2.557±0.051	391± 7	1.45± 0.03	1.02± 0.08
11[b]	θ^1 Ori A	B0V (H97)	Trapezium	2.626±0.100	380±14	4.81± 0.10	-2.53± 0.12
4/107[ac]	Brun 656	G2III (H97)	ONC	2.708±0.210	369±10	2.36±0.69	0.06±1.05
14	V1699 Ori		ONC	2.493±0.049	401± 7	1.76± 0.05	-0.89± 0.16
16[a]	Parenago 1469	G9IV (H97)	ONC	2.533±0.027	394± 4	-7.22± 0.06	-0.99± 0.08
18	Parenago 1724	K0III (S09)	ONC	2.509±0.044	398± 7	0.06±0.20	6.95± 0.16
19[b]	Parenago 1540	K3V+K5V (M88)	ONC	2.591±0.046	385± 6	-4.01± 0.08	-1.17± 0.07
22	HD 37150	B3III (H99)	ONC	2.536±0.046	394± 7	1.32± 0.05	-0.56± 0.12
34[b]	HD 37017	B2V (H99)	ONC	2.643±0.075	378±10	1.88± 0.09	1.20± 0.14
105[a]	Parenago 2148	M1 (H97)	ONC	2.575±0.389	388±58	0.33± 0.05	-1.34± 0.43
114	Parenago 1778		ONC	2.312±0.207	437±83	2.54± 0.30	-1.30± 0.64
45		B8.1 (H13)	L1641	2.348±0.069	425±12	0.68± 0.09	-0.51± 0.25
46			L1641	2.315±0.072	431±13	0.13± 0.25	-1.05± 0.18
58[c]			NGC 2024	2.223±0.121	449±24	0.04±0.31	0.20± 0.43
61/62[c]			NGC 2024	2.306±0.054	434±10	0.47±0.32	0.39±0.62
125[ad]			NGC 2024	1.865±0.105	536±30	-0.43± 0.16	1.03± 0.42
126[ad]			NGC 2024	2.804±0.032	356± 4	0.55± 0.10	-0.10± 0.15
148[a]	V621 Ori		NGC 2024	2.422±0.034	412± 5	0.19±0.44	-0.97± 0.27
145[ad]	HD 294300	G5 (A00)	σ Ori	3.303±0.353	302±32	-4.92± 0.66	4.67± 1.37
63			NGC 2068	2.608±0.047	383± 7	-1.02± 0.10	-0.52± 0.15
68[c]	HD 290862	B3 (S75)	NGC 2068	2.197±0.545	455±113	0.35± 0.27	0.83± 0.83
69		A0 (S75)	NGC 2068	2.547±0.034	392± 5	0.01± 0.10	-0.49± 0.08

[a] Detected only in 3 epochs. Uncertainties could be underestimated.

[b] Spectroscopic binary

[c] Astrometric binary

[d] Probable binary

[e] H97=Hillenbrand (1997), M12=Morales-Calderón et al. (2012), S09=Strassmeier (2009), M88=Marschall & Mathieu (1988), H99=Houk & Swift (1999), H13=Hsu et al. (2013), A00=Alcalá et al. (2000), S75=Strom et al. (1975)

Table 3.6. Orbital solutions for astrometric binaries

Parameters	VLBA 61/62			VLBA 4/107		
P (year)	9.50	±	0.67	6.27	±	0.54
T_p (HJD)	2456455	±	60	2457355	±	200
e	0.50	±	0.12	0.40	±	0.02
ω (deg)	92	±	20	268	±	7
$q = M_2/M_1$	0.50	±	0.26	0.99	±	0.24
a_1 (AU)	2.10	±	0.51	(2.63	±	$0.17)/\cos i$
a_2 (AU)	4.19	±	0.70	(2.53	±	$0.42)/\cos i$
M_1 ($M_\odot$)	1.85	±	0.58	(1.70	±	$0.16)/\cos^3 i$
M_2 ($M_\odot$)	0.95	±	0.22	(1.62	±	$0.38)/\cos^3 i$
i (deg)	141	±	6		—	
Ω (deg)	122	±	30		—	
N_{obs} (primary)	5			3		
N_{obs} (secondary)	3			3		

Table 3.7. Orbital solutions for spectroscopic binaries

Parameters	VLBA 11	VLBA 19	VLBA 34
P (days)	65.4314491 ± 0.0028542	33.73 ± 0.030	18.6561 ± 0.0002
T_p (HJD)	2444195.5773 ± 0.4426	2444972.95 ± 1.75	2446010.461 ± 0.080
e	0.6261 ± 0.0313	0.12 ± 0.01	0.468 ± 0.014
ω (deg)	183.2838 ± 5.1861	131.3 ± 6.7	118.3 ± 2.4
$a_1 \sin i$ (AU)	0.16 ± 0.01	0.081 ± 0.002	0.069 ± 0.003
$a_2 \sin i$ (AU)	—	0.107 ± 0.003	0.132 ± 0.009
Reference	Stickland & Lloyd (2000)	Marschall & Mathieu (1988)	Bolton et al. (1998)
i (deg)	87 ± 11	104 ± 12	52 ± 23
Ω (deg)	150 ± 20	61 ± 11	313 ± 26
M_1 ($M_\odot$)	—	0.49 ± 0.10	4.09 ± 4.44
M_2 ($M_\odot$)	—	0.37 ± 0.07	2.14 ± 2.22

by fitting the equations of motions of all the stars at the same time with a single distance but different proper motions for all stars. The result of this fit is also identical to the weighted average of the individual measurements. The weighted average distance of all the stars in the ONC is 388±2 pc. These values do not include possible systematic effects due to the phase gradient (see below). This is discrepant with the distance of 414±7 pc obtained by MR by 3σ, or ~ 0.2 mas in parallax. It is possible that there is a systematic offset of such magnitude between different epochs that cannot be reproduced during fitting by merely scaling the positional uncertainties until the χ^2 of the fit is equal to 1, so it is possible that the formal uncertainties are somewhat underestimated. And since all of these stars are observed in a single field, any systematic offset that is applied to the coordinates of the center of the field will be propagated to the positions of the sources, and the parallaxes and proper motions could be affected accordingly. However performing a fit with a reduced number of epochs in either work done by MR or this work offers no reconciliation, so the effect is not dominated by a pointing error in any single epoch.

Low-frequency radio observations could be affected by the dispersive delay (e.g. Reid & Honma, 2014), which is difficult to calibrate, resulting in a phase gradient across the sky and producing a slight offset in the absolute positions of the targeted objects. This effect becomes large the farther the object is from the primary calibrator. The effect does average out with the sufficiently large number of epochs; nonetheless, some of it can propagate to the parallax estimation. This effect can lead to somewhat different distances when using different calibrators as a reference for the absolute coordinates of the targeted sources.

To estimate the strength of this phase gradient, we compare the distances of the Trapezium sources with the coordinates referenced to the observed positions of the secondary calibrators (Figure 3.1). The primary calibrator for the field is J0539-0514, which is located 1.2° away from the targets. The simultaneous fit gives 394±3 pc when all the coordinates are referenced to J0529-0519 (1.3° away), 375±3 pc relative to J0541-0541 (1.6° away), and 382±3 pc relative to J0532-0307 (2.4° away). As the Trapezium sources are located approximately halfway between J0539-0514 and J0529-0519, we can estimate the systematic effect of the dispersive delay on the parallax toward it to be on the order of 0.033 mas (5 pc at the distance of the ONC). This effect is consistent throughout the ONC as long as these calibrators are separated by less than 1.5° from the target. Referencing the coordinates to J0529-0519 tends to produce somewhat larger distances than referencing them to J0539-0514. This is also true in the cases where J0529-0519 is used as the primary calibrator (i.e., in the cases of VLBA 14, 16, 18, and 19). We add 5 pc (or 0.033 mas) in quadrature to the uncertainties in the weighted average distance to account for this systematic effect. We adopt a distance of 388±5 pc toward the ONC, including the Trapezium.

This analysis cannot be performed on the solutions obtained by MR, as they have observed only a single calibrator. On the one hand, as their observations were obtained at a higher frequency (8.4 GHz), they should be less susceptible to the dispersive delay. On the other hand, they have obtained fewer epochs, so this effect is somewhat more likely to propagate to the parallax and their primary calibrator is somewhat farther away.

Some minor differences could also be attributed to the difference in the fitting routines. Both the codes used in this work and work done by MR produce fits within 1σ of each other when applied to a particular set of positions. However, MR assume a circular orbit for the Earth and fit parallax only from α, using δ only to fit μ_δ, whereas the code used in this work considers the effect of the parallax on both α and δ using the true orbit of the Earth. Fitting the positions quoted in MR produces a combined distance of 406±4 pc including GMR G, or a distance of 409±3 pc excluding it.

While it is possible to make a single fit for each star utilizing the data obtained by both S07, MR, and this work, the difficulty lies in the fact that each survey utilized a different observing and calibration strategy. S07 used J0541-0541 as a primary calibrator and J0529-0519 as the secondary calibrator. MR used J0541-0541 as the primary calibrator as well as the geodetic sources. This work used J0539-0514 as the primary calibrator with three secondary calibrators and geodetic sources. The absolute positions of the calibrators that are found in common between these works are assumed to be somewhat different, up to a $\sim$ 1 mas level. All of these factors introduce an offset in the absolute positions between these works that is not found in observing the sources repeatedly with the same calibration strategy. While it is possible to calibrate the magnitude of this offset, the exact fit is strongly dependent on the manner of calibration, so it is best to treat the data obtained by different projects independently. However, as both this work and S07 have a larger number of observations than the work done by MR, the fit utilizing all the positions does seem to favor a significantly closer distance than the one found by MR.

Multiplicity is another possible culprit of the difference between the fits. At least two stars observed by MR and used in their distance estimate are spectroscopic binaries, which makes distance solutions produced by them inherently more uncertain. We analyzed the effect that these orbits could have on the distance. The effect on the distance of GMR 12 is within 1 pc. No orbital solution currently exists for GMR F. For the remaining sources observed by this program and identified as spectroscopic binaries, the effect varies between 3 and 18 pc. While it is possible that the effect can contribute to the difference between these two works, it is unlikely that it could explain the systematic nature of the offset. However, it must be noted that the orbital motion parameters can be greatly affected by any systematic offsets in the data, particularly when the orbits cannot be fitted a priori.

Nonetheless, there is sufficient evidence to suggest that the ONC is located closer than has been previously estimated by MR. Systematic offsets would affect each pointing differently. Therefore, a larger number of fields with a larger number of epochs and a larger number of sources overall through the ONC implies that the overall effect of the systematic offsets, if it is present, would be more noticeable in this work than in the work done by MR. The consistency in both the fitted distance and the proper motion estimates of GMR A between this work and that done by S07 suggests that our results are reproducible, which would also be less likely if there was a significant positional offset in our data. Finally, the consistency in distance toward GMR G between this work and that done by MR is surprising, given the lack of consistency between other sources.

Finally, there exists the curious case of the NGC 1980 cluster, which is located south of Trapezium in the vicinity of Ori. This cluster has a somewhat older population of stars compared to the rest of ONC (4-5 Myr Alves & Bouy, 2012). Unfortunately we do not detect any YSOs toward it, but it is thought to be located at the distance of 380 pc obtained through pre-main-sequence fitting (Bouy et al., 2014). This is why this cluster was thought to exist in the foreground of ONC as a separate entity. Nonetheless, the kinematics of NGC 1980 do not show any unique features not present in ONC, and in fact, the velocity dispersion toward it is the smallest of any other region found toward the ONC (Da Rio et al., 2016; Kounkel et al., 2016a). If we assume a significantly closer distance toward the Trapezium and the ONC than what was previously assumed by MR, then NGC 1980 should not be considered a foreground cluster but rather an integral part of the ONC.

3.4.2 Structure of the Orion Complex

The weighted average distance with the weighted uncertainty of all the stars located toward the ONC, including the Trapezium, is 388±5 pc. The distance measurements to nearly all stars is consistent with the average distance for the cluster (Figure 3.5). There is some scatter in the individual measurements of distance. Most of this scatter is likely to be systematic in nature. Some of this scatter may be physical, as the stars detected toward the ONC span a 4 pc region in the plane of the sky at the distance of 388 pc. It is also possible that some substructure is present in the ONC; however, due to limited sampling this possibility is not definitive.

The southern end of L1641 appears to be located considerably farther away, at 428±10 pc (Figure 3.6). We include the effect of the dispersive delay in this value, which we estimate to be comparable to what we found in the ONC. Unfortunately we cannot measure it directly, as all of the secondary calibrators are located too far away from the targeted YSOs for their positions to be useful.

The exact manner in which L1641 connects to the ONC is unclear as there are no galactic sources detected in the northern part of the filament. However, it is not unreasonable to assume that the northern part of the L1641 filament should be located at a similar distance to the ONC. There is a smooth gradient in radial velocity (RV) along the Orion A molecular cloud, ranging from $\sim$8 to 4 km s^{-1} from the northern to the southern end of the L1641 (Bally et al., 1987; Nishimura et al., 2015). This could imply either a passive rotation of the cloud, moving from a very inclined to a more face-on orientation, or it could be the result of something actively pushing on the gas and causing it to accelerate (it is notable that the Orion Complex lies near the edge of the Orion-Eridanus superbubble, Ochsendorf et al., 2015). If the latter is true, it could potentially explain a large number of stars in the ONC that appear to

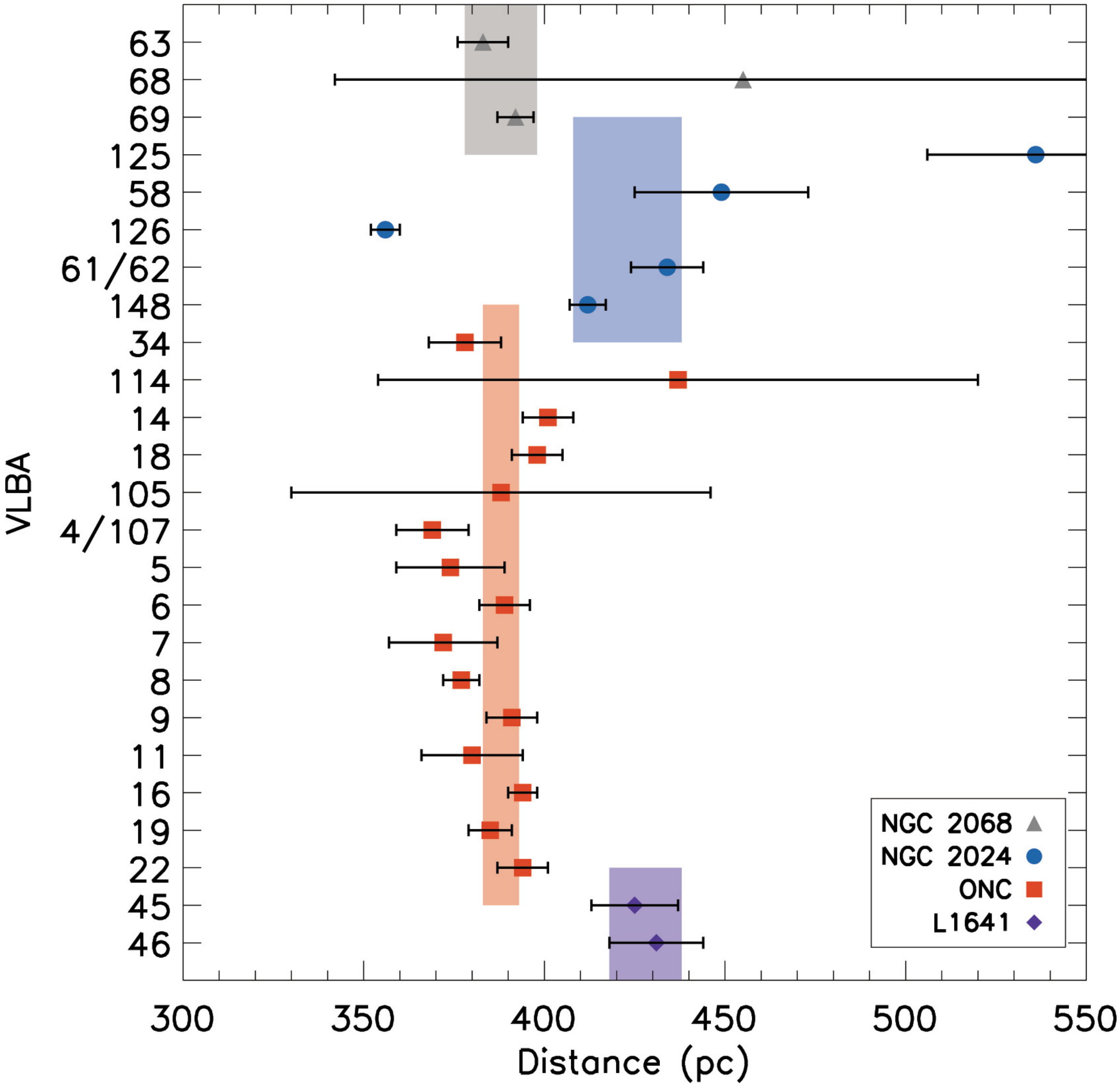

Figure 3.5 Measured distances to the individual stars in the four clusters, sorted according to their δ. The averages for each cluster are shown with semi-transparent rectangles.

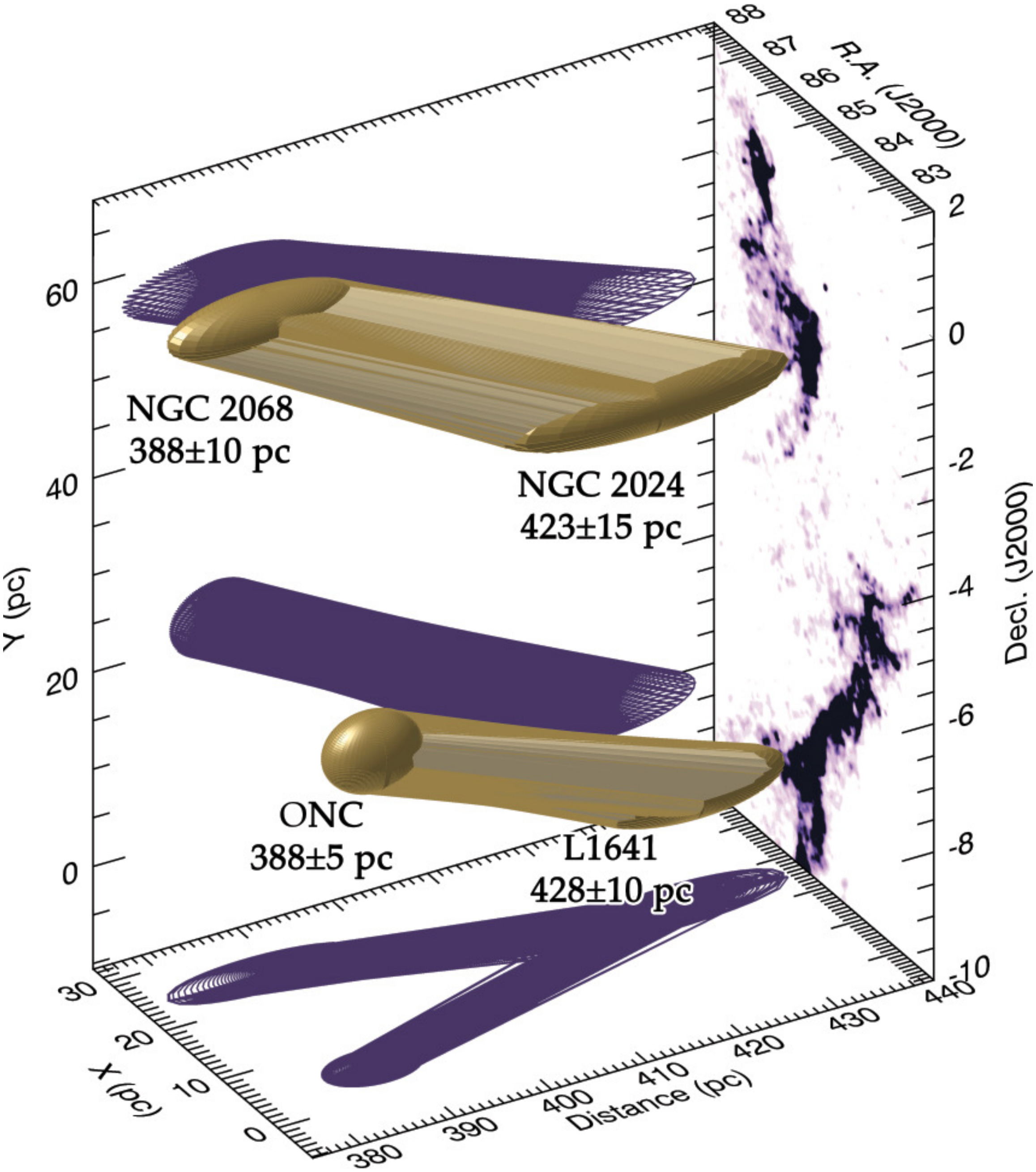

Figure 3.6 3d model of the Orion Complex. The width of the end ellipsoids in the model along the distance is representative of the uncertainties in the measurement and not the actual depth of each cluster. The plane of the sky plane shows the extinction map from Gutermuth et al. (2011). Purple shadows are the projections of the model onto the remaining planes. Conversion of the length along the plane of the sky to pc is done at the distance of 388 pc.

be blueshifted relative to the molecular gas (Kounkel et al., 2016a), as their RV would be representative of the initial velocity of the gas rather than the current velocity.

It is difficult to determine how accurate our measurement of the distance toward NGC 2068 is, as all of the calibrators, including the primary calibrator, are more than 3° away. We estimate the effect of the dispersive delay to be on the order of 0.066 mas or 10 pc at the distance of NGC 2068. We find a distance to NGC 2068 of 388±10 pc. Finally, a distance toward NGC 2024 at this time cannot be reliably measured, given the high incidence of multiplicity as well as a limited number of observations currently available for the stars found toward this region. Neither can we currently obtain a reliable distance toward the σ Ori cluster. This would be resolved with further monitoring. At this time, we estimate the distance toward NGC 2024 on the basis of measurements toward VLBA 61/62 and VLBA 148 to be 423±15 pc.

3.4.3 Proper motions and runaway stars

Parallax and proper-motion solutions (v_{pm}) are available for 15 systems in the ONC. While this is insufficient to perform a detailed analysis of the kinematics of the region, it is possible to obtain mean motions of the cluster.

Proper motions of long-period binaries (i.e., VLBA 8, 9, 11, and 4/107) are not representative of the v_{pm} of the cluster, as they are significantly affected by the orbital motion. Therefore, we do not include them in the calculation of the mean. Three stars can be considered significant outliers in terms of proper motions. VLBA 16, 18, and 19 have a v_{pm} range of between 4.2 and 7.3 mas year^{-1} (7.7-13.4 km s^{-1}). The difference is much larger than the typical dispersion velocity of 2.5 km s^{-1} found toward the ONC (Kounkel et al., 2016a), so they are also not included in the calculation of the proper motion of the cluster. The remaining seven stars suggest a v_{pm} for the ONC of $\mu_\alpha^{lsr} = 1.35 \pm 0.70$ mas yr^{-1} $= 2.49 \pm 1.29$ km s^{-1} and $\mu_\delta^{lsr} = -1.44 \pm 1.51$ mas yr^{-1}$=-2.66 \pm 2.79$ km s^{-1}, in the local standard of rest reference frame, corrected for the peculiar motion of the Sun (Figure 3.7). The uncertainties are obtained from the variance in the individual measurement, although they could be somewhat overestimated as the variance is largely driven by the peculiar velocity of stars within a cluster.

The most likely explanation for the high v_{pm} for VLBA 16, 18, and 19 is that they have been ejected from the cluster through a dynamical interaction within the cluster core, with the most notable suspect being θ^1 Ori C. Unfortunately this star has not been detected by this program, but assuming that its proper motion should be similar to the average proper motion of the cluster, all three runaway stars appear to originate in its vicinity. Assuming linear motion, VLBA 16 appears to have been ejected $\sim 8\times10^4$ year ago, VLBA 18 $\sim 12\times10^4$ year ago, and VLBA 19 $\sim 8\times10^4$ year ago. Some deceleration probably has occurred as they moved through the cluster; however, assuming the potential calculated by Hillenbrand & Hartmann (1998), this deceleration is not significant compared to the current v_{pm} of these stars.

VLBA 16, 18, and 19 are not alone in suffering the fate of being runaway stars. Additionally, Poveda et al. (2005) identified JW 451 and 349 as runaways from θ^1 Ori C; however this was later disproven byO'Dell et al. (2005). More famously, sources BN, I, and n in the Orion BN/KL nebula have been accelerated to speeds of up to 26 km s^{-1} through a dynamical interaction 500 yr ago (Gómez et al., 2008; Goddi et al., 2011). In an even more extreme case, μ Col, AE Aur, and the compact binary ι Ori are thought to be ejected from the Trapezium cluster some 2.5 Myr ago through a four-body interaction (de Zeeuw et al., 2001; Gualandris et al., 2004).

The average proper motion of L1641 is $\mu_\alpha^{lsr} = 0.82 \pm 0.39$ mas yr^{-1} $= 1.67 \pm 0.79$ km s1 and $\mu_\delta^{lsr} = -2.20 \pm 0.38$ mas yr^{-1}$=-4.48 \pm 0.78$ km s^{-1}. The southern end of the cloud appears to move westward relative to the ONC, although it is not collapsing into the ONC directly (Figure 3.8).

Analysis of the proper motions of NGC 2024 is once again made more complex

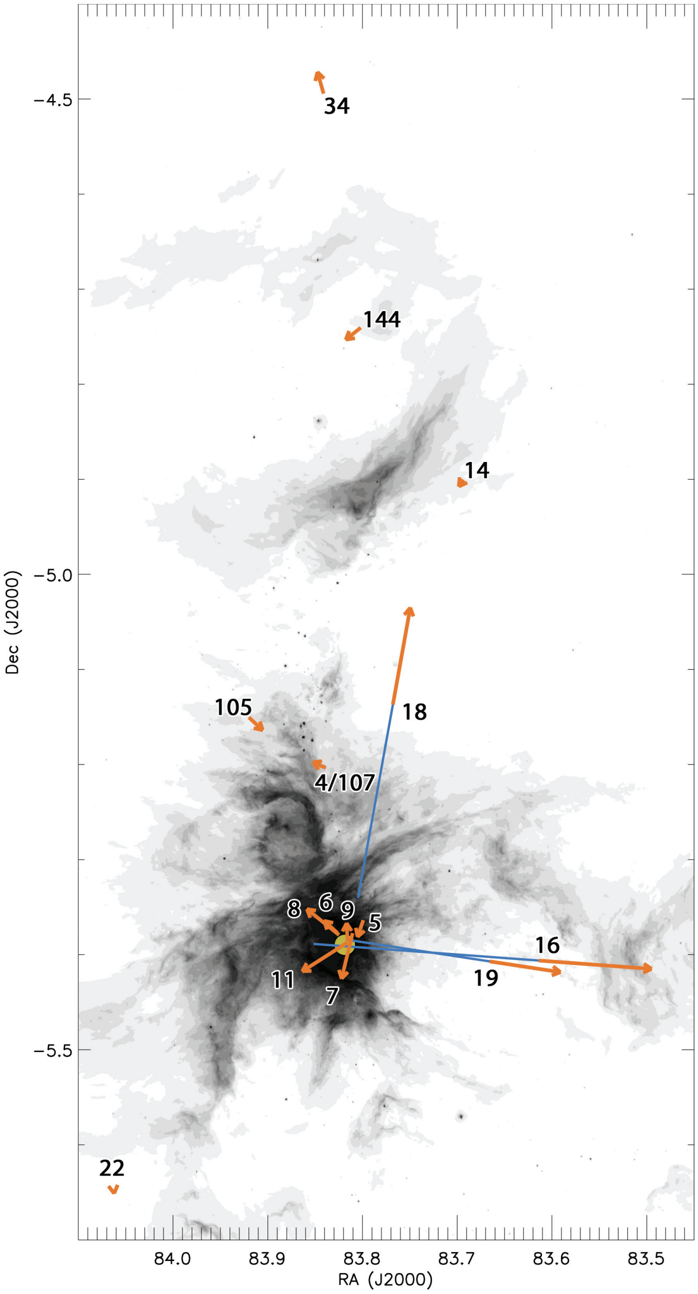

Figure 3.7 Proper motion vectors of the stars detected towards the ONC, corrected for the average motion of the cluster ($\mu_\alpha = 1.38$ mas year^{-1}, $\mu_\delta = -0.36$ mas year^{-1}). The length of the vectors corresponds to motions over 5×10^4 years. The yellow dot at the center shows the current position of θ^1 Ori C. Blue lines show the trajectory of the runaway stars over the last 10^5 years. All the sources are labeled with their VLBA number. The greyscale background is the 8 μm Spitzer map from Megeath et al. (2012).

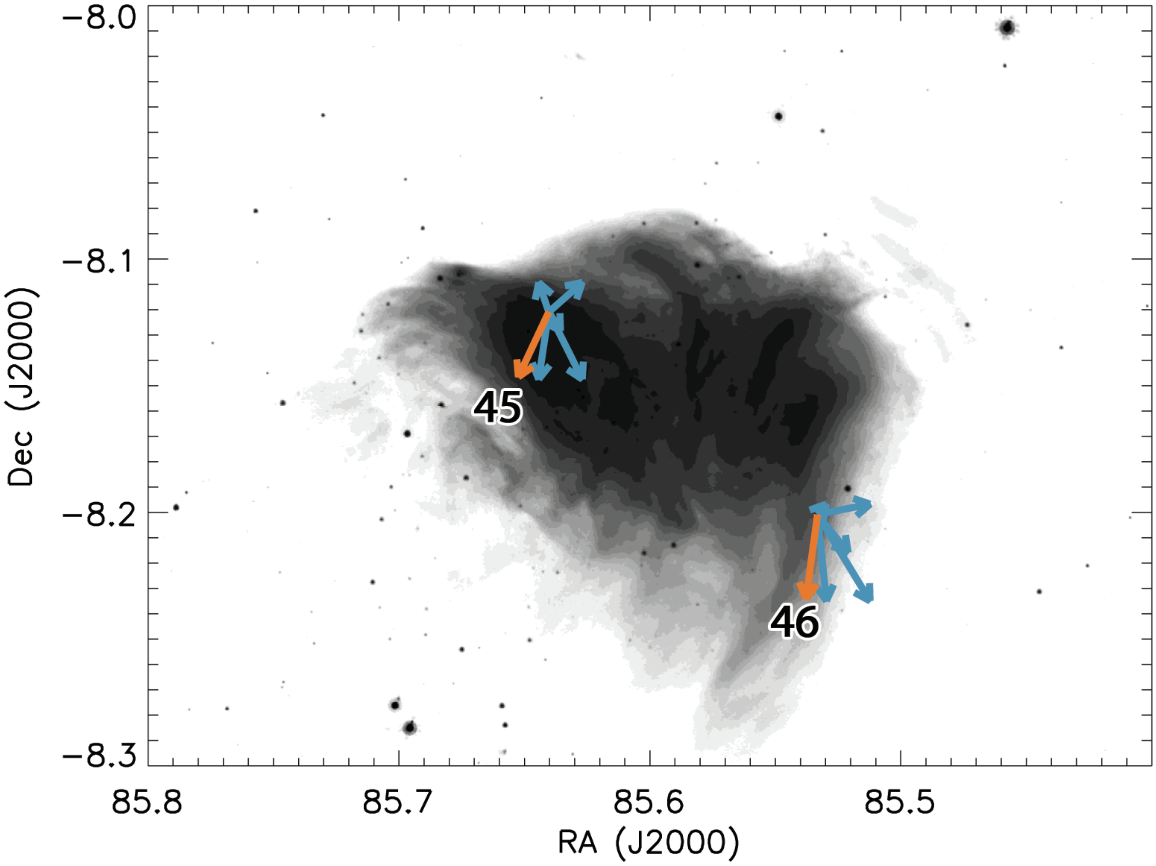

Figure 3.8 Proper motion vectors of the stars detected towards L1641 in the local standard of rest reference frame. The length of the vectors corresponds to motions over 5×10^4 years. Orange vectors are the measured proper motions, blue vectors are motions relative to the average motion of the ONC with a combination of $\pm 1\sigma$ formal uncertainty of the average motion of the ONC in both μ_α and μ_δ. All the sources are labeled with their VLBA number. The greyscale background is 8 μm Spitzer map from Megeath et al. (2012)

by the multiplicity of the sources. The motions of VLBA 58, 125, and 126, if they are indeed binaries, would be at least partially affected by the orbital motion. We obtained an orbital fit for VLBA 61/62, but the proper motions remain rather uncertain. Finally, VLBA 148 appears to be moving away from the cluster, and its motion appears to be rather distinct from the uncertain motions of the other stars. It is possible that it could have been ejected through dynamical interactions in the cluster, although further monitoring would be necessary to confirm this (Figure 3.9).

The proper motion of NGC 2068 based on VLBA 63 and 69 is $\mu_\alpha^{lsr} = -0.62 \pm 0.73$ mas yr^{-1} $= -1.15 \pm 1.34$ km s^{-1} and $\mu_\delta^{lsr} = -1.27 \pm 0.02$ mas yr^{-1} $= -2.35 \pm 0.04$ km s^{-1} (Figure 3.10). It appears to move toward NGC 2024, although this does not take into account the relative velocities of the two clusters.

It is clear that the entire complex appears to move in the southern direction on the equatorial globe, or in the direction of galactic rotation (Figure 3.11). Orion A also moves preferentially toward the East (toward the galactic plane), and the ONC has the largest eastward velocity compared to the other regions of the complex.

3.5 Conclusions

We monitored 36 nonthermal radio-emitting YSOs spread throughout the Orion Complex with VLBA over a period of two years, and we report measured stellar parallaxes toward 26 of them. Fifteen are located toward the ONC, and we find a distance of 388±5 pc to the cluster; this is somewhat closer than the canonical 414±7 pc distance found by MR that is typically used in the literature. This result has implications for the luminosity and ages of the cluster. If the cluster is 7% closer than previous estimations, then this implies that it is 12% fainter and 20% older (assuming a relation $t \propto L^{-3/2}$) than what was previously reported in surveys of the ONC such as the one by Da Rio et al. (2010).

We also report distances toward other regions located in the Orion Complex, such

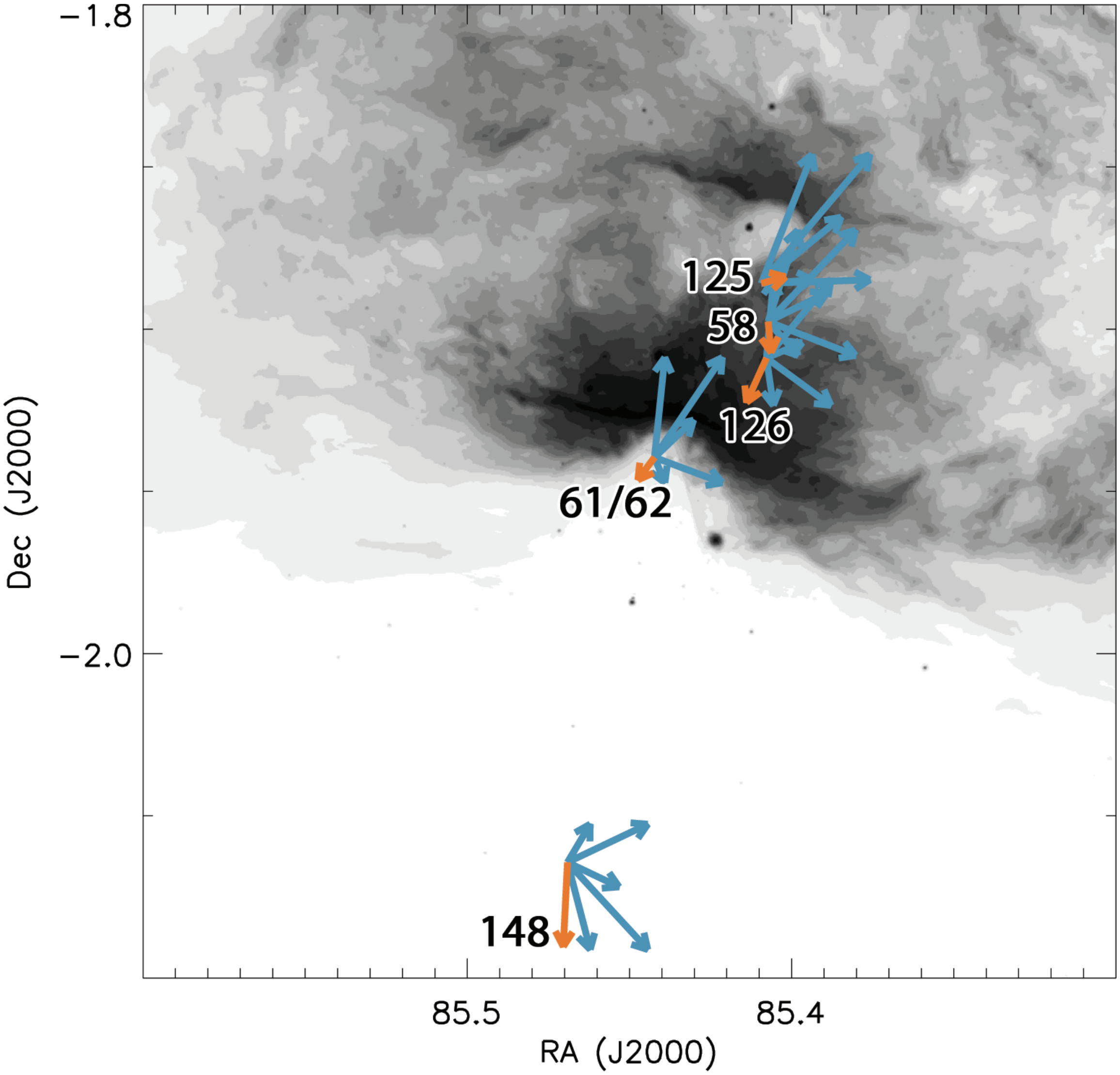

Figure 3.9 Same as Figure 3.8, but for NGC 2024.

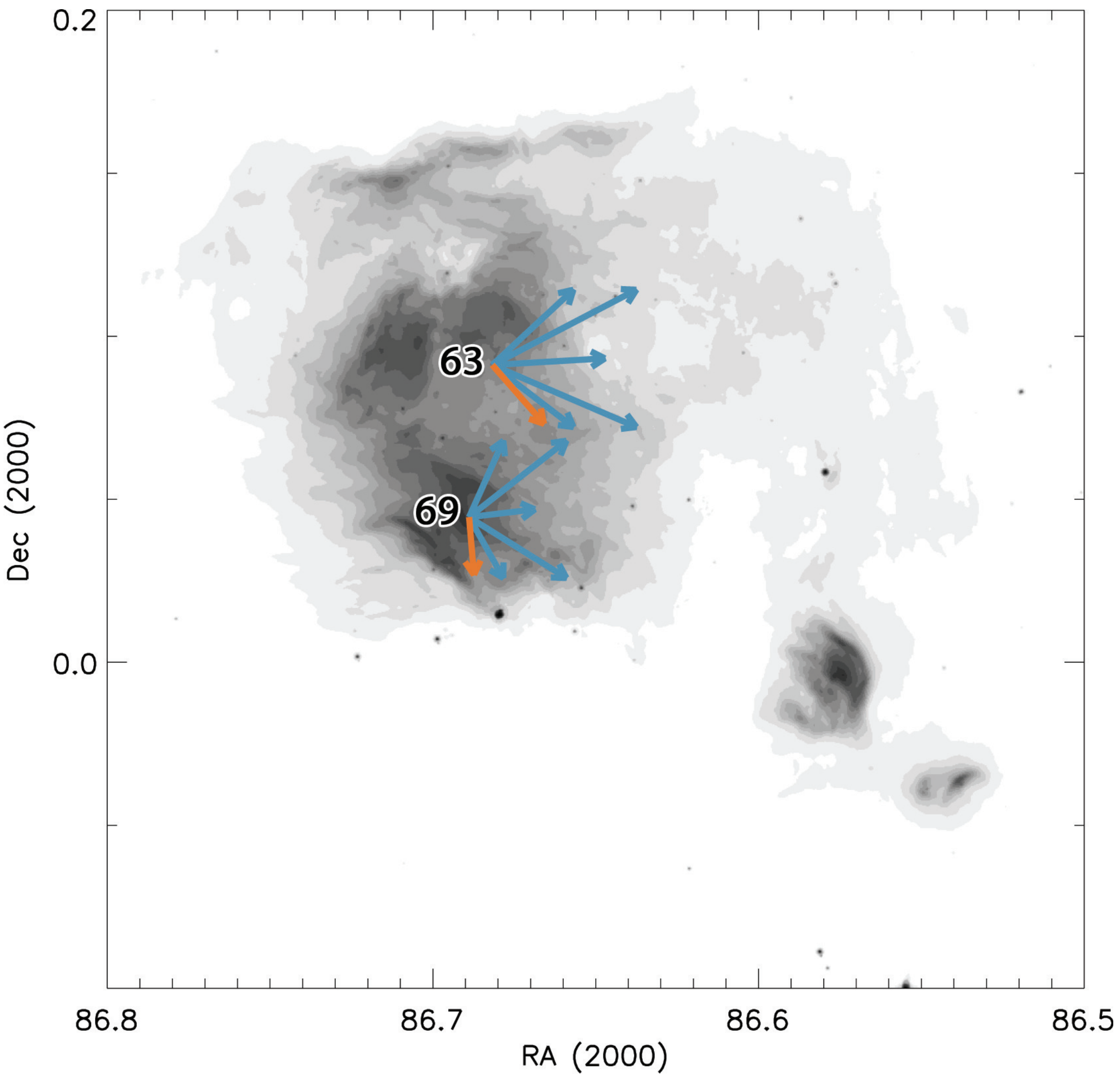

Figure 3.10 Same as Figure 3.8, but for NGC 2068.

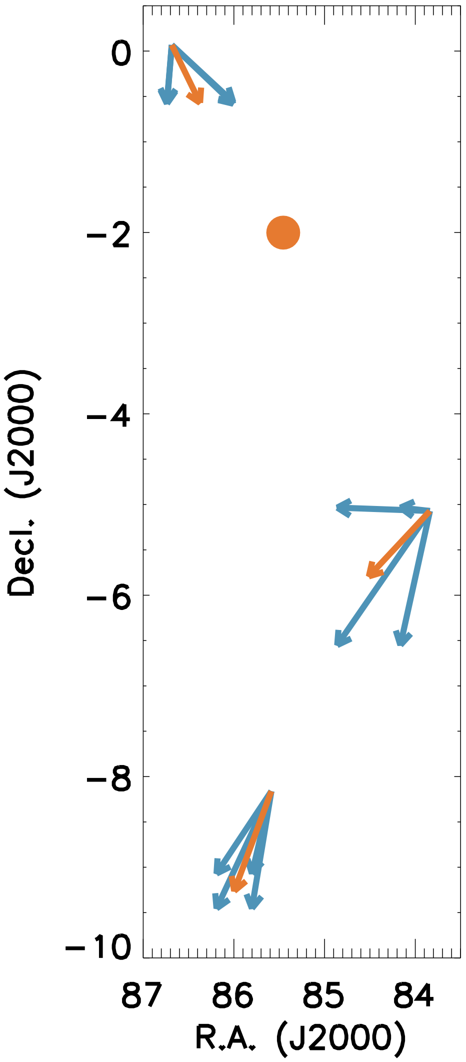

Figure 3.11 Orange arrows: lsr proper motions of the regions of the Orion Complex. The values are listed in Section 3.4.3. Blue arrows: 1σ uncertainty range in these values. Orange dot shows location of NGC 2024.

as L1641, NGC 2024, and NGC 2068. While these values are somewhat more uncertain due to a significantly smaller sample size, limited spatial coverage (particularly in case of L1641), and multiplicity, these are the first direct measurements of the stellar parallaxes toward these regions. This provides insight into the structure of the Complex.

We identify a possible region of a large degree of plasma scattering toward the λ Ori star-forming region. The degree of scattering is significant, with broadening of the observed size of the objects of up to 16.5 mas near the center of the cluster at 5 GHz. The scattering is spread all within the ring 2.5—3° in radius produced by supernova activity. Unfortunately, this effect made it impossible to measure the astrometry accurately enough to obtain a parallax toward the stars found in this region.

A persistent problem in the analysis of both the parallax and proper motions of the stars is the multiplicity. We conclusively identify five of 27 stars that have been detected in at least three epochs belonging to a multiple system with orbital periods between six months and 10 years, with at least three more systems identified as likely binaries, although further monitoring would be necessary to confirm them. It is impossible to accurately determine parallaxes to these systems without solving for the orbital motion of these systems, which we can presently do for only two of them. Six stars are known spectroscopic binaries with very short periods (one of them also has an aforementioned intermediate-period companion); a larger number of them could have very close companions that are yet to be identified, particularly since few surveys of spectroscopic binaries have been performed in the Orion Complex outside of the ONC. While an understanding of their orbits is not detrimental to finding the parallax, it could still influence the solution somewhat. Finally, four stars in the sample have long-period companions, although only one of them does not have a closer companion in a higher-order multiple system. These wide companions should not affect the solution for the parallax, although they do affect proper motions.

In all, at least 14 (possibly more) of 27 stars observed with VLBA belong to multiple systems. Whether this multiplicity fraction is consistent with that for the entire Complex is not yet known as it is difficult to identify companions with intermediate periods toward Orion due to its distance. Future generations of high-resolution optical and IR telescopes would make it possible to identify the full extent of multiplicity toward this region.

Further monitoring of the identified YSOs would be beneficial: due to variability in radio, only a limited number of detections are available to some stars. In the future, it will be possible to more effectively measure their parallax and proper motions. It will also be necessary to confirm multiplicity and constrain orbital parameters toward some sources.

The distance solutions produced by the GOBELINS survey will be used as an independent constraint on the accuracy of *Gaia*, as the systematic effects behind the sample selection and the individual observations are different between these two programs. Approximately half of the systems observed with VLBA toward the Orion Complex are optically visible, so it should be possible to compare the distance solutions toward them directly, at least in the ONC, although nebulosity could significantly degrade performance in the optical regime. However, star-forming regions toward Orion B suffer from high extinction; therefore only a few members of NGC 2024 and NGC 2068 would be detectable with *Gaia*.

CHAPTER IV

Spectroscopic Binaries in the Orion Nebula Cluster and NGC 2264

We examine the spectroscopic binary population for two massive nearby regions of clustered star formation, the Orion Nebula Cluster (ONC) and NGC 2264, supplementing the data presented by Tobin et al. with more recent observations and more extensive analysis. The inferred multiplicity fraction up to 10 au based on these observations is 5.3 ± 1.2% for NGC 2264 and 5.8 ± 1.1% for the ONC; these values are consistent with the distribution of binaries in the field in the relevant parameter range. Eight of the multiple systems in the sample have enough epochs to perform an initial fit for the orbital parameters. Two of these sources are double-lined spectroscopic binaries; for them, we determine the mass ratio. Our reanalysis of the distribution of stellar radial velocities toward these clusters presents a significantly better agreement between stellar and gas kinematics than was previously thought. Published in 2016, ApJ, 821, 8.

4.1 Introduction

Approximately half of Sun-like stars belong to binary or higher-order multiple systems (Raghavan et al., 2010), and this fraction increases for more massive primaries (e.g. Duquennoy & Mayor, 1991; Kouwenhoven et al., 2007; Rizzuto et al., 2013). Observations of several nearby non-clustered, star-forming regions and associations revealed that they contain a larger fraction of multiple systems compared to the significantly more evolved field stars. On the other hand, high-resolution imaging suggests that some young clusters are deficient in binaries (Duchêne & Kraus, 2013, and references therein). Since most stars are thought to form in dense clusters (Adams, 2010), studies of binary frequency as a function of young cluster structure and dynamics can shed light on the processes behind the present day stellar multiplicity.

The Orion Nebula Cloud (ONC) and NGC 2264 are two of the closest regions of clustered star formation (d ∼400 pc and ∼ 900 pc, ages 1—2 Myr and 1.5—3 Myr respectively, Menten et al., 2007; Sandstrom et al., 2007; Sung et al., 1997; Baxter et al., 2009; Hillenbrand, 1997). While the binarity of nearby stars is relatively well understood, it becomes increasingly more difficult to characterize the full membership of multiple stars in young star-forming regions due to their larger distances. Nonetheless, extensive studies of optical binaries in the ONC have led to interesting findings. Most of the studies concentrated on wider binaries that can be detected through photometric surveys with a smallest separation between two companions of ∼60 au, set by the diffraction limit of the optics (Köhler et al., 2006; Reipurth et al., 2007). A recent survey of Class I and II stars in the Orion Molecular Clouds by Kounkel et al. (2016b) revealed that, contrary to expectations, densely populated regions have a larger fraction of wide multiple systems than diffusely populated ones, highlighting the need to reexamine the environmental dependence on the evolution of multiplicity. Constructing a more well-defined sample of close binary systems that can be obtained through multi-epoch spectroscopic monitoring is an important step in this process.

In addition, identifying spectroscopic binaries and removing them from the sample in kinematic studies of star-forming regions can help refine tests of cluster formation. There is some debate over whether clusters form in a slow process, taking place in clouds initially supported by supersonic turbulence (e.g. Tan et al., 2006; Hennebelle, 2012), or whether clusters form rapidly on a free-fall scale due to gravitational collapse (e.g. Hartmann & Burkert, 2007; Elmegreen, 2007; Kuznetsova et al., 2015). Simulations have shown that in the case of the former, any subclustering in the initial environment would not change significantly in the cluster evolution; for the latter, any substructure would rapidly dissipate in only a few Myr (e.g. Scally & Clarke, 2002). By examining the cluster dynamics of massive and clustered star-forming regions, it is possible to set important constraints on models that would more effectively distinguish between these two theories.

Tobin et al. (2009, hereafter T09) attempted to identify spectroscopic binaries, which typically have significantly narrower separations, using multi-epoch spectroscopic monitoring of 1613 objects toward the ONC, searching for variability in the radial velocities (RVs) which can be attributed to the presence of a companion. NGC 2264 has not yet been the subject of a systematic binary survey, although Tobin et al. Tobin et al. (2015, hereafter T15) did report on multi-epoch spectra toward 695 objects in the direction of this region.

T09 and T15 have previously analyzed the kinematic structure of the ONC and NGC 2264, building on the efforts of Fűrész et al. (2006, 2008). They found that in both of these regions, there is general agreement in RV between stars and the gas from which they formed, which suggests that these regions are dynamically young with ages of 1–2 crossing times. Surprisingly, however, a significant fraction of the stars appeared to be blueshifted relative to the gas, and there does not appear to be a significant number of redshifted sources to balance the distribution. T15 showed that the spectra of some of these blueshifted objects found toward NGC 2264 exhibit Li i 6707Å absorption. This is an indicator of extreme youth, and while this is not a confirmation of the membership of the cluster, it does suggest that sources containing Li i are at least casually related. No similar confirmation has been found for the sources in the ONC in T09.

In this chapter, we revisit the published data, supplemented by more recent observations, to identify a more complete sample of the multiple stars in the ONC and NGC 2264, as well as to reexamine the kinematic structure of these regions. In Section 4.2, we present all of the additional data taken since the studies of T09 and T15. In Section 4.3, we discuss the construction of the final catalog and the identification of binary stars. Section 4.4 is focused on the specifics of the multiplicity in these regions, as well as the fitting of the orbits for select stars for which sufficient data were available. Meanwhile, Section 4.5 looks at the stellar velocity distribution. Finally, in Section 4.6, we summarize and discuss our findings.

4.2 Data

We reanalyzed all the spectra previously obtained by T09 for the ONC region and T15 for the NGC 2264 region (including several stars observed but not included in their published catalog) using Hectochelle (Szentgyorgyi et al., 1998) and MIKE fibers(Bernstein et al., 2003; Walker et al., 2007). In addition to these data we include new observations from these instruments and now from the Michigan/Magellan Fiber System (M2FS)(Mateo et al., 2012).

We reanalyzed all of the spectra previously obtained by T09 for the ONC region and by T15 for the NGC 2264 region (including several stars observed but not included in their published catalog) using Hectochelle (Szentgyorgyi et al., 1998) and MIKE fibers (Bernstein et al., 2003; Walker et al., 2007). In addition to these data, we include new observations from these instruments and from the Michigan/Magellan Fiber System (M2FS, Mateo et al., 2012).

4.2.1 M2FS

M2FS is a multi-object spectrograph on the *Magellan* Clay Telescope that is capable of both low-resolution and high-resolution echelle spectroscopy. Up to 256 targets can be observed over a 29' field of view. The fibers observing these targets are split into two independent yet identical spectrographs. M2FS fibers need to be plugged in manually into predrilled plates. The minimum allowed separations between fibers is 12". A slitwidth of 180 μm yields a typical resolution of $R \sim 20,000$.

We observed a total of four fields toward the ONC and two fields toward NGC 2264 in 2013 November and 2014 February (Table 4.1) using M2FS. We targeted a subset of stars from the T09 and T15 samples that was previously thought to be varying and/or had multiple reliable detections. The Mg i filter was used covering a wavelength range of ∼5100—5210Å.

In addition, we also observed three fields toward the ONC in 2014 December with M2FS, but using the Hα and Li i filters covering range of 6525—6750Å. Since two separate orders are observed simultaneously, only 128 targets can be observed in this configuration. We mainly obtained spectra for those sources that were originally identified by T09 as blueshifted relative to the gas in order to confirm their membership in the cluster via the presence of the Li i line, which can be used as an indicator of youth (Briceno et al., 1997). Additionally, given the available fibers, we observed objects that were previously monitored and had V fluxes between 12 and 13.5 mag.

Data were reduced using a custom Python code written by J. Bailey to merge the data and subtract the bias, and the IRAF pipeline HYDRA to trace the orders, extract the spectra, calculate and apply the wavelength solution using a set of ThAr exposures, and perform sky subtraction.

Spectra taken with the Li i and Hα filters were particularly affected by the strong nebular emission lines from S ii (6717 and 6731Å) and N ii (6549 and 6583Å), as well as Hα. These features are always narrow and appear in conjunction with each

Table 4.1. Dates and configurations of the observations.

Field[a] ID	Date (UT)	R.A. (J2000)	Dec. (J2000)	Exposure time (#×seconds)	Instrument
F1-E1-2008	2008/10/19	05:35:23.02	−04:46:26.37	3×1200	Hectochelle
F1-E2-2008	2008/10/21	05:35:23.02	−04:46:26.37	3×1200	Hectochelle
F2-E1-2008	2008/10/20	05:35:15.14	−05:15:08.42	3×1200	Hectochelle
F3-E1-2008	2008/10/19	05:35:13.17	−05:31:44.51	3×1200	Hectochelle
F3-E2-2008	2008/10/21	05:35:13.17	−05:31:44.51	3×1200	Hectochelle
F4-E1-2008	2008/10/18	05:35:07.48	−05:17:32.75	3×1200	Hectochelle
F4-E2-2008	2008/10/20	05:35:07.48	−05:17:32.75	3×1200	Hectochelle
F5-E1-2008	2008/10/18	05:35:22.22	−06:07:13.73	3×1200	Hectochelle
F5-E2-2008	2008/10/20	05:35:22.22	−06:07:13.73	3×1200	Hectochelle
F1-E1-2009	2009/02/14	05:35:09.15	−05:20:42.98	3×1200	Hectochelle
F1-E2-2009	2009/11/03	05:35:06.94	−05:17:36.21	3×1200	Hectochelle
F1-E3-2009	2009/12/01	05:35:06.94	−05:17:36.21	3×1200	Hectochelle
F1-E4-2009	2009/12/03	05:35:06.94	−05:17:36.21	3×1200	Hectochelle
F2-E1-2009	2009/03/14	05:35:14.69	−05:04:58.26	3×1200	Hectochelle
F3-E1-2009	2009/12/02	05:34:52.35	−05:54:23.11	3×1200	Hectochelle
F4-E1-2009	2009/12/02	05:35:26.82	−06:09:44.54	3×1200	Hectochelle
F5-E1-2009	2009/12/02	05:35:09.76	−05:16:54.04	3×1200	Hectochelle
F6-E1-2009	2009/12/02	05:35:20.82	−04:49:07.77	3×1200	Hectochelle
OA	2008/11/06	05:35:07.2	−05:52:14.2	4×1200	MIKE
OB	2008/11/07	05:35:00.0	−05:25:18.4	4×1200	MIKE
OC	2008/11/07	05:35:26.9	−05:13:13.2	4×1200	MIKE
OD	2008/11/06	05:35:26.9	−04:47:34.7	5×1200	MIKE
OA1	2014/02/21	5:35:12.00	−5:30:00.0	6×600	M2FS (Mg)
OB1	2013/12/01	5:35:24.61	−5:11:58.2	4×600	M2FS (Mg)
OC1	2013/11/26	5:35:12.00	−6:00:00.0	4×600	M2FS (Mg)
OD1	2013/11/26	5:35:24.00	−4:45:00.0	5×600	M2FS (Mg)
NA	2014/02/23	6:40:25.48	+9:48:26.0	5×600	M2FS (Mg)
NB	2014/02/25	6:41:19.45	+9:30:28.6	5×600	M2FS (Mg)
LOA	2014/12/18	5:35:12.00	−5:18:04.0	6×600	M2FS (Li)
LOB	2014/12/21	5:35:09.00	−6:02:00.6	3×1200	M2FS (Li)
LOC	2014/12/24	5:35:22.90	−4:43:27.8	4×1200	M2FS (Li)

[a] Data that have been presented in T09 and T15 is not listed in this table.

other in any given spectrum. They would be present as the only features even in the spectra of stars that were too faint to be detected. All of these features were masked out in the final data product if they were observed during the visual examination. However, because the Hα nebular line often interfered with the line that should have been observed due to stellar emission, often superimposed near the center of the line or barely offset from it, the masking process makes it impossible for us to reliably measure the equivalent widths of Hα for most spectra, and prevents us from detecting narrow stellar lines (both emission and absorption) in nearly all of the sources.

In addition to these narrow features, some spectra exhibited very broad and strong emission-like features at 6600 and 6725 Å in Hα and Li i, respectively, spanning ~20Å in width. These features appeared in approximately the same pixel range in both orders and are thought to be caused by Littrow ghosts from the optics. In the data taken with the Mg filter, a narrower and weaker feature appeared at 5181Å in the "blue" spectrograph, and at 5187Å in the "red" one. They are expected to have similar origins. In those cases where these features appeared to be significant, they were masked out.

4.2.2 Hectochelle

In addition to the T09 observations of the ONC made in 2007 with Hectochelle, data were also acquired in 2008 and 2009 (Table 4.1). The multi-fiber echelle spectrograph Hectochelle on the MMT has a 11° field of view and can observe up to 240 targets simultaneously which can be positioned via robotic arms. The RV31 filter was used to cover the wavelength range ~5150—5300Å with a typical resolution of $R \sim 35,000$. The data have been reduced using an IRAF pipeline developed by G. Fűrész. A more detailed description of the Hectochelle data reduction can be found in Sicilia-Aguilar et al. (2006).

4.2.3 MIKE

The stars that were previously observed by T09 in ONC using MIKE fibers on the Magellan Clay telescope had an additional epoch observed in 2008 November (Table 4.1). MIKE consists of two independent spectrographs that can observe 128 fibers each. One of the spectrographs was used to cover the wavelength ∼5120—5190Å, and the other one to cover ∼5140—5210Å, at a resolution of $R \sim 18,000$. A description of the data reduction is available in T09.

4.3 Radial velocity measurements

All the data were processed through the IRAF package RVSAO (Kurtz & Mink, 1998) in order to extract the RVs from all of the targets by performing cross-correlation against the synthetic stellar spectroscopic templates of Munari et al. (2005). As in T09, all of the templates had surface gravity $\log(g) = 3.5$, effective temperatures (T_{eff}) between 3500 and 7000 K in steps of 250 K, and solar metallicity. The previously reported spectra by T09 and T15 have also been re-correlated to achieve a homogeneous sample.

Default filtering parameters (low_bin=5, top_low=20, top_nrun=125, nrun=255) were used during cross correlation to filter noise and large-scale structure in the spectra. However, rapidly rotating stars have broad and occasionally overlapping lines which would not be effectively processed with these parameters. For such objects, different filtering parameters (low_bin=3, top_low=10) were used if the uncertainty from the revised correlation was no greater than 0.05 km s^{-1} and the resulting measure of the signal-to-noise R value was greater:

$$R = 2^{-\frac{1}{2}} h \sigma_a^{-1}$$

where h is the height of the peak of the correlation function, and σ_a is the error estimated from the rms of the asymmetric component of the correlation (Tonry & Davis, 1979).

In data taken in 2014 December, the Li I and Hα orders have been cross-correlated separately. The Hα line is the strongest feature in its order and the shape of the peak of the cross correlation is largely driven by the shape of this line. The Hα line is usually much wider than rotational velocity broadening and, because it is not photospheric, it can be affected by chromospheric motions. Additionally, because the center of the line was typically masked to remove scattered light, the velocities obtained from this order are inherintly more uncertain than those obtained from the Li I order. If the velocities obtained from both orders differed by less than the uncertainties added in quadrature, then the average velocity and uncertainy (v_{ave} and σ_{ave}) were calculated via the variance-weighted mean, and the R value was added in quadrature. This could only be done for 43% of the sources. If no reasonable cross-correlation could be achieved from the Li I order, then Hα velocities were used (9% of the sources).

Typical uncertainties for the individual RV measurements are 0.8 km s^{-1} in NGC 2264 and 1.2 km s^{-1} in the ONC. Weighted average uncertainties for individual stars are 0.4 km s^{-1} in NGC 2264 and 0.7 km s^{-1} in the ONC. It is possible that the larger uncertainties in the measurements toward the ONC are due to higher extinction.

When constructing the table of all of the available measurements for all of the sources, we retained only those measurements that had $R > 3$ and $-100 < \mathrm{RV} < 100$ km s^{-1}. After that, the time series of the measured velocities for each object was visually examined for inconsistent data. Common issues that were noted were as follows.

- Since the MIKE and M2FS fiber plates had to be drawn and plugged manually, a wrong star would occasionally be observed; this is found when the matched template for one or more is wildly different and would also exhibit velocity unlike the remaining observations of the same target.

- Measurements with $3 < R < 6$ could be inconsistent with the remaining data for the target; this is likely a result of poor signal to noise that was not caught through automatic filtering.
- Many of the measurements taken on 2009 February 12 with Hectochelle appear to be contaminated by moonlight; despite having a high R value, these would typically have an RV uncorrected for a barycentric motion of ~ 0 km s^{-1}.

Contamination from these measurements is one of the main reasons for the discrepancy between the results presented in this chapter and those in T09. These measurements have been removed from the final table and are not considered in any of the calculations. Any velocity measurement with $3 < R < 6$ that remained in the table was excluded from the following calculations described in this section as well, but they have been used only in visual examination of the data to confirm the presence of the variability and in fitting the orbits of the identified binaries (Section 4.4). Beyond removing contaminating data, no velocity zero-point offset was applied to the data taken on different days, as there appeares to be almost no systematic variability between the different epochs. The median offset of individual measurements relative to the vave of a given star within each epoch is typically within 0.3 km s^{-1} and less than 1 km s^{-1}, which is consistent with the measured uncertainties.

We use the reduced χ^2 as a measure of the consistency of the velocity in the time series. We identify systems as RV variable if they have reduced $\chi^2 > 16$ ($\sim 4\sigma$). In total, there are 2057 sources with at least a single velocity measurement with $R > 6$, of which 1154 are found toward ONC and 903 toward NGC 2264 (Table 4.2). A total of 130 sources have been identified as RV variable, with 79 toward the ONC region and 51 toward NGC 2264 (Table 4.3). Individual measurements of all of the non-variable sources are reported in Table 4.2. All of the sources identified as RV variable are listed in the Table 4.3.

Table 4.2. Sources that show no variation in radial velocity between multiple observations.

RV[a] #	R.A. (J2000)	Dec. (J2000)	Date (JD)	v (km s^{-1})	σ km s^{-1}	R	Temp (K)	RR?[b]	Instrument
1	05:33:17.95	-05:21:38.6	2454401.0	29.17	4.51	3.26	3500	—	Hectochelle
			2454401.8	30.38	4.55	3.07	3750	—	Hectochelle
			2454757.9	23.64	3.14	6.05	3750	—	Hectochelle
			2454760.0	25.86	3.88	5.63	3750	—	Hectochelle
			2454876.6	24.78	2.58	7.42	3750	—	Hectochelle
2	05:33:20.44	-05:11:24.0	2454757.9	25.83	1.07	12.19	4000	—	Hectochelle
			2454760.0	26.79	1.18	13.83	4000	y	Hectochelle
			2454904.6	24.57	1.12	14.51	4000	y	Hectochelle
			2455167.9	31.86	1.43	8.73	4000	y	Hectochelle

Only a portion of the table is show here. The full table is available on-line at
`http://iopscience.iop.org/0004-637X/821/1/8/suppdata/apj522991t2_mrt.txt`

[a] Includes sources with insufficient number of detections to determine variability.

[b] Measurement was processed with low_bin=3, top_low=10

[c] RV 1-1154 belong to the ONC, RV 1155-2057 to NGC 2264.

4.4 Multiplicity

4.4.1 Measured multiplicity fraction

Out of the 137 sources originally identified by T09 as RV variables in the ONC region, we can confirm only 15 as such in our final catalog. The remaining sources exhibited either little to no change in velocity or had variable velocity measurements that were of low significance. Some of those sources could still be multiple systems, but we do not consider them further here due to our stricter limits for significance to avoid false positives. Upon closer examination, those sources that were previously identified as double-lined binaries by the presence of the second peak in the correlation either could not be confirmed as such or were flagged as variable by our method. For this reason, we focus only on the 130 sources that we can identify as only RV variables with either new or reanalyzed spectra.

We consider two possible causes of the RV variability. First, it could be due to the orbital motion of the muliple systems. Second, the changing RV could be a result of RV jitter due to spots on the surface of magnetically active stars. The typical effect

Table 4.3. Sources with variable radial velocity.

RV #	R.A. (J2000)	Dec. (J2000)	Date (JD)	v_1 (km s^{-1})	σ_1 km s^{-1}	v_2[a] (km s^{-1})	σ_2 km s^{-1}	R	Temp (K)	RR?[b]	Instrument
10[c]	05:33:29.38	-05:07:49.1	2454401.0	31.39	1.95	—	—	8.24	5000	—	Hectochelle
			2454401.8	29.55	1.66	—	—	10.62	4750	—	Hectochelle
			2454757.9	30.34	1.44	—	—	11.24	5000	—	Hectochelle
			2454760.0	29.20	1.31	—	—	12.47	4250	—	Hectochelle
			2455138.8	19.19	1.01	—	—	13.12	5000	—	Hectochelle
			2455168.9	32.64	1.46	—	—	10.28	4250	—	Hectochelle
26	05:33:36.37	-05:01:40.5	2454759.9	99.50	2.40	—	—	12.37	5750	—	Hectochelle
			2455138.8	20.43	1.32	—	—	10.17	5000	—	Hectochelle
			2455166.9	72.24	6.11	—	—	4.43	5500	—	Hectochelle

Only a portion of the table is show here. The full table is available on-line at `http://iopscience.iop.org/0004-637X/821/1/8/suppdata/apj522991t3_mrt.txt`

[a] Velocity obtained from the second peak of the cross-correlation for double-lined binaries.

[b] Measurement was processed with low_bin=3, top_low=10

[c] Have at least 4 $R > 6$ measurements separated by more than 3 days with only single variable velocity.

of jitter in main-sequence stars is on the order of a few m s^{-1} (Hillenbrand et al., 2015), but it could be on the order of ~ 1 km s^{-1} in pre-main-sequence stars (Donati et al., 2013, 2014, 2015).

Given that RV variable sources typically had significant fluctuation from v_{ave}, RV jitter can only account for a handful of sources. We identify sources as multiple if they have at least one measurement $|v_{ave} - v| > 4$ km s^{-1}. A total of 113 sources satisfy this requirment. The remaining 17 sources fall below this threshold; while they do exhibit RV variability, we cannot confirm that it is due to orbital motion within a multiple system. Because of this, we exlcude them from any calculations involving the multiplicity fraction.

The velocity curves for most of our sources are very undersampled, and so we could fail to detect real RV variables. We consider the minimum number of epochs required for a guaranteed detection of an RV varying system to be three. With only 2 measurements, it is possible to miss a binary system due to coincidental timing between the observations. However, with three or more epochs of data, the fraction of the number of systems identified as multiples to the total number of stars remains relatively unchanged (Figure 4.1).

We attempted to identify false positive sources that were flagged as multiples if they had only a single discrepant measurement from the mean. To do that, we calculated the reduced χ^2 while throwing out the single most variable RV measure from vave and identified sources where this revised reduced $\chi^2 < 16$. We required that (a) all of the sources flagged by this method have at least four measurements with $R > 6$, since otherwise the lack of detected variability could be due to poor sampling; (b) at least four epochs during which the measurements were taken are separated in time by more than two days and, as such, short separations in time cannot detect variability due to orbital motion with orbits longer than a few days; and (c) only a single measurement has a discrepant RV, including $R < 6$ measurements if they have

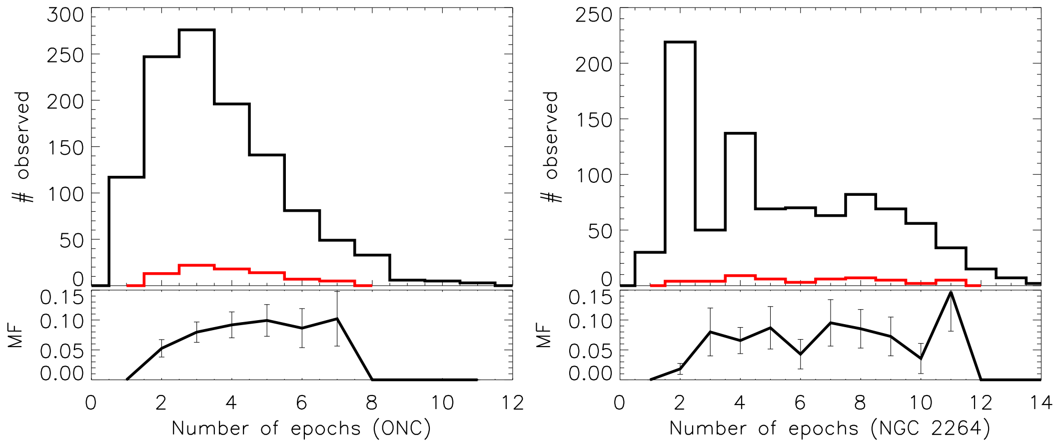

Figure 4.1 Number of observations made for all of the objects in the sample is shown in black. Red shows only those sources with $\chi^2 > 16$. The bottom section shows the ratio of the number of sources with $\chi^2 > 16$ per number of all sources with a given number of epochs observed. Left panel: ONC. Right panel: NGC 2264.

comparable variability from vave. This identified six sources: RV 10, 138, 929, 1372, 1496, and 1660. In the cases of RV 1372, 1496, and 1660, we provide detailed orbital fits (Section 4.4.3). These fits allow little doubt as to the nature of these sources as multiple systems; however, without a single strongly deviating RV they would not have been identified as such based on the data in this chapter. For this reason, while the remaining three sources (RV 10, 138, and 929) are flagged in Table 4.3 as possible false positives, we include them in the following calculations.

The observed multiplicity fraction (defined as the overall number of the multiple systems, hereafter MF) within the RV data set is $8.0 \pm 1.2\%$ toward the ONC and $6.7 \pm 1.1\%$ toward NGC 2264 if we include all of the sources in the Tables 4.2 and 4.3. However, if we require v_{ave}, converted from the heliocentric to local standard of rest (lsr) reference frame (Kerr & Lynden-Bell, 1986), to range from -5 to 20 km s^{-1} for both single stars and binaries to limit the contamination from the sources that are not the members of these clusters (T15, also more in Section 4.5), then MF becomes $5.8 \pm 1.1\%$ for ONC (30 multiples out of 518 stars observed) and $5.3 \pm 1.2\%$ for NGC 2264 (21 out of 397). Uncertainties were obtained as $N_{multiple}^{\frac{1}{2}} N_{total}^{-1}$..

4.4.2 Comparison to the field

To compare the MF that we observe toward ONC and NGC 2264 to that observed in the field, we ran a Monte-Carlo simulation producing a synthetic field population that would be consistent with the distribution of binary properties in the nearby G dwarfs (Raghavan et al., 2010). For each of the stars in our sample that had $-5 < v_{lsr} < 20$ km s^{-1} and >3 detections (i.e., those from which the MF was measured), we generated randomly configured systems (including both single and multiple) that had the same dates of observation and the same uncertainties as the data. We then ran the same detection test that would identify binary systems from the generated population, producing an MF for a single test case. This process was repeated 1000 times. The average MF from all of the test cases, both in the ONC and NGC 2264 regions, was determined separately. Uncertainty was determined from the 1σ dispersion in the generated MF between the 1000 test cases.

For the ONC, there are 518 systems that make up the population from which the MF was estimated. Of these systems, ~120 stars have uncertainties too large to be detected as variable in any of the runs. The average MF of the synthetic population is $4.8 \pm 0.9\%$. NGC 2264 had a total of 397 systems, of which ~70 cannot be identified as multiples in any run, and an average MF of $6.1 \pm 1.2\%$.

The estimate of the expected MF makes an implicit assumption concerning the mass of the primary stars. To simulate the population of the field stars to be consistent with what was measured by Raghavan et al. (2010), 1 $M_\odot$ primaries were chosen. However, the masses of the stars monitored in these clusters are expected to be significantly lower. The typical effective temperature template matched toward these stars is 4000 K (Figure 4.2). From this, we can estimate them to be K stars with typical masses on the order of 0.7 $M_\odot$ (Baraffe et al., 2015). Stellar multiplicity varies strongly with stellar mass, and lower-mass stars have been found to have lower MF than higher-mass stars (Fischer & Marcy, 1992; Duchêne & Kraus, 2013). G stars

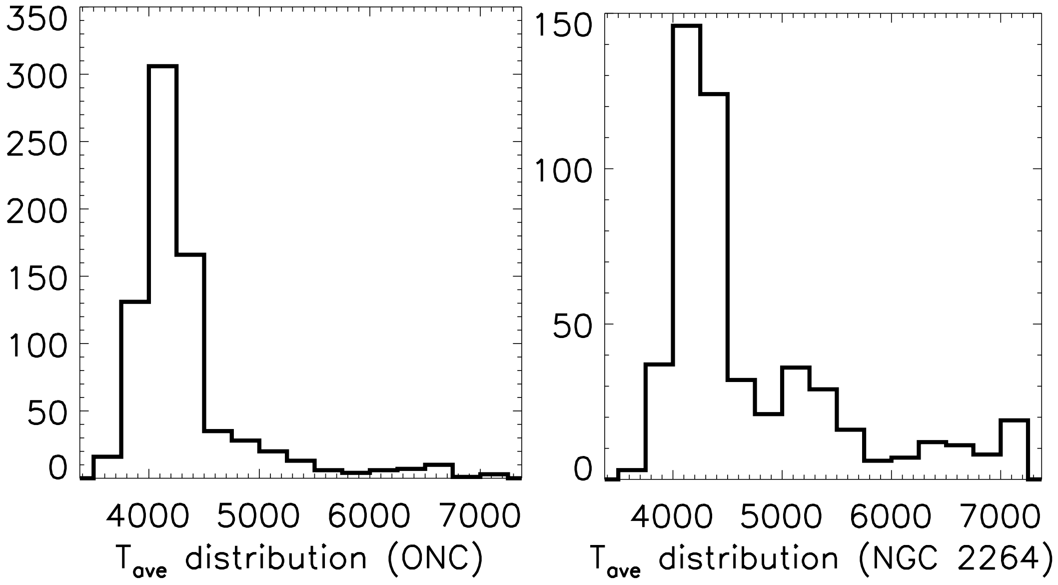

Figure 4.2 Average effective temperature disribution observed towards stars in ONC and NGC 2264.

have typically been used for comparison because surveys of their orbital parameters have been by far the most comprehensive.

In addition, because the mass of the primary is lowered, the distribution of the masses of the secondary is also cut off at smaller values. Because of this, the difference in the peaks of the RV fluctuations due to the presence of a companion would become smaller as well; therefore, fewer systems would be detected. By generating a population with identical orbital parameters around 0.7 $M_\odot$, we instead infer MFs of $4.5 \pm 0.9\%$ for ONC and $5.8 \pm 1.2\%$ for NGC 2264.

The dispersion in the MF generated with identical orbital parameters between separate runs (all consisting of 1000 test cases) observed with the cadence and uncertainties set by the same population is typically $< 0.1\%$. To estimate the systematic effects due to a potentially different distribution of periods and overall number of binary systems in these clusters compared to what was previously found in the field, we varied one parameter at a time and looked for a difference in MF. Varying the underlying binarity fraction by 2% (1σ values quoted by Raghavan et al., 2010) typically changes the extracted MF by 0.2%. No uncertainties on the orbital parameters were made apparent, although varying the peak of the period distribution by 0.1 log P (where P is measured in days) produces an MF that is different by 0.5% when the average period is decreased from 293 to 233 years, and by 0.3% when the period is increased to 369 years. Varying the standard deviation of the period distribution by 0.1 $\sigma_{\log P}$ changed the MF by 0.4%. Changing the mass ratio and eccentricity from uniformly distributed to those that are described by Duquennoy & Mayor (1991) decreases the MF by 0.5% and 0.4%, respectively.

To determine the completeness limits which we probe with these observations, we recorded orbital parameters from all the generated binary systems and determined a fraction that would be detectable relative to the all binaries that satisfy the specific orbital parameters (Figure 4.3). Unsurprisingly, most easily detectable systems have short orbital period, comparable masses between the primary and the secondary, and an edge on orientation. It is possible to detect only 60% of all the systems with separations < 1 AU because either the other orbital parameters make a detection difficult, or the uncertainty in the measurements that were applied to the generated velocity curves were too large for a reliable detection. Beyond the separations of 15 AU there are almost no systems that could be detected as a binary based on their RV variability. Combining all the possible separations and inclination angles, only 15% of multiple systems can be detected for stars with the mass ratio on the order of unity (in this case both stars have mass of 1 $M_\odot$), however, this rapidly decreases to ~5% for the companions with only 0.2 $M_\odot$.

To determine the completeness limits that we probe with these observations, we recorded orbital parameters from all of the generated binary systems and determined a fraction that would be detectable relative to all of the binaries that satisfy the specific orbital parameters (Figure 4.3). Unsurprisingly, the most easily detectable systems have short orbital periods, comparable masses between the primary and the secondary, and an edge-on orientation. It is possible to detect only 60% of all of the systems

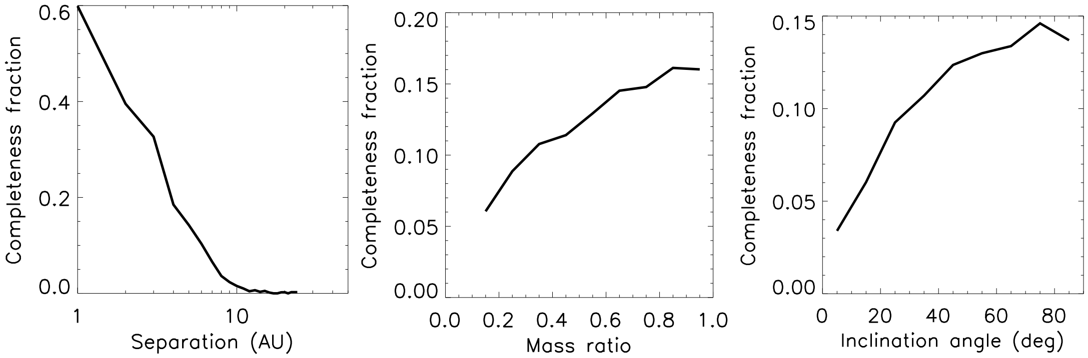

Figure 4.3 Completeness limits of the detection of the multiple systems depending on their orbital parameters.

with separations < 11 au because either the other orbital parameters make a detection difficult or the uncertainty in the measurements that were applied to the generated velocity curves were too large for a reliable detection. Beyond the separations of 15 au, there are almost no systems that could be detected as binaries based on their RV variability. Combining all of the possible separations and inclination angles, only 15% of multiple systems can be detected for stars with a mass ratio on the order of unity (in this case both stars have mass of 1 $M_\odot$); however, this rapidly decreases to ~5% for those companions with only 0.2 $M_\odot$.

4.4.3 Orbital parameters

Individual cross-correlations of all of the systems identified as binaries were visually examined to determine whether or not it is possible to see a second peak due to the presence of the second star. We required that any star flagged as a double-lined binary must exhibit multiple peaks or a skewed correlation function in at least two epochs to minimize spurious detections. There were a total of 15 of such systems, of which 10 were found toward NGC 2264 and 5 toward ONC. In epochs where it was possible, a Gaussian was fitted to both peaks to find the velocities of both components. We assigned uncertainties to these measurements of 2 km s^{-1}, limited by the resolution of the extracted cross-correlations function. All of these measurements are included in Table 4.3.

Out of 130 sources flagged as binaries in this chapter, 6 single-lined binaries have $\geq$ 10 RV measurements and 2 double-lined binaries have $\geq$ 9 measurements. We attempted to fit the velocity curves of these sources as they contained a sufficient number of measurements and redundancy on the measurements to obtain a unique solution. Because sources in NGC 2264 have been monitored more frequently than those in ONC (Figure 4.1), all 8 of these sources are found toward NGC 2264.

To fit the orbits, the IDL package RVFIT (Iglesias-Marzoa et al., 2015) was used, which fits the following quantities: P (the orbital period), T_P (the time of periastron passage), e (the eccentricity), ω (the argument of the periastron), γ (the systemic velocity of the system), and K_1 (the amplitude of the RV fluctuation) and K_2 (the amplitude of the RV fluctuation for the second star if the system in question is a double-lined spectroscopic binary.) The derived quantities are the semimajor axis $a_1 \sin i$ and the binary mass function f. $M \sin i$ contributions of the individual stars can be distinguished for double-lined systems.

RV 1768 showed the second peak in the correlation in 7 out of 11 epochs, and both peaks exhibited a similar strength. The remaining 4 epochs had measurements very close to the mean of the remaining measurements. Because we are unable to distinguish between the contributions of individual components, there could be a larger spread in the velocity due to line blending; to those measurements we assign an uncertainty of 5 km s^{-1}.

As RV 1768 appeared to have almost equal mass in both components, there was some difficulty in distinguishing which of the two lines in a given epoch belonged to which star in cases of resolved measurements, and the velocity of which star was the most dominant in cases of unresolved measurements. An attempt was made for all of the perturbations of the line combinations to be fitted and examined by eye - the combination which provided the best fit is listed in Table 4.3 and the resulting

Table 4.4. Orbital parameters for double-lined binaries

Parameter	RV 1768	RV 1659
	Adjusted Quantities	
P (d)	4.7878 ± 0.0002	15.3182 ± 0.0007
T_p (HJD)	2454289.50 ± 0.06	2454294.07 ± 0.05
e	0.55 ± 0.05	0.00 ± 0.02
ω (deg)	139.68 ± 3.16	0.00 ± 0.60
γ (km/s)	16.05 ± 0.54	22.83 ± 0.46
K_1 (km/s)	59.34 ± 6.34	41.56 ± 1.07
K_2 (km/s)	60.83 ± 6.32	52.20 ± 1.05
	Derived Quantities	
$M_1 \sin^3 i$ ($M_\odot$)	0.254 ± 0.066	0.73 ± 0.04
$M_2 \sin^3 i$ ($M_\odot$)	0.248 ± 0.065	0.58 ± 0.03
$q = M_2/M_1$	0.98 ± 0.15	0.80 ± 0.03
$a_1 \sin i$ (10^6 km)	3.26 ± 0.37	8.75 ± 0.23
$a_2 \sin i$ (10^6 km)	3.35 ± 0.37	11.00 ± 0.22
$a \sin i$ (10^6 km)	6.61 ± 0.52	19.75 ± 0.32
	Other Quantities	
χ^2	8.38	13.43
N_{obs} (primary)	10	9
N_{obs} (secondary)	8	8
Time span (days)	2308.7	2308.6
rms_1 (km/s)	1.62	1.22
rms_2 (km/s)	1.42	2.10
T$_{ave}$ (K)	4021	4203

fit is shown in Figure 4.4 and Table 4.4. The masses of the individual components (M $\sin^3 i$) are $\sim$ 0.25 M$_\odot$. Given that the spectra for this system are best fit by a $\sim$4000 K template, this is a reasonable fit requiring only a modest inclination angle.

RV 1659 had a double-peaked correlation function in 8 out of 9 epochs, with one component clearly dominating over the other. It was best fit by a circular orbit, a period of 15.3 days, and M $\sin^3$ of 0.73 and 0.58 M$_\odot$ (Figure 4.5, Table 4.4). For orbits with no eccentricity, the argument of periastron carries no meaningful information.

Fitting information on the six single-lined systems is presented in Table 4.5 (Figures 4.6–4.11). Based on the characteristic heliocentric velocity of RV 1372 of 32 km s^{-1} (v$_{lsr}$ ~ -47 km s^{-1}), it is unclear whether or not it is a member of NGC 2264. However, this system is typically best fit by a 4250 K template and has near-infrared fluxes of J = 12.270, H = 11.718, and K = 11.464 (Cutri et al., 2003). While there is some contamination in the fluxes from the companion, they are in a good agreement with those of other binary systems which follow the same templates (e.g., RV 1550, a

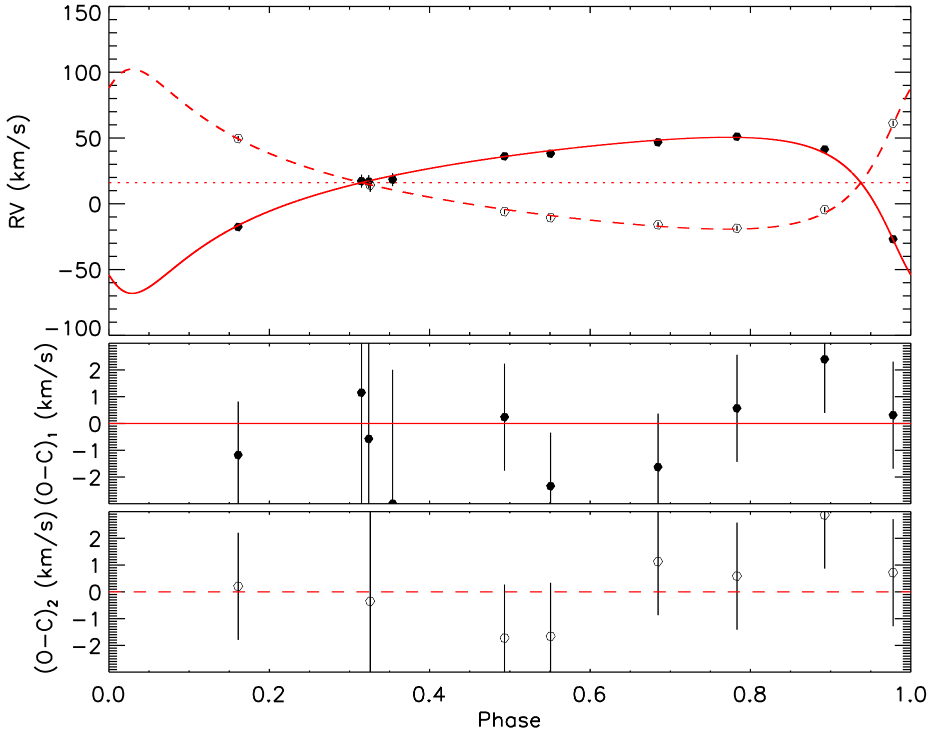

Figure 4.4 Orbital fit for RV 1768

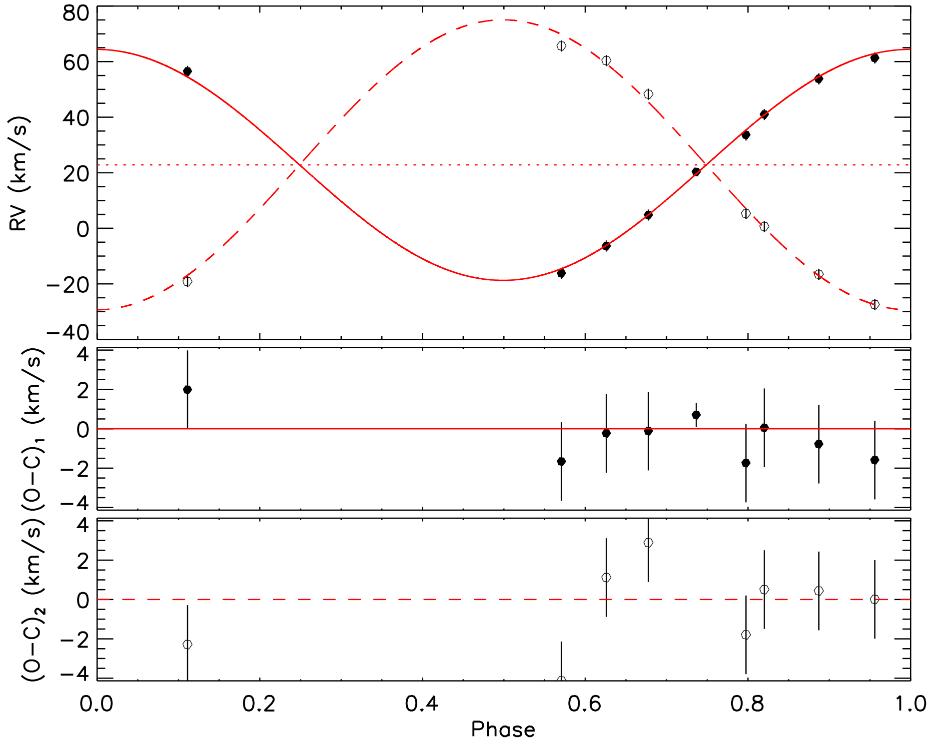

Figure 4.5 Orbital fit for RV 1659

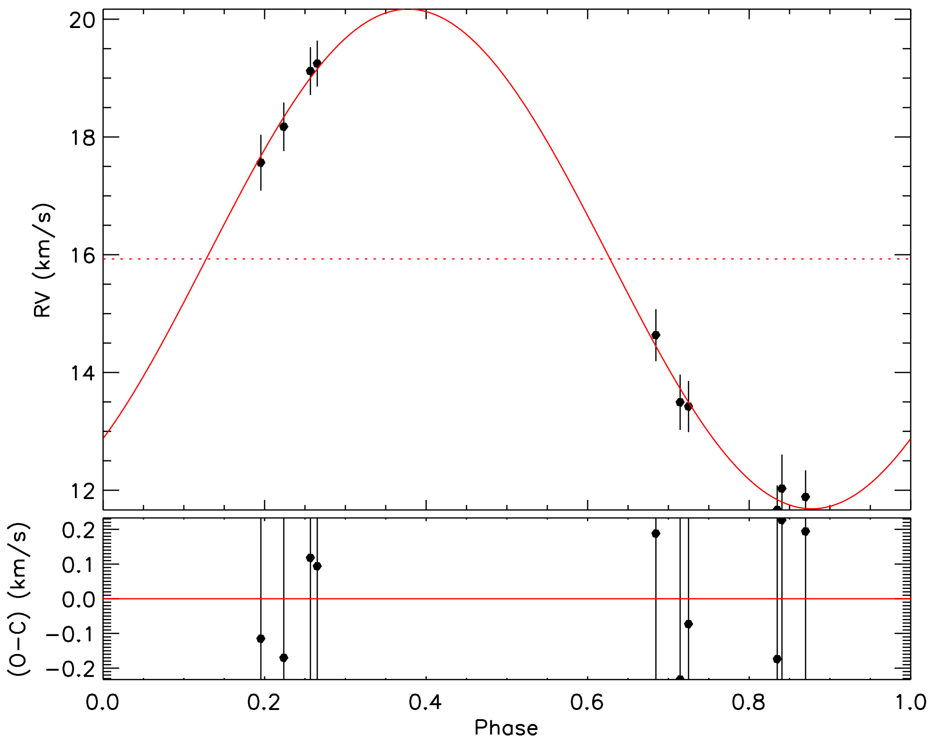

Figure 4.6 Orbital fit for RV 1166

system for which the orbital fit is also available and which has a systematic velocity that is consistent with the cluster mean, has J = 12.262, H = 11.566, K = 11.423), making it likely that RV 1372 is not a foreground or background system, but rather that it was ejected from the cluster.

Table 4.5. Orbital parameters for single-lined binaries

Parameter	RV 1166	RV 1372	RV 1496	RV 1550	RV 1660	RV 1753
Adjusted Quantities						
P (d)	105.82 ± 0.27	315.41 ± 5.79	588.93 ± 9.47	72.83 ± 0.03	622.00 ± 26.32	12.93 ± 0.01
T_p (HJD)	2452620.5 ± 29.3	2454382.4 ± 5.5	2454814.5 ± 22.1	2454329.0 ± 1.1	2454585.1 ± 31.4	2454299.3 ± 0.6
e	0.00 ± 0.07	0.65 ± 0.12	0.44 ± 0.07	0.32 ± 0.02	0.56 ± 0.08	0.170 ± 0.03
ω (deg)	224.02 ± 99.11	178.80 ± 5.31	8.61 ± 11.29	266.43 ± 7.12	135.59 ± 11.99	194.66 ± 19.74
γ (km/s)	15.93 ± 0.25	-29.97 ± 0.78	28.05 ± 0.30	20.80 ± 0.26	23.08 ± 0.39	17.97 ± 1.35
K_1 (km/s)	4.24 ± 0.46	20.00 ± 7.73	3.46 ± 0.87	16.91 ± 0.39	5.86 ± 0.51	16.11 ± 1.61
Derived Quantities						
$a_1 \sin i$ (10^6 km)	6.17 ± 0.67	65.91 ± 27.09	25.09 ± 6.38	16.06 ± 0.39	41.36 ± 4.93	2.82 ± 0.28
$f(m_1, m_2)$ ($M_\odot$)	0.0008 ± 0.0003	0.11 ± 0.15	0.0018 ± 0.0014	0.031 ± 0.003	0.007 ± 0.003	0.005 ± 0.002
Other Quantities						
χ^2	1.31	2.61	1.74	1.76	2.61	2.61
N_{obs} (primary)	10	11	10	11	11	11
Time span (days)	903.6	2308.7	2327.7	2325.7	2325.6	2327.7
rms_1 (km/s)	0.17	0.53	0.19	0.25	0.55	0.28
T$_{ave}$ (K)	6274	4267	5577	4361	4256	5301

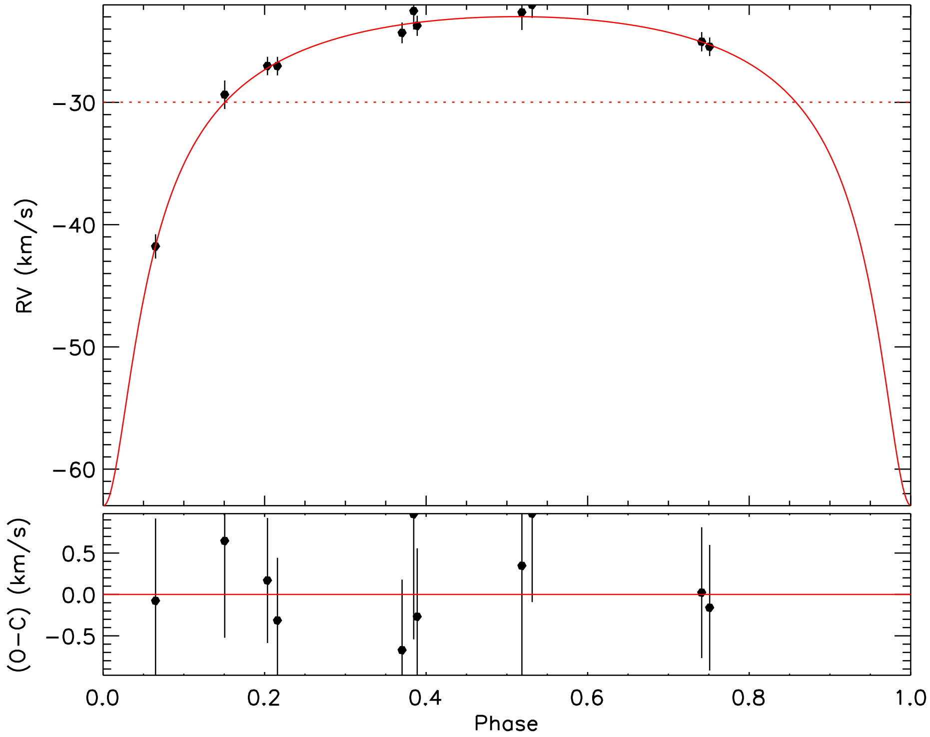

Figure 4.7 Orbital fit for RV 1372

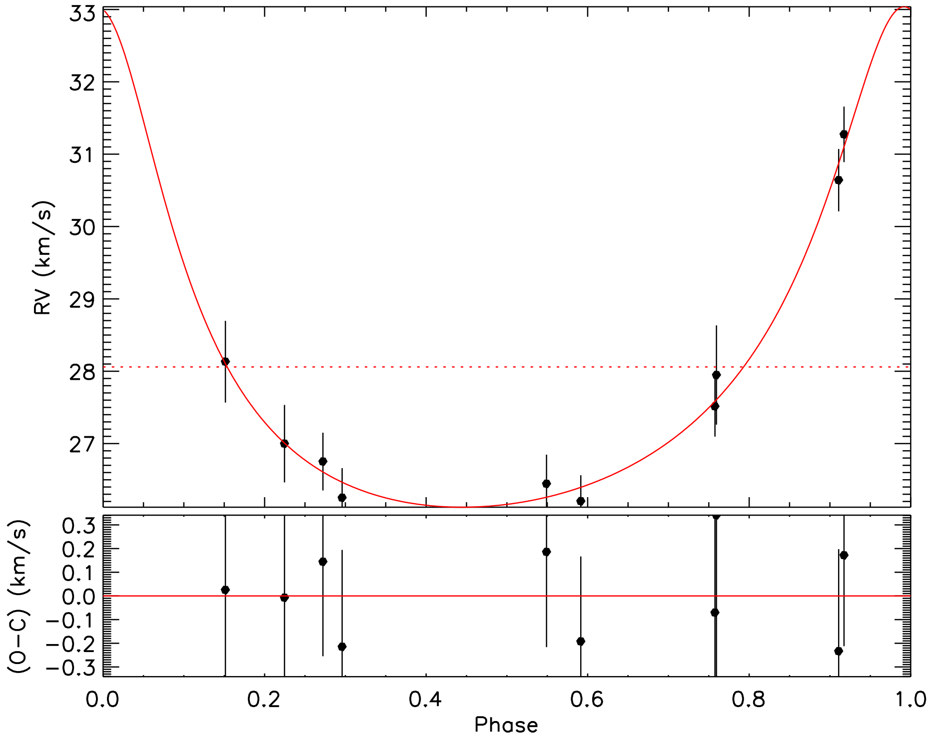

Figure 4.8 Orbital fit for RV 1496

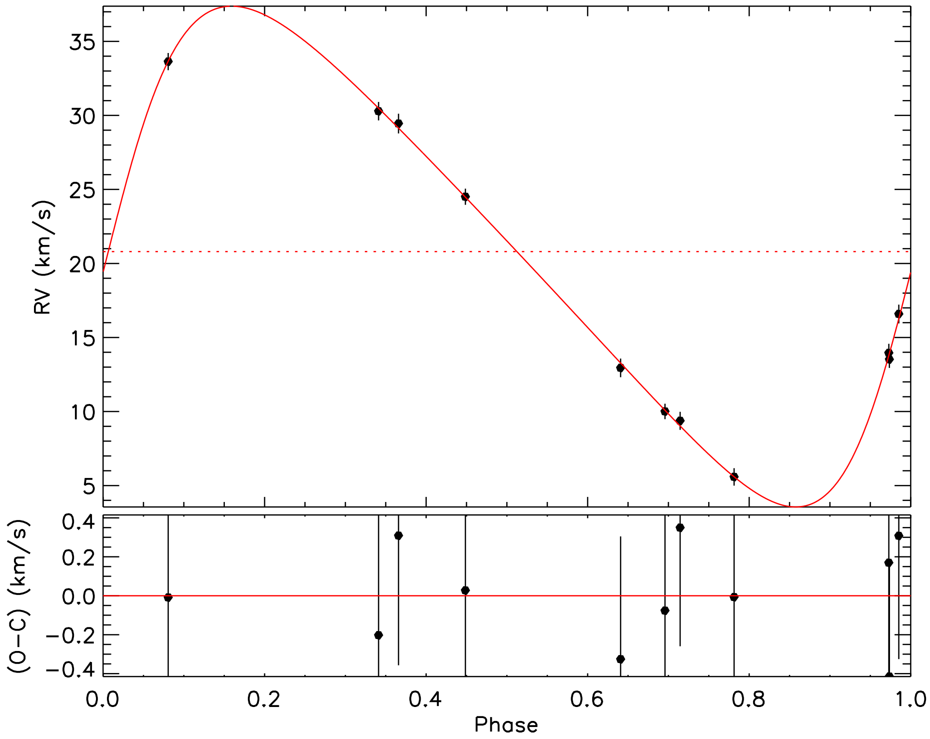

Figure 4.9 Orbital fit for RV 1550

RV 1753 was previously monitored for change in RV by Karnath et al. (2013) (2013) over a period of 20 years with 35 epochs. All of the fitted orbital parameters from that study are in excellent agreement with the fits presented in this chapter.

4.5 Velocity structure

4.5.1 ONC

Some of the analysis of the ONC region performed in T09 was affected by contamination from moonlight, and the lowest signal-to-noise data also added scatter. While the overall conclusions of T09 remain unchanged, the sample presented in this chapter has higher quality velocity measurements. For this reason, once again, we look at the relation between stellar RVs and ^{13}CO gas (Figures 4.12 and 4.13). All of the velocities in the plots are in the kinematic LSR reference frame to match that of the gas (Bally et al., 1987). To confirm that no binary stars contaminate the sample,

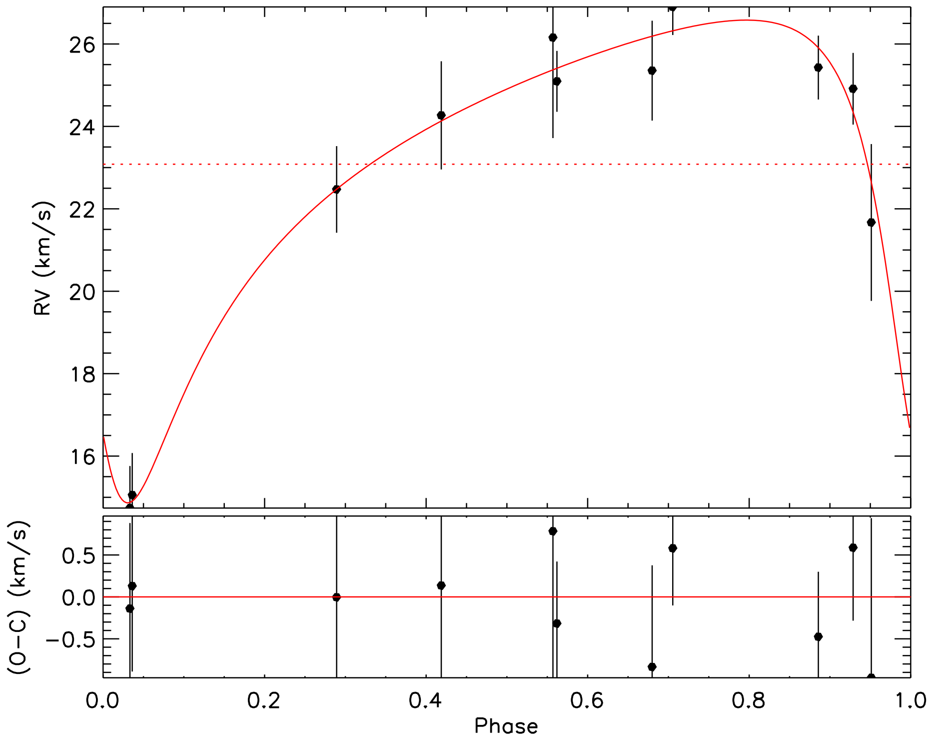

Figure 4.10 Orbital fit for RV 1660

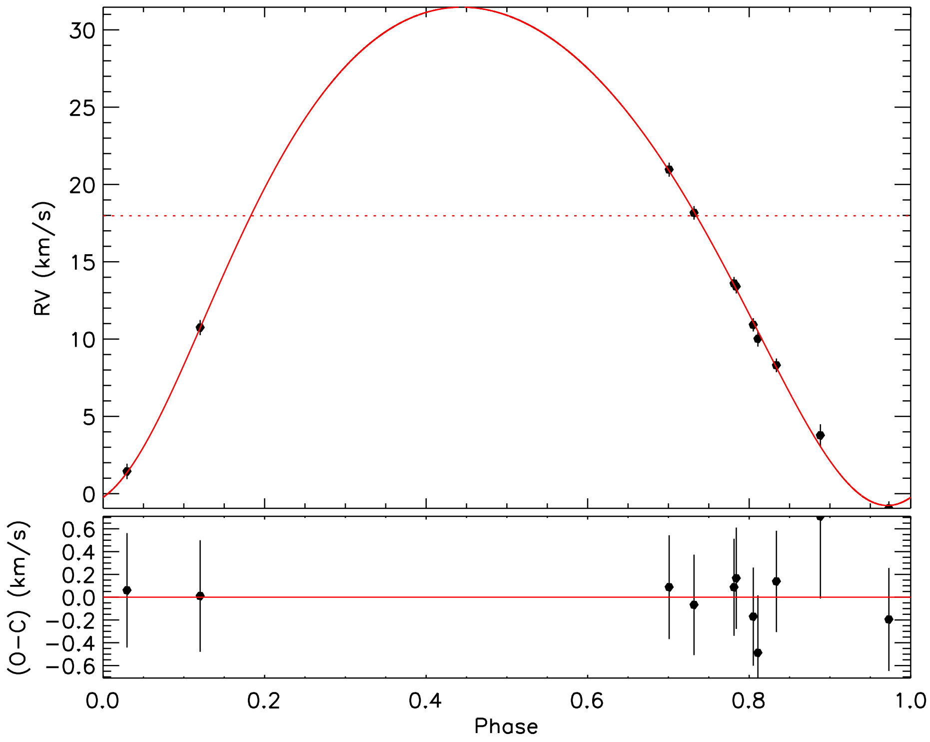

Figure 4.11 Orbital fit for RV 1753

we required that there be no variability in velocities with at least 3 epochs of observations. Unlike in T09, the peak of the RV distribution for stars follows the gas with no offset and a comparable velocity dispersion of $\sim$2.5 km s^{-1}. The only exception to this is the $-5.5^\circ < \delta < -5.0^\circ$ range, which coincides with the location of inner ONC regions such as Trapezium and OMC 2/3. A recent paper by Da Rio et al. (2016) measuring the RV from the infrared spectra in Orion A also found a lack of a blueshifted tail extending beyond $v_{lsr} < 0$ km s^{-1}.

However, while not quite as pronounced as reported by T09, we do observe some blueshifted tail component in the stellar RVs relative to the ^{13}CO motions. To determine whether or not the sources that populate that tail are members of the cluster or unrelated foreground or background stars, we searched for Li I detection toward some of them (Table 4.6, Figure 4.12) as a signature of their youth to establish whether or not these sources could be causally related to the ONC. Overall, many of the sources that occupy the same velocity space as the gas and blueshifted tail were indeed found to contain Li I. While there is some contamination from sources that appear to be somewhat more evolved, their low numbers alone cannot account for the entirety of the blueshifted tail. On the other hand, nearly all of the sources that occupy the velocity space outside what is presented in Figure 4.12 lack in Li I.

There are several possible explanations for this tail. There could be a separate foreground population of young stars that is not an immediate part of the ONC. Alves & Bouy (2012) and Bouy et al. (2014) argue that NGC 1980 is an example of such a foreground cluster. Unfortunately, it is located at $83.7^\circ < \alpha < 83.9^\circ$ and $-6.1^\circ < \delta < -5.8^\circ$, and the presence of the blueshifted population in that region is minimal and not spatially coherent. This is consistent with what has been found by Da Rio et al. (2016). However, south of it, the ONC is starting to turn into the L1641 cloud, and thus it is possible that the tail in the southernmost regions can be attributed to this.

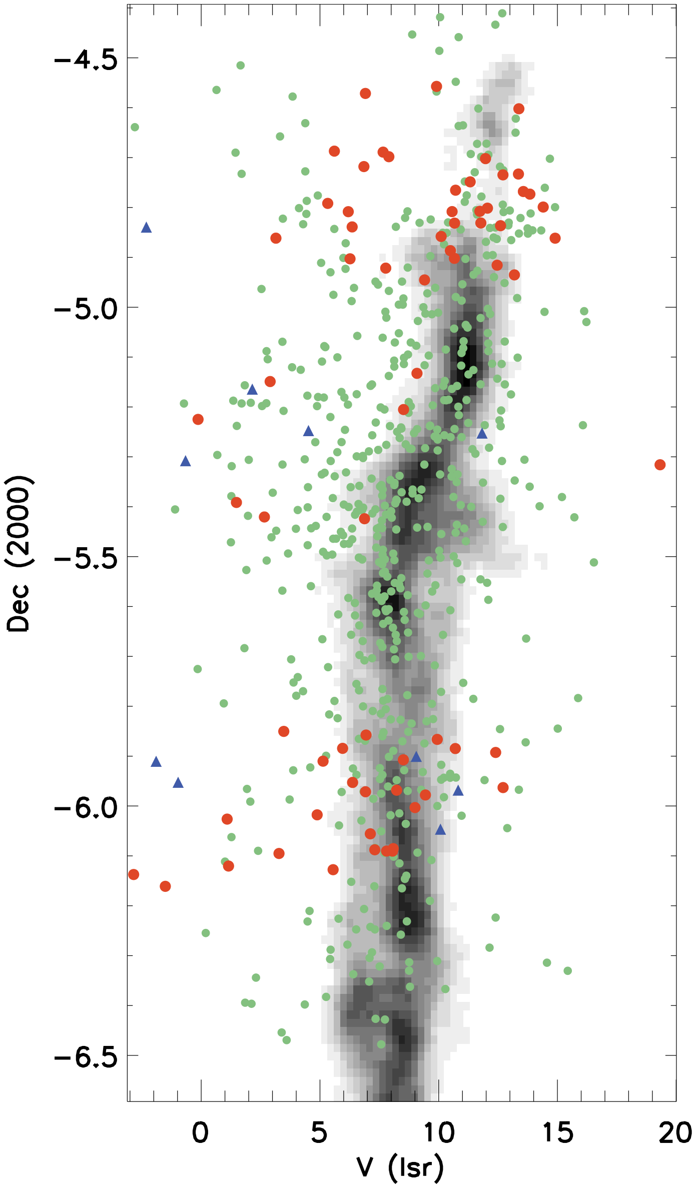

Figure 4.12 Position-velocity diagram for the ONC region, summed in right ascention. ^{13}CO map from Bally et al. (1987) is plotted in the background in grayscale. All the overplotted data points are non-binary sources that were observed in at least 3 epochs. Orange circles show sources where Li I has been detected, blue triangles show those that have been surveyed for the presence of Li I, but it was not detected. Green dots are all the remaining sources for which no Li I information is available.

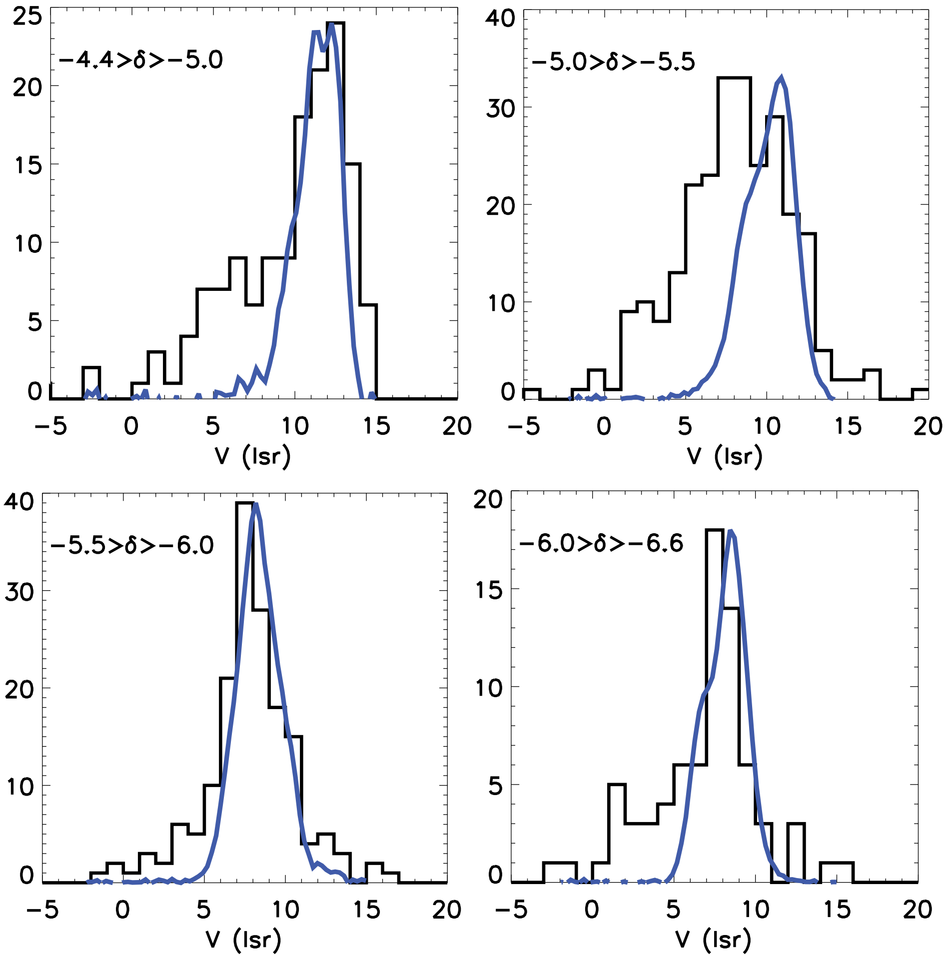

Figure 4.13 In black - distribution of of velocities of stars plotted in Figure 4.12 at four declination cuts. In blue - summed distribution of the ^{13}CO at those declinations, scaled to the peak of the histogram.

Table 4.6. Sources that were surveyed for the presence of Li I.

RV #[a]	R.A. (J2000)	Dec. (J2000)	v_{Li}[b] (km s^{-1})	σ_{Li} (km s^{-1})	R_{Li}	λ_{Li}[c] Å	W_{Li}[d] Å	Temp K.
113	05:34:15.45	-06:06:55.1	49.51	0.72	10.58	—	—	3750
120	05:34:17.78	-05:55:43.1	4.52	0.99	7.69	—	—	6000
133	05:34:20.80	-05:23:29.2	18.62	1.48	4.87	6708.32	0.39	3500
160	05:34:27.34	-05:24:22.2	26.02	2.26	9.18	6708.46	0.47	4000
164	05:34:28.22	-05:59:09.0	33.56	0.82	10.78	6708.62	0.10	6250

Only a portion of the table is show here. The full table is available on-line at `http://iopscience.iop.org/0004-637X/821/1/8/suppdata/apj522991t4_mrt.txt`

[a] Sources with RV# greater than 2057 have $R < 6$ for all detections, and thus they are not included in the Tables 4.2 and 4.3

[b] Velocity and other properties were measured only from Li I data.

[c] Typical uncertainty in λ_{Li} is 0.01 Å

[d] Typical uncertainty in W_{Li} is 0.01 Å

Some of these stars could have been dynamically scattered to achieve these velocities. While it is difficult to explain why there is no redshifted population to make the velocity distribution symmetric, it is possible that high extinction prevents us from observing it. The inner ONC is where this effect would be the most pronounced. Not only does this region have significantly higher stellar density than the rest of the cluster, allowing for more significant dynamical interactions between stars, but it is also more affected by extinction due to the high density of gas. It is possible that this can account for some of the observed blueshifted sources.

Alternatively, it is possible that the gas was being blown away by stellar feedback, leaving a somewhat older population of stars behind while newer stars formed. As suggested by T09, it is likely that in the northmost region, in the vicinity of NGC 1977, gas has been pushed back by irradiation from HD 37018, HD 37077, and HD 36958, which are B1V, B3V, and B3V stars, respectively, leaving behind a mini-cluster.

Proszkow et al. (2009) and T09 instead postulate that the redshift in the gas in Trapezium and OMC 2/3 could be due to the gravitational infall of the OMC 2/3 filament toward the Trapezium cluster. However, this would not entirely explain the presence of the blueshifted stellar population relative to the gas, and the location of these blueshifted stars is not correlated with either being on or off of the filament. More precise distances and proper motions, which could in part be obtained by the ongoing *Gaia* mission, are needed to confirm or deny the infall of the OMC 2/3.

4.5.2 NGC 2264

While there is little substantial difference between the velocities for the NGC 2264 region quoted in T15 and this chapter, some improvements could be made to the previous analysis of the velocity structure for the region through better filtering of the spectroscopic binaries. Similar to the case of the ONC, we restrict our analysis only to those sources that were detected in at least three epochs and show no RV variability. The positionvelocity diagram for the stars is compared to that for gas from Ridge et al. (2003) in Figures 4.14 and 4.15.

We impose a constraint on sources to have an R.A. of $100.05 \geq \alpha \geq 100.4$ in order to only trace those objects that are spatially correlated with ^{13}CO gas to limit contamination from foreground or background sources. As a result, stars that are located north of $\delta \sim 9.55°$ (i.e., Spokes Cluster and S Mon) have an agreement in RV with that of the gas that is significantly better than what was presented before by T15. This is partially due to the stricter spatial constraints than were originally imposed. No objects exhibit a significant blueshift in RV relative to the gas, with the slight exception of the southernmost declinations in the Spokes Cluster.

However, the entirety of the stellar population found toward the Cone Nebula does show a significant blueshift that is not dissimilar to what is found toward the Trapezium and OMC 2/3 regions in the ONC. However, unlike Trapezium where the dispersion velocity of the stars is wide enough to also correlate with the gas, the stars toward the Cone Nebula appear to be decoupled from the gas. The reason for this is not entirely clear.

In addition to these regions, there appears to be a small cluster of stars centered at $\alpha \sim 100.45°, \delta \sim 9.7°$ with a diameter of $\sim 0.1°$ (Figure 4.14). It was previously identified but not discussed in T15. The members of this cluster appear to have a systematic $RV_{lsr} \sim 2$ km s^{-1}, which is somewhat distinguishable from the main cluster. It is possible that it is a an older cluster that has managed to clear away all of its gas.

Since this cluster does not appear to be dynamically relaxed, as it exhibits a significant distinct substructure, a better determination of its age and further modeling will be needed to determine the degree of interaction between these subclusters. This could shed light on the dominant method of cluster formation, such as whether or not it is undergoing cold collapse (Scally & Clarke, 2002).

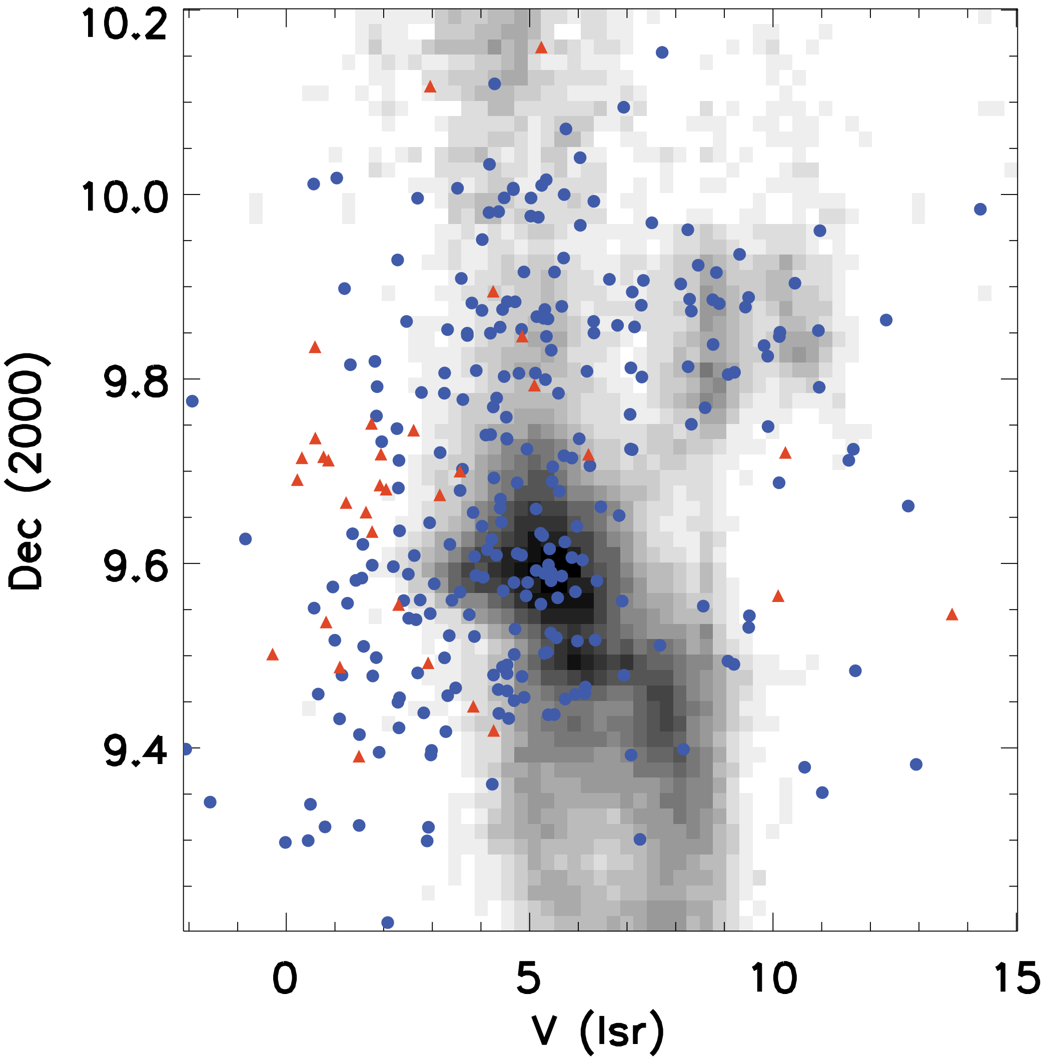

Figure 4.14 Position-velocity diagram for the NGC 2264 region, summed in right ascention. ^{13}CO map from Ridge et al. (2003) is plotted in the background in grayscale. All the overplotted data points are non-binary sources that were observed in at least 3 epochs. Blue dots have R.A. range between 100.05 and 100.4°, orange triangles range between 100.4 and 100.5° to show a subcluster centered at $\alpha \sim 100.45°, \delta \sim 9.7°$.

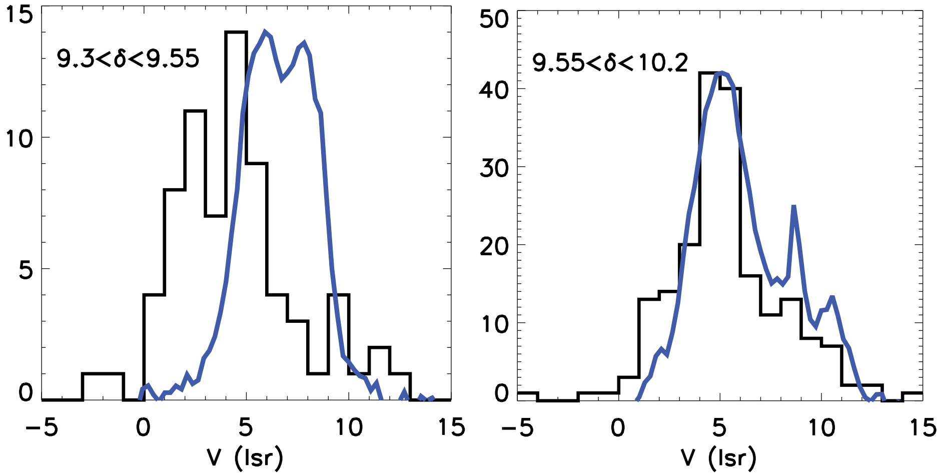

Figure 4.15 Black: distribution of the velocities of stars plotted in Figure 4.14 at two declination cuts. An R.A range between 100.05 and 100.4° has been imposed to minimize contamination from sources outside of the main cluster. Blue: summed distribution of ^{13}CO at those declinations scaled to the peak of the histogram.

4.6 Conclusions

In this chapter, we continue the efforts started in T09 and T15 toward characterizing the stellar RVs of the two closest massive star-forming regions, the ONC and NGC 2264. Using multi-epoch observations, we search for sources that exhibit a significant change in RV that could be attributed to the presence of a binary. We identify a total of 130 multiple system between the two regions. For 8 of the sources located in NGC 2264 we produce detailed orbital fits, and for two of these sources we can determine a mass ratio between the primary and the secondary.

The multiplicity fraction that we observe is $5.8\pm1.1\%$ for the ONC and $5.3\pm1.2\%$ for NGC 2264. If these systems were consistent with what is observed in nearby G dwarfs, then, considering the uncertainties of individual measurements and allowing primaries of 0.7 $M_\odot$, we would expect to observe MFs of $4.5 \pm 0.9\%$ and $5.8 \pm 1.2\%$, respectively, for these two clusters. Both NGC 2264 and ONC have a distribution of multiple stars that is largely consistent with what is observed in the field within the same parameter space. However, a study of the wide binaries in NGC 2264 would be needed to conclusively compare the MF of these two regions.

In addition to analyzing multiplicity, we reexamined the stellar RV distribution relative to that of gas for both of these clusters to find significantly better agreement between the two than has been previously reported, as both the peak of the distribution and the velocity dispersion of stars and gas are extremely similar in many regions of these clusters. The presence of the blueshifted young stars is reduced significantly in the cleaned sample, but they are not entirely absent. Some of these sources could be explained by the specifics of the star formation processes in these regions, for example, by stellar feedback pushing the gas away or by the presence of a separate foreground cluster.

CHAPTER V

Kinematics of the Optically Visible YSOs Toward the Orion B Molecular Cloud

We present results from high resolution optical spectra toward 66 young stars in the Orion B molecular cloud to study their kinematics and other properties. Observations of the Hα and Li I 6707 Ålines are used to check membership and accretion properties. While the stellar radial velocities of in NGC 2068 and L1622 show good agreement with that of the molecular gas, many of the stars in NGC 2024 show a considerable offset. This could be a signature of either expansion of the cluster, high degree of the ejection of the stars from the cluster through the dynamical interaction, or the acceleration of the gas due to stellar feedback. Published in 2017, ApJ, 844, 138.

5.1 Introduction

Most stars begin their lives in clusters (e.g. Lada & Lada, 2003). Therefore, in order to understand the conditions which lead to star formation, it is imperative to understand the dynamical state of the young clusters, with ages less than a crossing time, where the initial conditions have not yet been erased through the dynamical interactions between members. In particular, an important question that is yet to be answered is whether the cluster form quickly on a free-fall time scale (e.g. Elmegreen, 2007; Hartmann & Burkert, 2007; Kuznetsova et al., 2015), or whether the clouds are initially supported by turbulence preventing a rapid collapse (e.g. Tan et al., 2006; Hennebelle, 2012).

Several kinematic studies have been conducted in other nearby massive clusters, such as the ONC and NGC 2264 (Fűrész et al., 2006, 2008; Tobin et al., 2009, 2015; Da Rio et al., 2016; Kounkel et al., 2016a), analyzing the radial velocity (RV) of the young stellar objects (YSOs) within them. These observations revealed that these clusters are not dynamically relaxed and that they show a considerable RV substructure. In particular, they showed that, while typically the RV of the stars are similar to the kinematics of the gas from which they have formed, a large number of stars in both of these clusters are preferentially blueshifted relative to the gas; this blueshifted population is not compensated by an equal number of redshifted sources. In some extreme cases (e.g., toward the Cone Nebula, Chapter IV), the gas and the stars appear to be entirely decoupled from each other. Some explanations have been proposed to explain the blueshifted population; however, so far there is no conclusive answer.

The Orion B molecular cloud contains several clusters with an ongoing star-formation, such as NGC 2023/2024, 2068/2071, and L1622. These nearby clusters (390—420 pc, Kounkel et al., 2017c) are young, with ages of < 2 Myr (e.g. Levine et al., 2006; Flaherty & Muzerolle, 2008; Kun et al., 2008). These clusters are greatly affected by the high degree of extinction; only a few stars out of hundreds of known members have optical emission. Previously, Flaherty & Muzerolle (2008, hereafter, FM08) were able to obtain high-resolution optical spectra to measure RV to 32 stars in NGC 2068. To our knowledge, no currently published surveys obtained stellar RVs in the other Orion B regions. In the future, the IN-SYNC survey will present high-resolution near infrared spectra taken with APOGEE for the stars in the cloud; this is the extension of the observations of the Orion A molecular cloud (Da Rio et al., 2016, 2017). While infrared spectra enable the study of many highly-extincted stars that the present optical investigation cannot reach, observations of Hα and Li I are important for checking membership and addressing accretion properties.

In this chapter we present high-resolution spectral observations of optically emitting stars in the clusters associated with the Orion B molecular cloud. In Section 5.2 we describe our observations and define the membership sample. In Section 5.3 we discuss evolutionary classification of the sources and look at the properties of the Hα and Li I lines observed toward them. In Section 5.4 we look at the distribution of RVs in the clusters.

5.2 Observations and data reduction

We observed a total of 4 fields toward the Orion B with Michigan/Magellan Fiber System (M2FS, Mateo et al., 2012), a multi-object spectrograph on the Magellan Clay Telescope. These fields included regions toward NGC 2023, 2024, 2068, and L1622 (Table 5.1). Due to their spatial proximity, we consider NGC 2023 and NGC 2024 together in the analysis presented in this chapter. All regions were observed with the Hα and Li I filter, simultaneously spanning two orders covering the spectral range of 6525—6750Å with a spectral resolution $R \sim 20,000$. A maximum of 128 sources can be were observed in this configuration with the field of view of 29' in diameter. NGC 2068 has also been re-observed the second time with the Hα and the Li I filter, as well as Mg I filter, which spans the spectral range of 5100—5210Å.

The observed targets include all the objects found toward the fields from UCAC4 catalog (Zacharias et al., 2012), with the preference for r magnitude brighter than 16.5. Due to extinction, in all four fields there are only 413 sources that are part of the UCAC4 catalog (Figure 5.1). In contrast, near infrared surveys, such as 2MASS have more than ten times the number of sources in the same part of the sky.

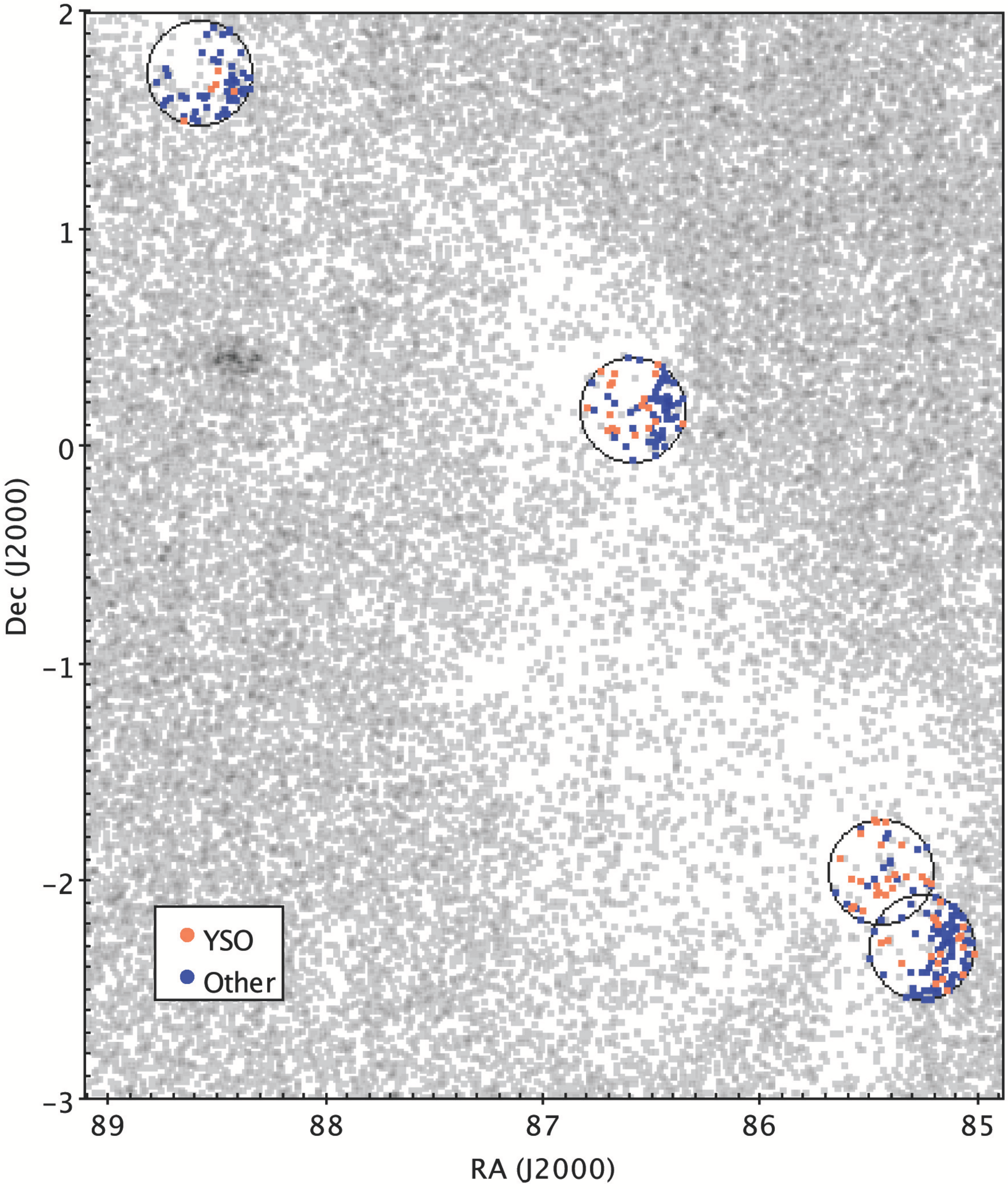

Figure 5.1 The distribution of sources in UCAC4 catalog toward the Orion B (greyscale). The observed fields as well as the sources within them are indicated. Sources with Li I absorption are identified as YSOs.

Table 5.1. Dates and configurations of the M2FS observations.

Field ID	Date (UT)	R.A. (J2000)	Dec. (J2000)	Exposure time (#×seconds)	Filter
NGC 2024	2014 Dec 11	05:41:48.0	−01:57:18	3×1200	Li I + Hα
NGC 2023	2015 Feb 03	05:41:02.7	−02:18:18	3×1800	Li I + Hα
NGC 2068	2015 Feb 28	05:46:21.6	00:10:23	3×1800	Li I + Hα
L1622	2015 Feb 27	05:54:20.1	01:42:57	3×1800	Li I + Hα
NGC 2068	2017 Mar 04	05:46:21.6	00:10:23	3×720	Li I + Hα
NGC 2068	2017 Mar 04	05:46:21.6	00:10:23	3×900	Mg I

The data were first processed by the custom Python code written by J. Bailey, and then reduced using the IRAF pipeline HYDRA. The narrow nebular emissi lines from [S II] (6717 and 6731Å), [N II] (6549 and 6583Å), and Hα appeared strongly toward many (but not all) sources. While sky spectra offset by a few arcseconds were taken, in many cases, particularly in NGC 2024, it was insufficient to reliably remove this emission which can strongly vary even over small angular distances. These lines were masked out (Figure 5.2). The same was done for the wide Littrow ghosts from the optics at 6600 and 6725Å in Hα and Li I orders.

The data were cross-correlated with the IRAF package RVSAO (Kurtz & Mink, 1998) relative to the synthetic spectra of Coelho et al. (2005). We also performed cross-correlation using the synthetic spectra from Munari et al. (2005), but while overall they produced consistent solutions, Coelho et al. (2005) spectra led to a somewhat better agreement in the solutions between the different simultaneously observed orders for the same stars. The synthetic spectra templates that were used had the effective temperatures (T_{eff}) between 3500 and 7000 K in steps of 250 K, the solar metallicity, and surface gravity $\log(g) = 3.5$. We obtained the radial velocities (RV) from the cross-correlations, and estimated T_{eff} from the best-matched template for each object. We include only RV measurements where the signal-to-noise R (Tonry & Davis, 1979) of the best cross-correlation was $R > 6$. The Li I and Hα orders were cross-correlated separately; however, both Li I and Hα lines were masked out

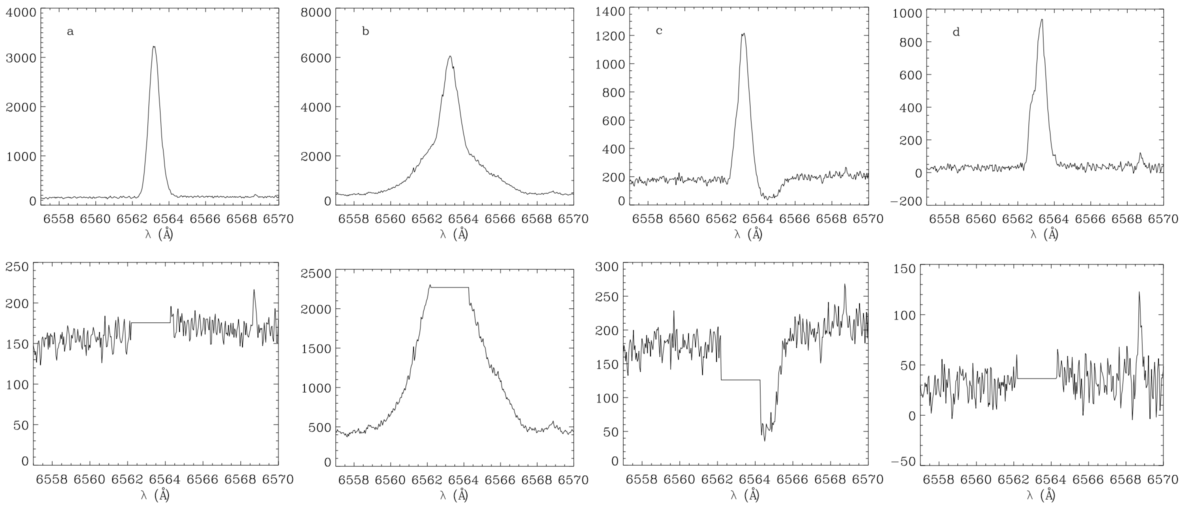

Figure 5.2 Examples of masking of the Hα nebular emission lines. Top row: before masking, bottom row: after masking. a) No residual Hα detected coming from the star. b) Strong Hα emission. c) Likely Hα absorption from a source redshifted relative to the nebular emission. d) No residual Hα detected after masking, however, nebular emission line does show some asymmetry in the blue wing which may suggest some Hα emission.

so as not to introduce additional biases due to the relative strength of these lines in comparison to the template spectra, as both lines are significantly stronger in YSOs. It is worth noting that after masking these lines, there appears to be some bias in the best-matched T_{eff} for the template. In particular, there is a strong preference for very low T_{eff} after masking Hα line; similarly, Li I masking may result in somewhat higher matched T_{eff}. This should not have a strong effect on the RV as the wavelength of the remaining lines is not affected. The best matched T_{eff} between all orders (including Mg) appears to be more consistent if the Li I and Hα lines are left unmasked. Therefore, the quoted T_{eff} that we include in Table 5.2 come from the unmasked cross-correlations.

Generally, the strongest feature in the order containing Hα line is Hα itself with few other lines present. The Li I order typically provides more reliable RV measurements. If the velocities obtained from each order for the same source differed by less

Table 5.2. Sources that were surveyed for the presence of Li I.

RV #	R.A. (J2000)	Dec. (J2000)	v km s^{-1}	σ km s^{-1}	R	W_{Li} Å	W_{H_α} [a] Å	V_{H_α} km s^{-1}	YSO	RR? [b]	Temp K.	Date JD	Order [c]	Field
2533	05:40:58.97	-02:32:52.0	-16.39	0.87	10.51	—	—	—		y	5750	2457084.5	Li+Hα	2023
2534	05:40:53.40	-02:32:27.6	-38.84	0.65	12.50	—	1.35	—		y	5500	2457084.5	Li+Hα	2023
2535	05:41:20.87	-02:32:06.6	41.00	0.54	18.91	—	1.24	—		y	6000	2457084.5	Li	2023
2536	05:41:12.08	-02:31:21.9	-31.40	0.96	7.12	—	1.35	—		y	5750	2457084.5	Li+Hα	2023
2537	05:41:05.44	-02:31:06.4	91.65	0.36	21.98	—	1.70	—		y	5250	2457084.5	Li+Hα	2023
2538	05:40:47.38	-02:30:52.9	32.13	1.19	6.35	—	—	—		y	6250	2457084.5	Li+Hα	2023
2539	05:40:44.56	-02:30:36.7	74.72	0.41	18.89	—	2.44	—		y	5750	2457084.5	Li+Hα	2023
2540	05:40:34.50	-02:30:22.3	17.97	1.68	10.21	0.60	-1.54	289	YSO (Class II) [d]	y	4000	2457084.5	Li+Hα	2023
2541	05:40:43.56	-02:30:15.7	11.97	0.90	8.43	—	0.77	—		y	5750	2457084.5	Li+Hα	2023
2542	05:40:52.22	-02:30:10.0	63.51	0.59	13.74	—	2.03	—		y	6500	2457084.5	Li+Hα	2023
2543	05:41:00.57	-02:30:04.0	39.97	1.93	4.91	—	1.47	—		y	6500	2457084.5	Li+Hα	2023
2544	05:40:33.22	-02:29:53.9	-9.49	0.90	8.82	—	—	—		y	5250	2457084.5	Li+Hα	2023
2545	05:40:49.84	-02:29:24.2	-40.16	0.80	10.21	—	—	—		y	5250	2457084.5	Li+Hα	2023
2546	05:41:13.06	-02:29:12.4	17.29	0.43	18.55	—	0.88	—		y	5750	2457084.5	Li+Hα	2023
2547	05:40:35.38	-02:28:22.7	109.04	1.02	7.36	—	1.15	—		y	5500	2457084.5	Li+Hα	2023

Only a portion of the table is show here. The full table is available on-line at `http://iopscience.iop.org/0004-637X/844/2/138/suppdata/apjaa7deat2_mrt.txt`

[a] Negative values show that the line appeared in emission. Most lines were contaminated by the nebular emission lines; this emission has been masked

[b] Whether or not the source was processed with the rapid rotator parameters during cross-correlation (see Chapter IV for full discussion)

[c] Order used for cross-correlation.

[d] Not observed with *Spitzer*, classified based on their Hα.

than the uncertainties of each correlation added in quadrature, then the variance-weighted average was calculated for the RV and the uncertainty σ of the fit, and the two R values were added in quadrature. If the RVs from the two orders were larger than the expected errors, only the RV from the Li I order was used. RVs from the Hα order were only adopted when no significant measurement was possible from the Li I order. The RV measurements from the Mg I order are presented separately.

In addition to the default filtering parameters of the cross-correlation to filter the noise and large scale structure, we used filtering parameters more suited for the rapidly rotating stars, and we recorded the resulting cross-correlation if the resulting R value was greater than in the default case, and the σ was not greater by more than 0.05 km s^{-1}. The complete description of the data reduction and cross correlation methods is presented in Chapter IV.

Some observations in the first epoch of NGC 2068 and L1622 have been contaminated by moonlight. The measured RVs of these stars are consistent with the barycentric velocity on the dates of the observations (~ -25 km s^{-1}), and the best-matched temperature template consistent with solar. The sources in which this contamination has been identified have been removed from the source list.

The 2015 epoch of observations of NGC 2068 field appears to be systematically blueshifted by 2 km s^{-1} relative to the 2017 epoch. There are not many telluric lines in the wavelength regime covered by the spectra (most apparent lines are found at 6542.313, 6543.907, 6547.705, 6572.086 6574.852Å), and they are generally relatively weak and not apparent toward most of the sources. However in the sources where it is possible to centroid these lines and it is clear that they are not contaminated by any other nearby lines, we can confirm that 2017 epoch for NGC 2068 field has accurately calibrated wavelength solution and 2015 epoch is the one that is responsible for the offset.

Additionally, a systematic redshift of $\sim$1 km s^{-1} can be observed in the data in

Chapter IV as well in the M2FS observations of Hα order and the Li I order, although the latter order is apparent only for non-members. As the Li I line was not masked out previously in members, and the templates do not have as strong Li I absorption, the cross-correlation was caught on this line in the YSOs, producing a slight RV shift, which happened to almost exactly cancel out the systematic offset for the entire field.

There is some evidence that NGC 2024 field is systematically blueshifted by ~2 km s^{-1}, and NGC 2023 field is systematically redshifted by ~2 km s^{-1} (see Section 5.4 for discussion). This offset is suggested by the telluric lines, although there are only a few sources where centroiding of these lines is possible. We unfortunately cannot confirm it since these fields have not been reobserved and there is a lack of previously published RV measurements of these sources. Nonetheless, we do correct all these offsets from the RVs in the Table 5.2.

The causes of these offsets are not clear. It has been observed by Walker et al. (2015) that temperature dependent offsets in the zero point of ~2 km s^{-1} can occur in the M2FS observations; since then a greater care has been taken in the calibration of the instrument. We can rule out the temperature dependence in this set of the observations, as the solutions are consistent between the individual frames. It is possible that the issue is isolated to the specific Hα/Li I filter set. Nonetheless, while the absolute zero point calibration may be uncertain, the relative RVs within each field should be consistent.

5.3 Spectral properties

A total of 151 sources have been detected toward NGC 2023/2024, 80 toward NGC 2068, and 59 toward L1622, they are presented in the Table 5.2. Figure 5.3 shows a wide spread of radial velocities, much larger than typically observed toward star-forming regions; most of these stars are non-members. We identify members in two ways: strong/broad Hα emission due to accretion in the classical T-Tauri stars

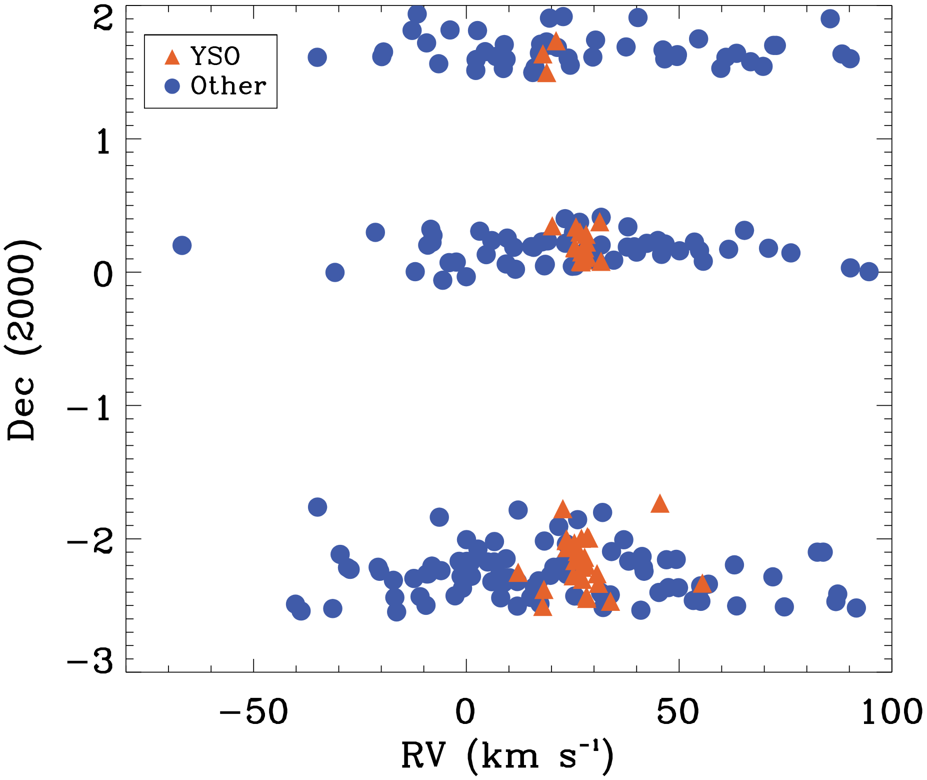

Figure 5.3 Measured RVs of all the sources observed toward the Orion B.

(CTTS), along with Li I absorption; and Li absorption alone for the weak-lined T-Tauri stars (WTTS). Stars with spectral types earlier than K4 show depleted Li I abundances even during the young age compared to their lower mass counterparts, therefore, uniform membership can be categorized only for stars with $T_{eff} < 4500$K (Figure 5.4). We report on Li I measurements of the sources with $W_{LiI} > 0.1$. We identify 42 sources in NGC 2024 that satisfy this criterion, 18 in NGC 2068, and 6 in L1622; these sources can be confirmed as the members of Orion B. Among the remaining sources, some YSOs with a higher T$_{eff}$ may remain, but most of them are likely to be foreground stars, or possibly background stars if they are not projected directly onto the cloud. CTTSs are identified using the criteria from White & Basri (2003), based on W$_{H\alpha}$ and the velocity width at 10% maximum of Hα ($V_{H\alpha}$, Figure 5.5). However, because of the nebular emission contamination, some W$_{H\alpha}$ measurements may not necessarily be reliable. To test this classification, we

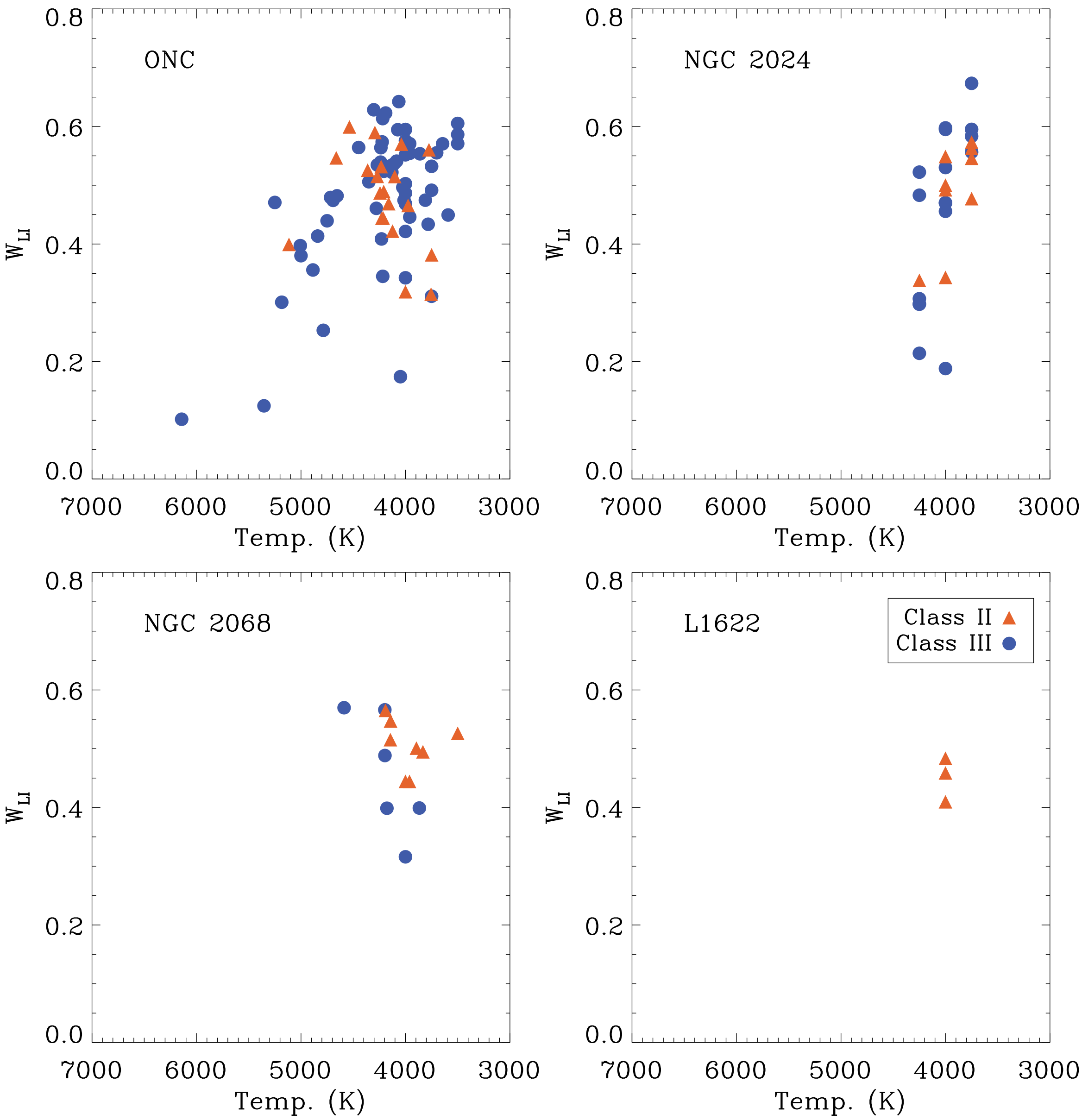

Figure 5.4 Equivalent width of Li I as a function of the best-matched cross-correlation template temperature (with R>6) in the four regions. Data for the ONC is taken from Chapter IV

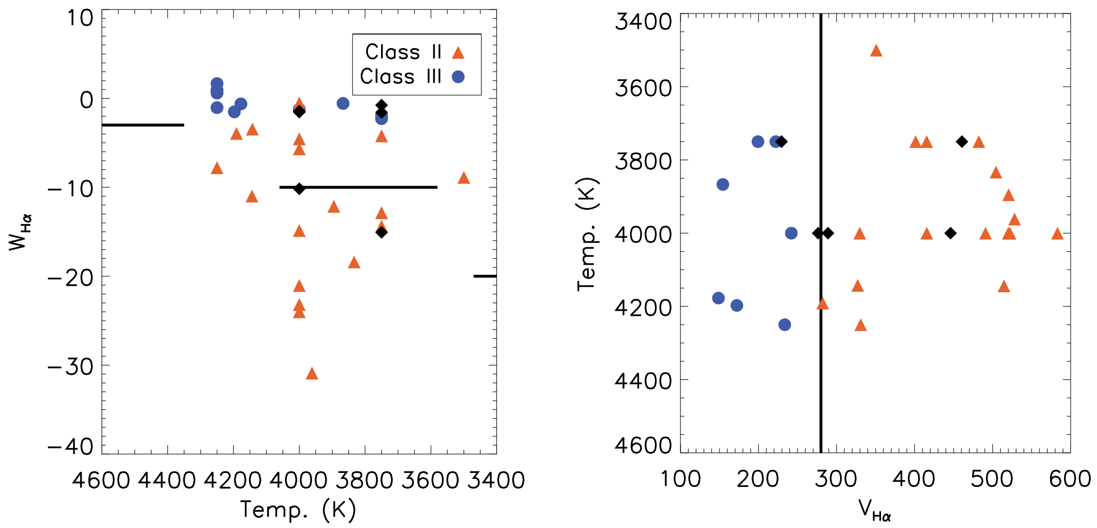

Figure 5.5 Comparison of classification based on the *Spitzer* photometry from Megeath et al. (2012) and the accretion signatures from Hα. Black diamonds are sources not in the *Spitzer* catalog. The black lines show the criteria separating CTTSs and WTTSs from White & Basri (2003).

use classification from *Spitzer* photometry from Megeath et al. (2012, Figure 5.6). In general, Class II sources (identified by the infrared excess attributed to a dusty disk surrounding them) are expected to be actively accreting CTTSs, and Class III sources (the onese that have colors similar to a naked photosphere) are typically WTTSs, however, the two classifications do not correlate in all cases. Nonetheless, in general, two classifications are comparable with each other. Throughout the text unless stated otherwise we use SED classification with exception of for 7 sources which were not detected with *Spitzer*. These sources were classified based on their Hα.

Two sources, RV 2670 and RV 2734, are double-line spectroscopic binaries. RV 2670 is a member of NGC 2024. RV 2734 is found in NGC 2068 field; however, it is probably not associated with the cluster. We extract the RVs of the second component from fitting a Gaussian to the cross-correlation function (Table 5.2).

We compare the distribution of the W_{LiI} for four regions (including the ONC data from Chapter IV) in Figure 5.4. The typical uncertainty in W_{LiI} of lines with $R > 6$ is ~0.05 Å, although it can increase up to 0.1 Å for noisier spectra. Generally,

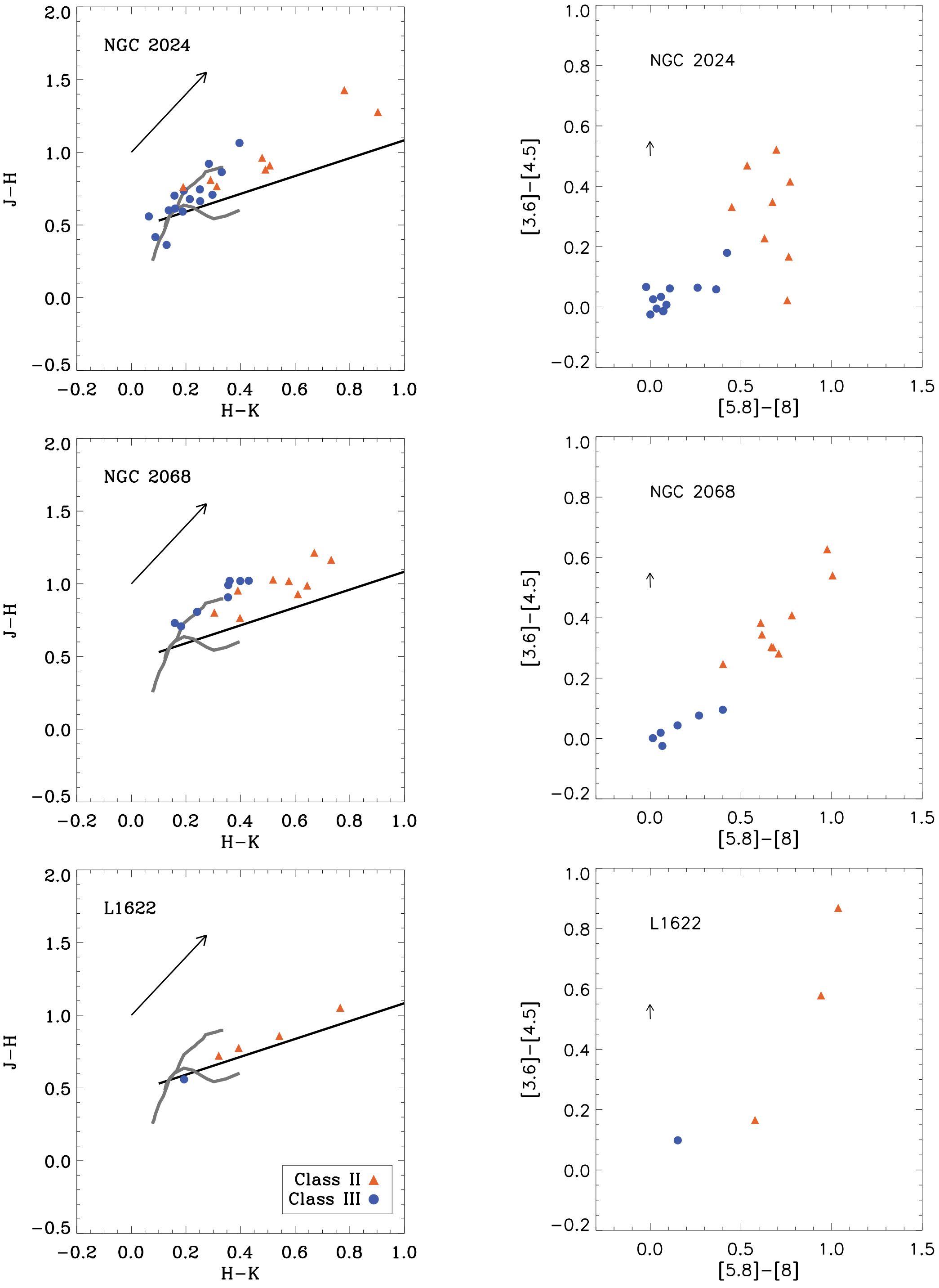

Figure 5.6 Color-color diagrams for sources with Li I, using *Spitzer* and 2MASS photometry, identified according to their evolutionary classification. Arrows show the reddening vector of 0.5 A_K, from Megeath et al. (2012). In the left panels, a black line shows the location of the CTTS locus as identified by Meyer et al. (1997), which corresponds to the intrinsic de-reddened colors of the young stars with disks. A gray lines shows typical colors for pure photospheres (Bessell & Brett, 1988).

there does not appear to be any significant differences between CTTSs and WTTSs in terms of the distribution of their W_{LiI}. However, accreting stars typically have a large degree of veiling, which may result in underpredicting the true W_{LiI} of these stars. Due to the limited spectral coverage, we cannot correct for veiling in this survey.

Among the non-accreting YSOs (which should not be affected by veiling), there are several sources that appear to be somewhat depleted in Li I relative to the rest. The two most extreme examples are RV 906 and RV 2603 with $W_{LiI} < 0.2$. RV 2603 may be an older foreground source, as its velocity is considerably different from the RV of most other identified members of NGC 2024; however, we cannot definitively confirm it. RV 906, on the other hand, was identified as a spectroscopic binary in Chapter IV, with most measurements kinematically similar to the rest of the ONC. Nonetheless, it is possible that this source is not a member of the ONC, as there are 15 other stars which have no Li I at all that are also found at the rest velocity of the cluster.

A number of other WTTSs have $W_{LiI} < 0.4$. Previously, Palla et al. (2005) also discovered 4 stars in the ONC that have shown a similar level of depletion and found their ages to be $\gtrsim$10 Myr, considerably older than members of the ONC or the Orion B. In general, YSOs begin to process Li I at age of 5–10 Myr, and become strongly depleted after 10 Myr (e.g. Baraffe et al., 1998). In some rare cases, strong episodic accretion bursts could accelerate the depletion to take place on a much faster rate (Baraffe & Chabrier, 2010; Baraffe et al., 2017). However, it is also possible there is a source of emission nearby that would increase the continuum, resulting in a lower W_{LiI}. We exclude all the sources found near strong nebulosity or other nearby bright sources identified by examining DSS images of the region. The remaining sources are RV 2550, 2581, 2682, 2725, and 2764. We further attempted to subtract the continuum from the spectra of these sources to test the limits of potential contamination, should it be there. It is notable that for RV 2550, in order to bring W_{LiI} toward a

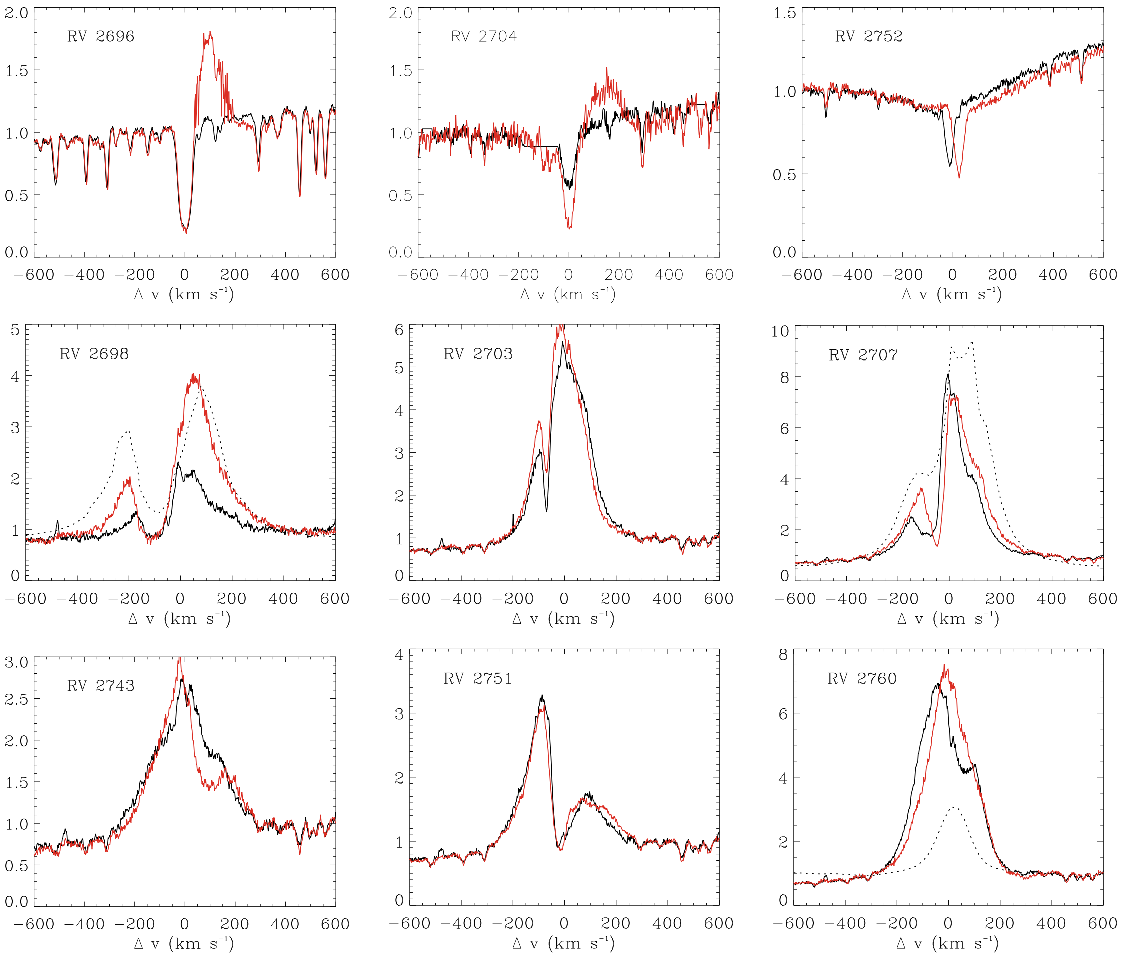

Figure 5.7 Sources with variable or assymetric Hα line. Black curves shows the spectra taken during 2015 epoch, and the red line shows the spectra taken during 2017 epoch. Dashed curves are the spectra from Fang et al. (2009).

more acceptable range after the continuum subtraction, the flux at the center of Li I line should be near zero.

One source, RV 2727 does not have any detectable Li I, but it has a clear presence of Hα emission (although it is not strong enough to be considered a CTTS by any criteria, although its $V_{H\alpha}$ is close to the threshold, nor does this source have any IR excess).

Many of the strongly accreting sources do have an assymetric or variable Hα line profile (Figure 5.7). These sources are most apparent in NGC 2068 cluster; in L1622 there are too few members observed, and in NGC 2024 the nebular emission is too strong to conclusively analyze the Hα line profile.

RV 2696 is not considered to be a member of NGC 2068 since it doesn't have a strong Li I absorption ($W_{LiI} \sim 0.05$), although it does have a T$_{eff} \sim 5,000$K, at which Li I may become depleted. This source does have RV similar to the RVs of the members of the cluster, however. In the second epoch of observations of this source, it exhibited an emission redward of its Hα line that was not present in the first epoch. A similar profile is seen toward RV 2704.

RV 2752 also has very weak Li I line, and therefore is not considered as a member. Its spectrum is very poorly correlated in all observations. This source does have a very broad Hα absorption line, it appears to be an early-type star. However, there is a narrow absorption superimposed onto the broad component. The wavelength of this narrow line appears to shift by almost 40 km s^{-1}. It is notable that the other lines remain unaffected. It is possible that this is a spectroscopic binary with a late-type companion that is responsible both for Li I absorption and variable Hα, however, it is difficult to confirm it.

The remaining sources we examine are all CTTSs. The Hα emission of RV 2698 has increased in strength by a factor of 3 relative to the continuum between 2015 and 2017. It has an assymetric line profile with two peaks, where the stronger peak is somewhat redshifted relative to the rest velocity of the source, and the dip in the flux is somewhat blueshifted, similar to a P Cygni line profile, although the absorption does not fall significantly below the continuum level. This source has been previously observed by Fang et al. (2009); the the strength of the primary peak was the same as it is in 2017, although the secondary peak was significantly stronger. Similar profile is seen in RV 2703 and RV 2707, although their absorption component is weaker. The size of the absorption in RV 2707 appears to evolve, becoming narrower over time, and this source has an additional bump in the red part of the line profile. This bump had the same strength as the primary peak in the observations by Fang et al. (2009).

RV 2743, 2751, and 2760 also have dual peaks, although the absorption is redshifted relative to the center of the line, which is indicative of the infalling gas. RV 2743 shows this only in 2017 epoch of observations, but not in 2015. On the other hand, for RV 2760, this infall is present only in 2015 epoch. Since Fang et al. (2009) observations, the intensity of emission has tripled.

Among the sources identified as members in this survey we measure the accretion ratio defined as [CTTS]/[CTTS+WTTS] ratio to be 0.66±0.33 (5/6) in L1622, 0.55±0.18 (10/18) in NGC 2068, and 0.38±0.09 (16/42) in NGC 2024. The optical regime is somewhat more biased against CTTSs as they may be more reddened and we are sensitive only to the sources with a very low extinction (Figure 5.6). Moreover, cluster cores usually contain younger population of YSOs than those found in the halo (e.g. Getman et al., 2014), and in Orion B we cannot observe any YSOs embedded in the clouds. Therefore, these values are probably the lower limits of the true disk fractions of these clusters.

5.4 Velocity Structure

We look at the velocity distribution of the confirmed members of the Orion B with detected Li I absorption with the $R > 6$. There are 31 such sources in NGC 2024, 13 in NGC 2068, and 4 in L1622. Similarly to Chapter IV, we compare this velocity distribution to that of the ^{13}CO gas after converting the measured RV to the local standard of rest (lsr). As the young stars have formed from the molecular gas which is traced by ^{13}CO, a natural assumption is that both stellar and gas velocity distribution should be comparable to each other.

It does appear to be the case in L1622. In this region, v_{lsr} of the ^{13}CO gas with the peak 1.17 km s^{-1} and line width at half maximum of 1.66 km s^{-1} (Kun et al., 2008). While the sample of members of L1622 that we detected in this survey is extremely

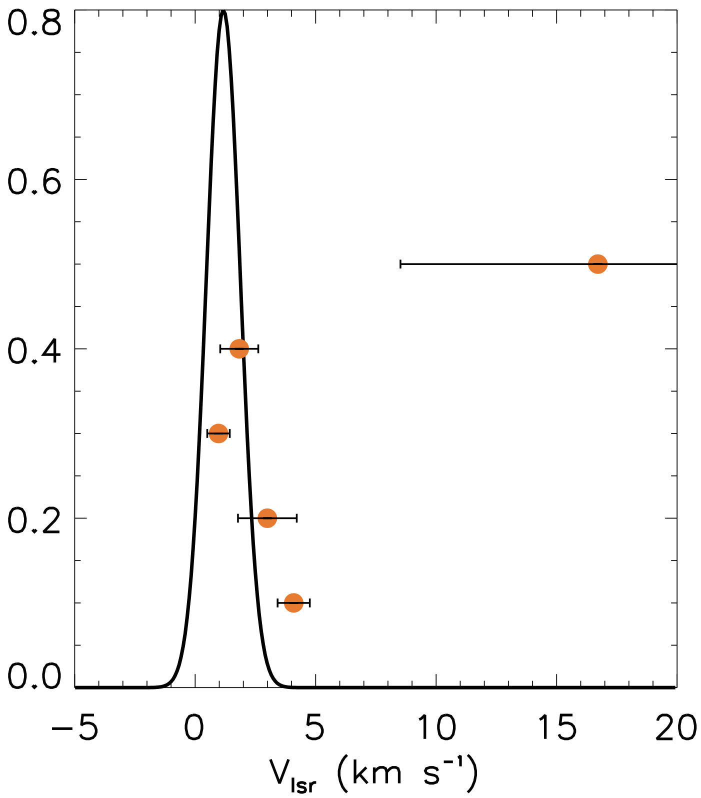

Figure 5.8 Velocity distribution of members toward L1622. Black line shows the distribution of the ^{13}CO gas described by Kun et al. (2008). Sources are arbitrarily scaled along the y-axis to maximize readibility.

small (only 5 sources, only 3 of which have confident RV measurements with R>6), v_{lsr} of all but one members of L1622 ranges between 0.9 to 4.1 km s^{-1} (Figure 5.8). The RV of the single outlying source is highly uncertain, has low R value. It is possible that this source may be affected by the multiplicity. Unfortunately, only a single epoch of measurements is available to confirm it. It is possible that there may be a systematic offset for the entire field, but it unlikely to significantly change the correlation between RVs of the stars and the molecular gas.

The systematic offset is much better calibrated in NGC 2068. After it is taken into the account, there does not appear to be any peculiar RV structure in NGC 2068. This is similar to what has been observed by FM08. We compare the RVs of the sources to the of ^{13}CO gas (Nishimura et al., 2015). Two sources appear to have RV different from the molecular gas (Figure 5.9). RV 2762 has been detected both in 2015

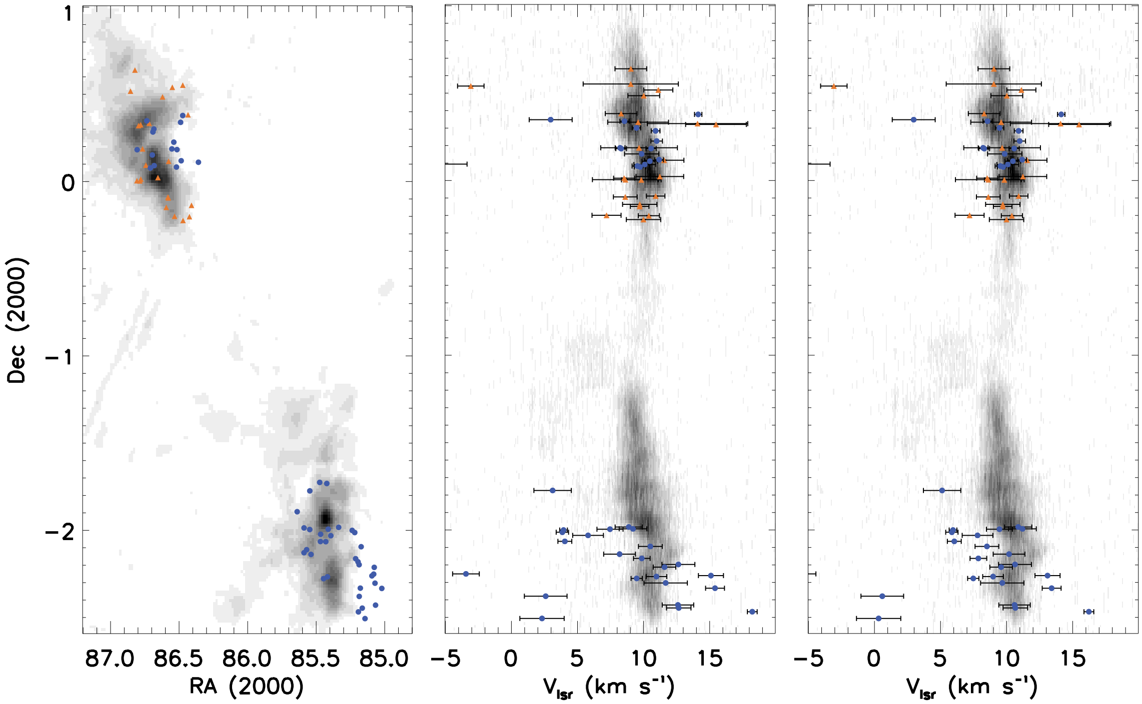

Figure 5.9 Left: Map of the observed members of the NGC 2024 and NGC 2068 clusters, plotted over ^{13}CO map from Nishimura et al. (2015). Blue circles are the sources from this work, orange triangles are the sources from FM08 survey. Middle: position-radial velocity diagram, summed in right ascention, using raw RVs. Right: same as before, but with the RVs of the two fields of NGC 2024 corrected for the offset.

and 2017, and it has been observed by FM08 (source ID 984). There is a big degree of scatter in RV between the measurements. However, since all the measurements are highly uncertain, this source cannot be identified as a RV variable using the criterion from Chapter IV. Similarly, RV 2764 has been detected in all epochs (FM08 228). All the measurements are consistent with each other within the uncertainties (typically $\sim$0.5 km s^{-1}), all $\sim$5 km^{-1} redshifted relative to the gas. While we cannot rule out that this source is RV variable due to the sparsity of measurements, it is more likely that it has been ejected from the cluster.

NGC 2024, on the other hand, is significantly less clear-cut in terms of its RV structure. There appears to be a gradient across the cluster in the raw RVs of the members of the cluster, completely decoupled from the kinematics of the molecular gas. However as the observations of this region are split into two fields, it is possible that there is a systematic offset in both of these fields that is applied in the opposite direction from each other. The magnitude of the offset suggested by the telluric lines in both cases is $\sim$2 km s^{-1}. After this offset is removed from the data, the agreement between the kinematics of the molecular gas and stars becomes better; however there is a substantial population of stars blueshifted to the gas, and a few sources (mostly located off-cloud) remain to be somewhat redshifted. Alternative offset values cannot help to improve the agreement in the RVs further.

As only one epoch of observations is currently available for all of these sources, it is possible that several of these sources are spectroscopic binaries, therefore their measured RV is different from the true RV of the system. Chapter IV estimated that only 5–6% of stars in the ONC and in NGC 2264 can be identified as spectroscopic binaries with the spectral resolution comparable to what is used in this survey. If this fraction is similar in the Orion B, we should expect only $\sim$3–4 spectroscopic binaries in the entire survey. While the multiplicity function does vary between different star-forming regions, the difference between RV of the gas and that of the detected stars cannot be due to binarity.

An important consideration in these observations is that since in the optical regime it is only possible to probe sources with very low extinction (Figure 5.6), we are not sensitive toward the deeply embedded objects that are located within the molecular clouds. Therefore the entirety of our sample consists of the sources that are located near the upper layer of the cloud; they are of some of the closest YSOs to the Sun in these regions. We estimate that in the fields covered by observations, there should be ∼220 Class 0/I and II YSOs toward NGC 2068, ∼475 toward NGC 2024, and ∼30 toward L1622 based on the density maps by Megeath et al. (2016). The number of Class III sources in these regions is more difficult to estimate, although, based on the observed ratio of Class II and Class III sources, it is possible that that the total number of YSOs would be ∼1.5 times higher than the value estimated based on the density of only Class 0/I and II YSOs.

With this in mind, since we observe only a very small fraction of the total number of sources, we cannot rule out a possibility that the RV of the entire population of the YSOs of NGC 2024 does follow the gas, with the same mean velocity and velocity dispersion, and that the sources we observe only the tail end of the Gaussian distribution. This would imply that the RV distribution in the cluster has some structure, and that both clusters are expanding. Another possibility is that these objects were dynamically ejected from the cluster.

However, the detected members could also trace the larger population of stars, the RV of which is systematically different from the gas, and that could be a result of gas being accelerated due to the stellar feedback, whereas the stars remain at the original RV of the gas at the time of the formation. The signature of it could potentially be seen in NGC 2023/2024 where the low density gas appears to be red-shifted relative to the two significantly denser clumps. Finally, this could be a signature of cold collapse; recent hydrodynamic simulations of globally gravitationally collapsing clouds demonstrate a similar assymetry between the distributions of young stars and molecular gas can be produced naturally toward massive clusters (Kuznetsova et al., 2017). Ultimately, high resolution infrared spectra (such as the ones APOGEE will be able to provide) would be needed to obtain RV of a significantly larger number of stars embedded within the gas to confirm the degree to which the stars follow the gas.

The observations of other massive clusters, such as the ONC and NGC 2264 (Da Rio et al., 2016; Kounkel et al., 2016a) did reveal that, while the majority of stars do follow the gas, they also contain a significant blueshifted populations. Unfortunately the cause of it is still not entirely clear. Most likely it is a combination of the aforementioned reasons, although previous APOGEE observations of the ONC did mostly rule out extinction as the cause of the discrepancy. Observations of the Orion B put these observations into the perspective as they adds the significant information about the spacial distribution of the YSOs as a function of depth of the clusters.

5.5 Conclusion

We obtained optical high resolution spectra of 295 stars toward the Orion B molecular cloud. Of these sources, 67 can be identified as members of the clusters associated with the cloud on the basis of presence of strong Li I absorption, which ca be used as an indicator of youth in stars later than K4. It is more difficult to distinguish the young stars with earlier spectral types from their more evolved counterparts; therefore there may be some bona fide members that we have not identified as such.

Despite their signatures of youth, we have identified 7 late type sources in the Orion B and in the ONC with somewhat depleted Li I, with $0.1 < W_{LiI} < 0.4$. These sources should not be affected by veiling. Typically stars will achieve this level of depletion at the ages of 5–10 Myr (Baraffe et al., 1998), which is significantly older than the estimated age of the clusters which these stars inhabit, and these sources may not necessarily be members of the clusters. However, it is possible that the accretion processes have accelerated the processing of Li I in these sources (Baraffe et al., 2017). We also identified a number of sources with variable and/or assymetric Hα line. Six of these sources are CTTSs, however, two sources are clearly more evolved and may not be associated with the cloud.

We measured RVs for all the sources. We find that members of NGC 2068 and L1622 tend to have RVs similar to those of the molecular gas. On the other hand, NGC 2024 does show a sizable population of stars that are preferentially blueshifted. Similar kinematics have been observed toward other clusters, such as the ONC and NGC 2264 (Chapter IV). It is still unclear what is the cause of it. Some possibilities include (a) sample bias due to e.g. extinction which prevents us from observing better agreement in RVs, (b) acceleration of the gas through stellar feedback, (c), observing older foreground population of stars that has dissipated their molecular gas and (d) a dynamical signature of cold collapse in the vicinity of a massive cluster.

Soon to be released distance and proper motion solutions by *Gaia* DR2 will further contribute to the interpretation of the stellar dynamics of these clusters. As it is an optical telescope, it will not peer into the depth of the clusters, but it will be able to constrain the dynamics of the other two dimensions of motion of the stars presented in this chapter. Additionally, APOGEE observations as part of the IN-SYNC program for the Orion B molecular cloud will allow RV measurements of much more embedded sources. Together, they will be instrumental in distinguishing between possibilities that may explain kinematic signatures observed in this chapter.

CHAPTER VI

Characterizing the stellar population of NGC 1980

NGC 1980 is a young cluster that is located about 0.5 degrees south of the Orion Nebula Cluster (ONC). Recent studies by Bouy et al. and Pillitteri et al. have suggested that NGC 1980 contains an older population of stars compared to a much younger ONC, and that it belongs to a foreground population that may be located in front of the Orion A molecular gas by as much as 40 pc. In this work we present low-resolution spectra towards 148 young stars found towards the NGC 1980 region. We determine the spectral types of these stars, examine accretion signatures and measure the extinction towards them. We determine that based on these observations, the age of the population of NGC 1980 is indistinguishable from L1641, estimated to be ∼3 Myr, comparable with the study by Fang et al. Published in 2017, AJ, 154, 29.

6.1 Introduction

The Orion A molecular cloud contains the nearest regions of massive star formation. Its most active component is the Orion Nebula Cluster (ONC), which contains a few thousands of young stellar objects (YSOs) ranging in mass from hydrogen burning limit to massive O stars. Extending to the south of the ONC is the L1641 cloud, which contains a somewhat more distributed population of YSOs. NGC 1980 is a cluster found between these two stellar populations. Loosely associated wtih a massive O9 binary star, ι Ori, this cluster could be an important jigsaw puzzle piece in understanding the star formation history of the region.

NGC 1980 is thought to be an older cluster than the population of stars that belong to the ONC (<1–3, Myr Da Rio et al., 2010) and L1641 ($\sim$ 3 Myr, Hsu et al., 2012). Alves & Bouy (2012) have estimated its age to be 4-5 Myr from the lifetime of ι Ori, and later revised the estimate to 5–10 Myr based on the optical colors of the stars in the vicinity of the region (Bouy et al., 2014, hereafter BA14). Pillitteri et al. (2013) performed an X-ray survey of Orion A; they found that towards NGC 1980 there exists an excess of low-extinction sources with $A_V \sim 0.1$ compared to L1641, and that it also contained a one of the largest fraction of YSOs that have already lost their dusty disks, with an age estimate of $\geq$5 Myr. More recently, however, Fang et al. (2017) suggested that the age of NGC 1980 is closer in agreement to that of the ONC, with the median age of 1.8 Myr.

Alves & Bouy (2012) and BA14 have questioned the degree to which NGC 1980 is related to the ONC, claiming it to be a foreground population of stars (by as much as 10–40 pc) located at $\sim$380 pc. Pillitteri et al. (2013) have also argued in support of it, demonstrating that the X-ray luminosities are 0.3±0.1 dex higher in the northern end of L1641 (onto which NGC 1980 is superimposed) compared to the southern end, suggesting that NGC 1980 is 1.4 times closer than the main cloud. However, recently Kounkel et al. (2017c) have found a distance toward the ONC of 388±5 pc using stellar parallaxes of non-thermally emitting YSOs; this is a revision to the previously commonly accepted distance of 414± 7 pc (Menten et al., 2007). In addition, Kounkel et al. (2017c) found the distance towards the southern end of L1641 of 428±10 pc; the difference in X-ray luminosities is most likely caused solely due to the spatial orientation of the cloud. Additionally, radial velocity monitoring of the ONC by Kounkel et al. (2016a) and Da Rio et al. (2016) showed that the radial velocities of the stars towards NGC 1980 are indistinguishable from those of the molecular cloud;

in fact, this agreement is better than towards any other region in the ONC. A possible argument in favor of NGC 1980 belonging to a foreground population may persist due to the lack of any reflection nebulosity towards ι Ori. However, the degree to which the the ι Ori is related to the cluster is unclear, particularly since this was involved in a dynamical ejection event (de Zeeuw et al., 2001; Gualandris et al., 2004). With these updated distances and radial velocity measurements, the nature of NGC 1980 as a foreground cluster falls into a considerable doubt.

NGC 1980 has been left out in many surveys of star formation in Orion that focused on the properties of individual stars. It is located southward of the Trapezium cluster, the heart of the star formation in the ONC, and it is outside of the field-of-view of the studies by Hillenbrand (1997) and Da Rio et al. (2010). On the other hand, it falls northward of the region covered by the surveys of L1641 filament (Fang et al., 2009; Hsu et al., 2012, 2013). Similarly to the work by Fang et al. (2017), in this chapter we seek to bridge the gap between these works. We present an analysis of the low resolution optical spectra of stars identified by BA14 towards this cluster. We asses the youth and determine the spectral types of these stars, as well as measure the equivalent width of Hα line (Section 6.2). On the basis of these measurements, we classify these as sources as Classical T Tauri Stars (CTTS) and Weak-lined T Tauri Stars (WTTS) based on the definitions from White & Basri (2003). Through analyzing the ratio of CTTS to WTTS, we compare the age of NGC 1980 to that of the ONC and L1641 to confirm its older age (Section 6.3.1). Finally, we estimate the extinction to these stars (Section 6.3.2)

6.2 Data

We conducted observations using the IMACS spectrograph on the Magellan Baade telescope (Bigelow & Dressler, 2003). Observations were done using the $f/2$ camera with the 300 line grism at a blaze angle of 17.5° and slit width of 0.6". In this configuration, the typical resolution is 4 Å, and the spectral coverage is approximately 4000–9000 Å. However, this coverage may be truncated for the stars close to the edge of the field. Additionally there is a chip gap $\sim$ 100Å in width that tends to fall in a random place along the spectrum depending on the position of the star within the field of view.

We observed 4 fields towards NGC 1980 using the multi-slit mode on January 7, 2016. We targeted 280 sources identified by BA14 with r <21 mag, of which 212 sources had probability of membership (P) greater than 50%. The exposure time was 5×10 min per field for the first three fields, and the last field had the exposure time of 8×10 min. The weather conditions deteriorated rapidly over the course of the night, therefore, while the first field had the full sensitivity, the last field, even with the increased exposure time, yielded little in terms of the number of sources detected (Figure 6.1).

Partially because of this, we have detected only 148 sources (Figure 6.2). However, the catalog of BA14 contains many spurious sources. Out of 165 sources that were targeted in the first two fields (of which 134 had $P > 50$), only 103 (97 with $P > 50$) have been detected. Similar trends persist in the other two fields within the sample limited to the detectable magnitudes. More than 20% of sources with $P > 50$, and the vast majority of sources with $P < 50$ do not appear to be associated with physical objects, despite falling into the typically detectable magnitude range. As the catalog of BA14 was compiled from individual frames as opposed to the stacked images, many detections of cross-talks, saturation trails, as well as ghosts and cosmic rays may be included in the final catalog (Bouy, private communication).

Several sources also appear to be duplicated in the catalog (some are listed as separate sources up to 3 times with the positional offset of up to 4”, Figure 6.3). To correct the astrometry to remove this offset, we cross-matched the detected sources with the *Gaia* DR1 source list (Gaia Collaboration et al., 2016). All but three sources

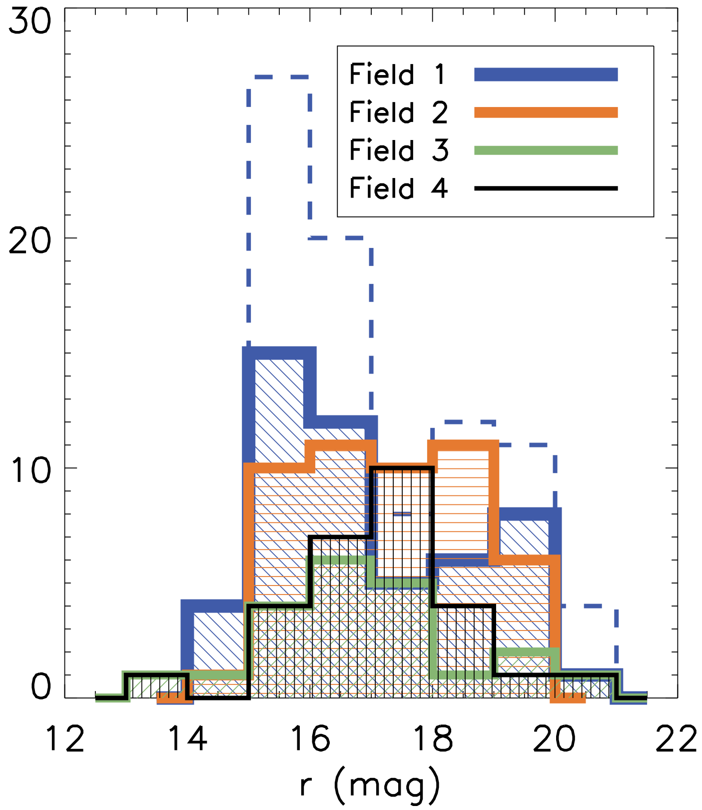

Figure 6.1 The distribution of the r magnitudes from BA14 for the detected sources with SNR>10 for each field. The dashed line shows the distribution of the total number of sources that were in the field 1.

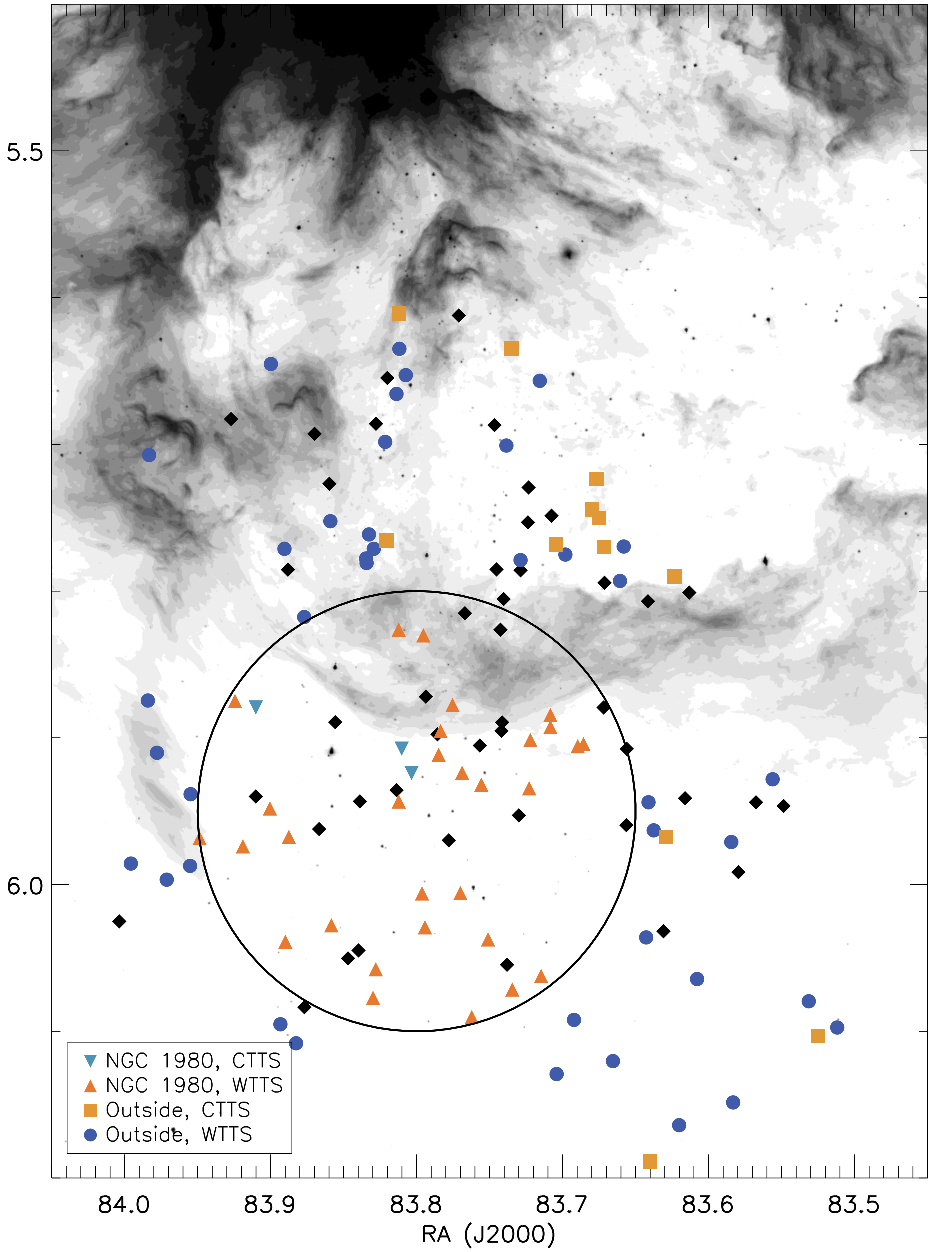

Figure 6.2 Sources observed by this program. Sources that fall into the cirle are identified as members of the cluster (see Section 6.3.1 for discussion). Black diamonds show the sources that are not part of the primary sample. The large circle is centered at $\alpha = 83.8°, \delta = -5.95°$, center of NGC 1980 as defined by BA14, 0.15° in radius. The greyscale background is 8 μm *Spitzer* map from Megeath et al. (2012).

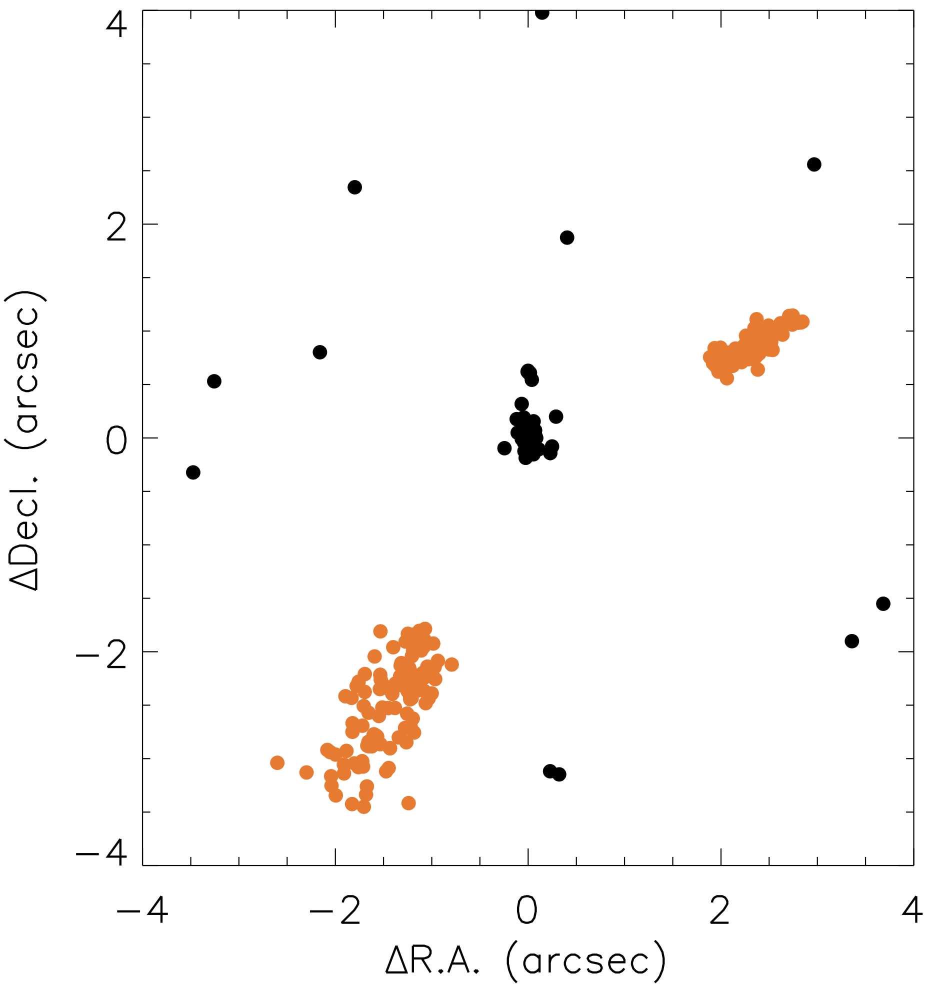

Figure 6.3 Comparison of the astrometry between Gaia DR1 for the sources observed by this program, and all the sources that match its position in BA14. The sources concentrated near the center have accurate astrometry, and the two groups shown in orange consist mostly of duplicates.

were matched with the DR1 list; for those that were not we used the astrometry from the initial Gaia source List (Smart & Nicastro, 2014). We also re-cross-matched the sources with 2MASS photometry (Cutri et al., 2003), as the positional offset has put many of the sources in BA14 outside of the cross-match radius, therefore, not all sources have their counterpart identified in that catalog. In addition, sources in BA14 that do have JHK photometry listed appear to have a systematic color offset from the 2MASS photometry.

The IMACS spectra were reduced using the COSMOS pipeline[1] following the standard prescription. The final data product does have some issues with the poor subtraction of the nebular emission lines, particularly Hα (6563Å). In general, this emission originates from across the entire slit, and it is modeled and subtracted in a similar manner to the sky lines for the vast majority of sources. However, in some cases the nebular emission varies strongly across the slit, making subtraction difficult. This issue has a stronger effect on very low signal-to-noise (SNR) sources. We measured the equivalent width of Hα (W_{H_α}) in all spectra with an overall SNR>5. We visually examined the sky subtracted spectra and flagged the sources with poor subtraction, such as in cases where the flux of Hα does not appear centered and/or confined to the star; in these cases we do not quote W_{H_α}. To test nebular subtraction and to provide an estimate of the uncertainties of W_{H_α} we add up all flux along the slit outside of the source (normalizing it by the pixel count) to the flux of the source itself and measure W_{H_α} again. We do it in two different ways, by measuring a simple total of the flux as is, and by measuring a total of the absolute value of the flux, because due to variable nebular emission some of it may be oversubtracted. The uncertainties we report are the average difference between W_{H_α} we measure and W_{H_α} with the residuals added. Examples of the Hα line profiles for low, medium, and high SNR data is shown in Figure 6.4.

The spectra were analyzed using SPTCLASS[2] (Hernández et al., 2004) in order to determine the spectral types of the detected stars. This program utilizes three different schemas optimized for three different ranges of stellar masses (K5 and later, late F to early K, and F5 and earlier) based on examining a number of spectral features. For late type stars (all the sources in this chapter were identified as such) the examined features are TiO (λ_{cen}=4775, 4975, 5225, 5475, 5600, 5950, 6255, 6800, 7100, 7150Å), and VO (λ_{cen}=7460, 7940, 7840, 8500, 8675, 8880Å) lines. We report

---

[1] `http://code.obs.carnegiescience.edu/cosmos`

[2] `http://www.cida.gob.ve/~hernandj/SPTclass/sptclass.html`

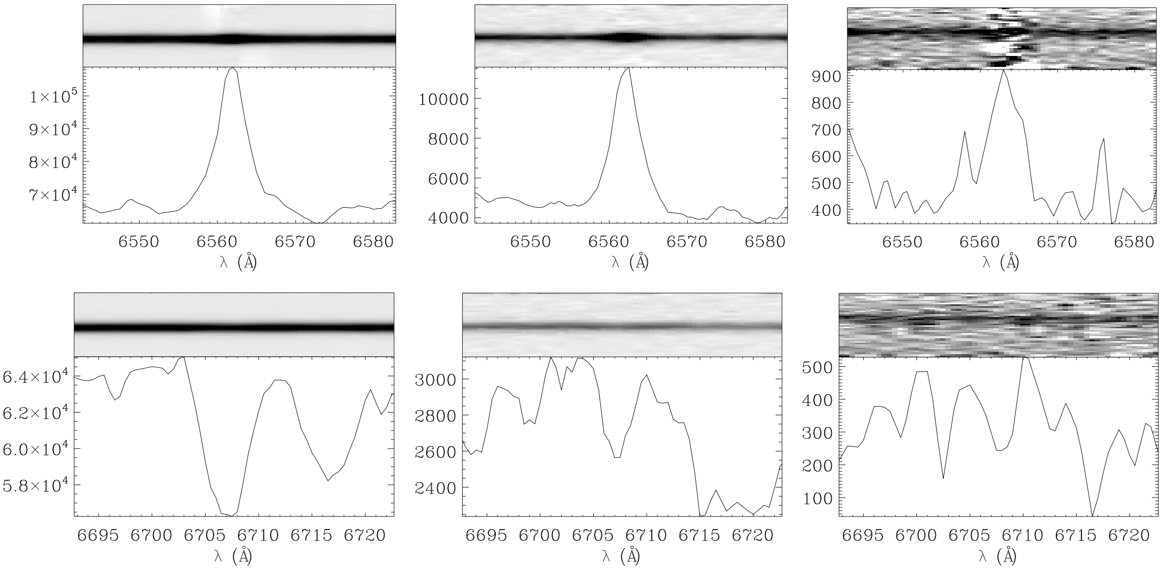

Figure 6.4 Examples of high (BA 349989), medium (BA 346977), and low (373101) SNR spectra, showing Hα and Li I lines.

only on those spectral types that were obtained using at least three features in Table 6.1.

Spectra for some stars have been analyzed in previous works. Spectral types for 25 stars that are in common with Hsu et al. (2012) and 76 stars in common with Fang et al. (2017) show a good agreement within the uncertainties of each survey (usually within one subclass). Same can be said for 13 stars reported on by Da Rio et al. (2010), although due to their use of measurements compiled from various publications utilizing different methodologies, some additional scatter persists. Spectral types for 13 sources that are in common with Rebull (2001) show the largest scatter in the agreement; however, they are typically consistent with each other within the uncertainties (Figure 6.5). Fifty stars presented in this work do not have pre-existing spectral classifications. We also compare the spectral types we measure to the effective temperature from Da Rio et al. (2016). Assuming typical spectral type to temperature conversions (e.g Pecaut & Mamajek, 2013), they also show relatively good agreement with each other.

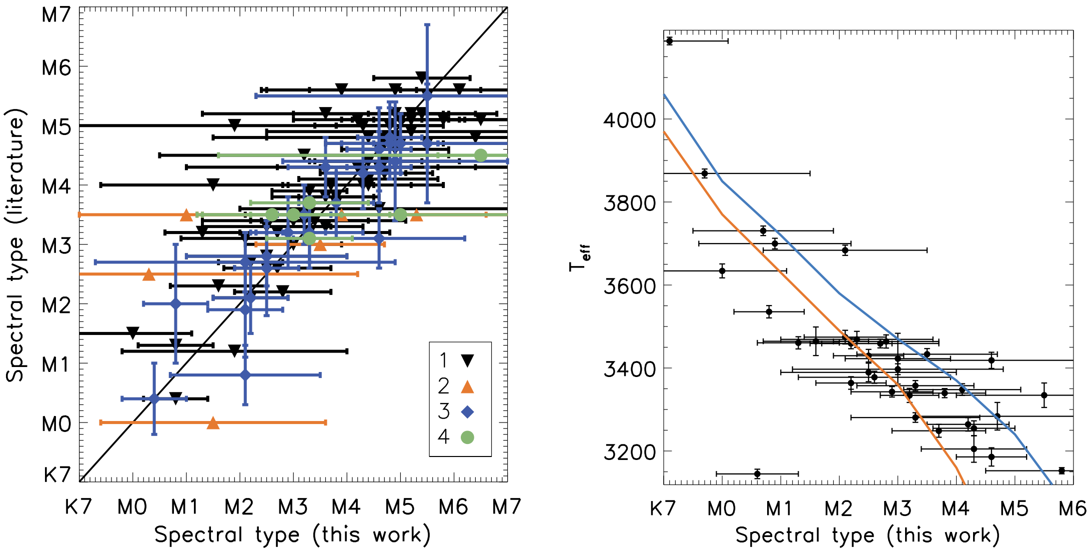

Figure 6.5 Left panel: comparison of the measured spectral types to those that are available in literature. 1: Fang et al. (2017), 3: Rebull et al. (2000) and Rebull (2001), 3: Hsu et al. (2012), 4: Hillenbrand (1997) and Da Rio et al. (2010). Right panel: comparison of the measured spectral types with the effective temperatures from Da Rio et al. (2016). Only sources with the spectral type measured better than two subclasses are included. The orange line shows spectral type to temperature conversion for young stars from Pecaut & Mamajek (2013), blue line from Kenyon & Hartmann (1995).

We also measured the equivalent widths of Li I line (6707Å, W_{Li}), as it can be used as an indicator of youth and membership of star-forming regions (Briceno et al., 1997). However, given the fact that it is a weak absorption line, due to the poor observing conditions in many sources the SNR was too small for a confident detection. In these cases the equivalent widths that can be measured from the random noise can be equivalent or greater than W_{Li}, which is typically expected to be ~0.5Å in the young stars. Therefore, we include the upper limits for sources where Li I line was not detected. We define the primary sample of the members consisting of sources with a confident Li I detection with $W_{Li} > 0.1$ (62 stars), as well as the sources that have been previously identified as YSOs in other studies, have SNR$>$ 5, but it is not sufficiently high enough for a confident Li I detection (43 stars). The remaining 10 sources with SNR$>$ 5 are not included in the list of members; however, neither can they be conclusively rejected as such. Examples of Li I line profiles for low, medium, and high SNR data are shown in Figure 6.4.

6.3 Discussion

6.3.1 Accretion

We apply the criteria developed by White & Basri (2003) to separate strongly accreting CTTSs from the WTTSs through analyzing W_{H_α} depending on the spectral type (Figure 6.6). Out of 85 stars in our total sample with measured W_{H_α}, 15 are CTTS, for a CTTS fraction (defined as $N_{CTTS}/N_{CTTS+WTTS}$ of 0.18).

Pillitteri et al. (2013) have argued that NGC 1980 extends by $> 1°$ on the sky, but BA14 confine it to a much more limited area, possibly due to the difference in the methods, since BA14 rely on the background cloud to identify the sources. Nonetheless, we use their density map and define the sources within 0.15° from the center of the cluster ($\alpha = 83.8°, \delta = -5.95°$ defined by BA14) as members, and

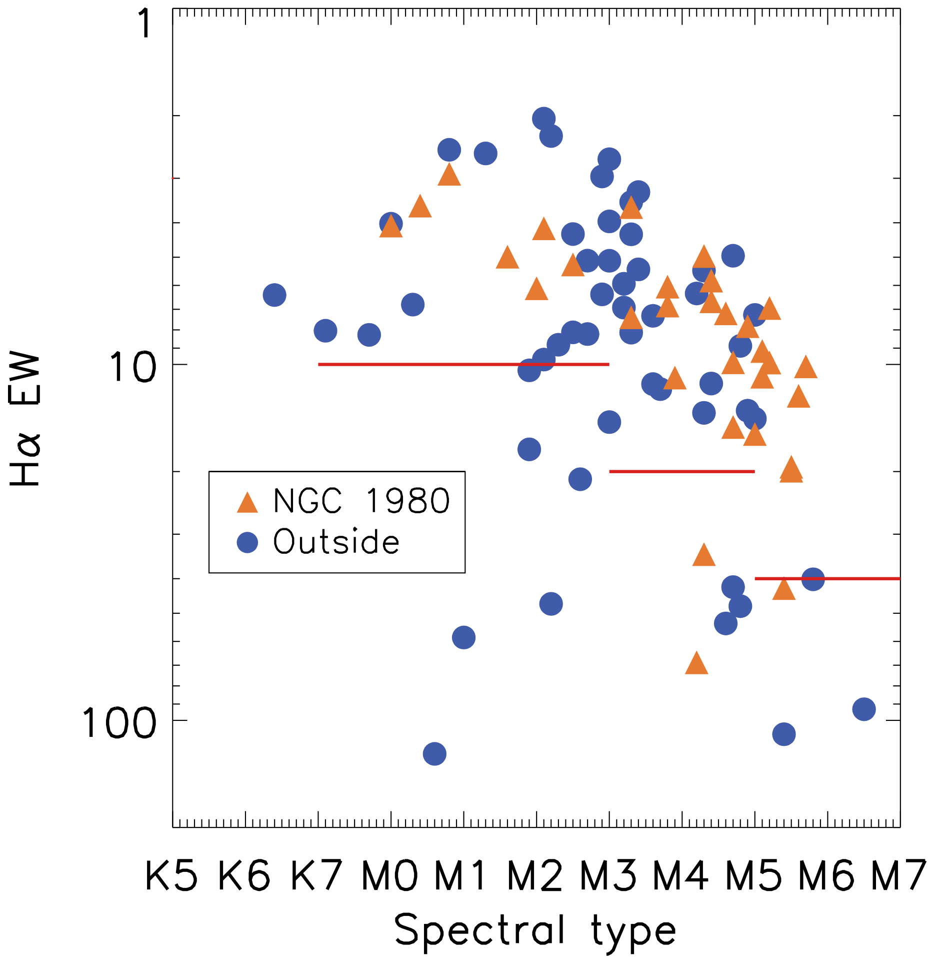

Figure 6.6 Hα equivalent width as a function of spectral type. Horizontal lines show the distinction between CTTS and WTTS objects based on the criteria by White & Basri (2003).

the sources outside of that as those that are found on the periphery. There may be bona fide members of NGC 1980 outside of this boundary as well. Nonetheless, this boundary can be used to compare the population that exists at the center of the cluster to its surroundings. At the distance of 388 pc (Kounkel et al., 2017c) the cluster diameter of 0.3° to a physical size of 2 pc. We find that within the cluster the CTTS fraction drops to only 0.09, where only three stars out of 33 show strong accretion signatures. On the other hand, outside of the cluster the CTTS fraction becomes 0.23 (12 out of 52 stars are accreting), which is dominated by the sources north of the cluster (0.27, 9 out of 33).

Fang et al. (2017) argue that the median age of NGC 1980 is 1.8 Myr. Therefore the question arises, how significant is the difference that we observe in the CTTS fraction between the two populations. The sample in Fang et al. (2017) is considerably larger, and it covers a bigger area of the ONC to the north, and L1641 to the south, in $-7^\circ < \delta < -4^\circ$ range, excluding the Trapezium cluster. The observed targets were also selected from BA14 catalog, however, there is not a direct 1–1 overlap between the surveys. In their sample there does appear to be little variation in the CTTS fraction of ~ 0.15 throughout the observed regions, whether it is inside NGC 1980 or outside of it. A possible exception to this is NGC 1981 region, where the fraction does drop to ~0.09. Fang et al. (2017) do argue, that BA14 survey is biased against the sources with the hot inner disks; therefore the true CTTS fraction should be much higher than what can be observed.

To minimize this bias, we search for sources with Hα observations in other surveys that fall into the NGC 1980 region. We include sources classified by Hsu et al. (2012), Fűrész et al. (2008), as well as analyze the Hα measurements by Kounkel et al. (2016a). In all the studies, we could identify 107 YSOs in the NGC 1980 region with Hα line observed, out of which 31 are CTTS, for the total CTTS fraction of 0.29 ± 0.05, assuming Gaussian statistics. 104 of these sources can be classified on the basis of the presence of a disk as indicated by infrared excesses detected with the IRAC camera on board the Spitzer Space Telescope (Megeath et al., 2012). Out of 73 WTTSs, only 7 still have a disk, and out of 31 CTTSs, 7 sources do not have infrared excess which would be indicative of a full disk. The disk fraction for these sources is 0.30±0.05, very similar to what is found by Fang et al. (2017) and Pillitteri et al. (2013).

6.3.2 Extinction

We estimated the extinction towards the sources in the survey via their 2MASS photometry from comparing the J-H and H-K colors to the intrinsic colors of young (5-30 Myr) stars from Pecaut & Mamajek (2013). We adopt the relations of A_J:A_K=2.65, A_J:A_K=1.55 (Megeath et al., 2012), and A_K:A_V=0.112 (Cardelli et al., 1989). Stars with very low extinctions may result in negative A_V measurements, in those cases A_V is set to 0. We report on the average A_V measured from both J-H and H-K colors for each star in Table 6.1 (Figure 6.7). The typical error due to an uncertainty in spectral type is $A_V \sim 0.1$. We have also attempted to measure A_V through artificially de-redenning the spectra (assuming the standard extinction law R_V=3.1, Cardelli et al., 1989) until the slope matches that of the template spectra of the corresponding spectral type from the X-Shooter Spectral Library (Chen et al., 2014). While this method does produce mostly comparable A_V measurements, they are also significantly more uncertain.

In general approximately half of all sources do have very low extinction with $A_V \sim 0$. This is true of almost all sources identified as members of NGC 1980, with only six sources (out of 39) with $A_V > 0.1$, and all with $A_V < 1.0$. The degree of extinction towards the cluster comparable to what has been found by Pillitteri et al. (2013) through X-ray observations of the region. On the periphery of the cluster, 32 out of 58 sources have $A_V > 0.1$, 11 of which have $A_V > 1.0$. The Kolmogorov-

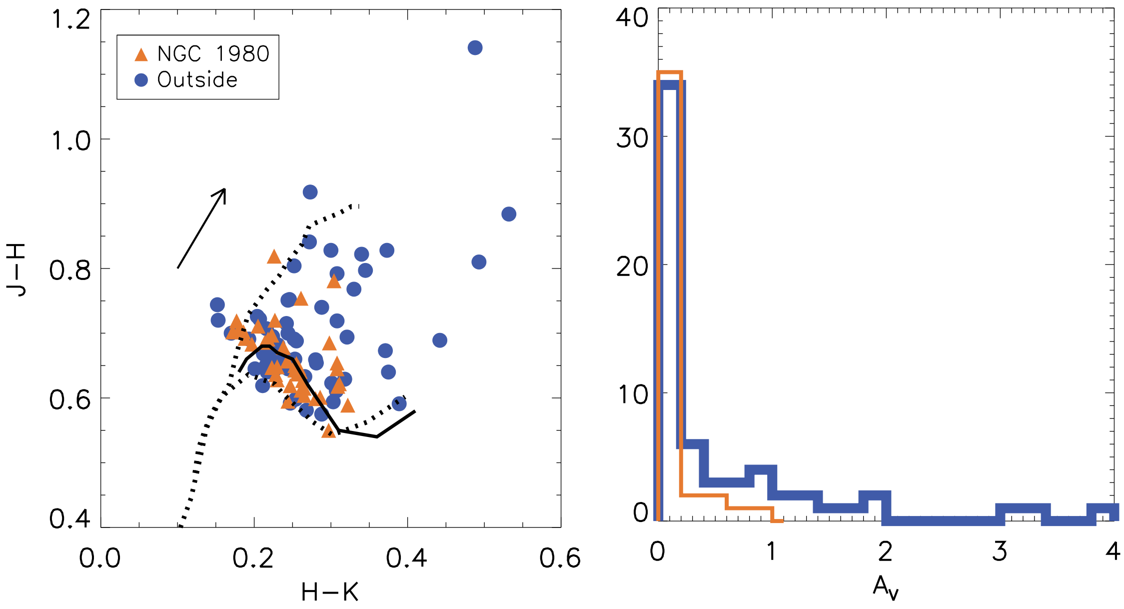

Figure 6.7 Left: 2MASS J-H vs. H-K color-color diagram. Black dashed lines show typical colors for dwarfs (lower line) and giants (upper line) from Bessell & Brett (1988) with transformations from Carpenter (2001). Solid line showes the intrinsic colors of young stars from Pecaut & Mamajek (2013). Black arrow corresponds to the extinction of 1 A_V (Megeath et al., 2012). Left: distribution of A_V measured towards the sources in the survey. Orange line corresponds to the sources within NGC 1980, blue to the sources located on the periphery.

Table 6.1. Sources observed towards NGC 1980 with IMACS.

BA14 #	R.A. J2000.0	Decl. J2000.0	SPType	W_{H_α} [a] Å	W_{Li} [a] Å	SNR	Accr.	Reference [b]	A_V mag.	Field
329411	05:34:02.85	-06:05:50.7	M4.8±0.9	-8.9± 0.2	0.5	59.4	WTTS	1 3 7	0.2	1
331374	05:34:05.99	-06:06:11.7	M4.6±0.6	-53.4± 2.7	0.5	66.2	CTTS	1 3 5 7	0.0	1
332392	05:34:07.52	-06:04:46.4	M2.5±0.6	-4.3± 0.2	0.4	170.5	WTTS	1 3 7	0.0	1
340962	05:34:19.95	-06:08:54.6	M3.3±0.5	-3.5± 0.2	0.5	116.9	WTTS	1 3	0.0	1
341157	05:34:20.26	-05:58:15.6	M4.7±1.4	-5.0± 1.2	< 0.2	29.0	WTTS	4 7	0.0	1
344878	05:34:25.89	-06:03:51.9	M5.0±0.5	-14.2± 0.6	[c]	75.0	WTTS	3 7	0.1	1
346977	05:34:28.84	-06:09:50.4	M5.0±0.7	-7.3± 0.4	0.5	35.3	WTTS	1	0.8	1
348520	05:34:30.97	-05:58:03.6	M6.5±1.3	-93.1±33.2	< 1.3	5.6	CTTS	56	0.0	1
348805	05:34:31.41	-06:01:54.7	M7.5±5.1	—	—	4.0	—		—	1
349989	05:34:33.02	-05:57:47.0	M0.0±0.6	-4.0± 1.1	0.6	172.8	WTTS	12 4 6	1.5	1

Only a portion of the table is show here. The full table is available on-line at
`http://iopscience.iop.org/1538-3881/154/1/29/suppdata/ajaa74dft1_mrt.txt`

[a] Reported only for sources with SNR>5

[b] 1: This work, 2: Pillitteri et al. (2013), 3: Hsu et al. (2012), 4: Fűrész et al. (2008), 5: Megeath et al. (2012), 6: Morales-Calderón et al. (2012), 7: Fang et al. (2017)

[c] Line has either fallen onto the chip gap or off the edge of the field

[d] Poor nebular line subtraction

Smirnov test shows that the two populations are different by 3.5σ.

Most of the sources with very high extinction in our survey originate north of the NGC 1980 cluster, towards the ONC. The A_V distribution of these northernmost sources does not mirror that measured towards the ONC by Da Rio et al. (2010), however, the sample selection of the two surveys is very different and our optical study is biased against highly extincted sources. However, in general our results are consistent with what has been observed in the other works. The extinction in the Orion A molecular cloud is low in the vicinity of the NGC 1980, it rises sharply towards the ONC, and gradually increases southward along the L1641 filament (Da Rio et al., 2010; Hsu et al., 2012; Pillitteri et al., 2013; Fang et al., 2017).

6.3.3 Li I distribution

As young stars evolve, eventually they will begin depleting Li, and more massive stars will deplete it faster. Therefore, in some cases the distribution of W_{Li} as a function of temperature can be used as an additional information from which age can

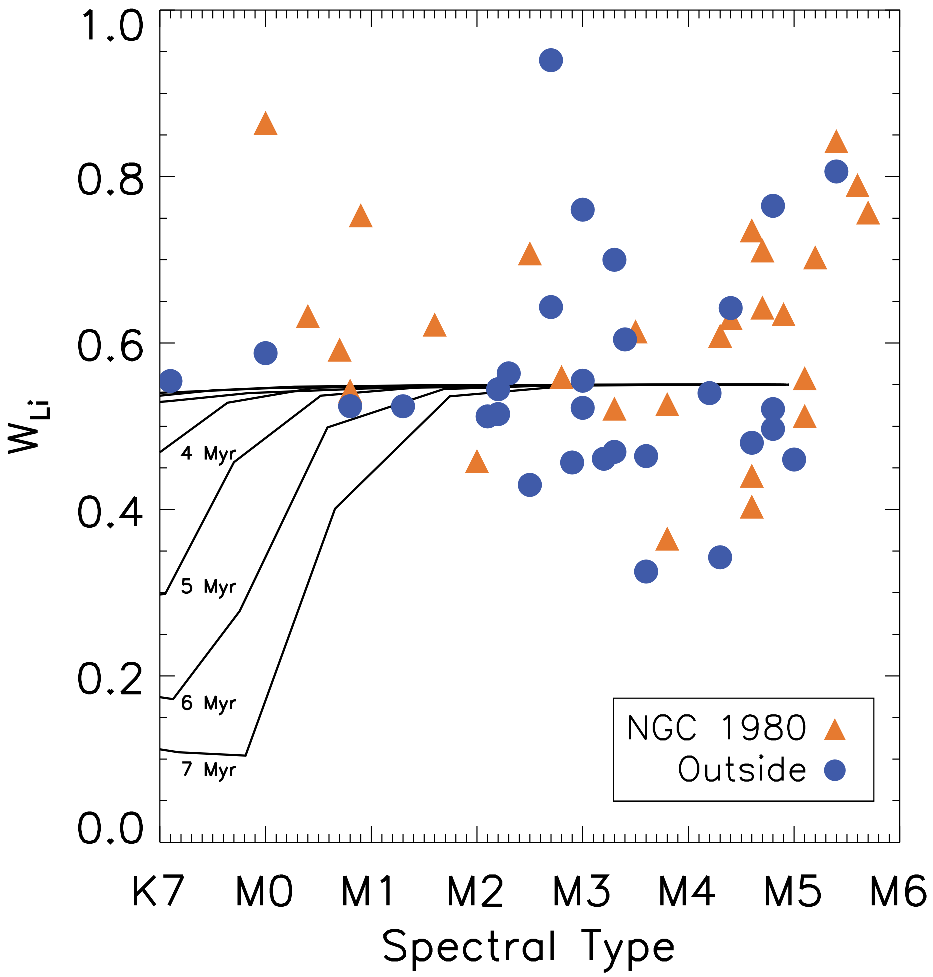

Figure 6.8 Distribution of W_{Li} as a function of spectral type. Black lines show the evolution of W_{Li} from Baraffe et al. (2015) tracks, from 1 to 7 Myr, converted using transformations from Pecaut & Mamajek (2013). The typical uncertainty in measured W_{Li} is ~0.1Å.

be inferred (e.g. Jeffries et al., 2017). We compare the measured W_{Li} for the sources with firm Li I detections to the expected Li I distribution from the evolutionary tracks from Baraffe et al. (2015). Nearly all of our sample consists of M type stars; these sources do not begin processing Li I until 5–10 Myr. From this comparison, we can rule out ages older than about 6 Myr for the sources found towards NGC 1980, however, this comparison cannot help to distinguish ages younger than that (Figure 6.8). A similar distribution of W_{Li} is found in the surveys by Hsu et al. (2012) and Fang et al. (2017) throughout the ONC and L1641.

6.4 Conclusion

We obtained low-resolution spectra from IMACS towards 148 sources towards NGC 1980, we determined spectral types of these sources, and determined whether or not they can be considered as YSOs on the basis of Li I absorption. Most sources have $A_V \sim 0$, in agreement with what have been found by Pillitteri et al. (2013) and BA14. We determined whether or not these sources have Hα excess due to the ongoing accretion, and searched for sources that fall into the region identified as NGC 1980 with Hα measurements in the previous works. We found that 31 out of 107 stars in the cluster can be identified as accretors, for a CTTS fraction of 0.29±0.05.

As the population ages, the CTTS fraction decreases (e.g. Mamajek, 2009; Briceño et al., 2017). Within the ONC, containing large population that spans in age between $< 1 - 3$ Myr, the CTTS fraction is ∼0.5 (Fűrész et al., 2008; Da Rio et al., 2009). Within the outlying L1641 cloud it decreases to is 0.35 (∼3 Myr) (Hsu et al., 2012). Within the Ori OB1b sub-association (4 Myr), CTTS fraction is 0.13, and only 0.06% towards 25 Ori (8 Myr) comoving group. (Briceño et al., 2007).

From this, it does appear that the population of NGC 1980 is indistinguishable from the population of L1641. This is similar to what has been observed by Fang et al. (2017). However, the CTTS fraction is considerably lower in this cluster than in the ONC itself. It is possible that the sample is highly incomplete. Given that all classifications were conducted from an optical surveys, there exists an inherent bias against deeply embedded and accreting sources. On the other hand, WTTSs typically have a much smaller IR excess, making them harder to identify as targets when planning a survey. Since the extinction in the vicinity of NGC 1980 is much lower than in the ONC, it would be unlikely for there to be a larger population of highly reddened undetected sources to be present in NGC 1980 over the ONC. Unless the CTTS fraction is significantly lower in the ONC due to a presence of previously unanalyzed WTTSs, NGC 1980 is probably somewhat older. It is unlikely to be as old as 5 Myr (the age that was previously estimated by BA14). We estimate its age to be ∼3 Myr, similar to L1641. A possible reason why Fang et al. (2017) do not see the difference between the ONC and NGC 1980 is because the sample for which they determined the ages is highly incomplete near the ONC (Trapezium and OMC 2/3) region, the youngest and most deeply embedded population. And, with the updated distances from Kounkel et al. (2017c), the ages measured by Fang et al. (2017) would be ∼20% older, which would also help in reconciling some of the differences.

As this work does not explicitly measure distances to the stellar populations, in this work we cannot conclusively confirm or disprove whether NGC 1980 is in the foreground of the ONC or not. The reason for low extinction near the region could be that cluster is located on the outer layer of the molecular cloud, in which case it would technically not be incorrect to refer to the cluster as a foreground population by the slimmest of margins. However, a more likely explanation would be that the stellar winds have cleared out the molecular gas, there could have been less gas near the cluster than there was near the ONC from the very beginning. Kounkel et al. (2017c) have shown that the ONC is found at the same distance that was suggested by BA14 for NGC 1980. Kounkel et al. (2017c) did not detect any of the stars towards NGC 1980 in their sample, therefore they were not able to estimate stellar parallax towards the region. The distance found by BA14 was found photometrically, therefore it has significantly larger uncertainty in its value.

Until the uncertainties in the distance are smaller than any distance offsets, it is not entirely meaningful to discuss substructure, as well as what is and what is not in the foreground. The future data releases from *Gaia* space telescope should would be instrumental in measuring the three-dimensional relations and intercluster kinematics in the region, and it should resolve this matter once and for all. Its observations should shed light on the initial conditions that have led to the current configurations of these star forming regions.

CHAPTER VII

Conclusions

7.1 Toward a six-dimensional understanding of the Orion Complex

In my thesis I used radial velocities and VLBI measurements of parallaxes and proper motions, along with radial velocity measurements from high resolution optical spectra to constrain membership and begin determining the spatial and kinematic structure of the Orion complex. The results provide a preliminary view of Orion's structure with the ultimate goal of understanding the star formation history and processes of star and cluster formation.

Chapters II and III were focused on measuring stellar parallax and proper motions towards non-thermally radio emitting YSOs. In Chapter II I surveyed the Orion Complex with VLA and I identified 374 radio sources. I then targeted these sources with VLBA to obtain their astrometry over the period of two years. In total, I obtained astrometric solutions for 27 YSOs. From these observations, I was able to measure average distances of 388±5 pc toward the ONC, 428±10 pc toward the southern portion of L1641, 388±10 pc toward NGC 2068, and roughly ∼420 pc toward NGC 2024, providing the first 3d view of the Orion Complex. My initial results suggest that the depth of the Orion complex is comparable to the lateral extent projected upon the sky; while not surprising, the results emphasize the importance of determining 3D and 6D structure for understanding the dynamical state of the star-forming regions

Unfortunately, the limited sample size as well as a contamination of the orbital motions of wide binaries to the true proper motions of their barycenter made it difficult to conclusively analyze the intercluster proper motions beyond a tenuous examination. However, in a few cases the proper motions of a few individual stars indicate high velocity ejection $\sim 10^5$ years ago, probably as a result of close binary or triple system interactions in the core of the ONC. Additionally, a number of stars have been identified as binaries or higher order multiple star systems.For two sources that had a sufficient number of astrometric observations, I was able to fit the orbital parameters and constrain their masses.

In chapters IV and V I analyzed the stellar RV distributions. Chapter IV presented multi-epoch high resolution optical spectra of the ONC and NGC 2264. From these observations I identified spectroscopic binaries and determined that the multiplicity function in these clusters (over the parameter space to which these observations were sensitive) is comparable to that of the nearby field stars. I also compared the distribution of the stellar RVs to those of the molecular gas, in a manner similar to Tobin et al. (2009, 2015). I found the global agreement between them to be much better than what was previously estimated; however, in the vicinity of the Trapezium and OMC 2/3 region, as well as near the Cone Nebula in NGC 2264, the distributions of stellar and gas RVs appear to be decoupled from each other, with the stellar RVs being preferentially blueshifted. In chapter V I extended this analysis to the clusters in the Orion B molecular cloud. Similarly I found that while the stellar RVs follow the molecular gas in L1622 and NGC 2068, this does not appear to be the case in NGC 2024, although, given that Orion B suffers from a high degree of extinction, the sample size is limited.

There are multiple possible explanations for this asymmetry. It is possible that extinction masks the full extent of stellar RVs, preventing us from observing the redshifted tail of the distribution, which could be behind the cloud and thus heavily extincted, although Da Rio et al. (2016) have ruled this out for the ONC. It is possible that the feedback from the first formed stars in a cluster accelerate the gas away from themselves. It is possible that several clusters with distinct kinematics are projected on top of each other, or this could be a potential signature of a cold collapse. With only a single dimension of motion available, it is still difficult to conclusively distinguish between these models.

Finally, I examined the nature of NGC 1980, a cluster that is thought to be older (∼5 Myr) and be positioned in a foreground of the ONC (∼380 pc Bouy et al., 2014). With the revised distance to the ONC of 388 pc, compared to the previously accepted value of 414 pc (Menten et al., 2007), the differences in distance between these regions become statistically insignificant. The stellar RV distribution over the volume of space occupied by NGC 1980 is indistinguishable from that of the molecular gas of the Orion A. In Chapter VI I examined the age of stars in the region and, although NGC 1980 does appear to be somewhat older than the Trapezium cluster, it has a comparable age to the stellar population of L1641, at ~ 3 Myr, which is not quite as old as the previous estimates.

7.2 Ongoing work

Some effort has been made regarding characterization of some of the sources observed with VLA presented in Chapter II. I used FIRE (Folded-port InfRed Echellette) mounted on the Magellan Baade Telescope to obtain infrared spectra of 40 YSOs, targeting primarily those that lack optical emission, with the purpose of determining their spectral types. The data have been fully reduced and analyzed, although the paper regarding these observations has not yet been written.

One of the sources observed towards the ONC in the VLBA survey in Chapter III was identified as having peculiar morphology. Upon later examination, it was determined that this morphology could be caused by scattering from plasma that originated from the wind shocks from θ^1 Ori C (Güdel et al., 2008). We observed this source with SMA, and recently follow up observations of this source with VLBA have been obtained to confirm scattering in this region. If confirmed, the ONC would be the third strongest region that is capable of producing interstellar scattering.

Since Chapter III has been originally published, follow up VLBA observations have continued with the main goal of obtaining a sufficient number of epochs in order to fit orbital motion of multiple stars. One additional epoch has been observed in L1641 due to previous uncertainty due to systematic offsets; three epochs have been observed in the ONC, NGC 2068, NGC 2024, and σ Ori.

The averages of the distances have changed little with respect to the fit quality of stars that can be fit as single stars with these additional epochs. The sources that have been previously identified as likely binary stars have been confirmed as such with additional epochs. The fits for binaries have substantially improved, although in some cases they are still somewhat tenuous due to insufficient data. I will defer a full discussion of the orbital parameters to the upcoming paper to be written after all observations will be concluded.

7.3 *Gaia*

On September 13, 2016, the first *Gaia* data release became available (DR1). This data release provided initial single-epoch astrometry for $\sim 1.15 \times 10^9$ sources. Due to the limited period of observations, DR1 was unable to decisively differentiate between contribution between parallax and proper motions for the vast majority of sources; this will be rectified in Data Release 2 (DR2). The degeneracy can be presently lifted only for those sources that have independent astrometry measurement that can extend the temporal baseline of monitoring. In particular, full astrometric solution was performed for objects that have been observed previously by *Hipparcos–Tycho* mission two decades earlier. *Tycho-Gaia* Astrometric Solution (TGAS) was released alongside DR1.

TGAS has many limitations. Because *Hipparcos* had both poor sensitivity and resolution compared to *Gaia*, TGAS consists only of $\sim 2 \times 10^6$ sources brighter than $G< 14$. The typical uncertainty of parallax for these sources is 0.32 mas, and the typical uncertainty in proper motions is 1.32 mas (Gaia Collaboration et al., 2016). For a small subset ($\sim 9 \times 10^5$ sources) of TGAS that includes *Hipparcos*-only sources, typical uncertainties in proper motions are significantly improved, to just 0.07 mas, although uncertainties in parallax remain to be similar, at 0.28 mas. In addition to this, systematic color-dependent and spatially-correlated zero point offsets in parallax on the order of 0.3 mas may also be present. Systematic offsets in proper motions cannot be determined due to a lack of previous large-scale surveys with a comparable level of precision. DR2 is expected to improve significantly on both the quoted and systematic uncertainties in all variables.

A number of papers have already have been published comparing parallaxes from TGAS to those obtained by other means (e.g., Stassun & Torres, 2016; Jao et al., 2016; Davies et al., 2017; Casertano et al., 2017; Gaia Collaboration et al., 2017; Yıldız et al., 2017). In general, there appears to be a good agreement between them, although there may be some evidence for the stronger systematic offset in parallax for the nearby stars compared to those that are further away, although this offset could be due to differences in sample selections and the way the comparison is performed. As was previously discussed in Chapter I, VLBI radio astrometric observations provide the best benchmark for the comparison.

At the present time, only 8 stars that have VLBI astrometry are part of TGAS. Two of these stars have been observed in Orion (Chapter III), five are in Taurus

(Torres et al., 2007, 2009, Galli et al., in prep.), and one star is in Pleiades (Melis et al., 2014). Similar to the other surveys, there appears to be an good agreement between the solutions found by *Gaia* and by VLBA (Figure 7.1). Only one source deviates from the line of identity, and this source is T Tauri, a triple star system. TGAS did not have a prescription for treating multiple stars, it will not be performed until DR3. Similarly, VLBA 145 is also a binary system with an intermediate period. A full orbital fit based on VLBA astrometry is still impossible hence the uncertainty in its parallax remains large; however VLBA and *Gaia* observations of if were obtained over a comparable period of time, therefore they obtain a comparable solution.

With a rather small sample size and large uncertainties of TGAS, the comparison of the solutions with those obtained from VLBA astrometry is presently not very meaningful. DR2 is scheduled to be released in April 2018. The uncertainties of that catalog should become comparable to those obtained by VLBA. Moreover, based on the contents of DR1, we expect to be able to perform a direct comparison of 5-dimensional astrometric solutions of over 40 sources.

Similarly, it may be somewhat premature to use the results of TGAS for all but the most basic analysis of distances and proper motions for a complex such as Orion, or for those regions that are even further away. Some attempts have been made, such as determining the distance towards σ Ori (Caballero, 2017), or finding a gradient in distance from 25 Ori to the ONC[1] (Zari et al., in prep), but with a limited and imprecisely determined sample size as well as large uncertainties and systematic calibration issues, it is still difficult to interpret these results.

7.4 Future Work

The orbital parameters produced by the fits to the VLBA astrometry of the binary stars allow for a direct determination of mass of the individual components of the bi-

---

[1] `http://www.arcetri.astro.it/~sfst2017/talks_all/zari.pdf`

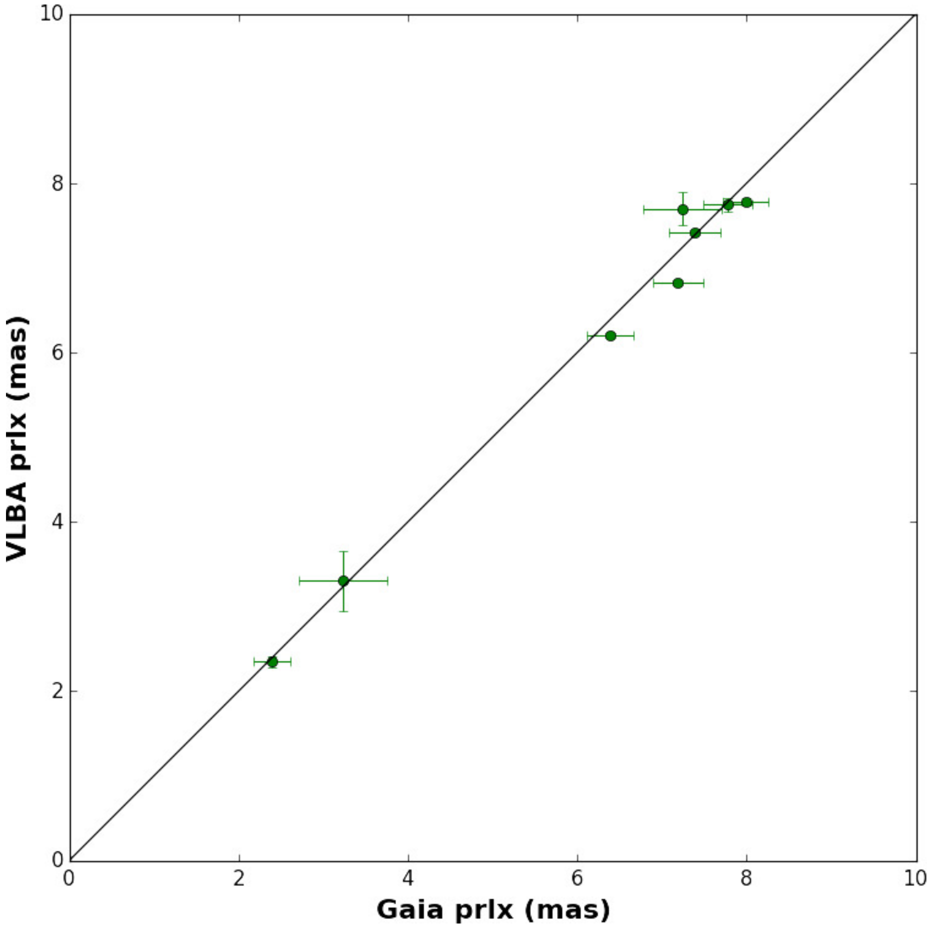

Figure 7.1 Comparison of parallactic solutions from TGAS and VLBA surveys. The best fit between them has a slope of 0.99±0.05, and an offst of 0.03±0.37. Systematic offset of 0.3 mas is not included in *Gaia* parallaxes.

nary system. Combining binaries from all the regions observed by the GOBELINS, including those outside of Orion, would allow for testing of various evolutionary models and pre-main-sequence tracks.

Once *Gaia* DR2 becomes public, I intend to work closely with it in order to compare VLBA solutions with *Gaia* and provide a more in-depth analysis of the structure and proper motions of stars in the Orion Complex. Given that both instruments have different sets of biases in both methodology of astrometry calibration (VLBA with referencing the coordinate systems to an unmoving source and *Gaia* with the consistent internal grid achieved by the wide angle monitoring), as well as sensitivity in their respective wavelength regimes which allows probing somewhat different populations of stars, both instruments are complementary to one another in this analysis. Most prominently I will look at the sources that are found in common between the two surveys, as well as determine what the respective differences in the samples can further reveal about the three-dimensional structure of the Complex. I will also focus on identifying stars that have been ejected through three-body interactions in order to constrain the effect of clustered environments on multiple systems.

My immediate future efforts will concentrate on the analysis of the APOGEE spectra taken as part of the INfrared Spectra of Young Nebulous Clusters (IN-SYNC) survey. Previously, this survey has targeted the Orion A molecular cloud and observed over 2,500 sources in it (Da Rio et al., 2016, 2017). Recent and ongoing observations extend the survey the Orion B molecular cloud, λ Ori, as well as some of Ori OB1a. These spectra allow for high resolution radial velocity measurements, as well as determination of temperature, metallicity, and surface gravity. Additionally, as multiple epochs are obtained, it is possible to better characterize short-period multiplicity of the stars in those regions. Combined with *Gaia*, this will make it possible to conduct an in-depth analysis of cloud and cluster structure and dynamics, and providing unprecedented new tests of theories of star and cluster formation and evolution.

APPENDICES

APPENDIX A

λ Ori scattering

As with all the other regions, λ Ori was observed at 5 GHz. During the first epoch of the observations, J0536+0944 was used as a primary calibrator, which is located only 0.4° from the center of the cluster. Calibrating on this source could produce a coherent signal only on the baselines shorter than 1000 km; that is, the baselines between Fort Davis, Kitt Peak, Los Alamos, Pie Town, and partially Owens Valley.

The second and third epochs were calibrated on J0532+0732, located 2.4° from the cluster center but still barely inside the λ Ori ring. While this produced a significant improvement on the calibration over the first epoch, any baselines involving antennas at Hancock and St. Croix could not be calibrated. Since the longest baseline of VLBA was not used, uncertainties in source positions remained large. However, surprisingly, some baselines longer than the baselines involving these two antennas (including most baselines involving Maunakea) did produce some coherent signal.

To determine the cause of the poor signal and potentially find a primary calibrator that could cause an improvement on the data, in 2015 August we observed four calibrators – J0536+0944, J0532+0732, J0544+1118, and J0547+1223at both 5 and 8 GHz. J0547+1223 was known to produce good calibration; it is located almost 4° from the cluster center. While it did appear as a point source at both wavelengths,

Table A.1. Parameters of elliptical gaussian model fit for the scattered calibrators towards λ Ori

Name	ν (GHz)	θ_{major} (mas)	θ_{minor} (mas)	P.A. (deg.)
J0536+0944	4.98	16.5±0.4	9.9±0.1	139.7± 10.2
J0536+0944	8.42	5.0±0.1	3.5±0.1	150.3± 1.7
J0532+0732	4.98	9.9±0.2	7.2±0.1	173.2±2.2
J0532+0732	8.42	4.3±0.1	3.0±0.1	174.0±1.2
J0544+1118	4.98	6.2±0.1	5.1±0.1	163.9±5.0
J0544+1118	8.42	2.9±0.1	2.5±0.1	7.3±2.0

such a large angular separation is larger than what is ideal for a primary calibrator. J0544+1118, located at 2.8° from the cluster center, had an appearance very similar to J0532+0732 – baselines involving HN and SC could not produce a coherent signal at 5 GHz. With the exception of J0547+1223, the other three calibrators showed a significant improvement at 8 GHz. However, even at this wavelength they did not appear like point sources. And even at 8 GHz, J0536+0944 did appear to be significantly poorer than any other calibrator.

The Gaussian model fits of the sizes of these sources is listed in Table A.1. These sizes are roughly consistent with λ^2. Because of this wavelength dependence, we believe that all radio observations of λ Ori are significantly affected by the plasma scattering. A possible source of this scattering is the ionized gas in the λ Ori ring that is currently 2.5—3° in radius (Figure 3.1), left behind by an SN blast that originated 1 Myr ago (Dolan & Mathieu, 2002). However, it is surprising that λ Ori is the only Orion region where scattering is a concern. Very few regions are known to be sources of significant plasma scattering processes that can be observed in this portion of radio regime; among them are the Galactic Center (Bower & Backer, 1998), NGC 6334 (Rodríguez et al., 2012), and Cygnus (Desai & Fey, 2001).

The fourth epoch of the observations was done at 8 GHz and used J0544+1118 as the primary calibrator. Only two sources were detectable at a higher frequency (VLBA 85 and 87). After considering positional offsets that were introduced with several alterations of the primary calibrators, we determined that neither of these sources appear to be galactic. No further monitoring was done for the region.

One object of interest identified toward λ Ori is VLBA 85. It has two components separated by 0.7 mas, possibly an AGN jet.

APPENDIX B

Comments on the parallax and proper motions measurement of the individual sources in the ONC

B.1 Trapezium

VLBA 5 (=GMR A) is found to be at a distance of 374±15 pc with a proper motion of $\mu_\alpha = 1.81 \pm 0.11$ mas year^{-1} and $\mu_\delta = -1.62 \pm 0.13$ mas year^{-1}. It has also been previously monitored with VLBA in a period from Jan. 2003 to Dec. 2004 by S07 and from Sept. 2006 to Mar. 2007 by MR. S07 found a distance solution to GMR A of 389^{+24}_{-21} pc with $\mu_\alpha = 1.89 \pm 0.12$ mas year^{-1} and $\mu_\delta = -1.67 \pm 0.19$ mas year^{-1}, which is consistent with the distance found in this work. On the other hand, MR found a distance solution of 418.4±18.2 pc with $\mu_\alpha = 1.82 \pm 0.09$ mas year^{-1} and $\mu_\delta = -2.05 \pm 0.18$ mas year^{-1}, a discrepancy on the order of 2σ in distance and μ_δ. The difference in proper motion is unlikely to be attributed to a long-period multiplicity due to the lack of acceleration observed between S07 and this work. No information is available in regards to whether or not GMR A belongs to a compact binary.

VLBA 6 (=GMR F) is observed to be at a distance of 389±7 pc with a proper motion of $\mu_\alpha = 2.38 \pm 0.08$ mas year^{-1} and $\mu_\delta = 0.55 \pm 0.14$ mas year^{-1}. MR find a distance solution of 406.1±8.4 pc with $\mu_\alpha = 2.24 \pm 0.09$ mas year^{-1} and $\mu_\delta = -0.66 \pm 0.18$ mas year^{-1}. While the two distance estimates disagree, the proper motions are consistent, suggesting that GMR F is unlikely to be a long-period binary. It has been identified as a double-lined spectroscopic binary by Prato et al. (2002) with $q \sim 0.31$, but no orbital solution is available.

VLBA 7 (=GMR H) was detected only in the first three epochs of the observations; therefore uncertainties in the solution are presented based only on the astrometric uncertainties and do not take into the account the systematic offsets. We obtain a distance solution of 372±15 pc and $\mu_\alpha = 2.22 \pm 0.18$ mas year^{-1} and $\mu_\delta = -3.08 \pm 0.55$. Not observed by MR.

VLBA 8 (=GMR G) is found to be at a distance of 377±5 pc with $\mu_\alpha = 3.82 \pm 0.10$ mas year^{-1} and $\mu_\delta = 1.60 \pm 0.17$ mas year^{-1}. MR only observed this object in three epochs. For this reason they do not present a distance solution; however, the data taken by their program suggest a distance of 382±4 pc, providing a good agreement to the distance obtained through in this work. On the other hand, proper motions obtained by MR are $\mu_\alpha = 4.29 \pm 0.17$ mas year^{-1} and $\mu_\delta = 3.33 \pm 0.37$ mas year^{-1}. This shows that this star underwent a significant acceleration in the 8 years between these observations, suggestive of a long-period binary; however, the magnitude of the acceleration is not sufficient to noticeably affect the proper motions during the $\sim$ 2 years covered by either program separately. No optical or IR companion to the system has been previously identified.

VLBA 9 (=GMR 25, = θ^1 Ori E) is a known spectroscopic binary (Costero et al., 2008; Morales-Calderón et al., 2012) with a circular orbit, period of 9.89520 days, $q \sim 1$, $i = 74°$ and masses of 2.807 and 2.797 $M_\odot$. Not previously observed by MR. We find a distance solution of 391± 7 pc with $\mu_\alpha = 1.45 \pm 0.03$ mas year^{-1} and $\mu_\delta = 1.02 \pm 0.08$ mas year^{-1}, without taking into the account the orbital motion. The lack of eccentricity makes it difficult to constrain the position of the star in its orbit with the astrometric data, but the typical effect of this orbit on the distance solution is within 3 pc.

VLBA 11 (=GMR 12, = θ^1 Ori A) is a known triple system. One of the components has been detected through the adaptive optics and VLTI imaging (Close et al., 2013; Grellmann et al., 2013), with the projected separation of $\sim 0.2''$ or ~70 AU. The other component is an eclipsing system that is also observed through spectroscopy with a period of 65.4 days (Stickland & Lloyd, 2000). Not accounting for the orbital motion we obtain a distance solution of 380±7 pc with $\mu_\alpha = 4.81 \pm 0.07$ mas year^{-1} and $\mu_\delta = -2.33 \pm 0.09$ mas year^{-1}. Incorporating the orbital motion of the spectroscopic binary while solving for i and Ω yields comparable distance of 380±14 pc with $\mu_\alpha = 4.81 \pm 0.10$ mas year^{-1}, $\mu_\delta = -2.53 \pm 0.12$, $\Omega = 150 \pm 20^\circ$ and $i = 87 \pm 11^\circ$, therefore, consistent with an eclipsing system. This does not change significantly by assuming that the emission is coming from the secondary instead of the primary. MR found a distance towards GMR 12 of 417.9±9.2 pc with $\mu_\alpha = 4.82 \pm 0.09$ mas year^{-1} and $\mu_\delta = -1.54 \pm 0.18$ mas year^{-1}. This solution did not take into the account the orbital motion; however, including it does not significantly alter the fit. The distances between two observations are discrepant by $\sim 2\sigma$. The difference in the measured proper motion is most likely driven by the acceleration due to the orbital motion of the long-period binary.

Other confirmed galactic sources that have been detected towards the Trapezium include VLBA 13, 149, and 150, but as they have been detected in only two epochs, currently it is impossible to do a parallactic fit.

B.2 Outside of the Trapezium

VLBA 4/107 (=Brun 656) is located westward of the OMC 2/3 filament. It was detected as an astrometric binary system, with VLBA 4 detected in epochs 1, 4, & 5, and VLBA 107 detected in epochs 2, 4, & 5. Orbital motion is clearly apparent in both stars. However, with only six positions it is impossible to fit all 13 parameters for both parallactic and orbital motion. Therefore we exclude i and Ω from the fit, assuming a face on orientation. In the follow up work with additional data it would be possible to present a full solution. Potentially a member of a triple system as Köhler et al. (2006) identify an additional companion 0.4" or ∼150 AU away; this should have little impact on astrometry after 2 year baseline. We obtain a distance solution of 369±10 pc with the proper motions of the compact system of $\mu_\alpha = 2.36 \pm 0.69$ mas year^{-1} and $\mu_\delta = 0.06 \pm 1.05$ mas year^{-1}, and the scatter and the dependence between these parameters is shown in the Figure 3.3. This proper motion is most likely not representative of the true proper motion of the triple system. We find the period of the compact system to be 6.27±0.54 years and $M \cos^3 i$ of both components of 1.70±0.16 and 1.62±0.38 $M_\odot$. The spectral type for the primary has been previously reported to be G2III (Hillenbrand, 1997)

VLBA 14 (=V1699 Ori) is located towards NGC 1977. We found a distance solution of 401±7 pc with $\mu_\alpha = 1.76 \pm 0.05$ mas year^{-1} and $\mu_\delta = -0.89 \pm 0.16$ mas year^{-1}.

VLBA 16 (=Parenago 1469) is located westward of the Trapezium. It was detected only in the epochs 1, 2, & 4. We find a distance solution of 394±4 pc with $\mu_\alpha = -7.22 \pm 0.06$ mas year^{-1} and $\mu_\delta = -0.99 \pm 0.08$ mas year^{-1}. Proper motions for this star are uncommonly large and appear to be projected from the Trapezium cluster (see Section 3.4.3).

VLBA 18 (=Parenago 1724) is located westward of the OMC 2/3 filament. We found a distance solution of 398±7 pc with $\mu_\alpha = 0.06 \pm 0.20$ mas year^{-1} and $\mu_\delta = 6.95 \pm 0.15$ mas year^{-1}. Similarly to VLBA 16, it also has a very large proper motion vector, which projects back to the center of the Trapezium cluster. It was previously identified by Neuhaeuser et al. (1998) as a runaway star.

VLBA 19 (=Parenago 1540) is located westward of the Trapezium. It is a known double-lined spectroscopic binary (Marschall & Mathieu, 1988). Without accounting for the orbital motion we obtain a distance solution of 404±11 pc with $\mu_\alpha = -3.88 \pm 0.13$ mas year^{-1} and $\mu_\delta = -1.10 \pm 0.15$ mas year^{-1}. Incorporating an orbital fit and solving for i and Ω yields a distance of 386±7 pc with $\mu_\alpha = -4.01 \pm 0.08$ mas year^{-1}, $\mu_\delta = -1.17 \pm 0.07$ mas year^{-1}, $i = 104 \pm 12^\circ$ and $\Omega = 69 \pm 11^\circ$. This results in the masses of the components of 0.49±0.10 and 0.37±0.07 $M_\odot$, however, the spectral types of K3V and K5V make these masses to be somewhat suspect. With an assumption that the emission is coming from the secondary with ω rotated by 180°, an alternate family of solutions is found at 413±12 pc with $\mu_\alpha = -3.85 \pm 0.14$ mas year^{-1}, $\mu_\delta = -1.12 \pm 0.08$ mas year^{-1}, $i = 56 \pm 12^\circ$ and $\Omega = 130 \pm 14^\circ$, and masses of 0.78±0.40 and 0.60±0.28 $M_\odot$. Similarly to VLBA 16 and 18, this system has a very large proper motion vector that projects back to the Trapezium cluster, and it has been previously theorized to be a runaway star by Marschall & Mathieu (1988).

VLBA 22 (=HD 37150) is located towards the south-east of the Trapezium. We obtain a distance solution of 394±7 pc with $\mu_\alpha = 1.32 \pm 0.05$ mas year^{-1}, $\mu_\delta = 0.56 \pm 0.12$ mas year^{-1}.

VLBA 27/28 (=NU Ori) shows considerable motion, but it cannot be fitted yet due to multiplicity. VLBA 27 has been detected in epochs 1, 3, & 5, and VLBA 28 has been detected in epoch 1, with the projected separation of 35 mas from VLBA 27. A single point source was detected in epoch 4, tentatively interpreted to be associated with VLBA 28, ~8 mas away from the expected position of VLBA 27. This companion system has been previously predicted to exist by Grellmann et al. (2013) based on the VLTI observations. In addition to this, this system contains a known spectroscopic binary with a period of 19 days and $a_1 \sin i$ of ~ 0.15 mas (Abt et al., 1991); a hint of extension is seen towards VLBA 27 in some epochs and this could be the source. This system also has a wider companion with a separation of $\sim 0.5''$ (Köhler et al., 2006). Given the fact that the primary was detected only in spring epochs without any fall epochs, we cannot provide even rough constraints on its distance. Follow-up monitoring would be needed in order to accurately understand the motions of this system.

VLBA 34 (=HD 37017) is a known double-lined spectroscopic binary (Bolton et al., 1998). Without orbital motion we obtain a distance solution of 360±7 pc with $\mu_\alpha = 1.87 \pm 0.07$ mas year^{-1}, $\mu_\delta = 1.17 \pm 0.24$ mas year^{-1}. Solving for i and Ω we obtain two possible results due to the lack of constrains in the direction of the orbit. These results are $i = 53 \pm 23^\circ$ and $i = 127 \pm 28^\circ$, both with $\Omega = 131 \pm 26^\circ$ and the distance solution of 378±10 pc with $\mu_\alpha = 1.88 \pm 0.09$ mas year^{-1}, $\mu_\delta = 1.20 \pm 0.14$ mas year^{-1}. This corresponds to masses of the components of 4.09±4.41 and 2.14±2.22 $M_\odot$. Assuming that the emission is coming from the secondary does not change the solution significantly, the estimated distance becomes 383±5 pc, although the inclination angle becomes $76 \pm 18^\circ$.

VLBA 105 (= Parenago 2148) is located towards OMC 2/3 filament. It was detected only in epochs 2, 3, & 5. The positional uncertainties, particularly in epoch 2, are rather substantial as the source appears to be marginally extended in α. Without accounting for any of the systematic offsets we find a distance solution of 388±53 pc with $\mu_\alpha = 0.33 \pm 0.05$ mas year^{-1}, $\mu_\delta = -1.34 \pm 0.43$ mas year^{-1}.

VLBA 114 (= Parenago 1778) is located towards NGC 1977. It was not detected in epoch 1. We obtain a distance solution of 437±83 pc with $\mu_\alpha = 2.54 \pm 0.30$ mas year^{-1}, $\mu_\delta = -1.30 \pm 0.64$ mas year^{-1}. The fit is rather poor, despite the substantial positional uncertainties. This could be attributed to acceleration due to multiplicity.

Other galactic sources identified in the region that have been detected only in two epochs are VLBA 33, 110, & 116. VLBA 115 has also been detected in 2 epochs, and although the α offset is consistent with belonging to the ONC (2.7 mas), the δ offset is over 13 mas; this is likely due to multiplicity.

APPENDIX C

Comments on the parallax and proper motions of the remaining regions

C.1 L1641

Only two galactic sources, VLBA 45 & 46, have been detected towards L1641. Both of them are located on the southern end of the cloud, at $\delta < -8°$. The solutions towards them are somewhat more uncertain than they are towards sources located within the ONC, with very large uncertainties and imprecise fit. Preliminary fits result in distance solutions of 424±12 pc with $\mu_\alpha = 0.68 \pm 0.06$ mas year^{-1}, $\mu_\delta = -0.31 \pm 0.22$ mas year^{-1} for VLBA 45 and 433±28 pc with $\mu_\alpha = 0.25 \pm 0.04$ mas year^{-1}, $\mu_\delta = -0.47 \pm 0.25$ mas year^{-1} for VLBA 46. The fit appears to be somewhat dubious and the observed positions do not agree with the best fits for both sources in the epochs 1 & 4. It is possible that this offset is attributable to multiplicity in both of these objects, although the fact that the magnitude of the offset is comparable for both sources at each epoch makes it more suspect. Therefore we treat this offset as the pointing error due to calibration and solve for a common offset for both sources.

We correct the positions of the first epoch by $\Delta\alpha = 0.256$ mas and $\Delta\delta = 0.771$ mas, and the fourth epoch by $\Delta\alpha = 0.204$ mas and $\Delta\delta = 0.659$ mas. It is somewhat curious that this offset is comparable in both epochs. After this correction, the distance solution becomes 425±12 pc with $\mu_\alpha = 0.68 \pm 0.09$ mas year^{-1}, $\mu_\delta = -0.51 \pm 0.25$ mas year^{-1} for VLBA 45 and 431±13 pc with $\mu_\alpha = 0.13 \pm 0.25$ mas year^{-1}, $\mu_\delta = -1.05 \pm 0.18$ mas year^{-1} for VLBA 46. This offset has a very small overall effect on the distance, but the proper motions are somewhat uncertain.

In addition to the galactic sources, there are a number of extragalactic sources that can be of interest. VLBA 39/40, 41/42, 47/48, 89/90, & 94/95/96 appear to exhibit no motion between epochs, but they appear to be extended, double or even triple objects. They can probably be attributable to the AGN jets. It is curious that so many of these extended sources appear to be in the direction of this particular region.

C.2 NGC 2068

The second epoch of the observations of this region was strongly affected by a pointing error, and this offset is also present in nearby sources that can otherwise be considered extragalactic. A possible explanation for this is that one of the secondary calibrators had an extremely weak detection in this epoch. We solve for a common offset for all sources of $\Delta\alpha = -0.559$ mas, $\Delta\delta = -0.515$ mas.

Three galactic sources have been detected towards NGC 2068. VLBA 63, 68 (=HD 290862), & 69. After removing the offset, we obtain a distance solution of 383±7 pc with $\mu_\alpha = -1.02 \pm 0.10$ mas year^{-1}, $\mu_\delta = -0.52 \pm 0.15$ mas year^{-1} for VLBA 63, and 392±5 pc with $\mu_\alpha = -0.01 \pm 0.10$ mas year^{-1}, $\mu_\delta = -0.49 \pm 0.08$ mas year^{-1} for VLBA 69. On the other hand, we can offer only an extremely noisy tentative solution for VLBA 68 of 455±113 pc with $\mu_\alpha = 0.35 \pm 0.27$ mas year^{-1}, $\mu_\delta = 0.83 \pm 0.83$ mas year^{-1}. The reason for this is that VLBA 68 appears to be a multiple system (although no companion has been directly detected) which greatly affects the positions. At this point in time we cannot perform an orbital fit for the system.

C.3 NGC 2024

VLBA 61/62 has been identified as an astrometric binary, with the first component present in all five epochs, while the second component detected only in epochs 1, 4, & 5. We find a distance to the system of 434±10 pc with $\mu_\alpha = 0.47 \pm 0.32$ mas year^{-1}, $\mu_\delta = 0.39 \pm 0.62$ mas year^{-1}, and the scatter and the dependence between these parameters is shown in the Figure 3.3. The period of the binary is 9.50±0.67 years, inclination of 141±6°, and masses of both components of 1.85±0.58 and 0.95±0.22 $M_\odot$. Unfortunately, this system has not been detected at any other wavelength regime other than in radio, therefore, a comparison of masses to spectral types is impossible. While the orbital fit itself is convergent, it must be noted that some uncertainty does remain due to the limited number of detections, and although unlikely, a possibility of a somewhat larger distance ~444 pc as well as a somewhat steeper inclination angle cannot be ruled out currently.

VLBA 58 is another star that was detected in all five epochs in this region, and it also appears to be a binary due to its peculiar motions from one epoch to the next. At this point in time, an orbit to it cannot be fitted, but we obtain a very tentative solution of 449±24 pc with $\mu_\alpha = 0.04 \pm 0.31$ mas year^{-1}, $\mu_\delta = 0.20 \pm 0.43$ mas year^{-1}.

Three other stellar objects have been detected towards the region, but only in three epochs, therefore, solutions are somewhat uncertain as they do not take into account any systematic offsets. VLBA 148 has a distance solution of 412± 5 pc with $\mu_\alpha = 0.19 \pm 0.44$ mas year^{-1}, $\mu_\delta = -0.97 \pm 0.27$ mas year^{-1}. VLBA 125 is presently found at a distance of 536±30 with $\mu_\alpha = -0.43 \pm 0.16$ mas year^{-1}, $\mu_\delta = 1.03 \pm 0.42$ mas year^{-1}; this solution is rather tentative due to the astrometric errors and a quality of the fit. On the other hand, VLBA 126 has a measured distance of 356±4 pc with $\mu_\alpha = 0.55 \pm 0.10$ mas year^{-1}, $\mu_\delta = -0.10 \pm 0.15$ mas year^{-1}.

It is clear that VLBA 125 and 126 have a measured distance that is decidedly different from what is found towards other objects in the region. A possible explanation to this is that these stars may belong to an as of yet unseen binary system. Whether this is could also be the case for VLBA 148 is as of yet unclear.

Other galactic sources identified towards NGC 2024 are VLBA 124 & 153, although only two epochs are currently available.

A number of extragalactic objects of interest have also been identified. VLBA 56 shows a clear signature of an AGN jet. VLBA 146/147 has two components, also a probable extragalactic jet. While previously VLBA 55 has been identified as a Class II YSO based on its infrared colors, it shows no positional offset between epochs. It was notable for being extremely bright in radio (highest VLBA flux of 338 mJy at 5 GHz).

C.4 σ Ori

Only one Galactic object has been identified towards σ Ori among those detected with VLBA. VLBA 145 (=HD 294300) was not monitored in epochs 1 & 2, therefore currently only three epochs of astrometry are available. It is found at a distance of 302±32 pc with $\mu_\alpha = -4.92 \pm 0.66$ mas year^{-1}, $\mu_\delta = 4.67 \pm 1.37$ mas year^{-1}. Whether this distance solution is trustworthy or not still remains to be tested; while σ Ori is most likely spatially separate from NGC 2024, a difference in distance of over 100 pc would be surprising. Sherry et al. (2008) previously estimated distance towards σ Ori based on main-sequence fitting to be 420±30 pc, quite close to the distances we obtain to NGC 2024 members. Combined with the rather high proper motions for VLBA 145 of 9.7 km s^{-1} as well as a somewhat poor fit could imply that this star belongs to a binary system; therefore, further monitoring would be needed to better understand the kinematics of the system.

C.5 L1622

In the VLA survey, only two sources have been identified towards L1622, of which one was a known YSO, and one did not have any classification. The former one was not detected with VLBA, the latter (VLBA 84) did not exhibit any positional offset between observations. No parallax towards this region can be measured. No further monitoring was done past epoch 2.

BIBLIOGRAPHY

Abt, H. A., Wang, R., & Cardona, O. 1991, ApJ, 367, 155

Adams, F. C. 2010, ARA&A, 48, 47

Adams, F. C., Lada, C. J., & Shu, F. H. 1987, ApJ, 312, 788

Adams, F. C., & Shu, F. H. 1986, ApJ, 308, 836

Alcalá, J. M., Covino, E., Torres, G., et al. 2000, A&A, 353, 186

Allen, L. E., & Davis, C. J. 2008, Low Mass Star Formation in the Lynds 1641 Molecular Cloud, ed. B. Reipurth, 621

Allen, L. E., Calvet, N., D'Alessio, P., et al. 2004, ApJS, 154, 363

Alves, J., & Bouy, H. 2012, A&A, 547, A97

Anderson, J. M., Li, Z.-Y., Krasnopolsky, R., & Blandford, R. D. 2005, ApJ, 630, 945

Andre, P. 1996, in Astronomical Society of the Pacific Conference Series, Vol. 93, Radio Emission from the Stars and the Sun, ed. A. R. Taylor & J. M. Paredes, 273–284

Anglada, G., Villuendas, E., Estalella, R., et al. 1998, AJ, 116, 2953

Avila, R., Rodríguez, L. F., & Curiel, S. 2001, Rev. Mexicana Astron. Astrofis., 37, 201

Ballesteros-Paredes, J., Hartmann, L. W., Vázquez-Semadeni, E., Heitsch, F., & Zamora-Avilés, M. A. 2011, MNRAS, 411, 65

Bally, J. 2008, Overview of the Orion Complex, ed. B. Reipurth, 459

Bally, J., Langer, W. D., Stark, A. A., & Wilson, R. W. 1987, ApJ, 312, L45

Baraffe, I., & Chabrier, G. 2010, A&A, 521, A44

Baraffe, I., Chabrier, G., Allard, F., & Hauschildt, P. H. 1998, A&A, 337, 403

Baraffe, I., Elbakyan, V. G., Vorobyov, E. I., & Chabrier, G. 2017, A&A, 597, A19

Baraffe, I., Homeier, D., Allard, F., & Chabrier, G. 2015, A&A, 577, A42

Barrado y Navascués, D., Stauffer, J. R., Morales-Calderón, M., et al. 2007, ApJ, 664, 481

Baxter, E. J., Covey, K. R., Muench, A. A., et al. 2009, AJ, 138, 963

Bayo, A., Barrado, D., Stauffer, J., et al. 2011, A&A, 536, A63

Bekki, K. 2009, MNRAS, 398, L36

Bernstein, R., Shectman, S. A., Gunnels, S. M., Mochnacki, S., & Athey, A. E. 2003, in Society of Photo-Optical Instrumentation Engineers (SPIE) Conference Series, Vol. 4841, Instrument Design and Performance for Optical/Infrared Ground-based Telescopes, ed. M. Iye & A. F. M. Moorwood, 1694–1704

Bertout, C. 1983, A&A, 126, L1

Bessell, M. S., & Brett, J. M. 1988, PASP, 100, 1134

Bigelow, B. C., & Dressler, A. M. 2003, in Proc. SPIE, Vol. 4841, Instrument Design and Performance for Optical/Infrared Ground-based Telescopes, ed. M. Iye & A. F. M. Moorwood, 1727–1738

Binney, J., & Tremaine, S. 1987, Galactic dynamics

Bolton, C. T., Harmanec, P., Lyons, R. W., Odell, A. P., & Pyper, D. M. 1998, A&A, 337, 183

Bouy, H., Alves, J., Bertin, E., Sarro, L. M., & Barrado, D. 2014, A&A, 564, A29

Bouy, H., Huélamo, N., Martín, E. L., et al. 2009, A&A, 493, 931

Bower, G. C., & Backer, D. C. 1998, ApJ, 496, L97

Briceño, C., Calvet, N., & Hernandez, J. 2017, in Star Formation from Cores to Clusters, 4

Briceño, C., Calvet, N., Hernández, J., et al. 2005, AJ, 129, 907

Briceño, C., Hartmann, L., Hernández, J., et al. 2007, ApJ, 661, 1119

Briceno, C., Hartmann, L. W., Stauffer, J. R., et al. 1997, AJ, 113, 740

Brown, A. G. A., de Geus, E. J., & de Zeeuw, P. T. 1994, A&A, 289, 101

Caballero, J. A. 2017, ArXiv e-prints, arXiv:1702.06046

Caballero, J. A., Albacete-Colombo, J. F., & López-Santiago, J. 2010, A&A, 521, A45

Calvet, N. 1998, in American Institute of Physics Conference Series, Vol. 431, American Institute of Physics Conference Series, ed. S. S. Holt & T. R. Kallman, 495–504

Calvet, N., & Gullbring, E. 1998, ApJ, 509, 802

Cardelli, J. A., Clayton, G. C., & Mathis, J. S. 1989, ApJ, 345, 245

Carpenter, J. M. 2000, AJ, 120, 3139

—. 2001, AJ, 121, 2851

Casertano, S., Riess, A. G., Bucciarelli, B., & Lattanzi, M. G. 2017, A&A, 599, A67

Chen, Y.-P., Trager, S. C., Peletier, R. F., et al. 2014, A&A, 565, A117

Clayton, D. D. 1983, Principles of stellar evolution and nucleosynthesis

Close, L. M., Males, J. R., Morzinski, K., et al. 2013, ApJ, 774, 94

Coelho, P., Barbuy, B., Meléndez, J., Schiavon, R. P., & Castilho, B. V. 2005, A&A, 443, 735

Cohen, M., & Kuhi, L. V. 1979, ApJS, 41, 743

Comeron, F., & Torra, J. 1994, A&A, 281, 35

Condon, J. J., Cotton, W. D., Greisen, E. W., et al. 1998, AJ, 115, 1693

Costero, R., Allen, C., Echevarría, J., et al. 2008, in Revista Mexicana de Astronomia y Astrofisica Conference Series, Vol. 34, Revista Mexicana de Astronomia y Astrofisica Conference Series, 102–105

Curiel, S., Canto, J., & Rodriguez, L. F. 1987, Rev. Mexicana Astron. Astrofis., 14, 595

Cutri, R. M., Skrutskie, M. F., van Dyk, S., et al. 2003, VizieR Online Data Catalog, 2246, 0

Da Rio, N., Robberto, M., Soderblom, D. R., et al. 2009, ApJS, 183, 261

—. 2010, ApJ, 722, 1092

Da Rio, N., Tan, J. C., Covey, K. R., et al. 2016, ApJ, 818, 59

—. 2017, ArXiv e-prints, arXiv:1702.04113

Davies, G. R., Lund, M. N., Miglio, A., et al. 2017, A&A, 598, L4 de Bruijne, J. H. J., Rygl, K. L. J., & Antoja, T. 2014, in EAS Publications Series, Vol. 67, EAS Publications Series, 23–29

de Zeeuw, P. T., Hoogerwerf, R., de Bruijne, J. H. J., Brown, A. G. A., & Blaauw, A. 1999, AJ, 117, 354

de Zeeuw, T., Hoogerwerf, R., & de Bruijne, J. 2001, in Astronomical Society of the Pacific Conference Series, Vol. 228, Dynamics of Star Clusters and the Milky Way, ed. S. Deiters, B. Fuchs, A. Just, R. Spurzem, & R. Wielen, 201

Desai, K. M., & Fey, A. L. 2001, ApJS, 133, 395

Dolan, C. J., & Mathieu, R. D. 2001, AJ, 121, 2124

—. 2002, AJ, 123, 387

Donaldson, J. K., Weinberger, A. J., Gagné, J., et al. 2016, ApJ, 833, 95

Donati, J.-F., Gregory, S. G., Alencar, S. H. P., et al. 2013, MNRAS, 436, 881

Donati, J.-F., Hébrard, E., Hussain, G., et al. 2014, MNRAS, 444, 3220

Donati, J.-F., Hébrard, E., Hussain, G. A. J., et al. 2015, MNRAS, 453, 3706

Duchêne, G., & Kraus, A. 2013, ARA&A, 51, 269

Dulk, G. A. 1985, ARA&A, 23, 169

Duquennoy, A., & Mayor, M. 1991, A&A, 248, 485

Dzib, S. A., Loinard, L., Rodríguez, L. F., & Galli, P. 2014, ApJ, 788, 162

Dzib, S. A., Loinard, L., Mioduszewski, A. J., et al. 2013, ApJ, 775, 63

Dzib, S. A., Loinard, L., Rodríguez, L. F., et al. 2015, ApJ, 801, 91

—. 2017, ApJ, 834, 139

Elmegreen, B. G. 2007, ApJ, 668, 1064

Espaillat, C., Andrews, S., Powell, D., et al. 2015, ApJ, 807, 156

Evans, II, N. J., Dunham, M. M., Jørgensen, J. K., et al. 2009, ApJS, 181, 321

Fang, M., van Boekel, R., Wang, W., et al. 2009, A&A, 504, 461

Fang, M., Kim, J. S., Pascucci, I., et al. 2017, AJ, 153, 188

Feigelson, E. D., & Montmerle, T. 1999, ARA&A, 37, 363

Fűrész, G., Hartmann, L. W., Megeath, S. T., Szentgyorgyi, A. H., & Hamden, E. T. 2008, ApJ, 676, 1109

Fűrész, G., Hartmann, L. W., Szentgyorgyi, A. H., et al. 2006, ApJ, 648, 1090

Fischer, D. A., & Marcy, G. W. 1992, ApJ, 396, 178

Flaherty, K. M., & Muzerolle, J. 2008, AJ, 135, 966

Forbrich, J., & Wolk, S. J. 2013, A&A, 551, A56

Franciosini, E., & Sacco, G. G. 2011, A&A, 530, A150

Gaia Collaboration, Brown, A. G. A., Vallenari, A., et al. 2016, A&A, 595, A2

Gaia Collaboration, Clementini, G., Eyer, L., et al. 2017, ArXiv e-prints, arXiv:1705.00688

Garay, G., Moran, J. M., & Reid, M. J. 1987, ApJ, 314, 535

Genzel, R., Reid, M. J., Moran, J. M., & Downes, D. 1981, ApJ, 244, 884

Getman, K. V., Feigelson, E. D., & Kuhn, M. A. 2014, ApJ, 787, 109

Getman, K. V., Flaccomio, E., Broos, P. S., et al. 2005, ApJS, 160, 319

Gibb, A. G. 1999, MNRAS, 304, 1

—. 2008, Star Formation in NGC 2068, NGC 2071, and Northern L1630, ed. B. Reipurth, 693

Goddi, C., Humphreys, E. M. L., Greenhill, L. J., Chandler, C. J., & Matthews, L. D. 2011, ApJ, 728, 15

Gómez, L., Rodríguez, L. F., Loinard, L., et al. 2008, ApJ, 685, 333

Greisen, E. W. 2003, Information Handling in Astronomy - Historical Vistas, 285, 109

Grellmann, R., Preibisch, T., Ratzka, T., et al. 2013, A&A, 550, A82

Gualandris, A., Portegies Zwart, S., & Eggleton, P. P. 2004, MNRAS, 350, 615

Gudehus, D. H. 2001, in Bulletin of the American Astronomical Society, Vol. 33, American Astronomical Society Meeting Abstracts #198, 850

Güdel, M., & Benz, A. O. 1993, ApJ, 405, L63

Güdel, M., Briggs, K. R., Montmerle, T., et al. 2008, Science, 319, 309

Gutermuth, R. A., Megeath, S. T., Myers, P. C., et al. 2009, ApJS, 184, 18

Gutermuth, R. A., Pipher, J. L., Megeath, S. T., et al. 2011, ApJ, 739, 84

Hartmann, L. 2001, AJ, 121, 1030

Hartmann, L., & Burkert, A. 2007, ApJ, 654, 988

Hartmann, L., Herczeg, G., & Calvet, N. 2016, ARA&A, 54, 135

Hennebelle, P. 2012, A&A, 545, A147

Herbig, G. H. 1952, JRASC, 46, 222

Hernández, J., Calvet, N., Briceño, C., Hartmann, L., & Berlind, P. 2004, AJ, 127, 1682

Hernández, J., Morales-Calderon, M., Calvet, N., et al. 2010, ApJ, 722, 1226

Hernández, J., Hartmann, L., Megeath, T., et al. 2007, ApJ, 662, 1067

Hillenbrand, L., Isaacson, H., Marcy, G., et al. 2015, in Cambridge Workshop on Cool Stars, Stellar Systems, and the Sun, Vol. 18, 18th Cambridge Workshop on Cool Stars, Stellar Systems, and the Sun, ed. G. T. van Belle & H. C. Harris, 759–766

Hillenbrand, L. A. 1997, AJ, 113, 1733

Hillenbrand, L. A., & Hartmann, L. W. 1998, ApJ, 492, 540

Hirota, T., Bushimata, T., Choi, Y. K., et al. 2007, PASJ, 59, 897

Houk, N., & Swift, C. 1999, in Michigan Spectral Survey, Ann Arbor, Dep. Astron., Univ. Michigan, Vol. 5, p. 0 (1999), Vol. 5, 0

Hovatta, T., Lehto, H. J., & Tornikoski, M. 2008, A&A, 488, 897

Hsu, W.-H., Hartmann, L., Allen, L., et al. 2012, ApJ, 752, 59

—. 2013, ApJ, 764, 114

Iglesias-Marzoa, R., López-Morales, M., & Jesús Arévalo Morales, M. 2015, PASP, 127, 567

Jao, W.-C., Henry, T. J., Riedel, A. R., et al. 2016, ApJ, 832, L18

Jeans, J. H. 1902, Philosophical Transactions of the Royal Society of London Series A, 199, 1

Jeffries, R. D. 2007, MNRAS, 376, 1109

Jeffries, R. D., Maxted, P. F. L., Oliveira, J. M., & Naylor, T. 2006, MNRAS, 371, L6

Jeffries, R. D., Jackson, R. J., Franciosini, E., et al. 2017, MNRAS, 464, 1456

Johns-Krull, C. M., Greene, T. P., Doppmann, G. W., & Covey, K. R. 2009, ApJ, 700, 1440

Jones, B. F., & Walker, M. F. 1988, AJ, 95, 1755

Joy, A. H. 1949, ApJ, 110, 424

Kapteyn, J. C. 1918, ApJ, 47, 104

Karnath, N., Prato, L., Wasserman, L. H., et al. 2013, AJ, 146, 149

Kenyon, S. J., Gomez, M., Marzke, R. O., & Hartmann, L. 1994, AJ, 108, 251

Kenyon, S. J., & Hartmann, L. 1987, ApJ, 323, 714

—. 1995, ApJS, 101, 117

Kerr, F. J., & Lynden-Bell, D. 1986, MNRAS, 221, 1023

Kim, M. K., Hirota, T., Honma, M., et al. 2008, PASJ, 60, 991

Kirk, J. M., Ward-Thompson, D., & André, P. 2005, MNRAS, 360, 1506

Köhler, R., Petr-Gotzens, M. G., McCaughrean, M. J., et al. 2006, A&A, 458, 461

Kounkel, M., Hartmann, L., Calvet, N., & Megeath, T. 2017a, AJ, 154, 29

Kounkel, M., Hartmann, L., Mateo, M., & Bailey, III, J. I. 2017b, ApJ, 844, 138

Kounkel, M., Hartmann, L., Tobin, J. J., et al. 2016a, ApJ, 821, 8

Kounkel, M., Megeath, S. T., Poteet, C. A., Fischer, W. J., & Hartmann, L. 2016b, ApJ, 821, 52

Kounkel, M., Hartmann, L., Loinard, L., et al. 2014, ApJ, 790, 49

—. 2017c, ApJ, 834, 142

Kouwenhoven, M. B. N., Brown, A. G. A., Portegies Zwart, S. F., & Kaper, L. 2007, A&A, 474, 77

Kramer, C., Stutzki, J., & Winnewisser, G. 1996, A&A, 307, 915

Kraus, S., Weigelt, G., Balega, Y. Y., et al. 2009, A&A, 497, 195

Kun, M., Balog, Z., Mizuno, N., et al. 2008, MNRAS, 391, 84

Kurtz, M. J., & Mink, D. J. 1998, PASP, 110, 934

Kuznetsova, A., Hartmann, L., & Ballesteros-Paredes, J. 2015, ApJ, 815, 27

—. 2017, MNRAS, submitted

Lada, C. J., & Lada, E. A. 2003, ARA&A, 41, 57

Leroy, A. K., Walter, F., Brinks, E., et al. 2008, AJ, 136, 2782

Levine, J. L., Steinhauer, A., Elston, R. J., & Lada, E. A. 2006, ApJ, 646, 1215

Lindegren, L., Lammers, U., Hobbs, D., et al. 2012, A&A, 538, A78

Loinard, L., Mioduszewski, A. J., Torres, R. M., et al. 2011, in Revista Mexicana de Astronomia y Astrofisica, vol. 27, Vol. 40, Revista Mexicana de Astronomia y Astrofisica Conference Series, 205–210

Loinard, L., Torres, R. M., Mioduszewski, A. J., et al. 2007, ApJ, 671, 546

Lombardi, M., Alves, J., & Lada, C. J. 2011, A&A, 535, A16

Madsen, G. J., Reynolds, R. J., & Haffner, L. M. 2006, ApJ, 652, 401

Maia, F. F. S., Corradi, W. J. B., & Santos, Jr., J. F. C. 2010, MNRAS, 407, 1875

Mamajek, E. E. 2009, in American Institute of Physics Conference Series, Vol. 1158, American Institute of Physics Conference Series, ed. T. Usuda, M. Tamura, & M. Ishii, 3–10

Mamajek, E. E., & Feigelson, E. D. 2001, in Astronomical Society of the Pacific Conference Series, Vol. 244, Young Stars Near Earth: Progress and Prospects, ed. R. Jayawardhana & T. Greene, 104–115

Markwardt, C. B. 2009, in Astronomical Society of the Pacific Conference Series, Vol. 411, Astronomical Data Analysis Software and Systems XVIII, ed. D. A. Bohlender, D. Durand, & P. Dowler, 251

Marschall, L. A., & Mathieu, R. D. 1988, AJ, 96, 1956

Mateo, M., Bailey, J. I., Crane, J., et al. 2012, in Society of Photo-Optical Instrumentation Engineers (SPIE) Conference Series, Vol. 8446, Society of Photo-Optical Instrumentation Engineers (SPIE) Conference Series, 4

Mathieu, R. D. 2008, The λ Orionis Star Forming Region, ed. B. Reipurth, 757

Megeath, S. T., Gutermuth, R., Muzerolle, J., et al. 2012, AJ, 144, 192

—. 2016, AJ, 151, 5

Melis, C., Reid, M. J., Mioduszewski, A. J., Stauffer, J. R., & Bower, G. C. 2014, Science, 345, 1029

Mendoza V., E. E. 1968, ApJ, 151, 977

Menten, K. M., Reid, M. J., Forbrich, J., & Brunthaler, A. 2007, A&A, 474, 515

Meyer, M. R., Calvet, N., & Hillenbrand, L. A. 1997, AJ, 114, 288

Meyer, M. R., Flaherty, K., Levine, J. L., et al. 2008, Star Formation in NGC 2023, NGC 2024, and Southern L1630, ed. B. Reipurth, 662

Mookerjea, B., Sandell, G., Jarrett, T. H., & McMullin, J. P. 2009, A&A, 507, 1485

Morales-Calderón, M., Stauffer, J. R., Hillenbrand, L. A., et al. 2011, ApJ, 733, 50

Morales-Calderón, M., Stauffer, J. R., Stassun, K. G., et al. 2012, ApJ, 753, 149

Muench, A., Getman, K., Hillenbrand, L., & Preibisch, T. 2008, Star Formation in the Orion Nebula I: Stellar Content, ed. B. Reipurth, 483

Munari, U., Sordo, R., Castelli, F., & Zwitter, T. 2005, A&A, 442, 1127

Murphy, E. J. 2011, in Astronomical Society of the Pacific Conference Series, Vol. 440, UP2010: Have Observations Revealed a Variable Upper End of the Initial Mass Function?, ed. M. Treyer, T. Wyder, J. Neill, M. Seibert, & J. Lee, 361

Muzerolle, J., Calvet, N., & Hartmann, L. 2001, ApJ, 550, 944

Najita, J. R., & Shu, F. H. 1994, ApJ, 429, 808

Neuhaeuser, R., Wolk, S. J., Torres, G., et al. 1998, A&A, 334, 873

Nishimura, A., Tokuda, K., Kimura, K., et al. 2015, ApJS, 216, 18

Ochsendorf, B. B., Brown, A. G. A., Bally, J., & Tielens, A. G. G. M. 2015, ApJ, 808, 111

O'Dell, C. R., Ferland, G. J., Porter, R. L., & van Hoof, P. A. M. 2011, ApJ, 733, 9

O'Dell, C. R., Poveda, A., Allen, C., & Robberto, M. 2005, ApJ, 633, L45

Olano, C. A. 2001, AJ, 121, 295

Ortiz-León, G. N., Loinard, L., Mioduszewski, A. J., et al. 2015, ApJ, 805, 9

Ortiz-León, G. N., Loinard, L., Kounkel, M. A., et al. 2017a, ApJ, 834, 141

Ortiz-León, G. N., Dzib, S. A., Kounkel, M. A., et al. 2017b, ApJ, 834, 143

Palla, F., Randich, S., Flaccomio, E., & Pallavicini, R. 2005, ApJ, 626, L49

Park, B.-G., & Sung, H. 2002, AJ, 123, 892

Peña Ramírez, K., Béjar, V. J. S., Zapatero Osorio, M. R., Petr-Gotzens, M. G., & Martín, E. L. 2012, ApJ, 754, 30

Pecaut, M. J., & Mamajek, E. E. 2013, ApJS, 208, 9

Pecaut, M. J., Mamajek, E. E., & Bubar, E. J. 2012, ApJ, 746, 154

Pech, G., Loinard, L., Dzib, S. A., et al. 2016, ApJ, 818, 116

Perryman, M. A. C., & ESA, eds. 1997, ESA Special Publication, Vol. 1200, The HIPPARCOS and TYCHO catalogues. Astrometric and photometric star catalogues derived from the ESA HIPPARCOS Space Astrometry Mission

Persson, M. V. 2014, doi:10.6084/m9.figshare.654555.v7

Pickering, W. H. 1917, Harvard College Observatory Circular, 205, 1

Pillitteri, I., Wolk, S. J., Megeath, S. T., et al. 2013, ApJ, 768, 99

Pöppel, W. G. L., & Marronetti, P. 2000, A&A, 358, 299

Porras, A., Christopher, M., Allen, L., et al. 2003, AJ, 126, 1916

Poveda, A., Allen, C., & Hernández-Alcántara, A. 2005, ApJ, 627, L61

Prato, L., Simon, M., Mazeh, T., et al. 2002, ApJ, 569, 863

Preibisch, T., & Zinnecker, H. 1999, AJ, 117, 2381

Proszkow, E.-M., Adams, F. C., Hartmann, L. W., & Tobin, J. J. 2009, ApJ, 697, 1020

Raghavan, D., McAlister, H. A., Henry, T. J., et al. 2010, ApJS, 190, 1

Ramírez, S. V., Rebull, L., Stauffer, J., et al. 2004, AJ, 128, 787

Rebull, L. M. 2001, AJ, 121, 1676

Rebull, L. M., Hillenbrand, L. A., Strom, S. E., et al. 2000, AJ, 119, 3026

Reid, M. J., & Brunthaler, A. 2004, ApJ, 616, 872

Reid, M. J., & Honma, M. 2014, ARA&A, 52, 339

Reipurth, B. 2008, Handbook of Star Forming Regions, Volume I: The Northern Sky

Reipurth, B., Guimarães, M. M., Connelley, M. S., & Bally, J. 2007, AJ, 134, 2272

Reipurth, B., Megeath, S. T., Bally, J., & Walawender, J. 2008, The L1617 and L1622 Cometary Clouds in Orion, ed. B. Reipurth, 782

Reipurth, B., Rodríguez, L. F., Anglada, G., & Bally, J. 2004, AJ, 127, 1736

Reipurth, B., Rodríguez, L. F., & Chini, R. 1999, AJ, 118, 983

Reynolds, S. P. 1986, ApJ, 304, 713

Ridge, N. A., Wilson, T. L., Megeath, S. T., Allen, L. E., & Myers, P. C. 2003, AJ, 126, 286

Rizzuto, A. C., Ireland, M. J., Robertson, J. G., et al. 2013, MNRAS, 436, 1694

Rodríguez, L. F., Gómez, Y., & Tafoya, D. 2012, MNRAS, 420, 279

Rodriguez, L. F., & Reipurth, B. 1994, A&A, 281, 882

Rupen, M. P. 1997, VLA Test Memorandum No.202: Referenced Pointing at the VLA (www.vla.nrao.edu/memos/test/202/), ,

Sacco, G. G., Franciosini, E., Randich, S., & Pallavicini, R. 2008, A&A, 488, 167

Saikia, D. J., & Salter, C. J. 1988, ARA&A, 26, 93

Sandstrom, K. M., Peek, J. E. G., Bower, G. C., Bolatto, A. D., & Plambeck, R. L. 2007, ApJ, 667, 1161

Scally, A., & Clarke, C. 2002, MNRAS, 334, 156

Schlafly, E. F., Green, G., Finkbeiner, D. P., et al. 2014, ApJ, 786, 29

—. 2015, ApJ, 799, 116

Seidelmann, P. K., ed. 1992, Explanatory Supplement to the Astronomical Almanac (Mill Valley, California: University Science Books)

Sherry, W. H., Walter, F. M., Wolk, S. J., & Adams, N. R. 2008, AJ, 135, 1616

Sicilia-Aguilar, A., Hartmann, L. W., Fürész, G., et al. 2006, AJ, 132, 2135

Sicilia-Aguilar, A., Hartmann, L. W., Szentgyorgyi, A. H., et al. 2005, AJ, 129, 363

Siess, L., Dufour, E., & Forestini, M. 2000, A&A, 358, 593

Skinner, S., Gagné, M., & Belzer, E. 2003, ApJ, 598, 375

Skinner, S. L. 1993, ApJ, 408, 660

Skinner, S. L., Sokal, K. R., Megeath, S. T., et al. 2009, ApJ, 701, 710

Smart, R. L., & Nicastro, L. 2014, A&A, 570, A87

Stassun, K. G., Mathieu, R. D., Vaz, L. P. R., Stroud, N., & Vrba, F. J. 2004, ApJS, 151, 357

Stassun, K. G., & Torres, G. 2016, ApJ, 831, L6

Stickland, D. J., & Lloyd, C. 2000, The Observatory, 120, 141

Stone, J. M., Ostriker, E. C., & Gammie, C. F. 1998, ApJ, 508, L99

Strassmeier, K. G. 2009, A&A Rev., 17, 251

Strom, K. M., Strom, S. E., Carrasco, L., & Vrba, F. J. 1975, ApJ, 196, 489

Sung, H., Bessell, M. S., & Lee, S.-W. 1997, AJ, 114, 2644

Szentgyorgyi, A. H., Cheimets, P., Eng, R., et al. 1998, in Society of Photo-Optical Instrumentation Engineers (SPIE) Conference Series, Vol. 3355, Optical Astronomical Instrumentation, ed. S. D'Odorico, 242–252

Tachihara, K., Toyoda, S., Onishi, T., et al. 2001, PASJ, 53, 1081

Tan, J. C., Krumholz, M. R., & McKee, C. F. 2006, ApJ, 641, L121

Tobin, J. J., Hartmann, L., Fűrész, G., Hsu, W.-H., & Mateo, M. 2015, AJ, 149, 119

Tobin, J. J., Hartmann, L., Furesz, G., Mateo, M., & Megeath, S. T. 2009, ApJ, 697, 1103

Tonry, J., & Davis, M. 1979, AJ, 84, 1511

Torres, R. M., Loinard, L., Mioduszewski, A. J., & Rodríguez, L. F. 2007, ApJ, 671, 1813

—. 2009, ApJ, 698, 242

Tsujimoto, M., Koyama, K., Kobayashi, N., et al. 2003, AJ, 125, 1537

Tsujimoto, M., Koyama, K., Tsuboi, Y., Goto, M., & Kobayashi, N. 2002, ApJ, 566, 974 van Leeuwen, F. 2007, A&A, 474, 653

Walker, M. G., Mateo, M., Olszewski, E. W., et al. 2015, ApJ, 808, 108

—. 2007, ApJS, 171, 389

Walter, F. M., Sherry, W. H., Wolk, S. J., & Adams, N. R. 2008, The σ Orionis Cluster, ed. B. Reipurth, 732

Ward-Thompson, D., Di Francesco, J., Hatchell, J., et al. 2007, PASP, 119, 855

White, R. J., & Basri, G. 2003, ApJ, 582, 1109

Wilking, B. A., Meyer, M. R., Robinson, J. G., & Greene, T. P. 2005, AJ, 130, 1733

Williams, J. P., & Cieza, L. A. 2011, ARA&A, 49, 67

Xmm-Newton Survey Science Centre, C. 2013, VizieR Online Data Catalog, 9044, 0

Yıldız, M., Çelik Orhan, Z., Örtel, S., & Roth, M. 2017, MNRAS, 470, L25

Zacharias, N., Finch, C., & Frouard, J. 2017, AJ, 153, 166

Zacharias, N., Finch, C. T., Girard, T. M., et al. 2012, VizieR Online Data Catalog, 1322